

Similarity in  
Adverse Pressure Gradient  
Turbulent Flows.

A Ph. D. thesis  
by  
Catherine M. Anderson

School of Engineering and Science  
Victoria University of Technology

Footscray Park Campus  
PO BOX 14428 MCMC  
Melbourne, Victoria 8001  
Australia

27<sup>th</sup> January 2011

## **I ABSTRACT**

The purpose of this research is to experimentally generate increasingly adverse pressure gradient flow data for comparison with published data, to find similarities allowing categorization leading to improved flow prediction.

Two new adverse pressure gradient flows were generated in an open-return wind tunnel. Hot wire anemometry, was used to measure the longitudinal and transverse velocity components along the centreline. Some measurements of the third velocity component were also taken. Single boundary layer type and x-wire probes were used, the former especially for near-wall and spectral measurements.

A pitch calibration technique by Zilberman (1981) was used for the x-wire probes. It involved taking measurements at pitch angles ranging from  $-30$  to  $+30$  degrees to simulate different velocity components. This information was utilized to generate a look-up table. The Siddall and Davies technique was used for calibration of single wire data.

Similar flows from the literature are presented and compared in regard to pressure parameter, freestream velocity, momentum thickness, shape factor, friction velocity and mean velocity scaling. Where available, flow comparisons are made also for Reynolds stresses.

Utilizing the classical APG equilibrium flow data of Clauser (1954b), Newman (1951) and Bradshaw (1966) an 'ideal APG line' for the collapse of velocity deficit profiles scaled with  $U_e \delta^* / \delta$  is defined. This sets a benchmark for comparison with other flows. An equation of this ideal APG line is provided. The standard error of this line is used to define a bandwidth of an acceptable collapse, thus other flows can be analysed and classified to decide the extent of an APG equilibrium region.

The onset of this equilibrium, as defined by the ‘ideal APG line’ and bandwidth, coincides with the onset of equilibrium as described by the pressure parameter,  $\Lambda_{\theta\text{calc}} \approx \text{constant}$ . Distinct characteristics are identified within the APG equilibrium region hence defined for the second and third order moments of the fluctuating velocities, as well as for the terms of the turbulent kinetic energy budget.

## **II DECLARATION OF AUTHENTICITY**

I, Catherine Michelle Anderson, declare that the PhD thesis entitled ‘Similarity in Adverse Pressure Gradient Turbulent Flows’ is no more than 100,000 words in length including quotes and exclusive of tables, figures, appendices, bibliography, references and footnotes. This thesis contains no material that has been submitted previously, in whole or in part, for the award of any other academic degree or diploma. Except where otherwise indicated, this thesis is my own work.

Portions of the data collected, analysed and compiled by me have been shared with Brian Brzek and published in his Master of Science thesis at Rensselaer Polytechnic Institute in 2004. Brian worked under my supervision for a period of 2 months. I provided him with my data in the spirit of collaborative research. It was intended that my Doctoral thesis would have been published before Brian’s thesis. However, due to life events, this did not happen.

Signature

Date

### **III ACKNOWLEDGMENTS**

Words cannot express the gratitude and respect I feel toward my supervisor Associate Professor Özden Turan. Her unwavering support and belief, in both the research and in me fuelled me through the difficult times. Even when she was on sabbatical, I always felt she was just a phone call away, willing to listen and guide me through any ‘experimental catastrophe’ or settle my infuriation with a difficult section of computer code. When I started my research I held Associate Professor Turan in the highest regard, a role model whom I could only ever aspire to be like. Over the years both she and Dr Eren Semercigil have become more than academic mentors: they have become more like family. I am sure that our friendship will continue well past the completion of this thesis.

Under the candidates supervision, two undergraduate students Adis Selmic and Don Chao assisted with some experimental work for one semester in 2004. Brian Brzek, also worked under the candidates supervision, for 2 months, collecting some of the Flow B data. The candidate provided Brian complete and compiled Flow A and Flow B data. These results were published in Brian’s Master of Science thesis at RPI in 2004. These data sets were shared willingly by the candidate and through life events, Brian’s thesis was published prior to the candidate’s own.

I wish also to acknowledge the support of the staff of the School of the Built Environment, in particular Lyn Alyis, Liz Smith, Merv Minnet, Michael Sek and Vincent Roulliard. I would also like to acknowledge the assistance of the friendly staff at the Postgraduate Research Unit, in particular Lesley Birch who always had time for a nice, sanity restoring chat.

I was a recipient of the Vice Chancellors Scholarship to conduct my research and am grateful for this financial support.

Last but not least, I would like to thank ALL of my family. My big brothers, Jeremy and Chris were always there to provide encouragement and guidance, in particular a special thank you to Chris for proof reading this thesis. My little sister, Tracey was always there as a balancing influence. Thank you to my parents, Pauline and Graeme, who, through hard work and personal sacrifice, always provided all their children with the foundations in childhood to achieve throughout life. The encyclopaedia’s, Lego blocks, trips to the museum, the adventure filled backyard, the computers and time spent together filled me with a desire to learn and the tools to achieve.

I hope that Victoria and James will be proud of their mum for completing this thesis and that they will know that I am proud of them every day. Thank you to my husband Brad, for his love and support.

Catherine Anderson

## IV TABLE OF CONTENTS

I	ABSTRACT	ii
II	DECLARATION OF AUTHENTICITY	iv
III	ACKNOWLEDGMENTS	v
IV	TABLE OF CONTENTS	vi
V	LIST OF FIGURES	ix
VI	LIST OF TABLES	xx
VII	NOTATION	xxii
	English	xxii
	Greek	xxiii
	Abbreviations	xxiiv
<b>1</b>	<b>INTRODUCTION</b>	<b>1</b>
<b>2</b>	<b>EXPERIMENTAL EQUIPMENT</b>	<b>5</b>
2.1	Wind Tunnel	5
2.1.1	Location	5
2.1.2	Fan, Diffuser and Settling Chamber	6
2.1.3	Contraction Cone and Pressure Taps	6
2.1.4	Test Section	6
2.1.5	Wall Static Pressure Taps	7
2.1.6	Flexible Top	7
2.2	Pipe flow apparatus.	10
2.2.1	Location	10
2.2.2	Fan and damper	10
2.2.3	Settling Chamber	10
2.2.4	Pipe	10
2.2.5	Wall Static Pressure Taps	11
2.3	Total Head Tubes and Pitot Static Tubes	13
2.3.1	Total Head Tubes	13
2.3.2	Pitot Static Tubes	13
2.4	Hotwire probe equipment.	14
2.4.1	Hardware	14
2.4.2	Hot Wire Probes	14
2.4.3	Data Measurement	14
2.5	Traversing Mechanism	16
<b>3</b>	<b>HOTWIRE CALIBRATION TECHNIQUE</b>	<b>18</b>
3.1	Determination of the extent of the core region:	21

3.2	Reference velocity calibration.	23
3.3	Pitch Calibration.	25
	3.3.1 Equipment Set-up.	25
	3.3.2 Hotwire Probe Data Collection.	26
	3.3.3 Results of the Pitch Calibration	26
3.4	Yaw Calibration	31
	3.4.1 Equipment set-up	31
	3.4.2 Hotwire Probe Data Collection	32
	3.4.3 Calibration Technique	32
3.5	Pipe Velocity Calibration	38
3.6	Single Wire Probe Calibration	40
	3.6.1 Equipment Set-up	40
	3.6.2 Hotwire Probe Data Collection	40
<b>4</b>	<b>FLOW DETAILS</b>	<b>45</b>
4.1	Flow A and Flow B	46
	4.1.1 Entrance shape for Flow A and Flow B	46
	4.1.2 Physical shape and pressure distribution	48
	4.1.3 Flow development, $U_e$ , $\delta$ , $H$	52
	4.1.4 Clauser's equilibrium pressure parameter, $\beta$	57
	4.1.5 Equilibrium Pressure Parameter, $\Lambda_\theta$	59
	4.1.6 Error Analysis for $\Lambda_{\theta calc}$	64
	4.1.7 Determining friction velocity, $u_*$	66
	4.1.8 Turbulence Intensity, $\mathcal{I}$	81
	4.1.9 Comment on relationship between location of transition from increasing APG to decreasing APG	83
4.2	Flow 141 and Flow Han	84
4.3	Classical Flows	94
4.4	Other Flows	103
4.5	Conclusions	116
<b>5</b>	<b>SCALING MEAN FLOW</b>	<b>117</b>
5.1	Velocity Deficit Profiles	118
	5.1.1 Velocity deficit scaled with friction velocity, $u_*$	118
	5.1.2 Discussion on the concept of 'Quality of Collapse'	124
	5.1.3 Velocity deficit scaled with free stream velocity, $U_e$	126
	5.1.4 Zagarola/Smits scaling and definition of the 'ideal' APG line with a band of acceptable collapse and FPG line	133
	5.1.5 Velocity deficit scaled with Zagarola/Smits scale ( $U_e \delta^*/\delta$ )	138
5.2	The ideal APG band and $\Lambda_{\theta calc}$ for 'other' flows	146
5.3	Conclusions	159
<b>6</b>	<b>REYNOLDS STRESSES AND HIGHER ORDER MOMENTS</b>	<b>161</b>
6.1	Reynolds Stresses	162
	6.1.1 Scaling shear stress, $\overline{uv}$ with $u_*^2$ , $uv_{max}$ and $U_e^2 \frac{d\delta}{dx}$	165

6.1.2	Scaling normal stress in the x direction, $\overline{u^2}$ , with $u_*^2$ , $U_e^2$ and $U_e^2 \delta^*/\delta$	177
6.1.3	Scaling normal stress in the y direction, $\overline{v^2}$ , with $u_*^2$ , $U_e^2$ and $U_e^2 \delta^*/\delta$	189
6.1.4	Scaling normal stress in the z direction, $\overline{w^2}$	199
6.1.5	Scaling shear stress, $\overline{uw}$ with $u_*^2$	205
6.2	Higher order moments.	207
6.3	Conclusions	217
<b>7</b>	<b>ENERGY BUDGETS</b>	<b>218</b>
7.1	Introduction	218
7.2	Advection	220
7.3	Production	223
7.4	Diffusion	226
7.5	Dissipation	229
7.5.1	Isotropy	229
7.5.2	Kolmogorov's 5/3rds law	231
7.5.3	Turbulent kinetic energy balance	232
7.5.4	Discussion of dissipation results	233
7.6	Turbulent Kinetic Energy Budget	235
7.7	Conclusions	240
<b>8</b>	<b>CONCLUSIONS</b>	<b>241</b>
<b>9</b>	<b>REFERENCES</b>	<b>244</b>
<b>10</b>	<b>APPENDICES</b>	<b>251</b>
	APPENDIX I Step-by-step instructions for producing the x-wire calibration look-up table.	252
	APPENDIX II Matlab® calibration and conversion code.	253
	APPENDIX III Use of Siddall and Davies technique for calibrating single wire probe.	261
	APPENDIX IV Matlab® code for converting voltage readings from a single wire probe.	262
	APPENDIX V Clauser charts for Flow B.	263
	APPENDIX VI Steps to convert log-law	266
	APPENDIX VII Tabulated data for the classical Flows 2200, 2300, 2500, 3300, and 3500	267
	APPENDIX VIII Velocity deficit scaled with friction velocity for 'other' flows.	269
	APPENDIX IX Velocity deficit scaled with the freestream velocity for 'other' flows.	272
	APPENDIX X Flow 141, plots.	275
	APPENDIX XI Comparison between Flow A and Flow B and Flow Skare	277
	APPENDIX XII Matlab® code for calculating isotropic dissipation.	280

## **V LIST OF FIGURES**

Figure 2.1 Wind tunnel, not to scale. (from Han (2000))	8
Figure 2.2 Pipe flow apparatus (from Han (2000)).	12
Figure 2.3 Schematic of equipment set up for hot wire probe measurements.	15
Figure 2.4 Schematic of the Traversing Mechanism, (from Han 2000).	17
Figure 3.1 X-type hotwire probe a) side view, (b) end view.	20
Figure 3.2 Vertical traverses with Pitot Tube at Location 41 in wind tunnel for a low velocity and high velocity setting.	22
Figure 3.3 Relationship between the reference velocity and the velocity at the location of the hot wire probe calibration.	24
Figure 3.4 Placement of probe holder at Location 41 in the wind tunnel. The large arrow indicates flow direction.	27
Figure 3.5 Probe holder orientation for pitch calibration (side view).	28
Figure 3.6 Voltage from Wire 1 ( $v_1$ ) versus voltage from Wire 2 ( $v_2$ ) for yaw angles ranging from $+45^\circ$ to $-45^\circ$ .	29
Figure 3.7 Probe holder orientation for yaw calibration with relation to center line of wind tunnel (top view).	34
Figure 3.8 Recorded data for the yaw calibration.	35
Figure 3.9 Calibration data of u velocity component for any E1 or E2 velocity pair.	36
Figure 3.10 Calibration data of v velocity component for any E1 or E2 velocity pair.	37
Figure 3.11 Pipe set-up for determining the relationship between pressure drop and velocity near the exit.	39
Figure 3.12 Single wire recorded calibration data and Siddall and Davies fit.	44
Figure 4.1 Configuration of the entrance shape.	47
Figure 4.2 Height and shape of adjustable top for Flow A and Flow B.	49

Figure 4.3 $C_p$ for (a) Flow A and Flow B, $C_p$ with favourable pressure gradient (FPG), zero pressure gradient (ZPG), and 'Increasingly' and 'Decreasingly' adverse pressure gradient (APG) zones labelled for (b) Flow A and (c) Flow B.	51
Figure 4.4 Freestream velocity, $U_e$ (a) Flow A and (b) Flow B	53
Figure 4.5 Velocity profile measured with an x-wire probe at a streamwise location of $x = 2.587$ m with a reference velocity of 22 m/s. Freestream velocity, $U_e = 19.4$ m/s is highlighted with a vertical line.	54
Figure 4.6 Boundary layer thickness, $\delta$ for (a) Flow A and (b) Flow B	55
Figure 4.7 Shape factor, $H$ for (a) Flow A and (b) Flow B	56
Figure 4.8 Clauser's equilibrium pressure parameter, $b$ , for Flow A and Flow B.	58
Figure 4.9 Pressure parameter $\Lambda_{\theta_{calc}}$ , for Flow A, Flow B, Flow Han and Flow 141. The star indicates the start of $\Lambda_{\theta_{calc}} \sim \text{constant}$ , corresponding to the equilibrium region.	61
Figure 4.10 Local equilibrium as defined by $\Lambda_{\theta}$ . (Figure 3, Castillo and Wang, 2004)	62
Figure 4.11 Clauser chart, single wire measurements for Flow B. Further results are given in Appendix V.	71
Figure 4.12 Pitot traverses $\pm 200$ mm from centreline at $x = 3.558$ m, Flow B, to demonstrate flow symmetry.	74
Figure 4.13 Total head tube readings on floor of tunnel at different distances from centreline, at 4 streamwise locations, for Flow B, to show symmetry.	75
Figure 4.14 Percentage difference in pressure readings either side of centreline for 4 streamwise locations, for Flow B.	76
Figure 4.15 Friction velocity, $u_*$ as determined by Clauser Charts, momentum integral and Preston Tubes with Patel's correction for (a) Flow A and (b) Flow B.	79
Figure 4.16 Average friction velocity, $u_*$ for (a) Flow A and (b) Flow B.	80
Figure 4.17 Turbulence intensity for the core region of (a) Flow A and (b) Flow B.	82
Figure 4.18 $C_p$ for Flows A, B, Han and 141.	86

Figure 4.19 Freestream velocity, $U_e$ , for Flow 141, Flow Han, Flow A and Flow B.	87
Figure 4.20 $\delta^*/\delta$ for Flows A, B, Han and 141.	88
Figure 4.21 Shape Factor, H, for Flow 141, Flow Han, Flow A and Flow B.	89
Figure 4.22 Friction velocity, $u_*$ for Flow 141, Flow Han, Flow A and Flow B.	90
Figure 4.23 Pressure parameter $\Lambda_{\theta\text{calc}}$ for Flow 141, Flow Han, Flow A and Flow B.	91
Figure 4.24 Pressure distribution $C_p$ , for the classical flows.	96
Figure 4.25 Freestream velocity, $U_e$ , for the classical flows.	97
Figure 4.26 Boundary layer thickness, $\delta$ , for the classical flows.	98
Figure 4.27 Shape factor, H, for the classical flows.	99
Figure 4.28 Clauser's equilibrium pressure parameter, $\beta$ , for the classical flows.	100
Figure 4.29 Friction velocity, $u_*$ , for Flow 2200, Flow 2300, Flow 2500, and Flow 3500.	101
Figure 4.30 Castillo and George equilibrium pressure parameter $\Lambda_{\theta\text{calc}}$ for classical flows.	102
Figure 4.31 Pressure distribution, $C_p$ for (a) Flow 1100, (b) Flow 1200, (c) Flow 2400, (d) Flow 2900, (e) Flow 3600, (f) Flow 3700, (g) Flow 3800, (h) Flow 4000, (i) Flow 5000, (j) Flow 5100, and (k) Flow Skare.	107
Figure 4.32 Shape factor H for (a) Flow 1100, (b) Flow 1200, (c) Flow 2400, (d) Flow 2900, (e) Flow 3600, (f) Flow 3700, (g) Flow 3800, (h) Flow 4000, (i) Flow 5000, (j) Flow 5100, and (k) Flow Skare.	109
Figure 4.33 Boundary layer thickness, $\delta$ for (a) Flow 1100, (b) Flow 1200, (c) Flow 2400, (d) Flow 2900, (e) Flow 3600, (f) Flow 3700, (g) Flow 3800, (h) Flow 4000, (i) Flow 5000, (j) Flow 5100, and (k) Flow Skare.	111

- Figure 4.34 Clauser's equilibrium pressure parameter,  $\beta$  for (a) Flow 1100, (b) Flow 1200, (c) Flow 2400, (d) Flow 2900, (e) Flow 3600, (f) Flow 3700, (g) Flow 3800, (h) Flow 4000, (i) Flow 5000, (j) Flow 5100, and (k) Flow Skare. Note the varying vertical scale for each flow. 113
- Figure 4.35 Castillo and George's pressure parameter,  $\Lambda_{\theta\text{calc}}$  for (a) Flow 1100, (b) Flow 1200, (c) Flow 2400, (d) Flow 2900, (e) Flow 3600, (f) Flow 3700, (g) Flow 3800, (h) Flow 4000, (i) Flow 5000, (j) Flow 5100, and (k) Flow Skare. 115
- Figure 5.1 Mean velocity deficit scaled with friction velocity  $u_*$  for classical Flows (a) 2200, (b) 2300, (c) 2500 and (d) 3500 120
- Figure 5.2 Friction velocity,  $u_*$ , for Flow 2200, Flow 2300, Flow 2500, Flow 3300 and Flow 3500. Repeat of Figure 4.29. The friction velocity for other flows is plotted in Figure 4.16 and Figure 4.22. 121
- Figure 5.3 Mean velocity deficit scaled with friction velocity  $u_*$  for (a) Flow 141, (b) Flow Han, (c) Flow A and (d) Flow B. The arrow indicates flow direction. 122
- Figure 5.4 Mean velocity deficit scaled with friction velocity  $u_*$  for (a) Flow 3600, (b) 3700, (c) Flow 3800. 123
- Figure 5.5 Mean velocity deficit scaled with freestream velocity  $U_e$  for classical Flows (a) 2200, (b) 2300, (c) 2500 and (d) 3500 130
- Figure 5.6 Mean velocity deficit scaled with freestream velocity  $U_e$  for (a) Flow 141, (b) Flow Han, (c) Flow A and (d) Flow B. The arrow indicates flow direction. 131
- Figure 5.7 Mean velocity deficit scaled with freestream velocity  $U_e$  for (a) Flow 3600, and (b) Flow 3700. 132
- Figure 5.8 Classical data of Newman, Clauser and Bradshaw, Flows 2200, 2300, 2500 and 3500. Illustrated with the determined curve fit for 'ideal' APG behaviour and the upper and lower limits of the acceptable range. 135
- Figure 5.9 Favourable pressure gradient Flow 1300 velocity deficit with Zagarola/Smits scaling. Illustrated with the determined arithmetic average for 'ideal' FPG behaviour. 137
- Figure 5.10 Mean velocity deficit scaled with Zagarloa/Smits scale  $U_e(\delta^*/\delta)$  for Flow 141. The two solid lines represent ideal APG behaviour and the ideal FPG behaviour. 140

Figure 5.11 Mean velocity deficit scaled with Zagarloa/Smits scale $U_e(\delta^*/\delta)$ for Flow 141. Ideal APG line and the bandwidth of acceptable collapse are also given. Profiles falling outside the acceptable band have been removed.	141
Figure 5.12 Pressure parameter $\Lambda_{\theta\text{calc}}$ , for Flow A, Flow B, Flow Han and Flow 141	142
Figure 5.13 Mean velocity deficit scaled with Zagarloa/Smits scale $U_e(\delta^*/\delta)$ for (a) Flow Han, (b) Flow A, and (c) Flow B. The two solid lines represent ideal APG and FPG behaviour.	143
Figure 5.14 Mean velocity deficit scaled with Zagarloa/Smits scale $U_e(\delta^*/\delta)$ for (a) Flow Han, (b) Flow A, and (c) Flow B. Ideal APG line and the bandwidth of acceptable collapse are also given. Profiles falling outside the acceptable band have been removed.	144
Figure 5.15 Flow 1100 (a) $\Lambda_{\theta\text{calc}}$ , (b) mean velocity deficit profiles scaled with $U_e^2(\delta^*/\delta)$ , (c) only the profiles within the ideal APG band.	147
Figure 5.16 Flow 1200 (a) $\Lambda_{\theta\text{calc}}$ , (b) mean velocity deficit profiles scaled with $U_e^2(\delta^*/\delta)$ , (c) only the profiles within the ideal APG band.	148
Figure 5.17 Flow 2400 (a) $\Lambda_{\theta\text{calc}}$ , (b) mean velocity deficit profiles scaled with $U_e^2(\delta^*/\delta)$ , (c) only the profiles within the ideal APG band.	149
Figure 5.18 Flow 2900 (a) $\Lambda_{\theta\text{calc}}$ , (b) mean velocity deficit profiles scaled with $U_e^2\delta^*/\delta$ , (c) only the profiles within the ideal APG band.	150
Figure 5.19 Flow 3600 (a) $\Lambda_{\theta\text{calc}}$ , (b) mean velocity deficit profiles scaled with $U_e^2\delta^*/\delta$ , (c) only the profiles within the ideal APG band.	151
Figure 5.20 Flow 3700 (a) $\Lambda_{\theta\text{calc}}$ , (b) mean velocity deficit profiles scaled with $U_e^2\delta^*/\delta$ , (c) only the profiles within the ideal APG band.	152
Figure 5.21 Flow 3800 (a) $\Lambda_{\theta\text{calc}}$ , (b) mean velocity deficit profiles scaled with $U_e^2\delta^*/\delta$ , (c) only the profiles within the ideal APG band.	153
Figure 5.22 Flow 4000 (a) $\Lambda_{\theta\text{calc}}$ , (b) mean velocity deficit profiles scaled with $U_e^2\delta^*/\delta$ , (c) only the profiles within the ideal APG band.	154

Figure 5.23 Flow 5000 (a) $\Lambda_{\theta_{\text{calc}}}$ , (b) mean velocity deficit profiles scaled with $U_e^2 \delta^* / \delta$ , (c) only the profiles within the ideal APG band.	155
Figure 5.24 Flow 5100 (a) $\Lambda_{\theta_{\text{calc}}}$ , (b) mean velocity deficit profiles scaled with $U_e^2 \delta^* / \delta$ , (c) only the profiles within the ideal APG band.	156
Figure 5.25 Flow Skare (a) $\Lambda_{\theta_{\text{calc}}}$ , (b) mean velocity deficit profiles scaled with $U_e^2 \delta^* / \delta$ , (c) only the profiles within the ideal APG band.	157
Figure 6.1 Shear stress $\overline{uv}$ scaled with friction velocity $u_*^2$ for Flow A. (a) All stations, (b) before APG equilibrium region, and (c) APG equilibrium region.	168
Figure 6.2 Shear stress $\overline{uv}$ scaled with friction velocity $u_*^2$ for Flow B. (a) All stations, (b) before APG equilibrium region, and (c) APG equilibrium region.	169
Figure 6.3 Shear stress $uv$ scaled with friction velocity $u_*^2$ . The solid lines are the DNS results of Sung and Lee (2008). The symbols present the experimental data of Nagano et al (1992). The arrow indicates the streamwise direction and highlights the shift in the $y$ location of the peak. (Figure 11 of Lee and Sung, 2008, p 574)	170
Figure 6.4 Flow 141, $\overline{uv}$ scaled with friction velocity. (Onset of equilibrium occurs at $x = 2.1$ m)	171
Figure 6.5 Shear stress $\overline{uv}$ scaled with the maximum shear stress $uv_{\text{max}}$ for Flow A. (a) All stations, (b) before APG equilibrium region, and (c) APG equilibrium region.	172
Figure 6.6 Shear stress $\overline{uv}$ scaled with the maximum shear stress $uv_{\text{max}}$ for Flow B. (a) All stations, (b) before APG equilibrium region, and (c) APG equilibrium region.	173
Figure 6.7 Shear stress $\overline{uv}$ scaled with $U_e^2(d\delta/dx)$ of Castillo/George for Flow A. (a) All stations, (b) before APG equilibrium region, and (c) APG equilibrium region.	174
Figure 6.8 Shear stress $\overline{uv}$ scaled with $U_e^2(d\delta/dx)$ of Castillo/George for Flow B. (a) All stations, (b) before APG equilibrium region, and (c) APG equilibrium region.	175

- Figure 6.9 Normal stress  $\overline{u^2}$  scaled with the friction velocity  $u_*^2$  for Flow A. (a) All stations, (b) before APG equilibrium region, and (c) APG equilibrium region. 180
- Figure 6.10 Normal stress  $\overline{u^2}$  scaled with the friction velocity  $u_*^2$  for Flow B. (a) All stations, (b) before APG equilibrium region, and (c) APG equilibrium region. 181
- Figure 6.11 DNS results of Sung and Lee (solid line) and experimental results of Nagano et al (1992) (solid symbols) for  $u_{rms}$  scaled with  $u_*$ . The arrow indicates the streamwise direction and highlights the shift in the  $y$  location of the peak. (Figure 10a of Lee and Sung, 2008, p 573) 182
- Figure 6.12 Normal stress  $\overline{u^2}$  scaled with the Castillo/George scaling, freestream velocity  $U_e^2$  for Flow A. (a) All stations, (b) before APG equilibrium region, and (c) APG equilibrium region. 183
- Figure 6.13 Normal stress  $\overline{u^2}$  scaled with the Castillo/George scaling, the freestream velocity  $U_e^2$  for Flow B. (a) All stations, (b) before APG equilibrium region, and (c) APG equilibrium region. 184
- Figure 6.14 Reynolds stress  $\overline{u^2}$  scaled with  $U_e u_\tau$  (Figure 7(a) of Aubertine and Eaton (2005)) 185
- Figure 6.15 Normal stress  $\overline{u^2}$  scaled with the Zagarola/Smits scaling,  $U_e^2(\delta^*/\delta)$  for Flow A. (a) All stations, (b) before APG equilibrium region, and (c) APG equilibrium region. 186
- Figure 6.16 Normal stress  $\overline{u^2}$  scaled with the Zagarola/Smits scaling,  $U_e^2(\delta^*/\delta)$  for Flow B. (a) All stations, (b) before APG equilibrium region, and (c) APG equilibrium region. 187
- Figure 6.17  $v_{rms}$  scaled with friction velocity. The symbols represent the data of Nagano et al (1992) while the solid lines are the DNS results of Lee and Sung (2008). The arrow indicates the streamwise direction. (Figure 10(a) of Lee and Sung, 2008, p 573) 191
- Figure 6.18 Normal stress  $\overline{v^2}$  scaled with the friction velocity,  $u_*^2$  for Flow A. (a) All stations, (b) before APG equilibrium region, and (c) APG equilibrium region. 192
- Figure 6.19 Normal stress  $\overline{v^2}$  scaled with the friction velocity,  $u_*^2$  for Flow B. (a) All stations, (b) before APG equilibrium region, and (c) APG equilibrium region. 193

Figure 6.20 Normal stress $\overline{v^2}$ scaled with the freestream velocity, $U_e^2$ for Flow A. (a) All stations, (b) before APG equilibrium region, and (c) APG equilibrium region.	194
Figure 6.21 Normal stress $\overline{v^2}$ scaled with the freestream velocity, $U_e^2$ for Flow B. (a) All stations, (b) before APG equilibrium region, and (c) APG equilibrium region.	195
Figure 6.22 Normal stress $\overline{v^2}$ scaled with Zagarola/Smits scaling, $U_e^2(\delta^*/\delta)$ for (a) Flow A, (b) Before APG equilibrium region, (c) APG equilibrium region.	196
Figure 6.23 Normal stress $\overline{v^2}$ scaled with Zagarola/Smits scaling, $U_e^2(\delta^*/\delta)$ for Flow B. (a) All stations, (b) before APG equilibrium region, and (c) APG equilibrium region.	197
Figure 6.24 Normal stress $\overline{w^2}$ scaled with friction velocity, $u_*^2$ for 2 locations in Flow A.	202
Figure 6.25 Comparison between measured $\overline{w^2}$ and the estimate $\overline{w^2} = 0.3(\overline{u^2} + \overline{v^2})$ .	203
Figure 6.26 Comparison between measured $\overline{uw^2}$ and the estimate $\overline{uw^2} = 0.3(\overline{u^3} + \overline{uv^2})$ .	204
Figure 6.27 Lateral shear stress $\overline{uw}$ scaled with friction velocity, $u_*^2$ for 2 locations of Flow A.	206
Figure 6.28 $\overline{u^3}$ scaled with friction velocity $u_*^3$ for Flow A (left column) and Flow B (right column). (a) and (b), All stations; (c) and (d), before APG equilibrium region; (e) and (f), within the APG equilibrium region.	209
Figure 6.29 $\overline{u^3}$ scaled with freestream velocity $U_e^3$ for Flow A (left column) and Flow B (right column). (a) and (b), All stations; (c) and (d), before APG equilibrium region; (e) and (f), within the APG equilibrium region.	210
Figure 6.30 $\overline{v^3}$ scaled with friction velocity $u_*^3$ for Flow A (left column) and Flow B (right column). (a) and (b), All stations; (c) and (d), before APG equilibrium region; (e) and (f), within the APG equilibrium region.	211

Figure 6.31  $\overline{v^3}$  scaled with freestream velocity  $U_e^3$  for Flow A (left column) and Flow B (right column). (a) and (b), All stations; (c) and (d), before APG equilibrium region; (e) and (f), within the APG equilibrium region. 212

Figure 6.32  $\overline{uv^2}$  scaled with friction velocity  $u_*^3$  for Flow A (left column) and Flow B (right column). (a) and (b), All stations; (c) and (d), before APG equilibrium region; (e) and (f), within the APG equilibrium region. 213

Figure 6.33  $\overline{uv^2}$  scaled with freestream velocity  $U_e^3$  for Flow A (left column) and Flow B (right column). (a) and (b), All stations; (c) and (d), before APG equilibrium region; (e) and (f), within the APG equilibrium region. 214

Figure 6.34  $\overline{u^2v}$  scaled with freestream velocity  $U_e^3$  for Flow A (left column) and Flow B (right column). (a) and (b), All stations; (c) and (d), before APG equilibrium region; (e) and (f), within the APG equilibrium region. 215

Figure 6.35  $\overline{u^2v}$  scaled with friction velocity  $u_*^3$  for Flow A (left column) and Flow B (right column). (a) and (b), All stations; (c) and (d), before APG equilibrium region; (e) and (f), within the APG equilibrium region. 216

Figure 7.1 Advection terms from location  $x = 3.663$  m demonstrating their equal but opposite nature. Where Term 1 is  $U \frac{1}{2} \frac{\partial}{\partial x} (1.3\overline{u^2} + 1.3\overline{v^2})$ , and Term 2 is  $V \frac{1}{2} \frac{\partial}{\partial y} (1.3\overline{u^2} + 1.3\overline{v^2})$ . 221

Figure 7.2 Advection, production, dissipation and diffusion terms at location  $x = 3.663$  m. 222

Figure 7.3 Production terms non-dimensionalised with  $\delta/u_*^3$  at locations (a)  $x = 3.379$  m and (b)  $x = 3.663$  m for Flow B. Both locations are within the ideal APG band. The terms are defined as Term 1:  $-(\overline{u^2} - \overline{v^2}) \frac{dU}{dx}$ , Term 2:  $-\overline{uv} \frac{dU}{dy}$ . 225

Figure 7.4 Diffusion terms, non-dimensionalised with  $\delta/u_*^3$  for Flow B at 3 locations before the APG equilibrium region, namely a)  $x = 0.758$  m, b)  $x = 1.392$  m, and c)  $x = 1.881$  m. The terms are defined as Term 1:  $\frac{\partial}{\partial x} (1.3\overline{u^3} + 1.3\overline{uv^2})$  and Term 2:  $\frac{\partial}{\partial y} (1.3\overline{v^3} + 1.3\overline{u^2v})$ . 227

Figure 7.5 Diffusion terms, non-dimensionalised with  $\delta/u_*^3$  for Flow B at 3 locations in the APG equilibrium region, a)  $x = 3.074$  m, b)  $x = 3.379$  m, and c)  $x = 3.663$  m. The terms are defined as Term 1:  $\frac{\partial}{\partial x} (1.3\overline{u^3} + 1.3\overline{uv^2})$  and Term 2:  $\frac{\partial}{\partial y} (1.3\overline{v^3} + 1.3\overline{u^2v})$ . 228

Figure 7.6 Comparison plots for 3 different ways off determining the rate of dissipation of turbulent kinetic energy, namely, dissipation based on isotropy, dissipation based on the Kolmogorov's 5/3rds law and dissipation as the remainder of the turbulent kinetic energy balance. At two locations for Flow B, (a)  $x = 2.587$  m before APG equilibrium and (b)  $x = 3.553$  m, within APG equilibrium region 234

Figure 7.7 Turbulent kinetic energy budget for three locations before the APG equilibrium region, for Flow B. The horizontal scale is  $y/\delta$ . 236

Figure 7.8 Turbulent kinetic energy budget for three locations within the APG equilibrium region, for Flow B. The horizontal scale is  $y/\delta$ . 237

Figure 7.9 Streamwise development of the rate of dissipation for Flow B. The arrow indicates the flow direction. The first three locations are before the APG equilibrium region and the last three profiles are within the APG equilibrium region. 238

Figure 7.10 Streamwise development of the turbulent kinetic energy production rate for Flow B. The arrow indicates the flow direction. The first three locations are before the APG equilibrium region and the last three profiles are within the APG equilibrium region. 239

Figure 10.1 Clauser charts for Flow B. Single wire probe data. Each plot a) to i) is labelled with the gradient which is used to determine the friction velocity  $u_*$ , the  $R^2$  value which is an indication of the quality of fit, and  $x$  the stream wise location. See Chapter 4.1.6 for more details. 265

Figure 10.2 Velocity deficit scaled with friction velocity, $u_*$ for a) Flow 1100, b) Flow 1200, c) Flow 2400, d) Flow 2900, e) Flow 3600, f) Flow 3700, g) Flow 3800, h) Flow 4000, i) Flow 5000, j) Flow 5100 and k) Flow Skare.	271
Figure 10.3 Velocity deficit scaled with free stream velocity, $U_e$ for a) Flow 1100, b) Flow 1200, c) Flow 2400, d) Flow 2900, e) Flow 3600, f) Flow 3700, g) Flow 3800, h) Flow 4000, i) Flow 5000, j) Flow 5100 and k) Flow Skare.	274
Figure 10.4 Flow 141, $uv$ scaled with $U_e$ . Demonstrating, in the flow direction, $x$ , an increase in magnitude and a shift away from the wall of peak location.	275
Figure 10.5 Flow 141. $u_{rms}$ scaled with freestream velocity $U_e$ .	275
Figure 10.6 Flow 141. $v_{rms}$ scaled with freestream velocity $U_e$ .	276
Figure 10.7 Flow 141. $w_{rms}$ scaled with freestream velocity $U_e$ .	276
Figure 10.8 Comparison between Flow A, Flow B and Skare, demonstrating similarity of freestream velocity.	277
Figure 10.9 Comparison between Flow A, Flow B and Skare, demonstrating development of boundary layer thickness.	277
Figure 10.10 Comparison between Flow A, Flow B and Skare, demonstrating development of shape factor, $H$ .	278
Figure 10.11 Comparison between Flow A, Flow B and Skare, demonstrating difference in behaviour of friction velocity.	278
Figure 10.12 Comparison between Flow A, Flow B and Skare, demonstrating difference in skin friction coefficient, $C_f$ .	279
Figure 10.13 Comparison between Flow A, Flow B and Skare, demonstrating behaviour of $\Lambda_{\theta calc}$ . Note that all three flows exhibit a region of near constant $\Lambda_{\theta calc}$ .	279

## VI LIST OF TABLES

Table 2.1 Location of Wall Static Pressure Taps.	9
Table 3.1 Coefficients of least squares, linear fits to measured data of voltage from Wire 1 and Wire 2 for different Yaw Angles. Data recorded at Location 41.	30
Table 3.2 Single wire calibration data	42
Table 3.3 Coefficients for Equation 3-4 ( $E_2 = AU_e + BU_e^{1/2} + C$ ) for single wire probe	43
Table 4.1 Height of adjustable top for Flow A and Flow B.	50
Table 4.2 The location of the onset of APG flow equilibrium as defined by the pressure parameter $\Lambda_{\theta_{calc}}$ where $x = 0$ corresponds to the start of the test section.	63
Table 4.3 Uncertainty of each term appearing in the expression for $\Lambda_{\theta_{calc}}$ for Flow A, Flow B, Flow 141, and Flow Han.	65
Table 4.4 Summary data Flow 141.	92
Table 4.5 Summary data Flow Han.	92
Table 4.6 Summary data Flow A.	93
Table 4.7 Summary data Flow B.	93
Table 4.8 Summary and description of classical adverse pressure gradient flows. Flow designation from the 1968 Stanford Conference (Coles et al)	95
Table 4.9 Summary and description of additional Adverse Pressure Gradient flows.	105
Table 5.1 Quality of collapse data for mean velocity deficit scaled with friction velocity.	125
Table 5.2 Coefficients for the 10 <sup>th</sup> order polynomial fit to define bandwidth of acceptable APG equilibrium collapse.	136

Table 5.3 Location of the first velocity deficit profile to fall within the APG equilibrium band.	145
Table 5.4 Onset of equilibrium as defined by $\Lambda_{\theta_{calc}}$ and first profile to fall within ideal APG band	158
Table 6.1 Quality of collapse (Average from $y/\delta = 0.2, 0.4$ and $0.6$ )	176
Table 6.2 Quality of collapse for (Average from $y/\delta = 0.2, 0.4, 0.6$ and $0.8$ )	188
Table 6.3 Quality of collapse for (Average from $y/\delta = 0.2, 0.4, 0.6$ and $0.8$ )	198
Table 7.1 Location of the peak value of stresses for Flow B in the APG equilibrium region.	224

## VII NOTATION

### English

$C_P$	Dimensionless pressure parameter, [-]
$D$	Probe diameter, [m]
$D$	Outer diameter of total head tube, [m]
$E$	Voltage required to maintain constant wire temperature, [volts]
$E$	Total error, [-]
$E_1$	Wire 1 voltage, [volts]
$E_2$	Wire 2 voltage, [volts]
$f_o$	a function for the mean velocity deficit, [-]
$f_u, f_v$	functions for the Reynolds normal stresses, [-]
$f_{uv}$	A function for the Reynolds shear stresses, [-]
$\xi$	Turbulence intensity, [-]
$P$	Static pressure, [N/m <sup>2</sup> ]
$\Delta P$	Dynamic pressure, [N/m <sup>2</sup> ]
$P_d$	Pressure drop, [mmH <sub>2</sub> O]
$P_0$	Pressure at the reference location [N/m <sup>2</sup> ]
$p_o$	Stagnation pressure, [N/m <sup>2</sup> ]
$p_s$	Static pressure, [N/m <sup>2</sup> ]
$Q$	Reference velocity [m/s]
$R$	Pipe radius, [m]
$Re$	Reynolds numbers, [-]
$T$	Time period, [s]
$U$	Longitudinal mean velocity, [m/s]
$U_e$	Freestream velocity, [m/s]
$U_0$	Freestream velocity at the reference location, [m/s]
$U_{so}$	is the outer scale for velocity deficit, [m/s]
$R_{sou}, R_{sov},$	are the outer scales for the Reynolds stresses
$R_{souv}$	is the outer scale for the Reynolds shear stress
$u$	x-component of the instantaneous velocity, [m/s]
$\overline{u^2}$	Normal stress in the x direction, [m <sup>2</sup> /s <sup>2</sup> ]
$u'$	Fluctuating part of the instantaneous velocity, in the x-direction, [m/s]
$u^+$	Non-dimensional velocity, [-]
$u^*$	Friction velocity, [m/s]
$u_{rms}$	Root mean square of the velocity fluctuation in u
$\overline{uv}$	Shear stress, [(m <sup>2</sup> /s <sup>2</sup> )]
$\overline{uw}$	Lateral shear stress, [m <sup>2</sup> /s <sup>2</sup> ]
$V$	Mean velocity, in the y direction [m/s]

$V_{cal}$	Velocity at the hot wire probe calibration location, [mmH <sub>2</sub> O]
$V_{cl}$	Centreline velocity, measured with a total head tube, [ mmH <sub>2</sub> O]
$V_{ref}$	Velocity at the reference location, [mmH <sub>2</sub> O]
$\overline{v^2}$	Normal stress in the y direction, [m <sup>2</sup> /s <sup>2</sup> ]
$w$	Velocity in the z-direnction, [m/s]
$\overline{w^2}$	Normal stress in the z direction, [m <sup>2</sup> /s <sup>2</sup> ]
$x$	Distance in the flow direction, [m]
$x_{max}$	Maximum x value, the streamwise distance of the final measurement location
$y$	Vertical height from the floor, [m]
$y^+$	Non-dimensional distance from the wall, [-]
$z_o$	Elevation of the inner tube, [m].
$z_s$	Elevation of the outer tube, [m],
Greek	
$\alpha$	Pressure parameter, [m/s <sup>2</sup> ]
$\beta$	Clauser's equilibrium pressure parameter, $\beta \equiv -\frac{\delta^*}{\rho u_*^2} \frac{dP_\infty}{dx}$ , [-]
$\Delta$	Non-dimensional pressure parameter, [-]
$\gamma$	Pitch angle, [degrees]
$\delta$	Boundary layer thickness, [m]
$\delta^+$	$\delta^+ = \frac{\delta u_*}{\nu}$
$\delta^*$	Displacement thickness, [m]
$\theta$	Momentum thickness, [m]
$\kappa$	Constant, [-],
$\Lambda_\theta$	Pressure parameter, [-]
$\Lambda_{\theta calc}$	Pressure parameter determined using direct calculation method, [-]
$\mu$	Dynamic viscosity, [N s/m <sup>2</sup> ]
$\nu$	Kinematic viscosity, [m <sup>2</sup> /s]
$\rho$	Fluid density, [kg/m <sup>3</sup> ]
$\tau_w$	Wall shear stress, [kg m/s <sup>2</sup> ]
$\omega$	Experimental uncertainty of each term, [-]

## Abbreviations

AIP	Asymptotic Invariance Principal
APG	Adverse Pressure Gradient
ADC	Analogue to Digital Converter
C/G	Castillo and George in relation to the $U_e$ scale
CTA	Constant Temperature Anemometer
DAC	Digital to Analogue Converter
DNS	Direct Numerical Simulation
fft	Fast Fourier transform
FPG	Favourable Pressure Gradient
OD	Outside Diameter
PC	Personal Computer
RANS	Reynolds Averaged Navier-Stokes
rms	Root Mean Square
ZPG	Zero Pressure Gradient
Z/S	Zagarola and Smits in relation to the $U_e \delta^*/\delta$ scale

# 1 INTRODUCTION

In an adverse pressure gradient flow, the pressure increases in the flow direction, and thus, the fluid travels from a region of low pressure to a region of higher pressure. The opposite occurs in pipe flow where the pressure gradient drives the flow. High pressure at the upstream end of the pipe produces flow along the pipe to a lower pressure region downstream. Adverse pressure gradient flows are common in daily life. An example is the flow in a diffuser. As the cross sectional area increases, the flow velocity slows down, and the pressure increases in the flow direction, resulting in adverse pressure conditions. The rear windshield of a moving car causes the same effect as a diffuser. The increasing cross-sectional area decreases the flow velocity, and an adverse pressure gradient results.

Whilst it is an extremely common phenomenon, there are still unknowns about the characteristics of adverse pressure gradient flows. The objective of this research is to conduct an experimental investigation to improve the understanding of these flows and to determine a set of universal characteristics. This type of information is essential in producing more accurate computer simulation models. These models can aid the design of cars and aircraft, producing more efficient vehicles.

Modelling the turbulent flow of smoke and air, which results from a fire, is an exciting application of the proposed research. During a fire, a hot plume of gas and smoke particles rises. After the plume hits a ceiling, producing a point of stagnation at the centre of the plume, it turns and travels along the ceiling. Thus, the plume moves under adverse pressure gradient conditions as it approaches the ceiling. Improved modelling of smoke spread will allow increased fire safe designs, and ultimately, save lives.

There are two types of adverse pressure gradient flows, namely ‘increasing’ and ‘decreasing’. There is a lack of empirical data on the ‘increasing’ adverse pressure gradient cases. This void in the literature gives rise to the need for a more thorough experimental investigation.

Most adverse pressure gradient flows are turbulent. Turbulence is found in most practical applications. Two processes dominate turbulent flows: the rate of production of turbulence kinetic energy and the rate of dissipation of that energy. Rate of dissipation is one of the most important parameters for characterizing any class of turbulent flow. To measure the rate of dissipation, three techniques are employed in this work, namely, by the assumption of isotropy, the Kolmogorov  $5/3^{\text{rd}}$ 's law and by the remainder of the turbulence kinetic energy equation.

The significance of this research is in its potential to provide a fundamental understanding of adverse pressure gradient flows with direct practical applications resulting from this understanding. The existing experimental setup allows systematic variation of the pressure gradient to investigate a range of cases. With this understanding, comes the possibility of determining universal characteristics to describe adverse pressure gradient flows.

This thesis is presented in ten chapters. Whilst all terms are defined when they are first used, for the reader's convenience, a complete list of notation and an explanation of all abbreviations are provided in the forward matter. Each chapter has its own introduction, encompassing a literature review and where appropriate, conclusions are provided at the end of each chapter. To be accessible, figures are given at the end of each section, they are numbered sequentially with the chapter number, for example Figure 1.1, Figure 1.2. Table numbering has the same format. A list of figures and a list of tables with their captions and page numbers is given in the forward matter.

An alphabetic list of all references is given in Chapter 9. In the text, references are indicated by the surname of the author and the year of publication. The text also directs the reader to extra material contained in the appendices, contained in Chapter 10.

A detailed description of the experimental equipment used is contained in Chapter 2. Each section is devoted to a different apparatus, with clear sub-section titles used to allow the reader to easily access specific details by first reading the table of contents. A priority has been given to provide detailed information such as dimensions, model

types, material types and procedures followed, with the intent that the experiments can be easily reproduced by others.

Chapter 3 is devoted to the method used to calibrate the hotwire probes. This chapter includes a review of some other methods used. Pitch and yaw calibrations were carried out for x-type hotwire probes and these are discussed in their own sections. The method utilised for calibration of single wire probes is also provided.

In Chapter 4, flow details for the two new experimental flows are given. The details include information on how the flows were generated, the test section entrance shape and the physical shape of the test section roof. Also, 22 flows from the literature are given for comparison purposes. Measured and calculated quantities are presented to provide a basis of understanding of the flow characteristics. Freestream velocity development, boundary layer growth, shape factor, Clauser's equilibrium pressure parameter and the pressure parameter of Castillo and George are also provided. These basic characteristics form the foundation of classification and comparison with other flows.

Mean flow scaling is presented in Chapter 5, with mean deficit scaled with friction velocity, freestream velocity, and the Zagarola/Smits scaling of  $U_e \delta^*/\delta$ . Each scale is presented in a subsection with introductory explanations and review of the literature. Comparisons are made with the 22 flows described in Chapter 4. A method for quantifying the degree of collapse of profiles is described. This method is also utilised for Reynolds stress scaling. The Zagarola/Smits scaling of  $U_e \delta^*/\delta$ , is utilised to define an 'ideal' APG region. This region is shown to be in agreement with the  $\Lambda_{\theta_{calc}}$  definition of equilibrium, and is used in the next chapter to explain Reynolds stress scaling.

The Reynolds stresses with scaling factors of friction velocity,  $u_*$ , freestream velocity,  $U_e$ , Castillo/George scaling of  $U_e^2 d\delta/dx$  and the Zagarola/Smits scaling of  $U_e^2 \delta^*/\delta$  are presented in Chapter 6. A comparison based on quality of collapse is done amongst the scaling parameters. In addition, it is shown that for each parameter, a difference is evident between the region of flow identified by the ideal APG band, as defined in

Chapter 5. A better collapse of profiles is achieved within the APG equilibrium region. Higher order moments are also presented in this chapter in preparation for energy budgets.

The turbulent kinetic energy balance is presented in Chapter 7. The individual contributions of advection, production, diffusion and the rate of dissipation are given. Again, a difference between locations within the APG equilibrium region and those before it is discernable with the energy budgets.

Publications arising from this thesis:

‘An Adverse Pressure Gradient Turbulent Boundary Layer: New Measurements and Outer Scaling’, Anderson, C.M., Turan, Ö.F., Brzek, B. and Castillo, L., Poster presentation, AIAA, 2004

‘Adverse Pressure Gradient Turbulent Boundary Layer Flows: Part 1: Flow Development’ Anderson, C.M., Turan, Ö.F., Brzek, B. and Castillo, L., 15<sup>th</sup> Australasian Fluid Mechanics Conference, Sydney, Australia, 2004

‘Adverse Pressure Gradient Turbulent Boundary Layer Flows: Part 2: Scaling of Reynolds Stresses’, Brzek, B., Castillo, L., Anderson, C.M., and Turan, Ö.F., 15<sup>th</sup> Australasian Fluid Mechanics Conference, Sydney, Australia, 2004<sup>†</sup>

‘Scaling Laws and Measurements on Adverse Pressure Gradient Turbulent Boundary Layers’ Brzek, B., Castillo, L., Anderson, C.M., and Turan, Ö.F. 43<sup>rd</sup> AIAA Fluid Dynamics Conference, Reno, Nevada, 2005<sup>‡</sup>

‘Outer Scaling in Turbulent Boundary Layers’ Brzek, B., Turan, Ö.F., Anderson, C.M., and Castillo, L. 35<sup>th</sup> AIAA Fluid Dynamics Conference and Exhibit, Toronto, Canada, 2005

‘Adverse Pressure Gradient Turbulent Boundary Layers: Outer Flow Scaling and Measurements’ Anderson, C. M. and Turan, Ö.F., Experiments in Fluids, Paper under review.

---

<sup>†</sup> This publication was prepared jointly with Brian Brzek using the candidate’s experimental data. The order of the authors names was based on the expectation that Brian would come to present this paper, Part 2 of a two-part paper.

<sup>‡</sup> AIAA require that the presenting authors name is listed first. In the case of the publication marked here, the order of authors’ names does not necessarily represent the level of contribution from each author.

## **2 Experimental Equipment**

In this chapter, a detailed description is given of experimental equipment used. Each piece of equipment is discussed in an appropriate subsection. There are five subsections, namely, the Wind Tunnel, the Pipe Flow Apparatus, Pitot Static and Total Head Tubes, Hotwire Probe Equipment and the Traversing Mechanism.

### **2.1 Wind Tunnel**

The wind tunnel is the primary piece of equipment used in this research. It is used to calibrate some of the hotwire probes and to generate adverse pressure gradient boundary layer flow conditions.

In Figure 2.1, a schematic view of the wind tunnel is given. The tunnel is an open-return, blower type. The blower fan forces air into a wide-angle diffuser, and then, a settling chamber to slow and straighten the flow. The air is then accelerated as it passes through a contraction cone and through to the 4.5-m long test section. The air exits to the room via a diffuser. The test section is fitted with a flexible top that can be adjusted to produce different adverse pressure gradients (APG's), and a false floor to allow measurement of the static pressure. Detailed discussion of the wind tunnel components is given in Sub-sections 2.1.1 to 2.1.6.

#### **2.1.1 Location**

Victoria University's Research Wind Tunnel was used to produce an adverse pressure gradient boundary layer flow. The tunnel is located in the Fluid Dynamics Laboratory of the School of Engineering and Science at the Footscray Park campus.

This laboratory experiences a narrow ambient temperature range due to its sub-ground-level location. There are also no other climate-altering devices, such as windows or air-conditioning. When equipment is operating, over the course of the day, a 1-2° Celsius increase in the ambient temperature may occur. The temperature stability makes this an excellent facility for thermal anemometry measurements.

### **2.1.2 Fan, Diffuser and Settling Chamber**

A 45-kW motor drives the 1.3-m diameter axial blower fan, which was constructed by Richardson and Sons Ltd of Melbourne. The make of the motor is ASEA and its specifications are 415-Volt, 3-phase, 50-Hz power source producing a rotational speed of 1475 rpm. The pitch angle of the blades can be altered to produce different flow velocities ranging from 7.6 m/s to 32 m/s at the inlet of the test section.

After passing through a wide-angle diffuser with a length of 1.1-m, the flow enters the 0.55-m long settling chamber with a 1.9-m square cross section. To straighten the flow, the settling chamber is fitted with two layers of 7-mm nominal diameter honeycomb separated by and sandwiched in between 3 fine mesh screens.

### **2.1.3 Contraction Cone and Pressure Taps**

The flow passes through a 1.94-m long contraction cone with an area ratio of 9.4:1 to accelerate the flow before entering the test section.

The contraction cone is fitted with an inclined manometer, which contains water with a di-methyl yellow dye to sense the pressure change from the entry to the exit. Both sensing arrays are made up of 8 pressure holes. Pairs of holes are located on the top, bottom and both sides the contraction cone. The bottom two holes at the exit of the contraction cone are plugged because a 0.1-mm thick plexiglas sheet that is used to produce a smooth curve between the contraction cone and the false floor, covers them. The pressure drop along the contraction cone can be calibrated to the air velocity at the test section inlet.

### **2.1.4 Test Section**

The test section is 4.5 m long, with a 0.9-m square cross-section. 3 clear perspex hinged viewing windows allow observation of the test section and easy placement of equipment. The windows are a tight fit, and any gaps are plugged with sponge-type draft excluding tape, which is readily available from hardware stores.

### **2.1.5 Wall Static Pressure Taps**

Wall static pressure taps fitted in the false floor within the test section, measure static pressure distribution. Located on the centerline of the floor, the 32 taps are spaced at approximately 150-mm intervals and have a 1-mm diameter. The exact location of these taps is given in Table 2-1.

### **2.1.6 Flexible Top**

To produce different adverse pressure gradients within the test section, a flexible top has been fitted. It is made from 3 mm thick lexan, which is suspended from the ceiling of the test section by 9 pairs of screws. Adjusting these screws alters the shape and thus changes the adverse pressure gradient within the test section. 48 holes are located along the centerline of the flexible top to allow probes to be inserted for vertical traverses. These holes are 9 mm in diameter and are plugged when not in use.

The height settings of the flexible top are given in Chapter 3.

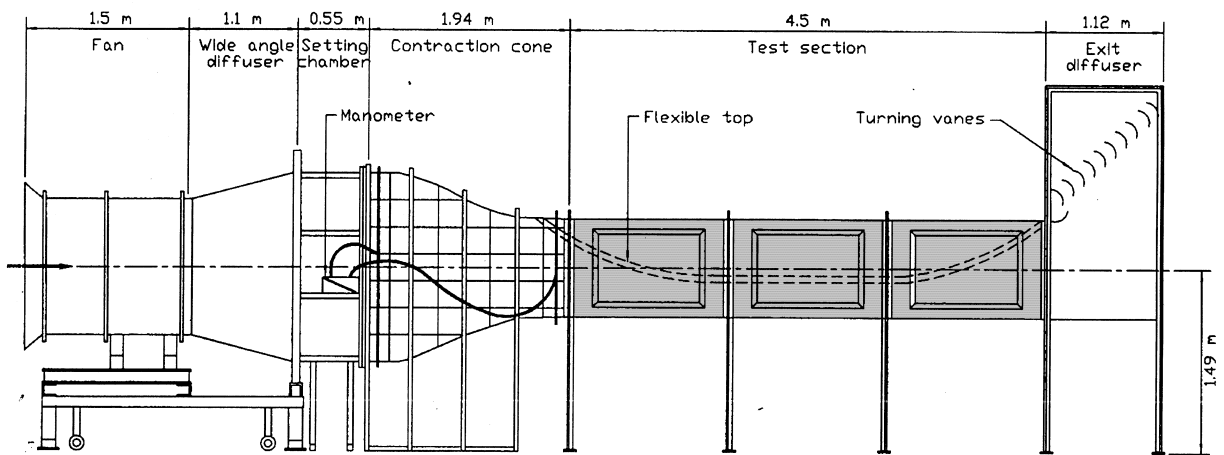


Figure 2.1 Wind tunnel, not to scale. (from Han (2000))

**Table 2.1 Location of Wall Static Pressure Taps.**

<b>Wall Static Pressure Tap Number</b>	<b>Distance from start of test section (m)</b>
1	0.100
2	0.250
3	0.400
4	0.550
5	0.700
6	0.850
7	1.000
8	1.150
9	1.300
10	1.450
11	1.600
12	1.750
13	1.900
14	2.050
15	2.200
16	2.352
17	2.502
18	2.652
19	2.802
20	2.952
21	3.102
22	3.252
23	3.402
24	3.552
25	3.702
26	3.852
27	4.002
28	4.152
29	4.302
30	4.452
31	4.602
32	4.752

## **2.2 Pipe flow apparatus.**

The pipe flow apparatus consists of an 18-m length of steel pipe and of 10.16-cm (4-in) inner diameter, a blower fan to force air into the pipe, as shown in Figure 2.2. The configuration of the pipe flow apparatus is presented in more detail below.

The long length of pipe provides fully developed conditions near the exit. This allows calibration of total head tubes and hotwire probes under known flow conditions.

### **2.2.1 Location**

The pipe flow apparatus is located in the Fluid Dynamics Laboratory of the School of Engineering and Science at Victoria Universities Footscray Park campus. It is located alongside the wind tunnel, and as such, is subjected to the same favourable ambient conditions.

### **2.2.2 Fan and damper**

A damper mounted on the fan inlet controls the velocity. The maximum centreline velocity achievable at the exit is 39.3 m/s and the minimum is 4.3 m/s.

Air is forced into the pipe by a centrifugal blower fan, which is belt driven by a 3.6-hp motor. There is a flexible connection between the blower fan and the settling chamber to reduce transmission of vibrations from the motor and fan to the pipe.

### **2.2.3 Settling Chamber**

The settling chamber is 3.35 m long, with an internal diameter of 197 mm. It contains two layers of 7-mm nominal diameter honeycomb to straighten the flow.

The air passes from the settling chamber, through a 3.8:1 area ratio contraction cone and into the pipe section.

### **2.2.4 Pipe**

As stated above, the total length of the pipe section is 18 m and the internal diameter is 101.6 mm (4 inches). The pipe length consists of 3 sections of stainless steel pipe, each 6 m long with a 3-mm wall thickness. Each pipe section is mounted on

adjustable height supports so that each can be aligned, minimizing a step change between sections, as shown in Figure 2.2.

### **2.2.5 Wall Static Pressure Taps**

There is a series of wall static pressure taps located between 6 and 12 metres from the pipe exit along the pipe. 5 sets of taps are located 1-m apart. Each set consists of 4 taps around the circumference of the pipe. These are used to determine the pressure drop per unit length of pipe.

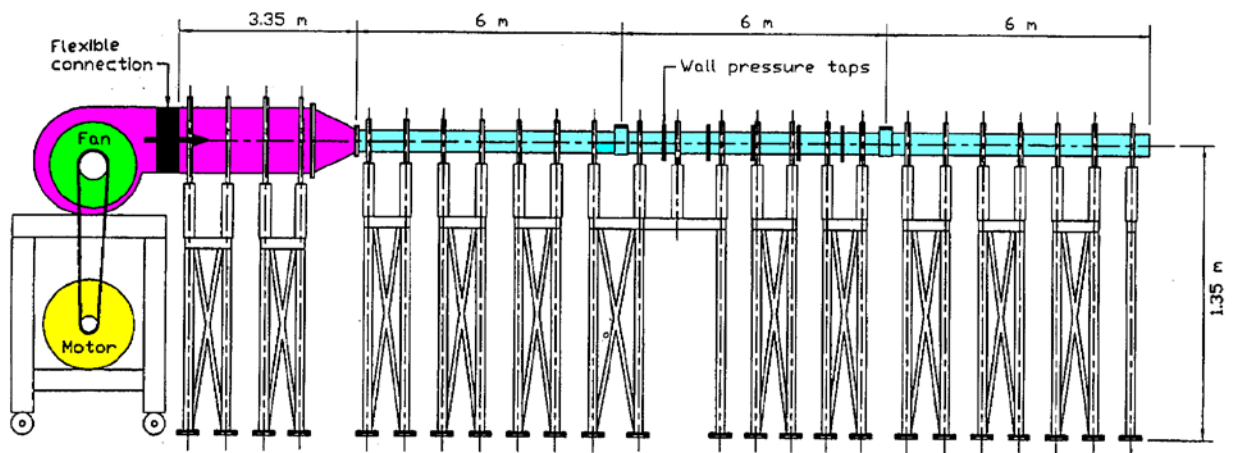


Figure 2.2 Pipe flow apparatus (from Han (2000)).

## **2.3 Total Head Tubes and Pitot Static Tubes**

Pitot-Static and Total-Head tubes can only measure mean velocity in the streamwise direction. The use of these devices is limited by the need to correctly align them with the flow direction, however their usefulness lies in their simplicity. Before the APG flows were examined with hotwire probes, Pitot static probes were used extensively to determine the mean velocity profile throughout the test section, on and off the centreline. This was quick and simple and provided a useful comparison for the x-wire measurements.

### **2.3.1 Total Head Tubes**

A total head tube is simply a small-diameter tube. Total pressure is sensed at the open end of the tube, and the other end is connected to a Furness Controls Limited FCO12 type digital micro manometer. The manometer detects the pressure difference between the total pressure from the tube and the atmospheric pressure in the laboratory. Total head tubes with a 3-mm OD were used for friction velocity measurements, as discussed in Sub-Section 4.1.7.1 and for velocity calibration of the pipe flow apparatus, as discussed in Section 3.5.

### **2.3.2 Pitot Static Tubes**

Pitot Static tubes are used to measure velocity by way of a pressure difference. The device consists of two slender tubes. The inner tube is open at the tip where the flow comes to a stop. Therefore, the total (stagnation) pressure is sensed from the inner tube. The outer tube has a ring of small holes to sense the static pressure of the fluid.

Pitot-static tubes were used to aid in calibration of the x-wire probes, as discussed in Section 3.1 and Section 3.2.

## **2.4 Hotwire probe equipment.**

### **2.4.1 Hardware**

Dantec Measurement Technology manufactures the hot wire probes and software utilized in these experiments. A schematic of the setup is given in Figure 2.3. The hot wire probe is connected to the Constant Temperature Anemometer (CTA) by coaxial cables. Parallel lines are run through an oscilloscope so that the signal can be monitored. The Dantec® *Streamline* CTA is directly connected to a Personal Computer (PC) for data manipulation and control. The CTA is also connected to the PC via an analogue-to-digital converter (ADC) to facilitate data collection. A temperature probe is also fitted to measure the ambient temperature.

### **2.4.2 Hot Wire Probes**

The x-wire used here is a Dantec® 55R51, with probe wires of nickel film deposited on a 70- $\mu\text{m}$  diameter quartz core. Measurements can be obtained at a minimum distance of 3 mm. The overall length of the wire is 3 mm, with a sensing length of 1.25 mm. The wires are angled at 45° to the plane of the probe support. The calibration of an x-wire probe is detailed in a later section.

Single wire, boundary-layer-type probes were also used for near-wall and spectral measurements. These were Dantec® 55P05 probes, with a 5- $\mu\text{m}$  platinum plated tungsten core and bent prongs to allow near wall measurements, starting at 0.15 mm.

### **2.4.3 Data Measurement**

For x-wire traverses, a sampling frequency of 10-kHz was used to record 262,144 samples which provides a record length of 26 seconds. This sampling frequency was the highest possible with the software and hardware, which provided stability for x-wire measurements. A sampling frequency of 100-kHz was utilized with the single wire probe, recording 524,288 samples yielding a record length of 5 seconds.

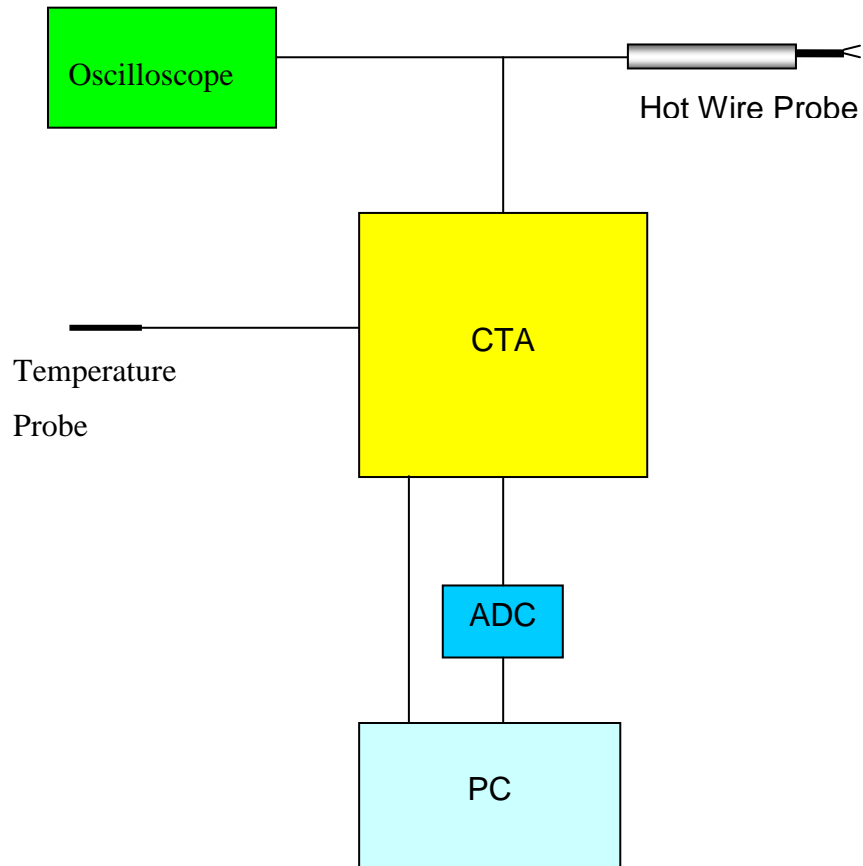


Figure 2.3 Schematic of equipment set up for hot wire probe measurements.

## **2.5 Traversing Mechanism**

A schematic of the traversing mechanism is given in Figure 2.4. The traversing mechanism is mounted on top of the wind tunnel test section, positioned to allow vertical traverse at the centerline. The traversing mechanism consists of a stepping motor operated by an electric controller. The electric controller works by means of a slotted disk. The disk contains 50 slots, which are read by slotted opto switches from RS Components Limited. The controller houses an 8-digit Add/Subtract Totalising Counter, also from RS Components Limited, which processes the information from the Opto Switches.

The stepping motor is mounted on a threaded shaft with a pitch diameter of 1.5 mm. A carriage is mounted on the shaft with facilities for holding probes. When the stepping motor turns the shaft, it acts as a power screw raising or lowering the carriage. As there are 50 slots on the slotted disk, equating to one full revolution of the shaft, with a pitch diameter of 1.5-mm, the minimum traverse step is 0.03-mm.

Hence, the expected accuracy is  $\pm 0.015$ -mm. The backlash of the power screw has been determined to be within this limit (Han, 2000, p 23).

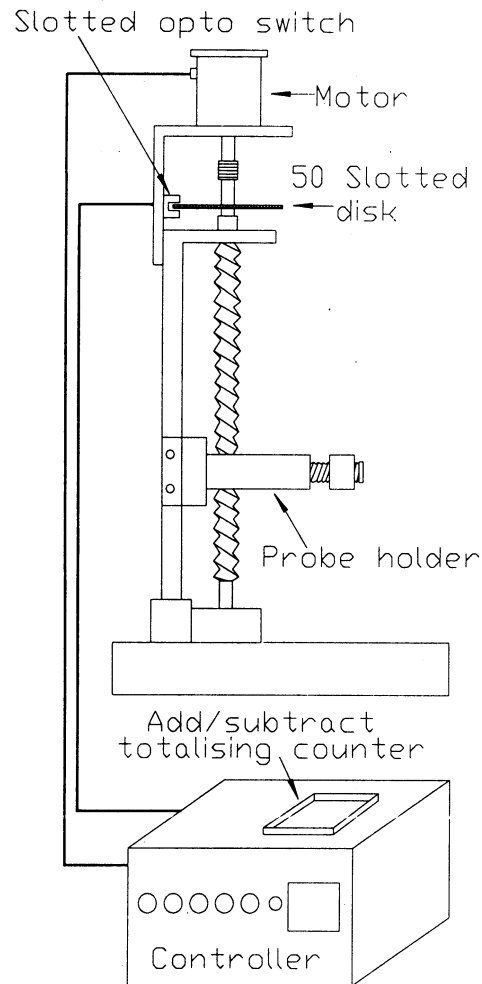


Figure 2.4 Schematic of the Traversing Mechanism, (from Han 2000).

### **3 Hotwire Calibration Technique**

In this chapter, the details of the calibration of single wire and x-type hotwire probes are presented. As discussed in Chapter 2, a hotwire probe is a small sensing element used for measuring flow velocities. It consists of a wire stretched between fork-like prongs. The wire is heated to a constant temperature by applying a voltage, as one arm of a Wheatstone bridge, subjecting the wire to a flow has a cooling effect on the wire. By measuring the voltage required to keep the wire at a constant temperature, it is possible to determine the flow velocity. An x-type hotwire probe consists of two sets of prongs supporting two wires. When viewed from the side these two wires form an 'X', as shown in Figure 3.1.

The use of an x-wire probe facilitates measurement of two components of velocity. The two wires of the probe are perpendicular to each other, which allows measurement of the Reynolds stress, as well as mean velocity components in two directions.

There are a number of ways to calibrate x-wire probes. Traditional methods of calibrating x-wire probes require determining a relationship between voltage and velocity based on a King's Law (1914) fit. This traditional method requires the probe to be mounted at a fixed point in the flow, whilst the voltage is recorded for different velocities, thus it is termed a 'stationary point calibration'. This method was first discussed in detail by Bradshaw (1971).

A review of calibration techniques for x-wire probes in turbulent flows was presented by Brown, Antonia and Chua (1989). They compared different techniques including single angle or 'stationary point', and multiple angle yaw calibrations with look-up tables. They also looked at stationary point calibrations with the use of calibration factors. The techniques suggested or used by Bradshaw (1971), Champagne et al (1967), Andreopoulos and Rodi (1984), Brunn (1971), Willmarth and Bogar (1977), Johnson and Eckelman (1986) and Lueptow et al (1988) amongst others were examined.

Brown et al. (1989) found that for  $\overline{u^2}$  and  $\overline{uv}$ , the single angle and yaw calibrations produced similar results. However, for the turbulence quantity  $\overline{v^2}$ , the single angle stationary point technique generated higher values. They concluded that when accurate measurements pertaining to velocity fluctuations and flow structure are required, it is beneficial to use a yaw calibration technique.

An improved scheme, involving variations of pitch or yaw angle, was reported by Zilberman (1981) but was first presented in detail by Lueptow et al (1988). This yaw technique involves taking voltage measurements over a range of velocities for several different yaw angles. Altering the probe angle to the mean flow simulates different velocity components. Lueptow et al (1988) reported an accuracy of  $\pm 0.3\%$  and  $\pm 0.6\%$  for U and V respectively, for velocities above 2.4 m/s.

John and Schobeiri (1993) suggest a way of simplifying the yaw calibration of Lueptow, which may also improve accuracy. The method involves doing both a stationary calibration with numerous velocities and a yaw calibration by keeping velocity constant and alternating the probe angle. This is quicker than doing a 'full' yaw calibration involving recording a range of velocities for numerous angles. It is considered desirable to calibrate a probe *in situ* however this would not be possible with the current equipment in the Victoria University tunnel. Presently the probe angle cannot be altered while the tunnel is operational. Thus, the calibration scheme of Lueptow et al (1988) is utilized here.

Both the stationary point and pitch/yaw calibrations are discussed later in this chapter, along with a calibration to determine the relationship between the pressure drop and centreline velocity at the exit of the pipe flow apparatus. An experiment to determine the extent of the core region in the wind tunnel is also presented in detail.

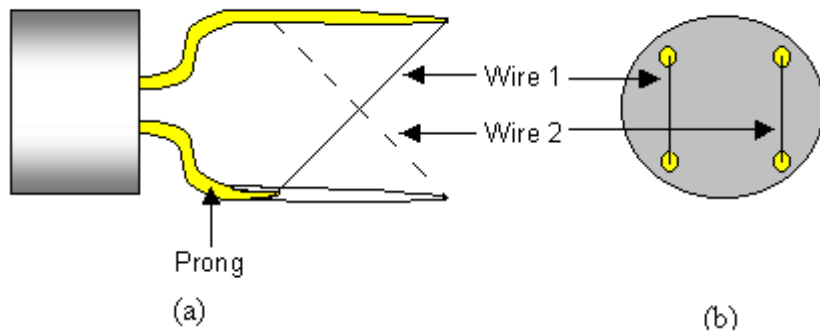


Figure 3.1 X-type hotwire probe a) side view, (b) end view.

### **3.1 Determination of the extent of the core region:**

Both the stationary point and pitch/yaw calibration techniques require known flow conditions. To facilitate the x-wire calibration, the flow conditions at a particular location were investigated in detail. Vertical and horizontal traverses were performed at different velocities to determine the extent of the core region.

A 4-mm outer diameter brass tip Pitot tube was mounted on the vertical traversing mechanism. The vertical traversing mechanism is located on top of the wind tunnel test section and the Pitot extends down, through the flexible top. The flexible top has numerous holes, along the centreline, to allow probes to be used in this manner. Adhesive foam tape is used to seal the small gap between the Pitot tube and the flexible top. All other holes are sealed with plugs or adhesive tape to prevent leakage.

The hole used in this case was Number 41, which allowed the tip of the probe to be located 3978-mm from the test section entry. Henceforth, this position is referred to as Location 41. Location 41 was chosen because it was able to accommodate the equipment required for the yaw and pitch calibrations, and had a core region larger than other upstream location with similar access.

The Pitot was connected to a Furness Controls Limited FCO12 type digital micro manometer to determine the pressure difference sensed by the probe.

The extent of the core region at Location 41 was established by carrying out two vertical traverses, one at low velocity and one at high velocity. The results of these are shown in Figure 3.2. The boundary layer thickness with a core velocity of 12 m/s was found to be approximately 250 mm. At a higher core velocity of 24 m/s, the boundary layer was 300 mm thick. Thus, it has been determined that placing a probe at a height of 320 mm at Location 41 will ensure that it is within the core region for core velocities ranging from 12 m/s to 24 m/s.

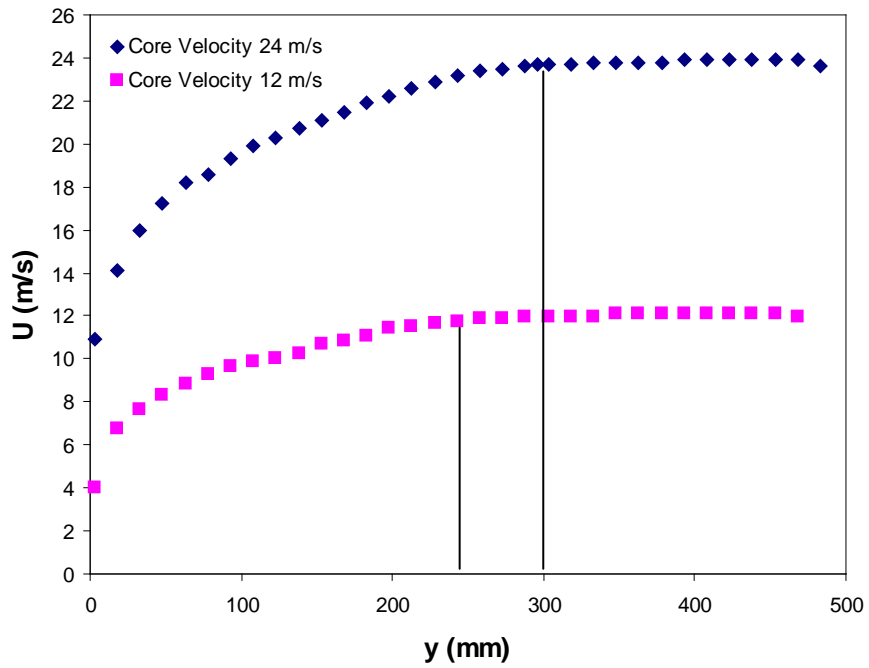


Figure 3.2 Vertical traverses with Pitot Tube at Location 41 in wind tunnel for a low velocity and high velocity setting.

### **3.2 Reference velocity calibration.**

A Pitot tube is permanently located in the test section of the tunnel near the entrance. It is used to determine the reference velocity. It is necessary to know the relationship between the reference velocity and the velocity in the core at the location where hot wire probes are calibrated (Location 41). This linear relationship is determined by simultaneously reading the reference Pitot and another Pitot located at the calibration location for a range of velocities. This relationship was found to be:

$$V_{\text{cal}} = 0.57V_{\text{ref}} \qquad \text{Equation 3-1}$$

where  $V_{\text{cal}}$  is the velocity at the hot wire probe calibration location, [mm H<sub>2</sub>O], and  $V_{\text{ref}}$  is the velocity at the reference location, [mm H<sub>2</sub>O].

The experimental data and this relationship are given in Figure 3.3.

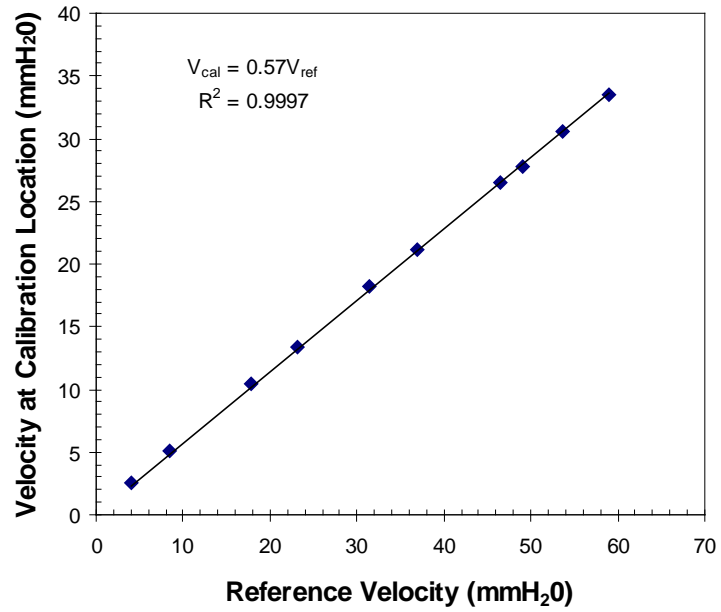


**Figure 3.3 Relationship between the reference velocity and the velocity at the location of the hot wire probe calibration.**

### **3.3 Pitch Calibration.**

With an x-wire probe, it is necessary to perform calibrations that involve rotating the probe in different planes. By conducting measurements in the core region of the flow, it is possible to move the probe and remain in a region with the same flow characteristics.

So as to avoid confusion about the orientation of the probe for the pitch and yaw calibrations, the standard aviation definitions have been used. Therefore, pitch relates to the nose up - nose down aspect as with aircraft, and yaw is related to the nose left - nose right.

To determine a probe's sensitivity to pitch angle, a pitch calibration was performed. This involved taking a set of hotwire measurements over a range of velocities at a given pitch angle, then altering the angle and repeating the measurements.

#### **3.3.1 Equipment Set-up.**

A stand was constructed to facilitate both the pitch and yaw calibrations. The calibration was carried out at Location 41 as illustrated in Figure 3.4. The probe holder allowed pitch rotation of the probe and height adjustment. For different angles, it was necessary to adjust the height from the base of the holder, so that the tip of the probe remained at the same height in the tunnel. This was to avoid positioning of the probe outside the core region. The tip was positioned at a height of 320 mm from the base of the tunnel. In Figure 3.5, the probe holder and stand are shown for different angles. Rotating the probe up was defined as a positive angle.

The blockage presented by the stand and holder was minimal as determined by a series of vertical traverse before and after the stand. The tunnel was operated at maximum calibration velocity to ensure that the stand was stable for all expected flows before the probe was inserted.

The pitch angle was varied between  $\pm 45^\circ$ . For each angle, a series of hotwire probe data was collected corresponding to different velocities.

### **3.3.2 Hotwire Probe Data Collection.**

Using a sampling rate of 1 kHz, 5000 samples of voltage were recorded per wire. The average voltage from each wire can be calibrated to a velocity by using the relationship with the recorded upstream reference velocity (Equation 3-1).

### **3.3.3 Results of the Pitch Calibration**

In Figure 3.6, voltage from Wire 1 is plotted against voltage from Wire 2 as indicated by the resulting straight line with a 45° slope, adjusting the pitch angle has little influence on the sensitivity of the wires. For different pitch angles, the linear relationship between the voltage from Wire 1 and Wire 2 is almost the same, as listed in Table 3.1. The wires do not interfere with each other when the probe is rotated in this manner. In Figure 3.1, the wire configuration is shown when viewed from the front and side. The wires do not cross. If a probe has wires that do cross, then the wake shed by the first wire can affect the second wire, this would then make the probe more sensitive to pitch angle. For flow measurements, the x-wire probes have always been aligned to the horizontal. However, the probe has minimal sensitivity to pitch angle so this alignment does not require a high degree of accuracy.

In Figure 3.6 an apparent ‘gap’ in the data is observed. This is a result of the minimum steady speed of the wind tunnel being 6.6 m/s at the calibration location. The cluster of data points in the lower left of the figure represents the zero velocity readings. The ‘gap’ represents the velocity range from 0 m/s to 6.6 m/s.

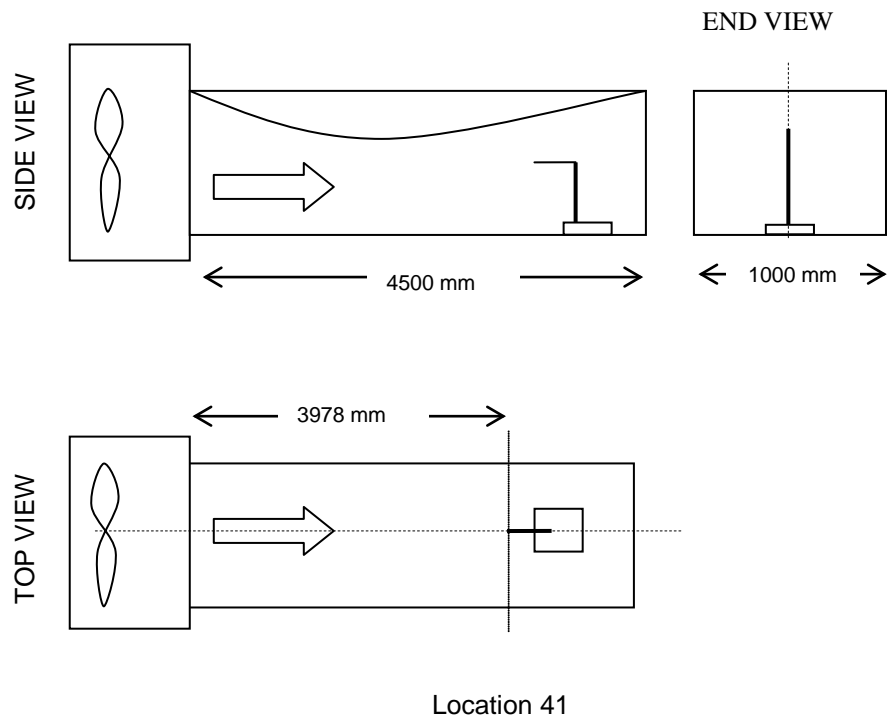


**Figure 3.4 Placement of probe holder at Location 41 in the wind tunnel. The large arrow indicates flow direction.**

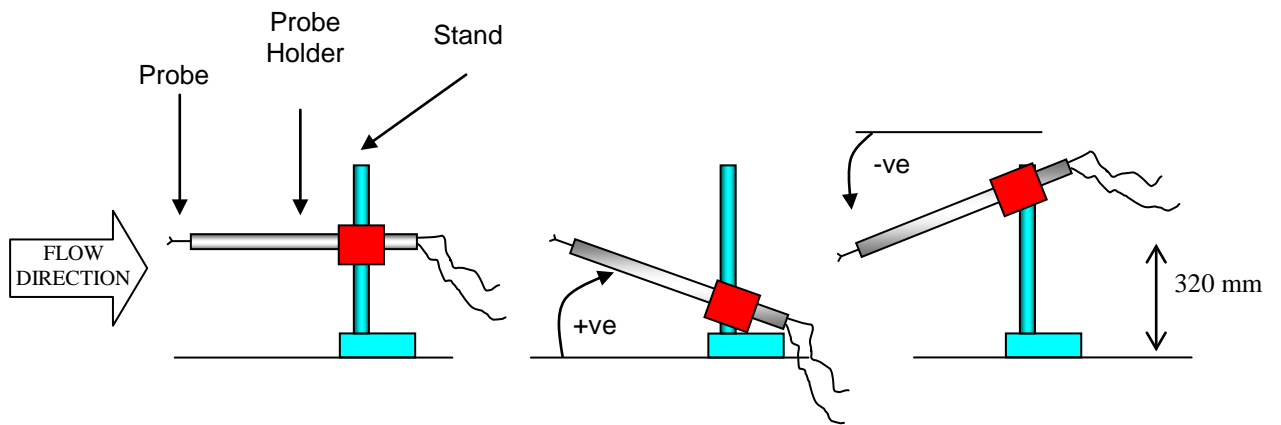


Figure 3.5 Probe holder orientation for pitch calibration (side view).

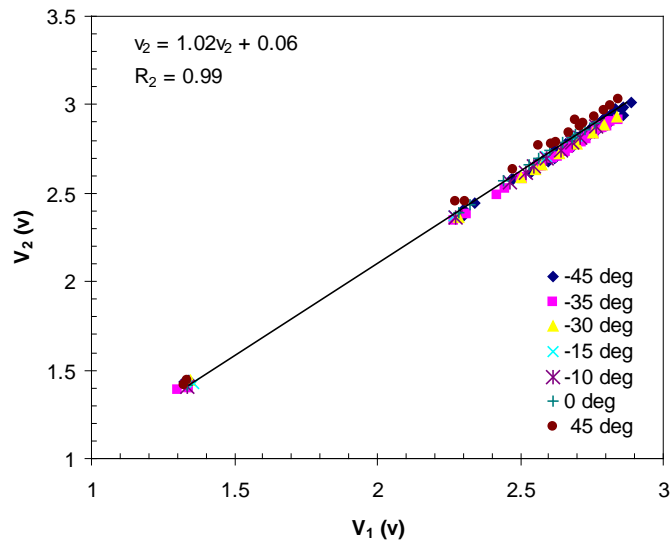


Figure 3.6 Voltage from Wire 1 ( $v_1$ ) versus voltage from Wire 2 ( $v_2$ ) for yaw angles ranging from +45° to -45°.

**Table 3.1 Coefficients of least squares, linear fits to measured data of voltage from Wire 1 and Wire 2 for different Yaw Angles. Data recorded at Location 41.**

<b>Angle (Deg)</b>	<b>Gradient</b>	<b>Intercept</b>	<b>R<sup>2</sup></b>
<b>-45</b>	1.01	0.08	1.00
<b>-35</b>	1.01	0.06	1.00
<b>-30</b>	1.00	0.09	1.00
<b>-15</b>	1.04	0.01	1.00
<b>-10</b>	1.03	0.03	1.00
<b>0</b>	1.04	0.02	1.00
<b>45</b>	1.06	0.03	1.00

### **3.4 Yaw Calibration**

A yaw calibration was performed by collecting a set of voltage data at different velocities for a given yaw angle. The yaw angle was varied between  $\pm 30^\circ$  with intervals of  $10^\circ$ . This method is similar to that detailed by Lueptow et al (1988).

#### **3.4.1 Equipment set-up**

With the probe set at a horizontal height of 320 mm, the entire stand was rotated to produce different yaw angles. A clockwise rotation was defined in the positive direction, as shown in Figure 3.7.

The tip of the probe was aligned on the centreline of the tunnel at Location 41, which is 3978 mm from the test section entry. For each angle, a series of hotwire probe data was collected corresponding to different velocities.

### 3.4.2 Hotwire Probe Data Collection

The technique used for hotwire measurements for the yaw calibration was similar to that used for the pitch calibration. A sampling rate of 10-kHz was used to record 65,532 samples of voltage. The average voltage for each wire was recorded.

### 3.4.3 Calibration Technique

The purpose for this technique is to generate a lookup table containing angle and velocity data for any given pair of wire voltage readings. Voltage pairs were recorded for different velocities. By reading the reference velocity and using Equation 3-1, the calibration velocity was determined.

In Figure 3.8, a plot is shown of the recorded data. For each data point, the following information is known:

1	Wire 1 voltage, [volts]	E1
2	Wire 2 voltage, [volts]	E2
3	Yaw angle, [degrees]	$\gamma$
4	Reference velocity, [mm H <sub>2</sub> O] → Calibration velocity, [m/s]	Q

This is used to generate a look-up table so that any voltage pair can be translated into velocity components  $u$  and  $v$ . Essentially, the end result of this calibration is to generate many more points in the 3 dimensions illustrated in Figure 3.8 and also in the fourth pseudo-dimension, the pitch angle.

The procedure used to determine the calibration lookup table as described by Lueptow et al. (1988), with slight modification, is detailed in Appendix I. The result of this technique is a list of finely spaced E1 and E2 voltage pairs and their corresponding  $u$  and  $v$  velocity components. This information is represented graphically in Figure 3.9 and Figure 3.10.

To use the calibration lookup table each experimentally measured voltage pair is analysed in turn. First, the calibration table is searched to locate the nearest match for wire voltages E1 and E2. Wire voltages are recorded to 2 decimal places. If an exact match is not found the nearest neighbours are found. The average of these values is used to determine the  $u$  and  $v$  velocity components.

Files to be analysed generally had in excess of 200,000 points and each experiment usually had at least 20 of these files. The program written to use the look-up table for converting experimentally measured data into  $u$  and  $v$  velocities and other associated values, on average took about 25 hours for each set of traverse data. This computer program was written using Matlab®, and for completeness, it is provided in Appendix II.

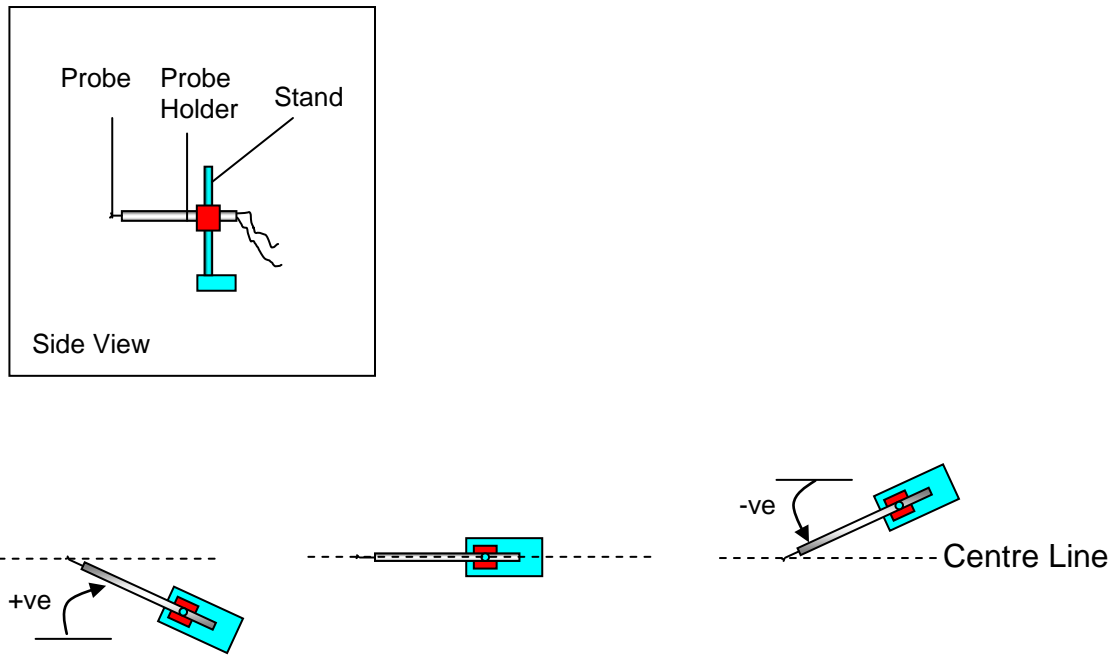


Figure 3.7 Probe holder orientation for yaw calibration with relation to center line of wind tunnel (top view).

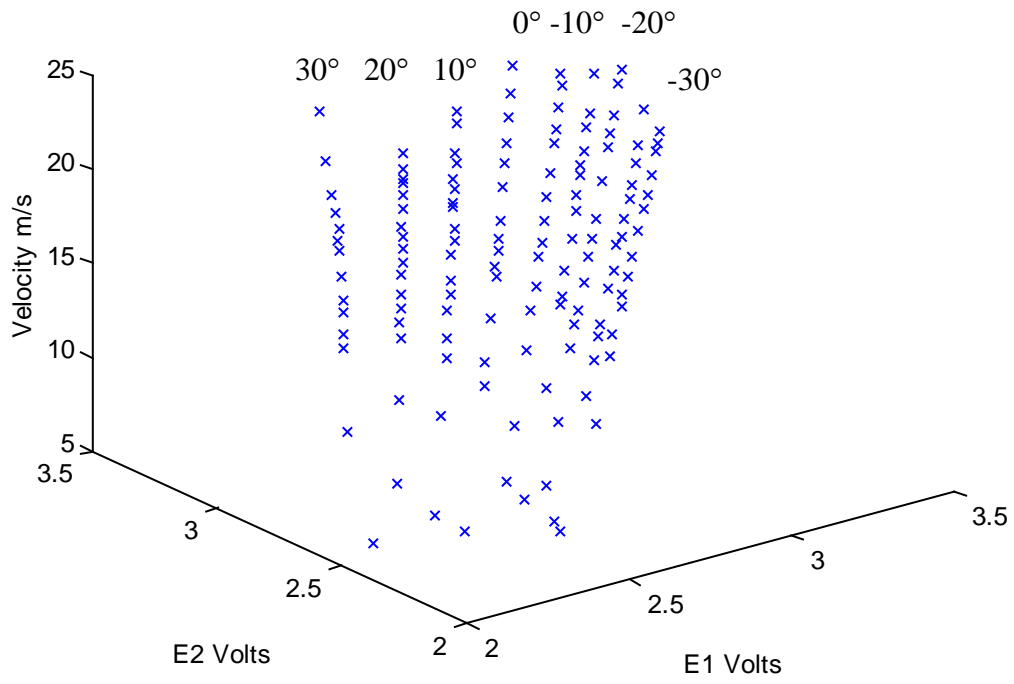


Figure 3.8 Recorded data for the yaw calibration.

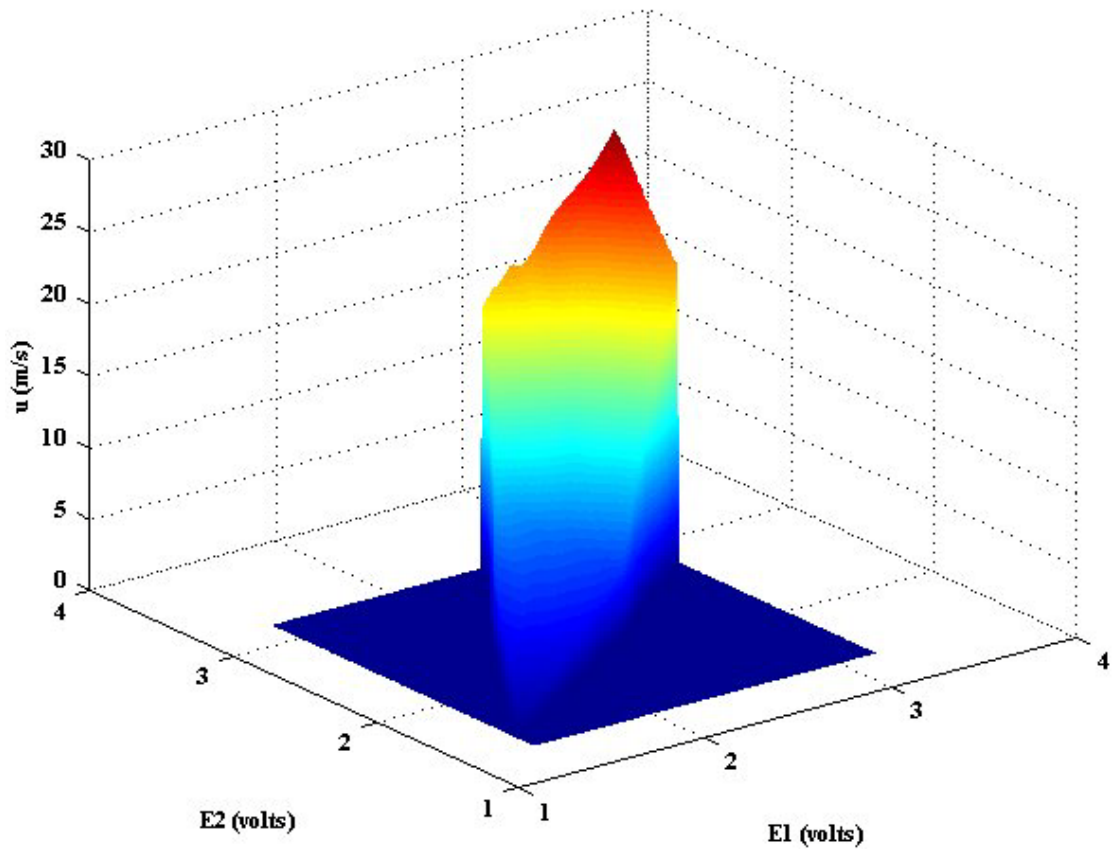


Figure 3.9 Calibration data of u velocity component for any E1 or E2 velocity pair.

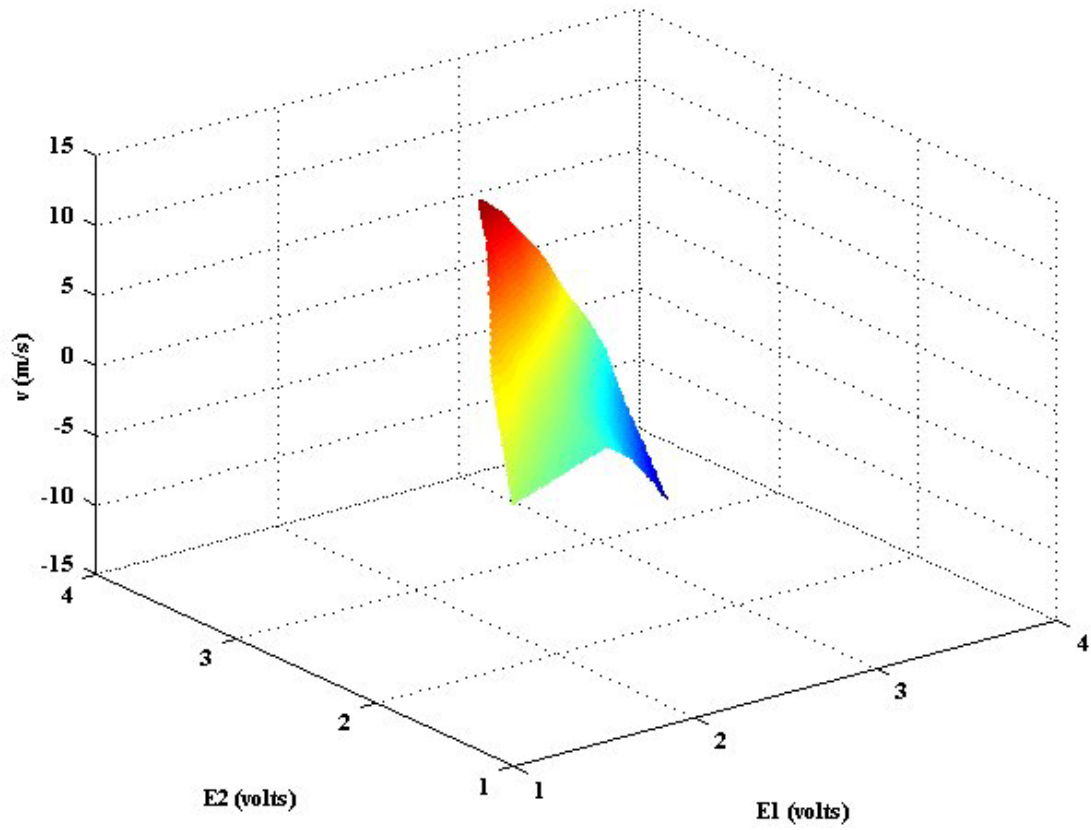


Figure 3.10 Calibration data of  $v$  velocity component for any  $E1$  or  $E2$  velocity pair.

### 3.5 Pipe Velocity Calibration

A relationship between pressure drop in the pipe and centreline velocity near the exit can be determined. A total head tube is used to record the centreline velocity inside the pipe, at one radius from exit, where the static pressure remains almost atmospheric, Preston (1950). Simultaneously, the static pressure drop is measured by the taps located between 7 m and 11 m from the inlet. In Figure 3.11, the experimental set-up is illustrated. The relationship between the pressure drop and centreline velocity is:

$$\begin{aligned} V_{cl} &= 2.24P_d - 0.45 & P_d < 10 \\ V_{cl} &= 2.60P_d - 4.29 & P_d > 10 \end{aligned} \qquad \text{Equation 3-2}$$

where  $P_d$  is the pressure drop, [mm H<sub>2</sub>O], and  
 $V_{cl}$  centreline velocity, measured with a total head tube, [mm H<sub>2</sub>O].

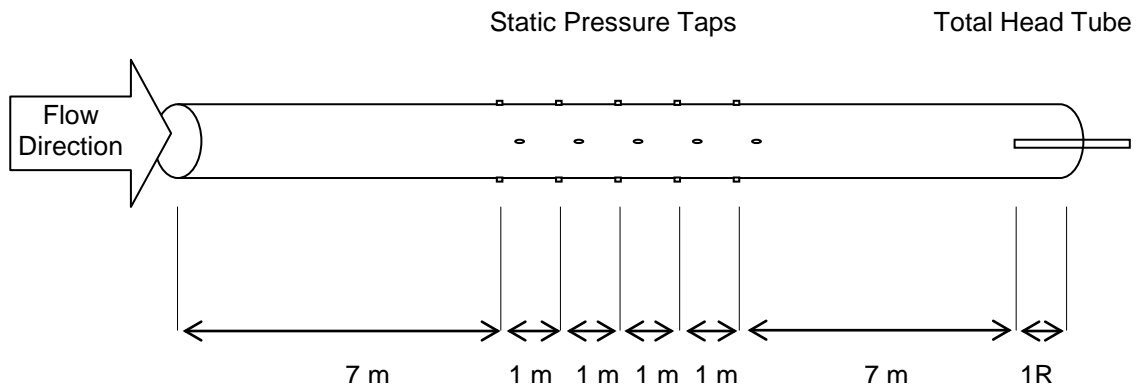


**Figure 3.11** Pipe set-up for determining the relationship between pressure drop and velocity near the exit.

### 3.6 Single Wire Probe Calibration

The calibration produces a set of equations relating local velocity to the voltage recorded from the hotwire. The pipe flow apparatus was utilized due to the ability to generate low velocity flows. The single wire probes are used for measurements close to the wall where velocities are the lowest, thus a calibration providing accuracy at low velocities is required.

#### 3.6.1 Equipment Set-up

The probe was orientated at the centreline of the pipe flow apparatus and was positioned horizontally by using a spirit level. Different velocities were achieved by closing the damper at the inlet of the pipe. By using a manometer fitted to the pressure taps along the length of the pipe, the pressure drop could be recorded and calibrated to a velocity by using Equation 3-2.

#### 3.6.2 Hotwire Probe Data Collection

The details of the hotwire equipment are given in Section 2.4. A sampling frequency of 100-kHz was used to record 524,288 samples. The centreline velocity was set to 21 different values ranging from 4.3 m/s to 39.3 m/s. For each velocity, a reading was taken with the single wire probe and the average voltage was determined. The centreline velocities and corresponding voltages are given in Table 3.2.

Typically, a King's law (1914) fit was used to define the relationship between voltage and velocity. The theoretical relationship is based on the idealised case of flow around an infinitely long cylinder in cross flow. The law is:

$$E^2 = a + bU_e^{0.5} \quad \text{Equation 3-3}$$

where  $E$  is the required voltage to maintain constant wire temperature, [volts]  
 $U_e$  is the velocity, [m/s]  
 $a$  and  $b$  are constants.

The difficulty with utilising this relationship is in curve-fitting the highly non-linear expression. Siddall and Davies (1972) suggested an improvement to the traditional King's law. Instead of the usual power law relationship Siddall and Davies used a

second order polynomial of  $U_e^{0.5}$ , Equation 3-4. This method provides superior accuracy over King's law due to the extra velocity term in the expression.

$$E^2 = AU_e + BU_e^{1/2} + C \quad \text{Equation 3-4}$$

where  $U_e$  is the effective cooling velocity acting on the wire, [m/s], and  $E$  is the wire voltage, [volts].

Further details on the use of this technique are given in Appendix III. According to Siddall and Davies (1972), the standard error estimate of  $E^2$  on  $U_e^{1/2}$  from King's law is 0.311, whilst for Equation 3-4 it is 0.027. As stated above, the improved accuracy is a result of the addition of an extra velocity term.

By applying this technique to the recorded data, the coefficients A, B and C can be determined with a least squares approach. The values obtained are given in Table 3.3. The voltage and velocity data pairs along with the Siddall and Davies fit are plotted in Figure 3.12.

**Table 3.2** Single wire calibration data

<b>Centreline Velocity (m/s)</b>	<b>Voltage (v)</b>
39.3	2.49
39.2	2.49
38.9	2.49
38.7	2.49
38.0	2.48
37.0	2.47
35.7	2.45
34.1	2.43
31.3	2.40
28.8	2.37
24.8	2.31
22.8	2.29
20.0	2.24
17.4	2.19
15.4	2.15
13.1	2.09
11.0	2.05
9.2	1.99
6.9	1.92
5.4	1.86
4.3	1.80

**Table 3.3 Coefficients for Equation 3-4 ( $E^2 = AU_e + BU_e^{1/2} + C$ ) for single wire probe**

<b>Coefficient</b>	<b>Value</b>
A	-0.014
B	0.824
C	1.613

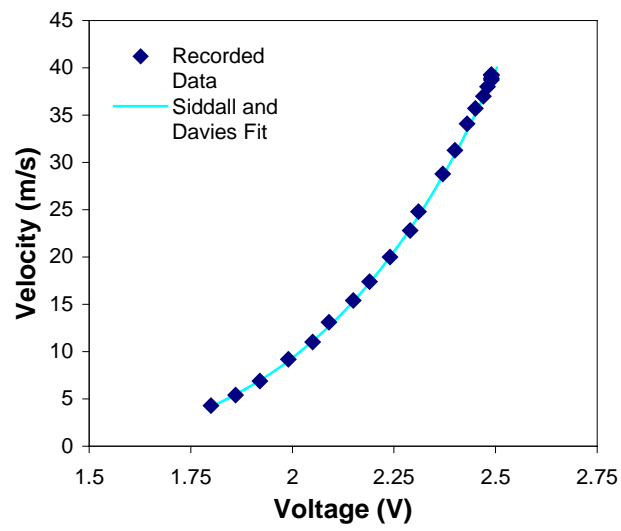


Figure 3.12 Single wire recorded calibration data and Siddall and Davies fit.

## **4 Flow Details**

In this chapter, details are presented of the flows generated using the Victoria University wind tunnel and 20 flows from the literature that have been used for comparison purposes. Detailed flow information is given, including pressure distribution,  $C_p$ , freestream velocity,  $U_e$ , boundary layer thickness,  $\delta$ , shape factor,  $H$ , friction velocity,  $u_*$ , turbulence intensity,  $\mathcal{I}$ , and the equilibrium pressure parameters of Clauser,  $\beta$ , and Castillo and George,  $\Lambda_\theta$ . Also, where appropriate, the physical dimensions of the test section used to generate the flows are listed.

Flow A and Flow B are discussed first and each of the flow parameters is introduced. Next, in Section 4.2, two flows that are very similar to Flows A and B are introduced and the flow parameters are again explored. Also, flow data for Flows A, B, Han, and 141 are tabulated in Section 4.2.

For comparison and contrast, 2 flows by Clauser, one by Bradshaw and one by Newman are considered in Section 4.3. These are termed the ‘classical’ flows. This section contains a table (Table 4.8) which provides the authors’ details, the flow reference number, and a description of the flow and pressure gradient.

In Section 4.4, 14 more adverse pressure gradient flows are presented. Similar to ‘classical’ flows, these flows are discussed in relation to the introduced flow parameters.

This chapter aims to introduce and explore the known flow parameters of the two new flows, along with 20 APG flows from the literature. These flows are used for comparisons in the next chapters. The flow data is brought together here from different sources and presented in a uniform way to facilitate easy comparison.

## **4.1 Flow A and Flow B**

Flows A and B were generated using the Victoria University wind tunnel for the purpose of examining increasing APG flows. In this section, detailed information is presented on the way these flows were produced. Along with the equipment description in Section 2.1, adequate detail is provided for others to reproduce these results. Flow data are also given so that these flows can be compared with those from the literature and to provide a comprehensive understanding of the flow behaviour.

### **4.1.1 Entrance shape for Flow A and Flow B**

As discussed in Chapter 3, the wind tunnel test section is fitted with a false bottom to house the static pressure taps. In Figure 4.1, the false floor of the wind tunnel is shown, with the true floor and part of the contraction cone. The false floor has a height of 100 mm above the true floor. Plastic sheeting is attached between the true floor and the false floor to provide a smooth transition from the contraction cone to the test section.

The shape of this plastic sheeting evolved through extensive experimental testing. 3 shapes, shown in Figure 4.1 as 1, 2 and 3, were chosen for further investigation here.

It was found that with shapes 1 and 2, re-circulation occurred in approximately the first 600 mm of the test section. With these shapes, the false bottom acted as a forward-facing step, and flow separation resulted. The velocity profiles down stream were irregular and the core was non-existent at some locations.

To form the plastic sheeting into Shape 3, it was necessary to support it with internal reinforcing vanes attached to the true floor. This shape did not produce re-circulation at the inlet of the test section and provided much more uniform flow conditions. This shape was used for both Flow A and Flow B.

The origin of  $x$  is also defined in Figure 4.1, all streamwise locations are measured from this location.

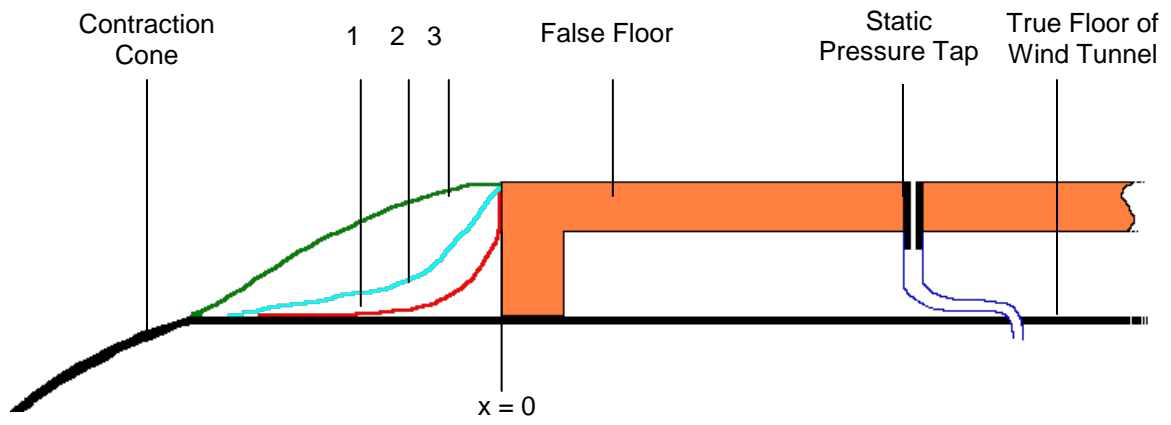


Figure 4.1 Configuration of the entrance shape.

### 4.1.2 Physical shape and pressure distribution

Flow A was designed to be similar to Flow 141 (discussed in Section 4.2). Flow A was designed to have an increasing APG. Flow B also has an increasing APG, but the transition to decreasingly APG occurs much sooner, as quantified next. The effect, if any, of this transition is explored in 4.1.9.

To generate these flows, the adjustable top in the tunnel was set to a smooth, diffuser-type shape. The height settings of the adjustable top are represented graphically in Figure 4.2 and given in Table 4.1. The adjustable top settings for Flow A are the same as those used in previous research using the same tunnel, given as Flow Han by Han (2000). Flow Han is also discussed in more detail in Section 4.2.

In Figure 4.3, the  $C_p$  values are presented for Flows A and B.  $C_p$  is defined as the dimensionless pressure parameter:

$$C_p = \frac{(P - P_0)}{\frac{1}{2}\rho U_0^2} \quad \text{Equation 4-1}$$

where  $P$  is the static wall pressure, [ $\text{N}/\text{m}^2$ ],  
 $\rho$  is the density, [ $\text{kg}/\text{m}^3$ ]  
 $P_0$  is the pressure at the reference location, [ $\text{N}/\text{m}^2$ ], and  
 $U_0$  is the freestream velocity at the reference location, [ $\text{m}/\text{s}$ ].

The pressure distribution of Flow A indicates that the first 0.3 m of the test section has a favourable pressure gradient (FPG), followed by a shorter zero pressure gradient (ZPG) section. The flow then develops under an increasing adverse pressure gradient until a streamwise distance of approximately 3.4 m. After 3.4 m, the flow is decreasingly adverse. These regions are labelled in Figure 4.3(b) for Flow A and Figure 4.3(c) for Flow B. Flow B initially has the same flow development as Flow A, however the transition to decreasing APG occurs much sooner, at approximately 2 m. An ‘increasing’ adverse pressure gradient is such that the adverse pressure gradient gets stronger in the streamwise direction. This is seen clearly in the plot of pressure parameter,  $C_p$ , as a concave up shape. Conversely, with a ‘decreasing’ APG, the strength of the gradient decreases in the flow direction, as demonstrated by a concave down shape in the pressure parameter plot.

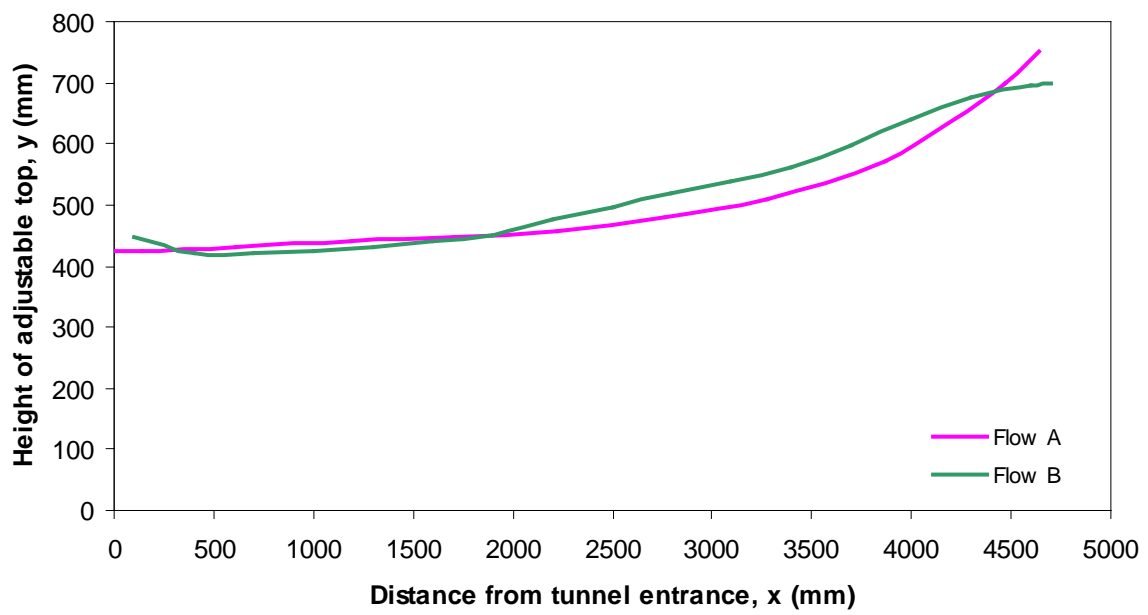
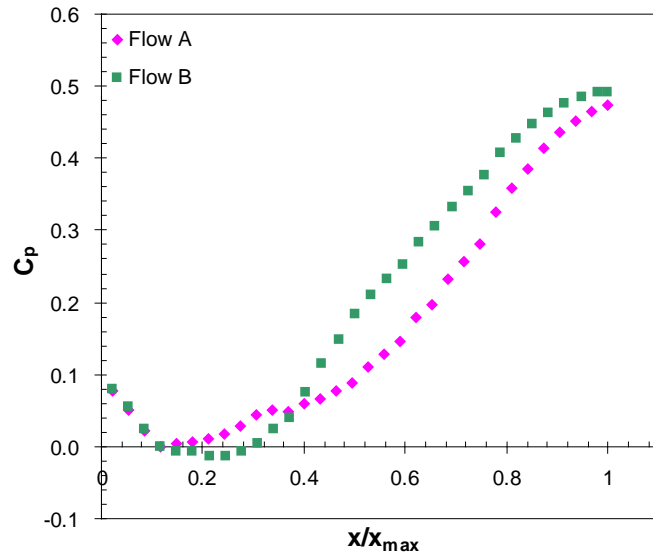


Figure 4.2 Height and shape of adjustable top for Flow A and Flow B.

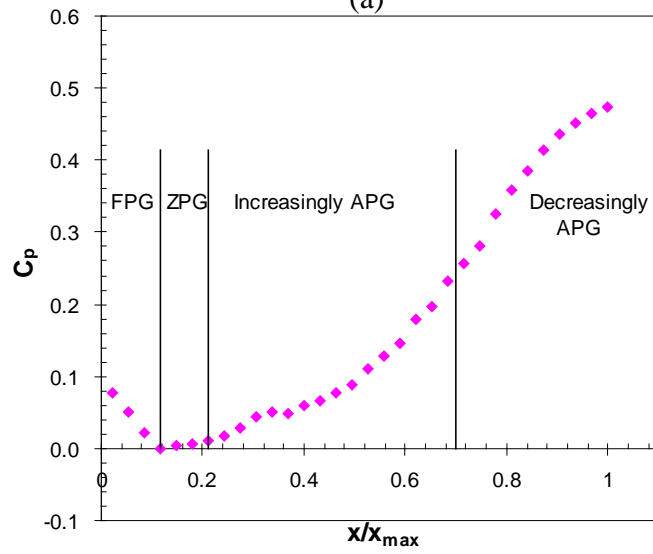
**Table 4.1 Height of adjustable top for Flow A and Flow B.**

Flow A	
Distance from entrance, x (mm)	Height of Adjustable Top (mm)
0	425
143	425
615	430
1193	440
1703	448
2226	457
2765	480
3280	511
3865	571
4470	700
4640	751

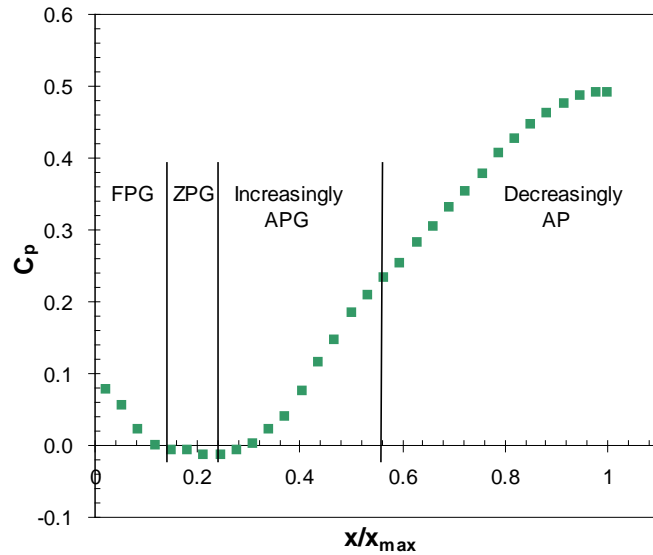
Flow B	
Distance from entrance, x (mm)	Height of Adjustable Top (mm)
100	447
400	420
700	422
1000	426
1300	431
1600	440
1900	450
2200	476
2500	497
2800	518
3100	540
3400	562
3700	597
4000	640
4300	675
4600	695
4700	700



(a)



(b)



(c)

Figure 4.3  $C_p$  for (a) Flow A and Flow B,  $C_p$  with favourable pressure gradient (FPG), zero pressure gradient (ZPG), and ‘Increasingly’ and ‘Decreasingly’ adverse pressure gradient (APG) zones labelled for (b) Flow A and (c) Flow B.

### 4.1.3 Flow development, $U_e$ , $\delta$ , $H$

A reference velocity of 22 m/s, recorded at a streamwise distance of 0.25 m, was used for both flows. The streamwise development of the freestream velocity,  $U_e$ , is presented in Figure 4.4. As expected, the freestream velocity decreases in the flow direction.

A sample velocity profile is given in Figure 4.5, where mean velocity,  $U$ , is plotted against the distance from the wall,  $y$ . This is an x-wire traverse in Flow A, at a streamwise direction of  $x = 2.587$  m. The freestream velocity is clearly visible as the region where velocity is no longer increasing, in this case  $U_e = 19.4$  m/s. The boundary layer thickness,  $\delta$ , is defined as the height,  $y$ , where the velocity has reached 99% of the freestream velocity. It is determined by linear interpolation of the measured values and is given in Figure 4.6.

The shape factor,  $H$ , is given in Figure 4.7, as a further flow development parameter. A near constant shape factor is an indication of flow stability, a sudden change, or an increasing value of  $H$  may indicate a flow approaching separation. The shape factor is defined as:

$$H = \frac{\delta^*}{\theta} \quad \text{Equation 4-2}$$

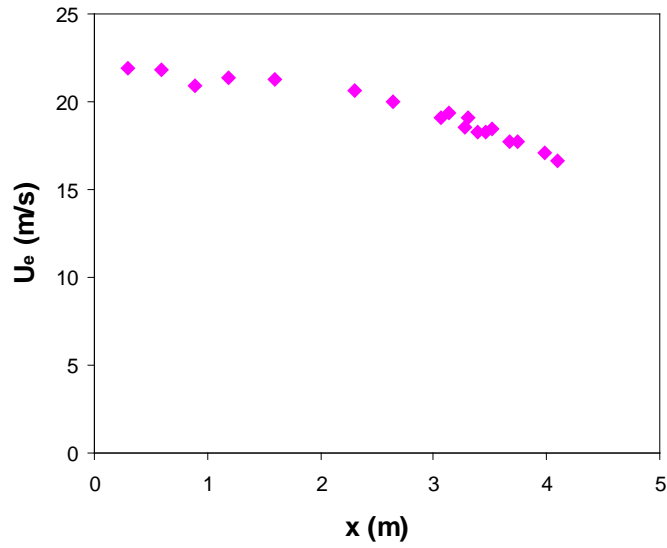
where  $\delta^*$  is the displacement thickness, [m], as defined in Equation 4.3 and  $\theta$  is the momentum thickness, [m], as defined in Equation 4-4.

$$\delta^* = \int_0^{\infty} \left(1 - \frac{U}{U_0}\right) dy \quad \text{Equation 4-3}$$

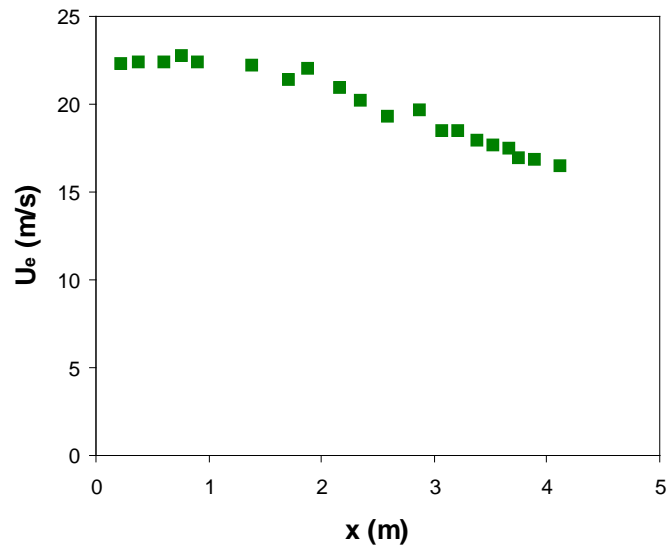
$$\theta = \int_0^{\infty} \frac{U}{U_0} \left(1 - \frac{U}{U_0}\right) dy \quad \text{Equation 4-4}$$

where  $U$  is the local streamwise mean velocity, [m/s]  
 $U_e$  is the freestream velocity, [m/s], and  
 $y$  is the vertical height from the floor, [m].

The momentum thickness,  $\theta$  and its derivative with respect to streamwise distance  $x$ , are important quantities in determining Castillo and Georges pressure parameter,  $\Lambda_\theta$ , to be discussed later in this section.



(a)



(b)

Figure 4.4 Freestream velocity,  $U_e$  (a) Flow A and (b) Flow B

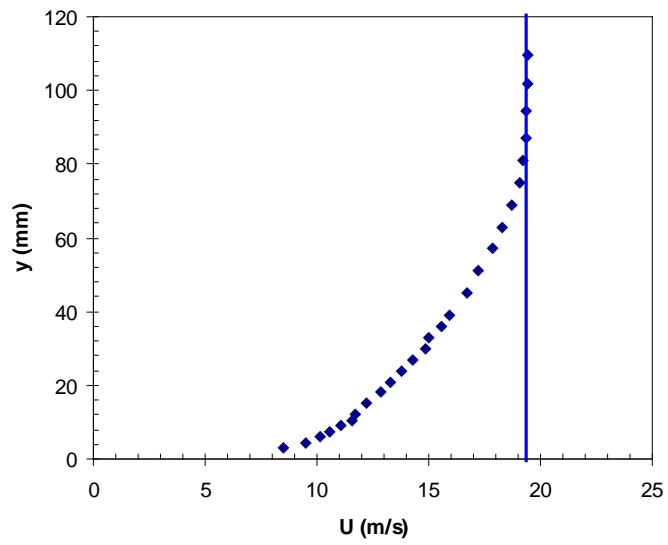
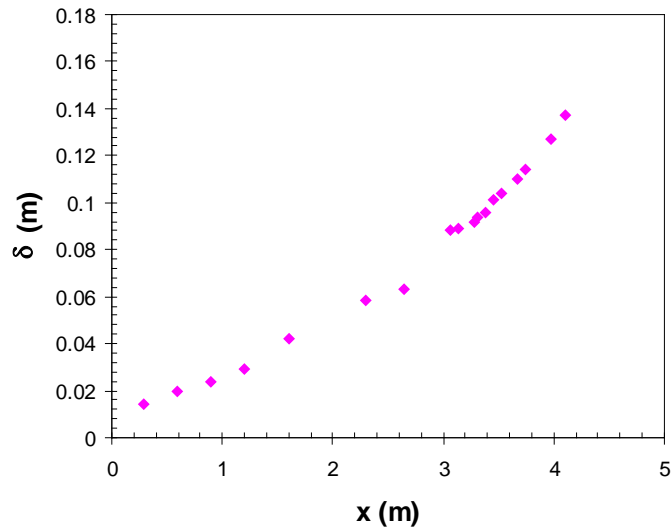
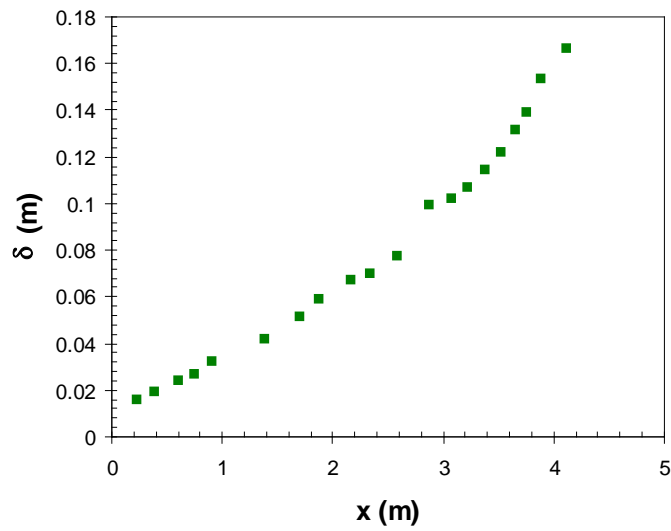


Figure 4.5 Velocity profile measured with an x-wire probe at a streamwise location of  $x = 2.587$  m with a reference velocity of 22 m/s. Freestream velocity,  $U_e = 19.4$  m/s is highlighted with a vertical line.

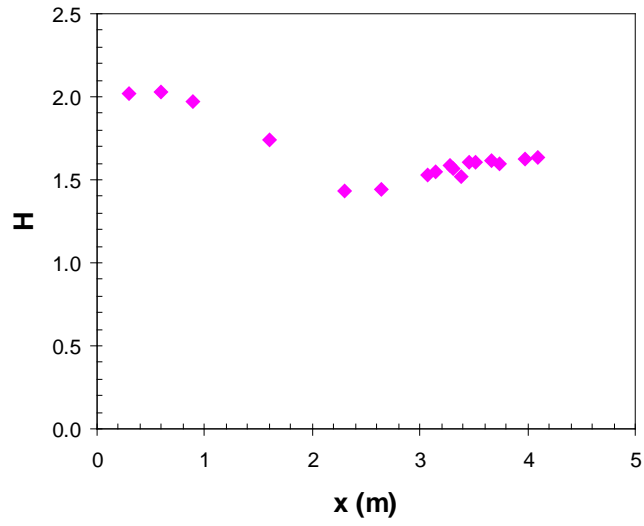


(a)

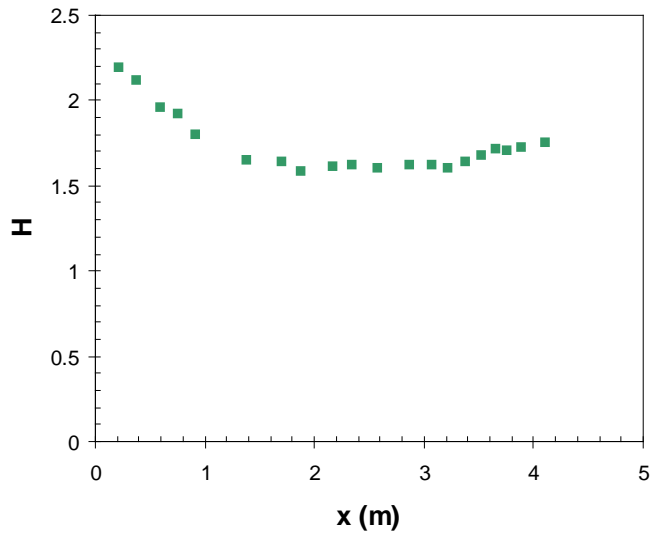


(b)

Figure 4.6 Boundary layer thickness,  $\delta$  for (a) Flow A and (b) Flow B



(a)



(b)

Figure 4.7 Shape factor,  $H$  for (a) Flow A and (b) Flow B

#### 4.1.4 Clauser's equilibrium pressure parameter, $\beta$

An equilibrium boundary layer flow was defined by Clauser (1954a) such that the parameter  $\beta$  is constant where  $\beta$  is defined as per Equation 4-5.

$$\beta \equiv -\frac{\delta^*}{\rho u_*^2} \frac{dP_\infty}{dx} \quad \text{Equation 4-5}$$

where  $\delta^*$  is displacement thickness, [m]  
 $\rho$  is density, [kg/m<sup>3</sup>]  
 $u_*$  is friction velocity, [m/s]  
 $P_\infty$  is pressure, [Pa], and  
 $x$  is streamwise distance, [m].

For Flow A and Flow B, Clauser's equilibrium pressure parameter is not constant, as seen in Figure 4.8, meaning that by this definition, these flows are not in an equilibrium state.

This parameter allows comparisons of different flows, many published flow data include  $\beta$ . Later in this chapter, 20 other flows are discussed, including some considered as equilibrium flows. It is useful to compare  $\beta$  values from different flows and also to contrast this with a more recent definition of an equilibrium pressure parameter by Castillo and George (2001) discussed in the next section.

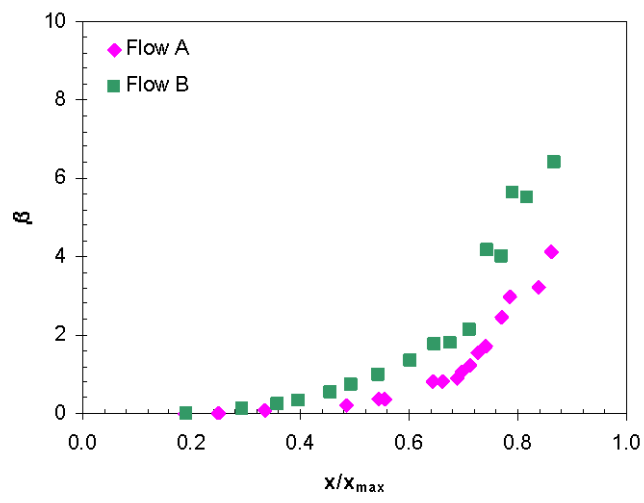


Figure 4.8 Clauser's equilibrium pressure parameter,  $\beta$ , for Flow A and Flow B.

#### 4.1.5 Equilibrium Pressure Parameter, $\Lambda_\theta$

The pressure parameter  $\Lambda_\theta$  (Castillo and George, 2001), is introduced here and discussed in again in Section 5.2. It is an important parameter used to help characterise flow development and define flow equilibrium.  $\Lambda_\theta$  is given in Equation 4-6 below. Equilibrium APG flows are expected to have  $\Lambda_\theta \sim 0.2$ , for FPG flows  $\Lambda_\theta \sim 1.9$  and for ZPG  $\Lambda_\theta \sim 0$ .

$$\Lambda_\theta = -\frac{\theta}{U_e} \frac{dU_e}{d\theta/dx} = \text{constant} \quad \text{Equation 4-6}$$

where  $\theta$  is the momentum thickness, [m]  
 $U_e$  is the free stream velocity, [m/s], and  
 $x$  is the streamwise distance, [m].

The commercial software package, Table Curve 2D™ was used to determine the curve fits to calculate  $dU_e/dx$  and  $d\theta/dx$  to evaluate  $\Lambda_\theta$ . This software produces a list of over three thousand different curve fits, with associated statistical quantities and it ranks them in the order of goodness of fit. The most accurate and physically realistic curve was selected in each case for each flow. For instance, a curve with sudden changes or asymptotic behaviour may yield a high goodness of fit value but was deemed physically unrealistic.  $\Lambda_{\theta\text{calc}}$  was determined based on these curves, and it is presented in Figure 4.9 for Flows 141, Han, A and B. Flows 141 and Han are discussed in more detail in Section 4.2.

An alternative method to find  $\Lambda_\theta$  is used by Castillo and George (2001) where the gradient of a log-log relationship between momentum thickness and freestream velocity defines  $\Lambda_\theta$ . By integrating Equation 4-6 a power law relationship is obtained:

$$\theta \approx U_e^{-1/\Lambda_\theta} \quad \text{Equation 4-7}$$

Castillo and Wang (2004) demonstrated that for flows with a changing pressure gradient, from FPG to ZPG then APG that whilst the flow is not in overall

equilibrium, it is in local equilibrium. An example used by Castillo and Wang (2004) is the flow of Schubauer and Klebanoff (1944), Figure 4.10. This method assigns a single value of  $\Lambda_\theta$  for each user-defined region. This method was not suitable for flows that have a gradual transition from one pressure gradient state to another, as it was very difficult to justify where each section should begin. Thus, a direct calculation method is used here instead, and is denoted thus:  $\Lambda_{\theta\text{calc}}$ .

Each of the four mentioned flows are expected to approach an asymptotic state where  $\Lambda_\theta \sim \text{constant}$ . When  $\Lambda_\theta$  is constant, the flow is regarded as being in equilibrium. The longitudinal location of the onset of this equilibrium state is given in Table 4.2 and represented graphically by a star in Figure 4.9. The existence of equilibrium as defined by  $\Lambda_\theta \sim \text{constant}$  is further examined in Chapter 5.

The parameter  $C_p$  is useful for identifying the pressure gradient as ZPG, or FPG or increasing or decreasing APG.  $\Lambda_\theta$  allows classification of regions of flow equilibrium and regions of transition, facilitating prediction of flow behaviour. This parameter helps to classify the flow and categorise the behaviour of other scaling values, as shown in Chapter 5. For instance,  $u^*$  is much more effective as a scaling parameter for the portion of the flow that is in 'equilibrium' as defined by  $\Lambda_{\theta\text{calc}}$ , than elsewhere.

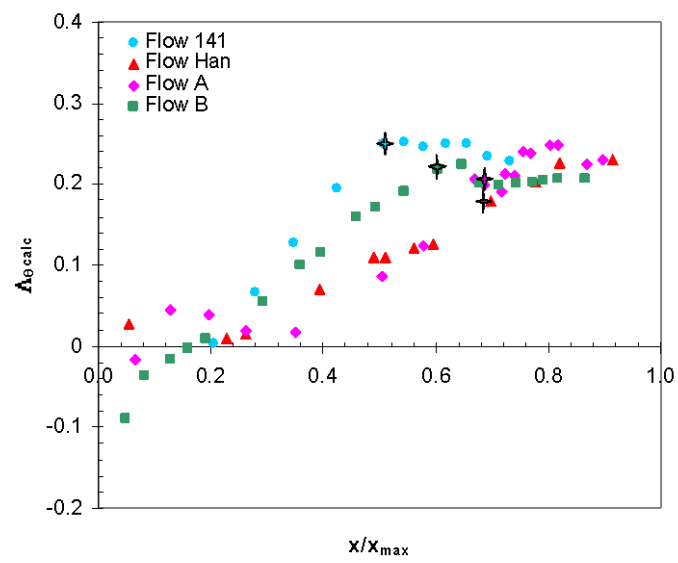


**Figure 4.9** Pressure parameter  $\Lambda_{\theta_{calc}}$ , for Flow A, Flow B, Flow Han and Flow 141. The star indicates the start of  $\Lambda_{\theta_{calc}} \sim \text{constant}$ , corresponding to the equilibrium region.

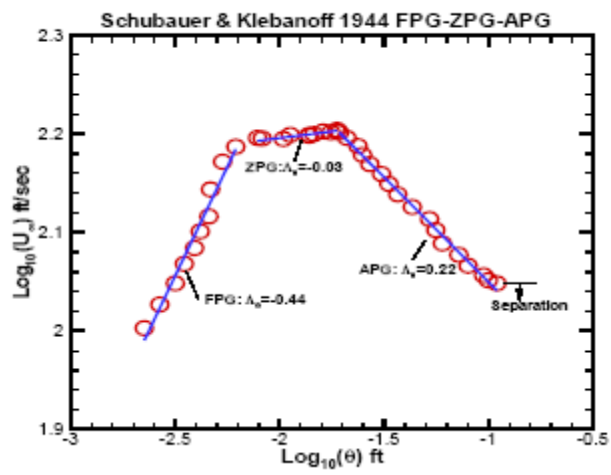


Figure 4.10 Local equilibrium as defined by  $\Lambda_\theta$ . (Figure 3, Castillo and Wang, 2004)

**Table 4.2** The location of the onset of APG flow equilibrium as defined by the pressure parameter  $\Delta\theta_{calc}$  where  $x = 0$  corresponds to the start of the test section.

Flow	Location of onset of equilibrium
141	2.10m (x/xmax =0.5)
Han	3.32m (x/xmax =0.7)
A	3.39m (x/xmax =0.7)
B	2.87m (x/xmax =0.6)

#### 4.1.6 Error Analysis for $\Lambda_{\theta\text{calc}}$

A Kline and McClintock (1953) type error analysis was used in estimating uncertainty in the experimental results used for calculating  $\Lambda_{\theta\text{calc}}$ . The experimental uncertainty,  $\omega$ , for each term of Equation 4-6 is given in Table 4.3, along with the total error  $E$  in  $\Lambda_{\theta\text{calc}}$  for each flow. Equation 4-8 below is used to calculate the total error,  $E$ .

$$E = \sqrt{\left(\frac{\partial\Lambda}{\partial\theta}\omega_1\right)^2 + \left(\frac{\partial\Lambda}{\partial U_e}\omega_2\right)^2 + \left(\frac{\partial\Lambda}{\partial d\theta/dx}\omega_3\right)^2 + \left(\frac{\partial\Lambda}{\partial dU_e/dx}\omega_4\right)^2} \quad \text{Equation 4-8}$$

where  $\Lambda$  is the pressure parameter, [-]  
 $\theta$  is the momentum thickness, [m],  
 $U_e$  is the free stream velocity, [m/s],  
 $x$  is the streamwise distance, [m], and  
 $\omega$  is the experimental uncertainty of each term, [m].

As seen in the last column of Table 4.3, the overall error in  $\Lambda_{\theta\text{calc}}$  is between 16 to 32% for Flows A, B, 141 and Han.

**Table 4.3** Uncertainty of each term appearing in the expression for  $\Lambda_{\theta\text{calc}}$  for Flow A, Flow B, Flow 141, and Flow Han.

<b>Experiment</b>	$\omega_1$	$\omega_2$	$\omega_3$	$\omega_4$	<b><i>E</i></b>
Flow A	0.01	0.01	0.012	0.016	29%
Flow B	0.01	0.01	0.003	0.013	16%
Flow 141	0.01	0.01	0.002	0.003	32%
Flow Han	0.01	0.01	0.003	0.003	17%
Uncertainty of measurement	$\theta$	$U_e$	$d\theta/dx$	$dU_e/dx$	

### 4.1.7 Determining friction velocity, $u_*$

Friction velocity,  $u_*$ , is defined as:

$$u_*^2 = \frac{\tau_w}{\rho} \quad \text{Equation 4-9}$$

where  $\rho$  is the fluid density, [ $\text{kg}/\text{m}^3$ ], and  
 $\tau_w$  is the wall shear stress, [ $\text{kg m}/\text{s}^2$ ].

The friction velocity for Flows A and B was determined as the arithmetic average of 3 methods, namely, Clauser charts (1954a), the two-dimensional integral momentum equation and measured values using total head tubes. Accurate knowledge of the friction velocity is necessary if it is to be used to scale velocity components. These techniques are next described in detail.

#### 4.1.7.1 Total Head Tube Measurement Technique

A total head tube can be used to determine the friction velocity. This technique assumes the existence of a log-law in the flow. This assumption, applied to adverse pressure gradient flows, continues to be debated in the literature (George and Castillo, 1997, Zagarloa et al. 1997, Barenblatt and Chorin, 1998). The uncertainty about the existence of the log-law is the reason that three techniques were utilised here, so as to compare the results and to justify the final values. One advantage of this method is that the equipment can be calibrated by performing experiments with fully developed pipe flow, where the log-law is known to exist and friction velocity can be determined exactly from the static pressure drop. This also allows the experimentalist to fine tune their skills at probe alignment.

This direct measurement technique involves placing a 2 mm OD total head tube on the floor of the tunnel aligned with the flow direction. This was done along the centerline of the test section where static pressure was also recorded via the wall taps. The relationship between the wall shear stress,  $\tau_w$  and the pressure was devised by Preston (1950):

$$\frac{\tau_w d^2}{4\rho v^2} = F\left(\frac{\Delta P d^2}{4\rho v^2}\right) \quad \text{Equation 4-10}$$

where  $\Delta P$  is the dynamic pressure, [N/m<sup>2</sup>],  
 $d$  is the outer diameter of the total head tube, [m],  
 $\rho$  is the density, [kg/m<sup>3</sup>], and  
 $v$  is the kinematic viscosity, [m<sup>2</sup>/s].

The dynamic pressure is the pressure difference between the total pressure from the total head tube and the static pressure, measured by the wall taps. The original curves plotted by Preston were later shown to be erroneous (Patel, 1965). Patel took the original equation from Preston and defined calibration ranges based on a variable,  $y^*$  and an independent variable  $x^*$ , given in Equation 4-11 and Equation 4-12 respectively.

$$y^* = \log\left(\frac{1}{4}\left(\frac{u_* d}{v}\right)^2\right) \quad \text{Equation 4-11}$$

$$x^* = \log\left(\frac{\Delta P d^2}{4\rho v^2}\right) \quad \text{Equation 4-12}$$

where  $u_*$  is the friction velocity, [m/s],  
 $d$  is the outer diameter of the total head tube, [m],  
 $v$  is the kinematic viscosity, [m<sup>2</sup>/s],  
 $\Delta P$  is the dynamic pressure, [N/m<sup>2</sup>], and  
 $\rho$  is the density, [kg/m<sup>3</sup>].

The appropriate calibration ranges are defined below:

$$y^* = 0.8287 - 0.1381x^* + 0.1437x^{*2} - 0.006x^{*3} \quad \text{for } 2.9 < x^* < 5.6$$

$$x^* = y^* + 2\log(1.95y^* + 4.10) \quad \text{for } 5.6 < x^* < 7.6$$

To use Patel's method, one must first calculate  $x^*$  from Equation 4-12 then using the appropriate calibration range determine  $y^*$ . Finally, Equation 4-11 is used to find the friction velocity.

To confirm the calibration of the total head tube, the fully developed pipe flow apparatus was used. Log-law is known to exist in fully developed pipe flow and the friction velocity can be obtained exactly from the 2-D momentum integral equation, as given in Equation 4-13 (Hinze, 1975, p 712). At a Reynolds number of 260,000 the friction velocity was found to be 1.44 m/s. For comparison two different size total head tubes, namely 2 mm and 3 mm (internal diameter), were used to determine the friction velocity by Patel's method. This yielded values of 1.44 and 1.45 m/s, respectively. As there was little difference between the calculated friction velocity and the results from the 2 mm and 3 mm tubes, the 2 mm tube was used in the wind tunnel.

$$u_*^2 = -\frac{R}{2\rho} \frac{dP}{dx} \quad \text{Equation 4-13}$$

where  $R$  is the pipe radius, [m],  
 $\rho$  is the density, [kg/m<sup>3</sup>], and  
 $dP/dx$  is the rate of change of pressure drop along the pipe, [N/m<sup>2</sup>/m].

Previously, this calibration using the pipe flow apparatus and the same equipment was also done for a Master of Engineering thesis (Han, 2000). Han reported results at 3 Reynolds numbers, namely  $Re = 146,000, 274,000$  and  $281,000$  and for 7 different total head tube diameters ranging from 1-mm to 6 mm. The largest difference between the actual  $u_*$  value and that obtained by Patel's correction was found to be  $\pm 5\%$  using a 4 mm tube at the highest Reynolds number. The average difference, for the 1 mm and 2 mm tubes was only  $\pm 0.2\%$  and for all 21 possibilities, the average difference was only  $\pm 0.4\%$ .

It should be noted that a further correction was suggested by Frei and Thomann (1980). The technique was applied to the current data and was not found to significantly alter the results, and thus was discarded. The required correction was less than  $\pm 1\%$ .

Use of a total head tube in this manner, within the wind tunnel presents some physical difficulties. Alignment, both on the floor and parallel to the flow are critical. The results from this technique were slightly higher than the results from the momentum integral technique, which is discussed in Section 4.1.7.3.

#### 4.1.7.2 Clauser Chart Technique

The Clauser chart method relies on the existence of the log-law region near the wall, thus it is necessary to have accurate velocity measurements close to the wall. For this purpose, a Dantec 55P05 single wire probe was used, (see Appendix IV for the Matlab code to convert single wire voltage readings to velocity). By plotting  $U/U_e$  against  $yU_e/\nu$  with a semi logarithmic scale, the boundary overlap region plots as a straight line. Figure 4.11 is the combined Clauser charts for Flow B. The individual charts with the gradient values can be found in Appendix V. The straight line relationship is known as the ‘log-law’ and is given in Equation 4-14, where  $y$  is the distance from the wall and  $U$  is the local streamwise mean velocity. The constants,  $B$  and  $\kappa$  are assumed independent of Reynolds number. Recently, it was shown that this assumption may lead to inaccuracies, particularly at low Reynolds numbers (Wei et al., 2005). The value of the constants applied in this case are those originally suggested by Clauser, namely  $B = 5.2$  and  $\kappa = 0.41$ . The gradient is independent of constant  $B$  in the log-law and involves only the constant  $\kappa$ .

$$\frac{U}{u_*} = \frac{1}{\kappa} \ln\left(\frac{yu_*}{\nu}\right) + B \quad \text{Equation 4-14}$$

where  $U$  is the local streamwise mean velocity, [m/s],  
 $\kappa$  is a constant, [-],  
 $y$  is the vertical height from the floor, [m],  
 $u_*$  is the friction velocity, [m/s],  
 $\nu$  is the kinematic viscosity, [m<sup>2</sup>/s], and  
 $B$  is a constant, [-].

The log-law can be re-written in the form given in Equation 4-15. The mathematical steps required for this can be found in Appendix VI. In this form, it is clear that the gradient of the  $\frac{U}{U_e}$  versus  $\frac{yU_e}{\nu}$  plot can be utilised to obtain the friction velocity.

$$\frac{U}{U_e} = \frac{u_*}{\kappa U_e} \ln\left(\frac{yU_e}{\nu}\right) + C \quad \text{Equation 4-15}$$

where  $U$  is the local streamwise velocity, [m/s],  
 $U_e$  is the freestream velocity, [m/s],  
 $u_*$  is the friction velocity, [m/s],

$\kappa$  is a constant, [-],

$y$  is the vertical height from the floor, [m],

$\nu$  is the kinematic viscosity, [m<sup>2</sup>/s], and

$C$  is a constant, [-].

The existence of the ‘law of the wall’ is still a contentious issue. Other difficulties with this technique lie in its reliance on accurate measurements close to the wall and in the influence the observer has in selecting the range of data to use. This technique yielded the most scatter in results and the greatest deviation from the other two methods.

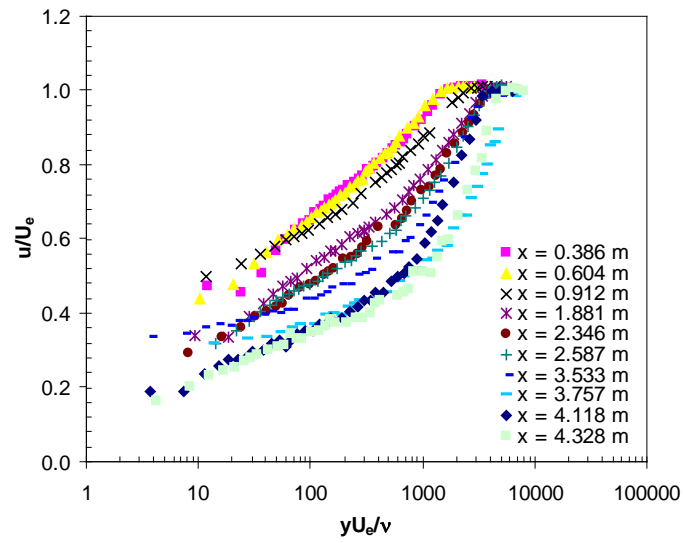


Figure 4.11 Clausner chart, single wire measurements for Flow B. Further results are given in Appendix V.

### 4.1.7.3 Momentum Integral Technique

In steady, two dimensional, incompressible flow we have:

$$\int_{y=0}^{\delta} \left( \bar{u} \frac{\partial \bar{u}}{\partial x} + \bar{v} \frac{\partial \bar{u}}{\partial y} - U \frac{dU}{dx} \right) dy = -u_*^2 \quad \text{Equation 4-16}$$

where  $\bar{u}$  is the time averaged stream wise velocity component, [m/s],  
 $x$  is the streamwise distance, [m],  
 $\bar{v}$  is the time averaged velocity component in the y direction, [m/s],  
 $y$  is the height, [m],  
 $U$  mean velocity, [m/s] and  
 $u_*$  is the friction velocity, [m/s].

From Equation 4-16 with application of the equation for continuity, and integration with the boundary condition  $y \rightarrow \infty$ , the expression given in Equation 4-17 can be obtained, (Schlichting, pp 158-160, 1979).

$$u_* = \sqrt{\frac{d}{dx} (U_e^2 \theta) + \delta^* U_e \frac{dU_e}{dx}} \quad \text{Equation 4-17}$$

where  $u_*$  is the friction velocity, [m/s],  
 $x$  is the distance in the streamwise direction, [m],  
 $U_e$  is the freestream velocity, [m/s],  
 $\theta$  is the momentum thickness, [m], and  
 $\delta^*$  is the displacement thickness, [m].

This technique requires knowledge of the displacement thickness, the streamwise development of momentum thickness and the free stream velocity. The difficulty is in determining the streamwise derivatives. In this case, the source computer program as utilised for  $\Lambda_{\theta \text{calcs}}$ , Curvefit 2D was utilised. This software produces a list of over three thousand different curve fits, with associated statistical quantities and it ranks them in the order of goodness of fit. Again, the most accurate and physically realistic curve was selected in each case.

This method relies on the flow being two-dimensional. To investigate 2-dimensionality, vertical Pitot static traverses were performed equidistance from the centreline. As expected this yielded symmetric results, as evident in the plot of velocity scaled with freestream velocity in Figure 4.12. The average difference was  $\pm 1.7\%$ , which is an acceptable deviation.

The flow pattern on the floor was investigated using two identical total head tubes placed equidistance from the centreline. This was done at four streamwise locations as shown in Figure 4.13. These results are also an indication of the streamwise pressure distribution within the tunnel. The percentage difference from the corresponding centreline location value is given in Figure 4.14. Most readings are less than  $\pm 2\%$  different, and the biggest difference is  $\pm 8\%$  at  $x = 0.386$  m and  $0.25$  m from the centreline. Given the difficulty in placing and aligning the probes this difference is acceptable.

The momentum integral technique is criticised because it neglects the normal stress components, and these terms are considered to become strong in APG flows approaching separation.

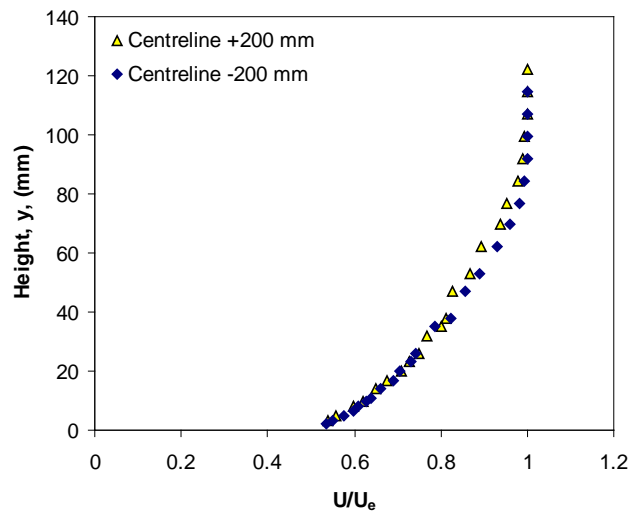


Figure 4.12 Pitot traverses  $\pm 200$  mm from centreline at  $x = 3.558$  m, Flow B, to demonstrate flow symmetry.

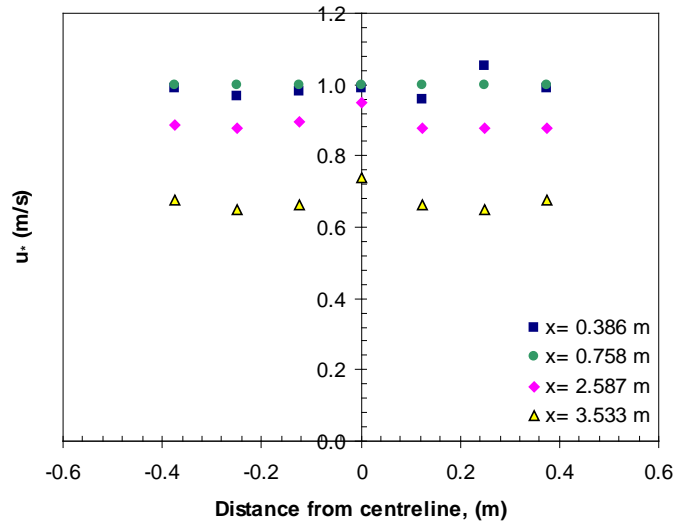


Figure 4.13 Total head tube readings on floor of tunnel at different distances from centreline, at 4 streamwise locations, for Flow B, to show symmetry.

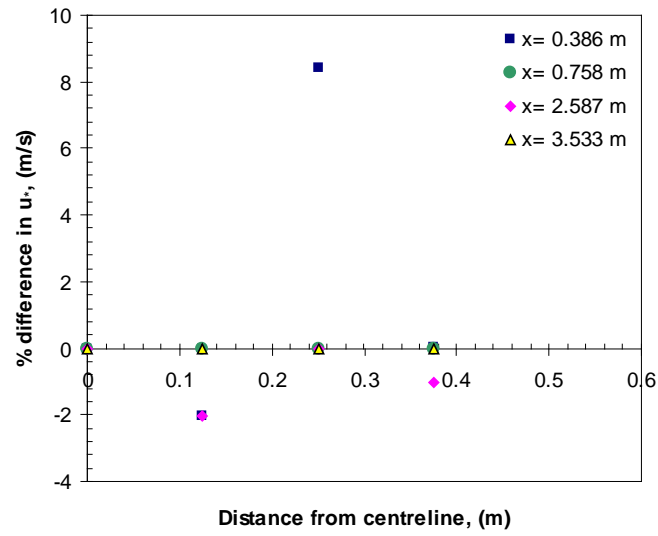


Figure 4.14 Percentage difference in pressure readings either side of centreline for 4 streamwise locations, for Flow B.

#### **4.1.7.4 Determining friction velocity, $u_*$**

In Figure 4.15, the results for determining friction velocity by total head tubes, Clauser charts and the momentum integral technique are presented for Flow A and Flow B. All the afore mentioned techniques for calculating friction velocity have their shortcomings, as such it was decided to use the average of all 3 to arrive at a final  $u_*$  value for Flow B, Figure 4.16(b). Single wire measurements were not done for Flow A, thus the average of the 2-D momentum integral equation technique and the total head tube measurement technique was used, Figure 4.16(a).

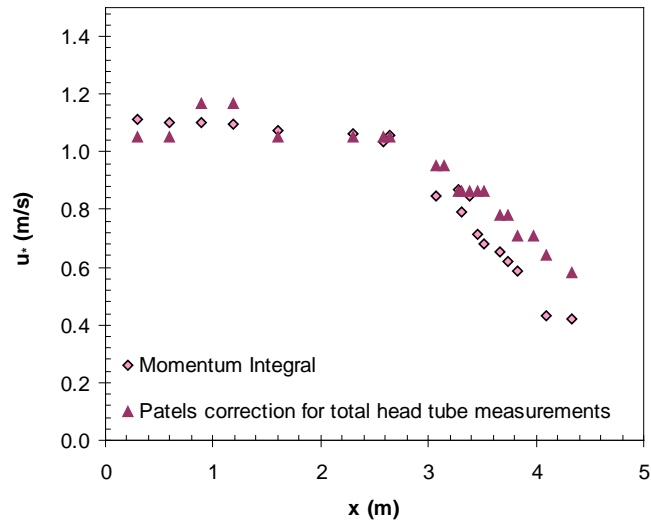
In addition to the three techniques used here, other methods to evaluate  $u_*$  exist. Of these, three others are discussed here because of their popularity. The techniques are, direct numerical simulation, oil fringe imaging and surface mounted hot film probes.

Direct numerical simulation involves detailed computer modelling of the flow. It was not done here because the purpose of this research is to experimentally generate and compare adverse pressure gradient flows with the aim of increasing the understanding of these flows. An increased understanding of APG flow behaviour may in fact lead to improved direct numerical techniques.

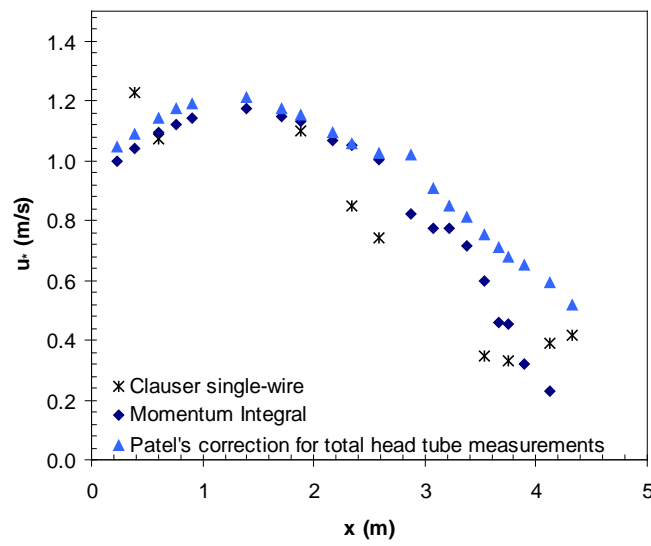
The oil-fringe imaging technique has been shown to have good accuracy (Driver, 2003). It involves placing a thin line of oil on the floor of the wind tunnel. This technique is well explained in Naughton and Sheplak (2000). When the airflow is initiated most of the oil is quickly forced downstream, leaving a thin wedge of oil behind. When this thin wedge is illuminated with a monochromatic light, interference fringes with uniform spacing can be seen near the leading edge. A digital camera can be used to record these patterns. By comparing the spacing of the fringes with that of an upstream reference location the friction velocity can be determined. The Victoria University wind tunnel was not suitable for this technique firstly because it is an open return type and any excess oil exiting the tunnel would have become a safety concern. Secondly, the placing of a light source and the imaging equipment would have been impossible at locations close to the end of the tunnel. Thirdly, this technique requires the tunnel to be impulsively set to the required wind velocity; the speed control device on the Victoria University tunnel does not allow this.

Thin hot-film sensors can be glued directly to the wall to facilitate friction velocity measurements. A typical hot-film sensor manufactured by Dantec (55R47) consists

of a 0.05 mm polyimide foil with a 0.001 mm coating of nickel. A protective coating of silicon dioxide is also applied. Ludweig (1949) was the first to define an analytical solution to the heat transfer relationship for flush mounted skin friction sensors. This type of probe works much like a hot-wire however a large amount of heat is conducted into the wall. Matthews and Poll (1985) reported that only a small proportion of the measured signal is dependent on the flow, they suggested an alteration to the equations. This technique has the advantage of being able to directly measure friction velocity after a velocity traverse has been done without having to restart the tunnel. Whilst the shortcomings of the technique are the difficulties in calibration and that a shift in calibration can occur when the probe is relocated. Reichert and Azad (1977) report that is likely due to minute changes in the contact between the probe body and the mounting. Thus, it is preferable to calibrate *in situ*, necessitating many probes be used in an experiment like this to map friction velocity along the length of the tunnel.

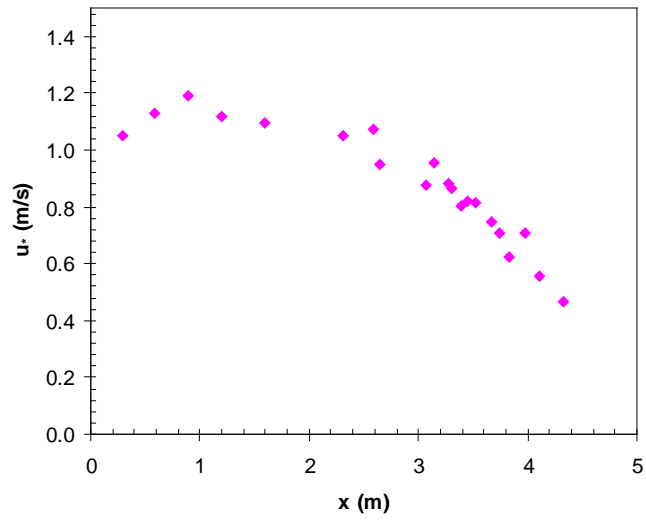


(a)

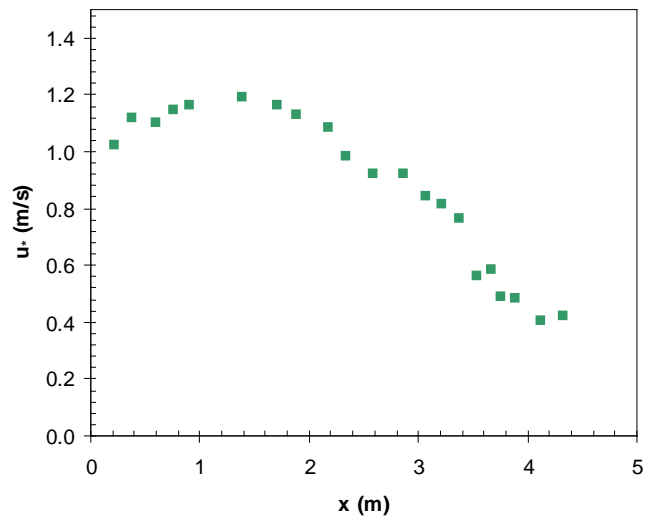


(b)

Figure 4.15 Friction velocity,  $u_*$  as determined by Clauser Charts, momentum integral and Preston Tubes with Patel's correction for (a) Flow A and (b) Flow B.



(a)



(b)

Figure 4.16 Average friction velocity,  $u_*$  for (a) Flow A and (b) Flow B.

#### 4.1.8 Turbulence Intensity, $\mathcal{I}$

The turbulence intensity,  $\mathcal{I}$ , as defined in Equation 4-18 is a measure of the level of turbulence. Typically, research wind tunnels have a turbulence intensity of approximately 1% in the free stream. The turbulence intensity for the core region of Flow A and Flow B are approximately 0.6 %, as evident in Figure 4.17. For comparison, the core intensity for Flow 141 is 0.3 %, and for Flow Skare is 0.5 %. Details of Flow 141 and Flow Skare are to come in the next sections.

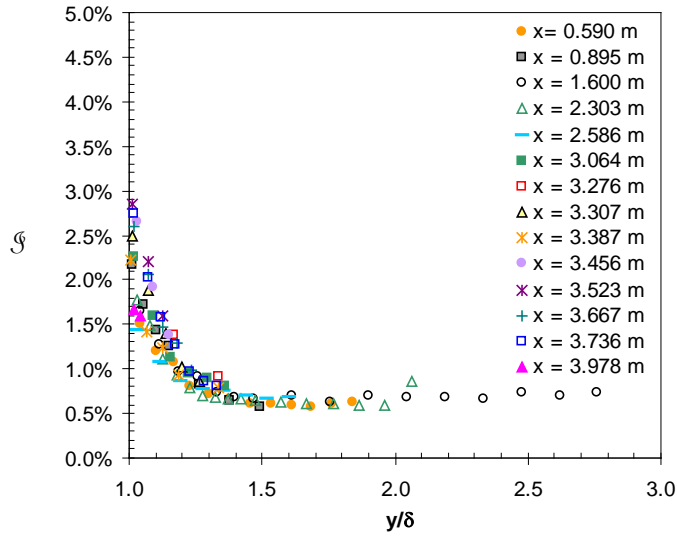
$$\mathcal{I} = \frac{\sqrt{\overline{(u')^2}}}{U} \quad \text{Equation 4-18}$$

where

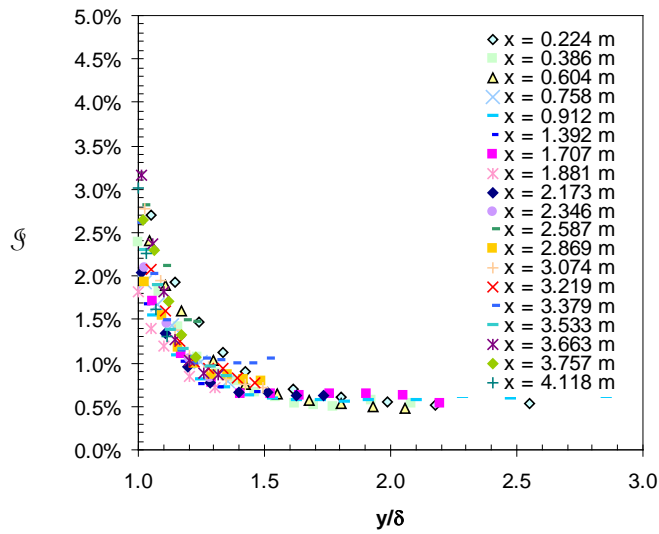
$\mathcal{I}$  is the turbulence intensity, [-]

$u'$  is the fluctuating velocity in the x direction, [m/s], and

$U$  is the time averaged velocity, [m/s]



(a)



(b)

Figure 4.17 Turbulence intensity for the core region of (a) Flow A and (b) Flow B.

#### **4.1.9 Comment on relationship between location of transition from increasing APG to decreasing APG**

Initial investigations revealed that for Flow 141, Flow Han and Flow A the streamwise location of the change in pressure parameter,  $C_p$ , from increasing APG to decreasing APG coincides with the onset of equilibrium as defined by  $\Lambda_{\theta_{calc}}$ . Therefore, Flow B was designed with a much earlier transition to explore this coincidence further. For Flow B the location of equilibrium defined by  $\Lambda_{\theta_{calc}}$  did not coincide with the location of transition to decreasing APG. As a result, it was concluded that a relationship between the two occurrences does not exist.

## **4.2 Flow 141 and Flow Han**

It is useful to compare the new flows with other reported flows of a similar nature. Two such flows are that of Flow Han (Han, 2000) and Flow 141 (Samuel and Joubert, 1974).

Flow Han was generated in the Victoria University Wind Tunnel and was designed to be similar to Flow 141. The height settings of the adjustable top are the same for Flow Han and Flow A as given previously in Table 4.1. Flow Han differs from Flow A only in the entrance conditions, in particular the shape of the transition from the contraction cone to the false floor, as discussed in Section 4.1.1 for Flow A and Flow B. Whilst the exact shape of this transition is not known for Flow Han, this flow did not experience flow separation or re-circulation. The effect of the different entrance conditions is evident in the pressure gradient (Figure 4.18); with Flow A initially having a more pronounced favourable pressure gradient.

The flow of Samuel and Joubert given as Flow 141 in the 1980 Stanford Conference (Kline et al, 1981) is an increasingly APG flow. The test section used to generate Flow 141 was fitted with a plane diffuser 3.5 m long with inlet dimensions of 1 m by 0.36 m. The diffuser flow had both increasing and decreasing APG regions, as seen in Figure 4.18, transition occurs at  $x/x_{\max} = 0.56$ .

Table 4.4 through to Table 4.7 present a summary of the flow data for each flow, consisting of measurement location, free stream velocity, boundary layer thickness, shape factor, friction velocity, and pressure coefficient. A visual comparison of the four flows, namely Flows A and B, Flow Han and Flow 141, is given in terms of freestream velocity and  $\delta^*/\delta$ . As indicated in Figure 4.19, these flows exhibit similar freestream development evident by the similar gradient, even though Flow 141 does have a higher magnitude. Furthermore, the boundary layer growth is also similar in these flows as evident in Figure 4.20.

The shape factor,  $H$ , defined previously in Equation 4-2, is one traditional way of demonstrating flow development and predicting flow separation. In Figure 4.21 Flow 141 and Flow Han show an almost steady shape factor over the entire flow, whilst Flow A and Flow B experience an initial decrease over the first stage of the flow followed by a levelling off at an  $x/x_{\max}$  of approximately 0.35. This levelling off

indicates a type of flow stability and occurs sooner than that defined by pressure parameter  $\Lambda_\theta$  which predicts flow equilibrium for Flow A and Flow B at  $x/x_{\max} = 0.7$  and 0.6 respectively. It is shown in Chapter 5 that when scaling mean flow, shape factor alone is not adequate for flow classification.

Clauser's pressure parameter  $\beta$ , was not available for Flow Han or Flow 141.

Friction velocity is presented in Figure 4.22. All four flows exhibit similar friction velocity values and development. This agreement further confirms the validity of the friction velocity measurements for Flow A and Flow B.

For completeness, the comparison of pressure parameter  $\Lambda_{\theta\text{calc}}$  is repeated here as Figure 4.23. Flow Han and Flow 141 exhibit flow equilibrium as defined by  $\Lambda_{\theta\text{calc}}$ . This is evident by the levelling off which occurs at  $x = 2.10$  m ( $x/x_{\max} = 0.5$ ) for Flow 141 and  $x = 2.87$  m ( $x/x_{\max} = 0.6$ ) for Flow Han.

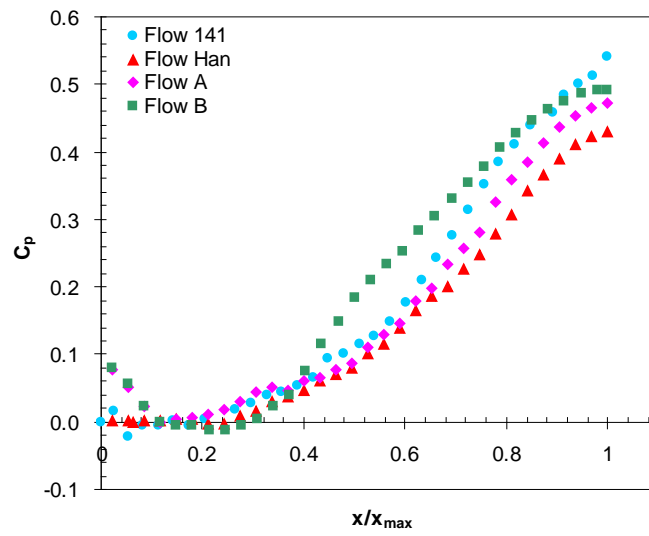


Figure 4.18  $C_p$  for Flows A, B, Han and 141.

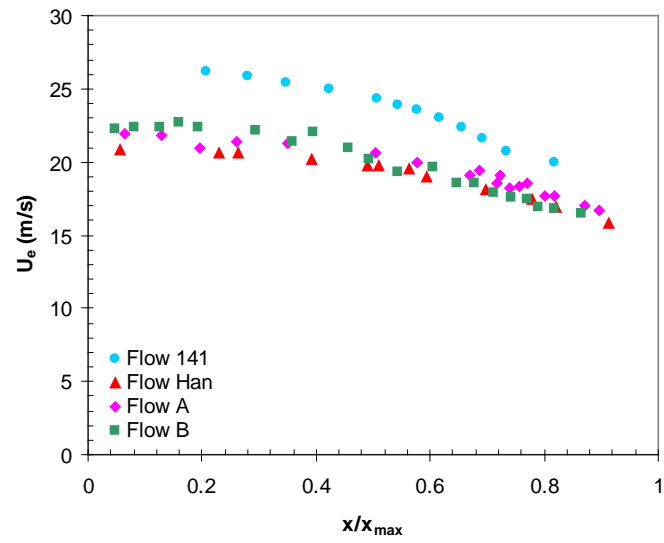


Figure 4.19 Freestream velocity,  $U_e$ , for Flow 141, Flow Han, Flow A and Flow B.

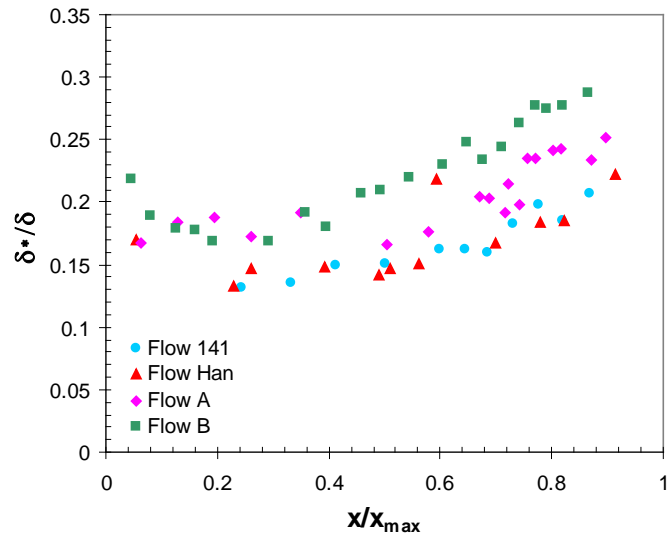


Figure 4.20  $\delta^*/\delta$  for Flows A, B, Han and 141.

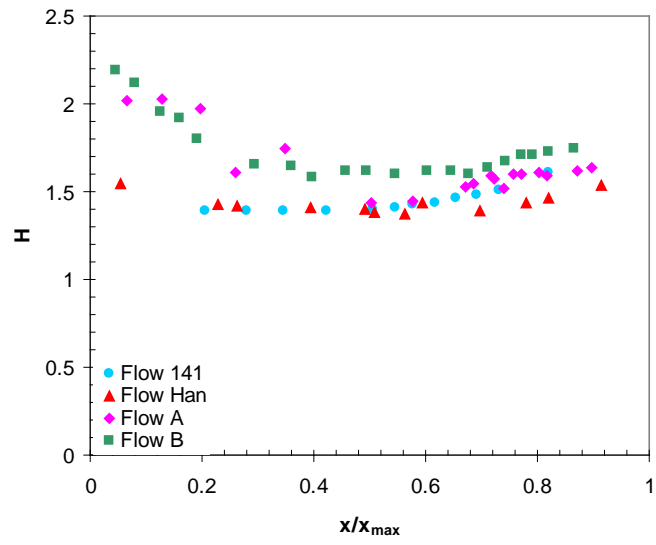


Figure 4.21 Shape Factor,  $H$ , for Flow 141, Flow Han, Flow A and Flow B.

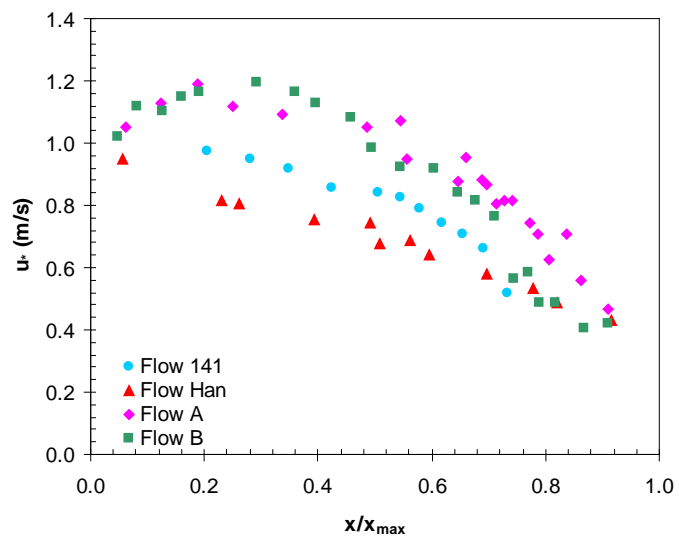


Figure 4.22 Friction velocity,  $u_*$  for Flow 141, Flow Han, Flow A and Flow B.

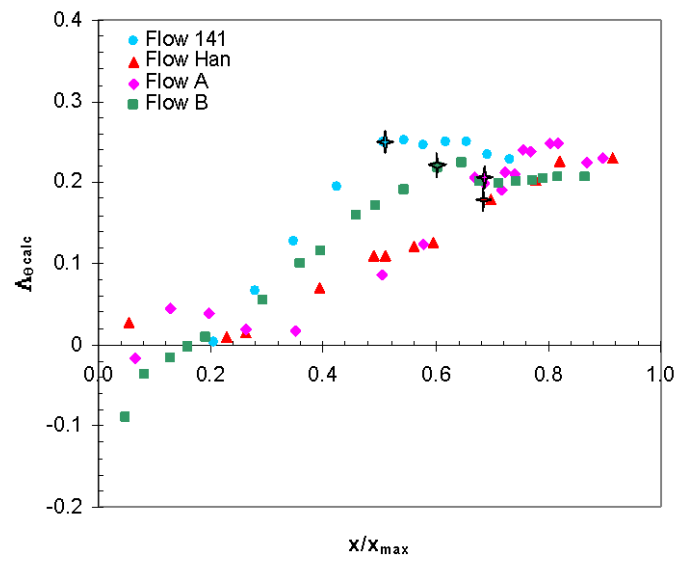


Figure 4.23 Pressure parameter  $\Delta\theta_{calc}$  for Flow 141, Flow Han, Flow A and Flow B.

**Table 4.4 Summary data Flow 141.**

$x/x_{\max}$	$U_e$ (m/s)	$\delta$ (m)	H	$u_*$ (m/s)	$\Lambda_{\theta\text{calc}}$
0.21	26.16	0.03	1.39	0.97	0.00
0.28	25.85	0.04	1.39	0.95	-0.07
0.35	25.45	0.04	1.39	0.92	-0.13
0.42	24.95	0.04	1.39	0.86	-0.19
0.51	24.29	0.05	1.40	0.84	-0.25
0.54	23.94	0.05	1.41	0.82	-0.25
0.58	23.56	0.06	1.43	0.79	-0.25
0.62	23.00	0.06	1.44	0.75	-0.25
0.66	22.33	0.06	1.46	0.71	-0.25
0.69	21.62	0.07	1.48	0.66	-0.23
0.73	20.74	0.07	1.51	0.52	-0.23
0.82	18.80	0.09	1.61		

**Table 4.5 Summary data Flow Han.**

$x/x_{\max}$	$U_e$ (m/s)	$\delta$ (m)	H	$u_*$ (m/s)	$\Lambda_{\theta\text{calc}}$
0.06	20.80	0.01	1.55	0.95	-0.03
0.23	20.60	0.03	1.43	0.82	-0.01
0.26	20.60	0.03	1.42	0.81	-0.02
0.39	20.20	0.04	1.41	0.75	-0.07
0.49	19.80	0.06	1.40	0.74	-0.11
0.51	19.70	0.05	1.38	0.68	-0.11
0.56	19.50	0.06	1.37	0.69	-0.12
0.59	19.00	0.05	1.43	0.64	-0.13
0.70	18.15	0.09	1.39	0.58	-0.18
0.78	17.50	0.10	1.43	0.53	-0.20
0.82	16.90	0.12	1.46	0.49	-0.23
0.91	15.80	0.13	1.54	0.43	-0.23

**Table 4.6 Summary data Flow A.**

$x/x_{\max}$	$U_e$ (m/s)	$\delta$ (m)	H	$u_*$ (m/s)	$\beta$	$Re_\theta$	$\Lambda_{\theta\text{calc}}$
0.06	21.90	0.01	2.02	1.05	-0.05	1694	-0.02
0.12	21.85	0.02	2.03	1.13	-0.03	2637	0.04
0.19	20.95	0.02	1.98	1.19	-0.01	3115	0.04
0.25	21.40	0.03	1.61	1.12	0.02	4423	0.02
0.34	21.23	0.04	1.74	1.09	0.08	6549	0.02
0.48	20.65	0.06	1.43	1.05	0.21	9308	0.09
0.54	20.40	0.07	1.56	1.07	0.37	12376	0.14
0.56	20.00	0.06	1.44	0.95	0.37	10267	0.12
0.64	19.10	0.09	1.53	0.88	0.83	15025	0.21
0.66	19.40	0.09	1.55	0.95	0.80	15132	0.20
0.69	18.52	0.09	1.59	0.88	0.90	13743	0.19
0.70	19.05	0.09	1.57	0.87	1.08	16256	0.21
0.71	18.25	0.09	1.52	0.80	1.22	15208	0.21
0.73	18.30	0.10	1.60	0.82	1.57	18056	0.24
0.74	18.50	0.10	1.60	0.81	1.71	18870	0.24
0.77	17.70	0.11	1.61	0.74	2.43	19470	0.25
0.79	17.70	0.11	1.59	0.71	3.00	20532	0.25
0.84	17.05	0.13	1.62	0.71	3.24	20858	0.22
0.86	16.65	0.14	1.64	0.56	4.13	23368	0.23

**Table 4.7 Summary data Flow B.**

$x/x_{\max}$	$U_e$ (m/s)	$\delta$ (m)	H	$u_*$ (m/s)	$\beta$	$Re_\theta$	$\Lambda_{\theta\text{calc}}$
0.06	21.90	0.01	2.02	1.05	-0.15	2379	-0.02
0.12	21.85	0.02	2.03	1.13	-0.10	2539	0.04
0.19	20.95	0.02	1.98	1.19	-0.07	3285	0.04
0.25	21.40	0.03	1.61	1.12	-0.03	3783	0.02
0.34	21.23	0.04	1.74	1.09	0.00	4480	0.02
0.48	20.65	0.06	1.43	1.05	0.11	6364	0.09
0.54	20.40	0.07	1.56	1.07	0.25	8503	0.14
0.56	20.00	0.06	1.44	0.95	0.33	9827	0.12
0.64	19.10	0.09	1.53	0.88	0.54	11983	0.21
0.66	19.40	0.09	1.55	0.95	0.73	12255	0.20
0.69	18.52	0.09	1.59	0.88	0.99	13587	0.19
0.70	19.05	0.09	1.57	0.87	1.35	18424	0.21
0.71	18.25	0.10	1.52	0.80	1.75	19240	0.21
0.73	18.30	0.10	1.60	0.82	1.78	19240	0.24
0.74	18.50	0.10	1.60	0.81	2.12	20287	0.24
0.77	17.70	0.11	1.61	0.74	4.14	22528	0.25
0.79	17.70	0.11	1.59	0.71	4.02	24827	0.25
0.84	17.05	0.13	1.62	0.71	5.61	25237	0.22
0.86	16.65	0.14	1.64	0.56	5.51	27552	0.23

### **4.3 Classical Flows**

For further comparison, particularly for mean velocity deficit scaling, flow data from Clauser (1954a, 1954b), Bradshaw (1966), and Newman (1951) were utilised. All are decreasingly APG flows and were reported at the 1968 Stanford Conference. In the proceedings of that conference, each flow was given a reference number, which is utilised henceforth in this thesis. These flows are collectively referred to as the ‘classical flows’ here. These reference numbers are given in Table 4.8.

The pressure distribution for these flows is given in Figure 4.24. All are decreasingly APG, evident by the concave down shape of the pressure distribution.

The freestream velocity, boundary layer thickness, and shape factor are given in Figure 4.25, Figure 4.26, and Figure 4.27, respectively. It is noteworthy that the shape factor is almost constant for all flows except for Flow 3500, indicating that this flow may be approaching separation.

The equilibrium pressure parameter,  $\beta$  is presented in Figure 4.28. Flow 2200 and Flow 2500 are near constant, indicating flow equilibrium as defined by Clauser. As also exhibited with shape factor, the rising value of  $\beta$  for Flow 3500 is further evidence that this flow may be approaching separation.

The friction velocity for the classical flows is presented in Figure 4.29. Flow 2200 and Flow 2300 have near constant friction velocity while the other flows have a decreasing friction velocity in the streamwise direction, similar to Flows A and B.

The symbols used for Flows 2200 and 2300 in Figure 4.24 to Figure 4.29 are purposefully similar. These flows by Clauser, have very similar pressure gradients, freestream velocities and friction velocities. However, significant difference between these two flows is seen in boundary layer thickness and equilibrium pressure parameter.

For convenience, the tabulated form of this data along with  $\Lambda_{0calc}$  is given in Appendix VII.

**Table 4.8 Summary and description of classical adverse pressure gradient flows. Flow designation from the 1968 Stanford Conference (Coles *et al*)**

<b>Author and Year</b>	<b>Reference Number</b>	<b>Flow Description</b>	<b>Pressure Gradient</b>
Clauser, 1954(b)	2200	Mild APG	Decreasing APG
Clauser, 1954(b)	2300	Moderate APG	Decreasing APG
Bradshaw, 1966	2500	Mild APG	Decreasing APG
Newman, 1951	3500	Airfoil boundary layer. Approaching separation.	Decreasing APG

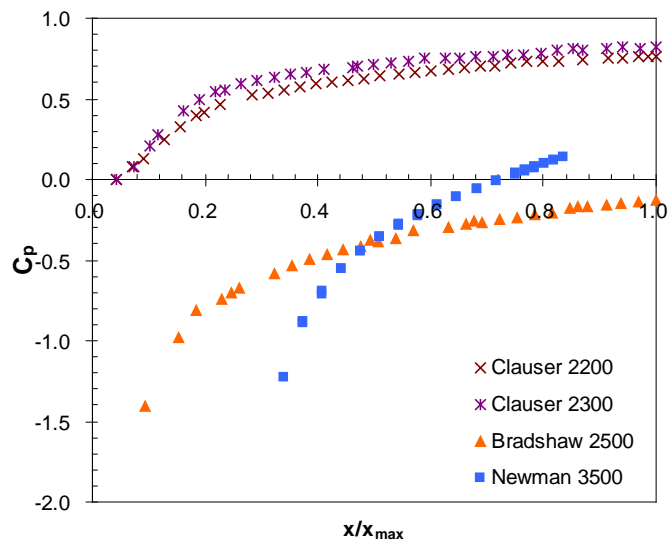


Figure 4.24 Pressure distribution  $C_p$ , for the classical flows.

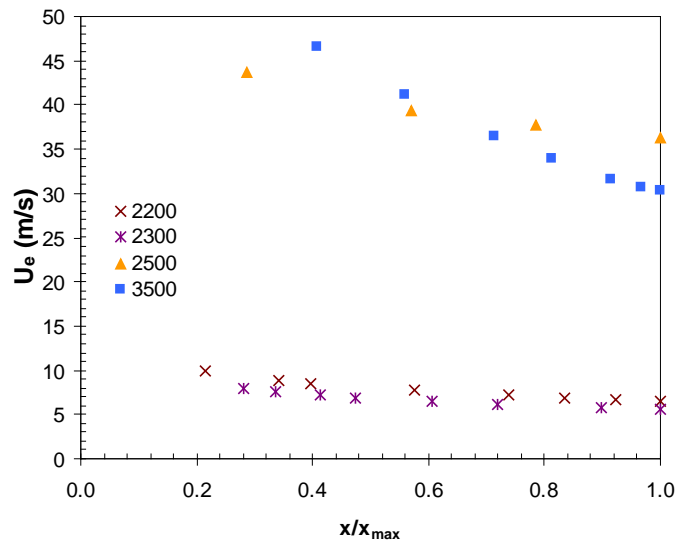


Figure 4.25 Freestream velocity,  $U_e$ , for the classical flows.

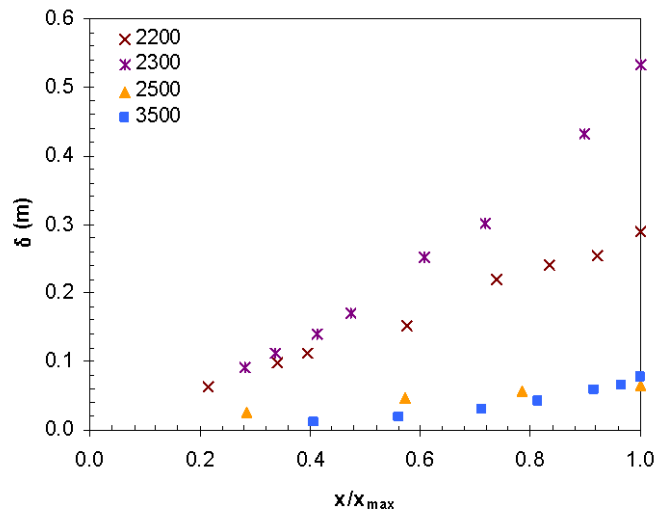


Figure 4.26 Boundary layer thickness,  $\delta$ , for the classical flows.

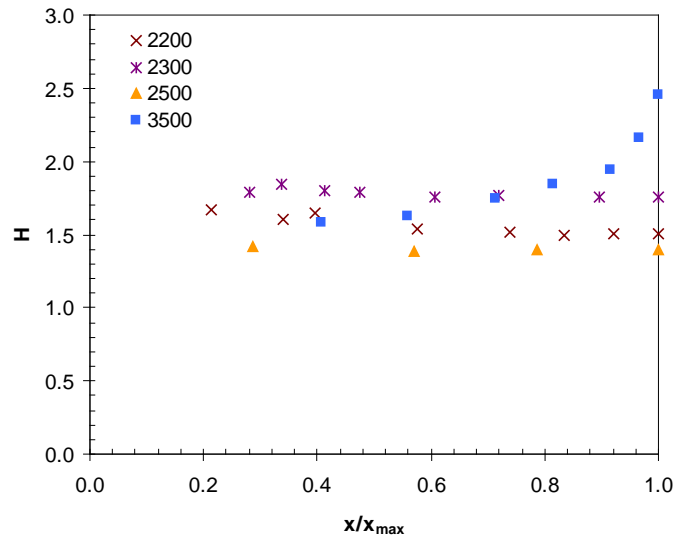


Figure 4.27 Shape factor,  $H$ , for the classical flows.

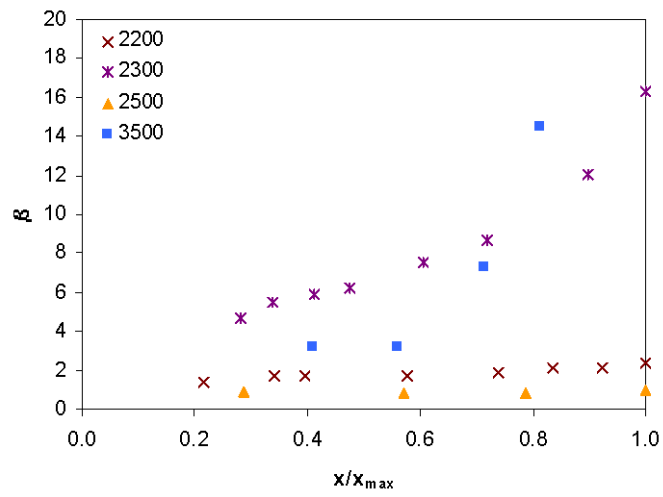


Figure 4.28 Clauser's equilibrium pressure parameter,  $\beta$ , for the classical flows.

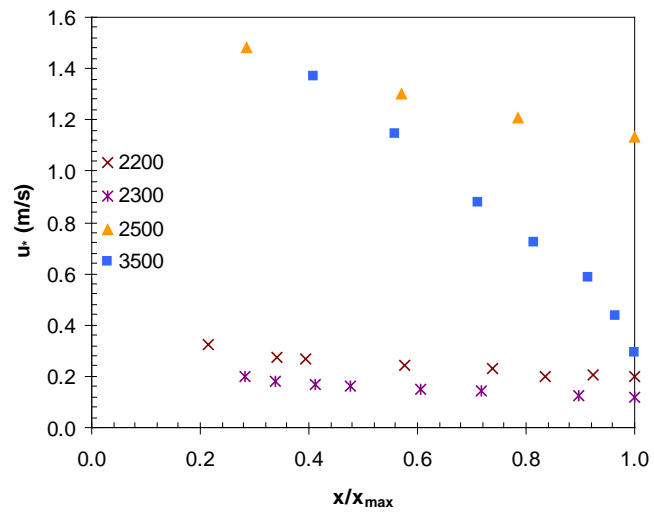


Figure 4.29 Friction velocity,  $u_*$ , for Flow 2200, Flow 2300, Flow 2500, and Flow 3500.

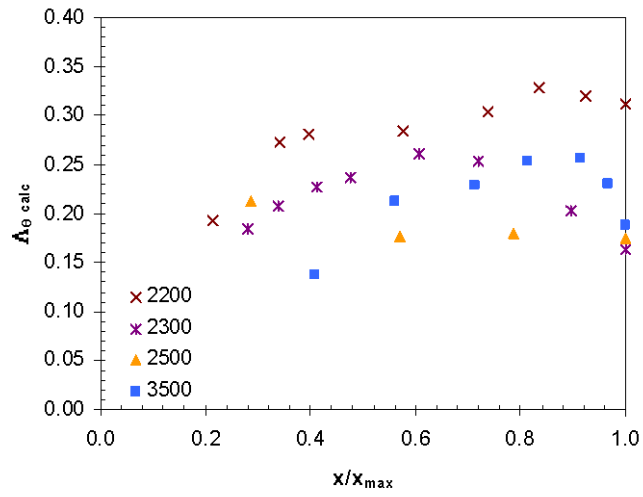


Figure 4.30 Castillo and George equilibrium pressure parameter  $\Lambda_{\theta \text{ calc}}$  for classical flows.

#### **4.4 Other Flows**

Fourteen other adverse pressure gradient flows from the literature were also reviewed and compared. A brief description of the flow and the pressure gradient is given in Table 4.9 along with a reference to each flow's literary source and a reference name or number by which the flow is subsequently referred. These flows are used throughout the thesis to further examine and compare findings. The pressure distribution in terms of pressure parameter  $C_p$ , shape factor  $H$ , boundary layer thickness  $\delta$ , Clauser's equilibrium pressure parameter  $\beta$  and the equilibrium pressure parameter  $\Lambda_{\theta_{calc}}$  are presented in Figure 4.31, Figure 4.32, Figure 4.33, Figure 4.34 and Figure 4.35 respectively. Note that plots of  $C_p$ ,  $H$ ,  $\delta$  and  $\Lambda_{\theta_{calc}}$  are presented with the same vertical scale for different flows. However, with plots of Clauser's equilibrium pressure parameter  $\beta$ , it is necessary to alter the vertical scale for each flow.

All these flows were chosen based on their  $C_p$  pressure distribution and their shape factor. Flows 1100, 1200, 2900 and 3800 were chosen because they have a similar uniform shape of  $C_p$ , namely decreasingly adverse pressure gradient. Thus, in the next chapter when mean flow scaling is explored it is anticipated that these flows would behave in a similar manner. In contrast to this, Flow 4000 was chosen because it has an interesting  $C_p$  profile, beginning adverse then levelling off to ZPG before returning to APG.

Flow 3700 was selected because it has a long section of near linear  $C_p$ .

The shape factor for Flow 3600 is near constant, which is in contrast to the  $C_p$  profile which indicates a near zero pressure gradient for half the profile then has a region of decreasingly APG before levelling off to ZPG again.

Flows 5000 and 5100 were also selected because they both have an initial short ZPG region, which is similar to Flows A and B.

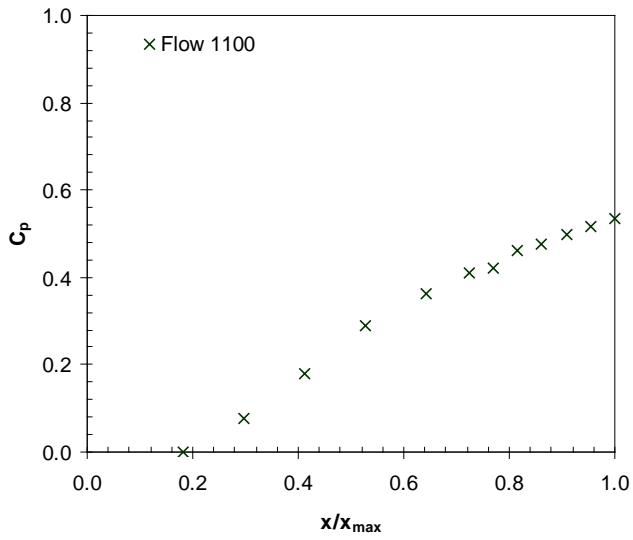
Flow L&S is an APG flow generated using direct numerical simulation (DNS), it too has an initial short ZPG region followed by decreasing APG. It was selected because

it has published Reynolds stress data. Flow A&E and Flow N&H were also selected for this reason.

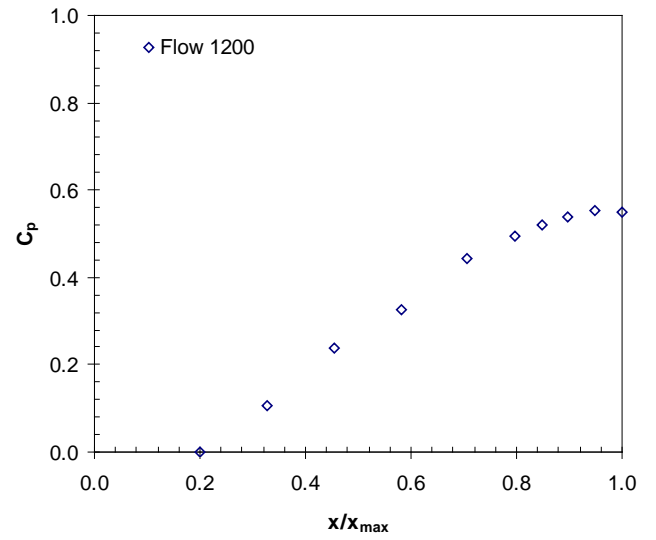
All the flows are examined to determine if any of flow parameters are sufficient to predict when a particular mean flow scaling will yield a collapse and when it won't.

**Table 4.9 Summary and description of additional Adverse Pressure Gradient flows.**

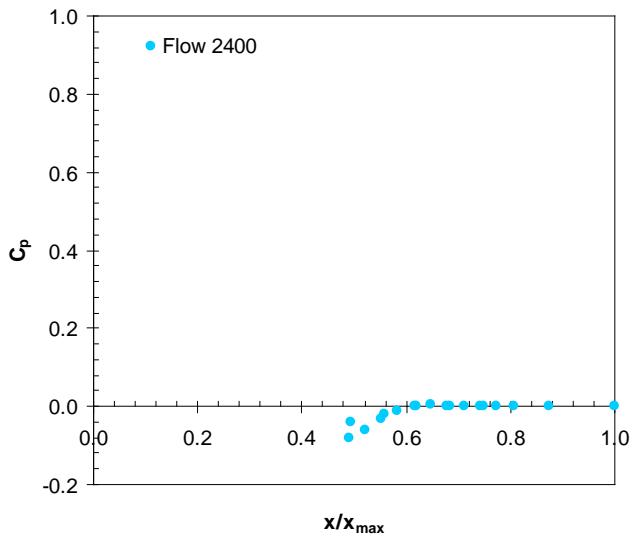
<b>Author and Year</b>	<b>Reference Number</b>	<b>Flow Description</b>	<b>Pressure Gradient</b>
Ludwig and Tillmann, 1949	1100	Mild APG	Decreasingly APG
Ludwig and Tillmann, 1949	1200	Strong APG	Decreasingly APG
Bradshaw and Ferriss, 1965	2400	Moderate APG	Decreasingly APG, then ZPG
Perry, 1966	2900	Decreasing APG	Decreasingly adverse, approaching ZPG
Moses, 1964	3600	Boundary layer on cylinder in axially symmetric flow	ZPG for 20 inches, then abruptly changes to increasingly APG over 10 inches, then ZPG for 10 inches
Moses, 1964	3700	Boundary layer on cylinder in axially symmetric flow	Almost linear APG
Moses, 1964	3800	Boundary layer on cylinder in axially symmetric flow	Decreasingly APG, approaching ZPG
Moses, 1964	4000	Boundary layer on cylinder in axially symmetric flow	Decreasingly APG, then ZPG for a substantial region then a short region of APG
Fraser, 1956	5000	Flow in round 10 degree diffuser	Initially zero, followed by decreasingly adverse section approaching ZPG
Fraser, 1956	5100	Flow in round 10 degree diffuser	Decreasingly APG, approaching ZPG
Skare	Skare		Decreasingly APG
Lee and Sung, 2008	L&S	DNS strong APG	Decreasing APG
Nagano and Houra, 2002	N&H	Flat plate with adjustable roof	Moderate to strong APG
Aubertine and Eaton, 2005	A&E	Laser Doppler anemometry tripped flat plate flow	Mild APG



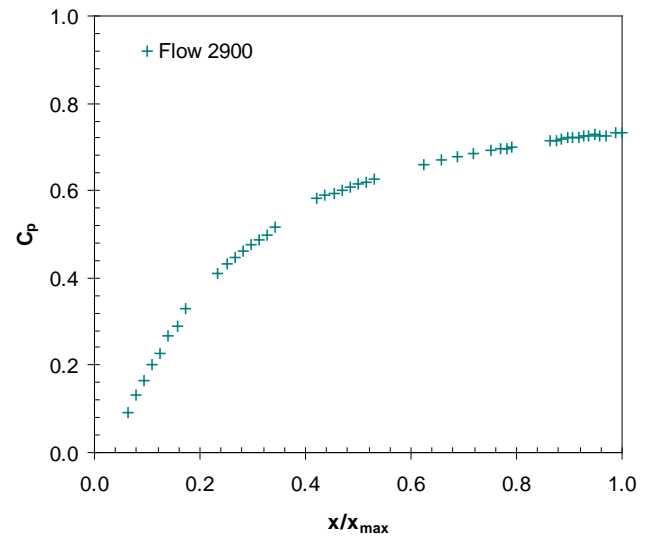
(a)



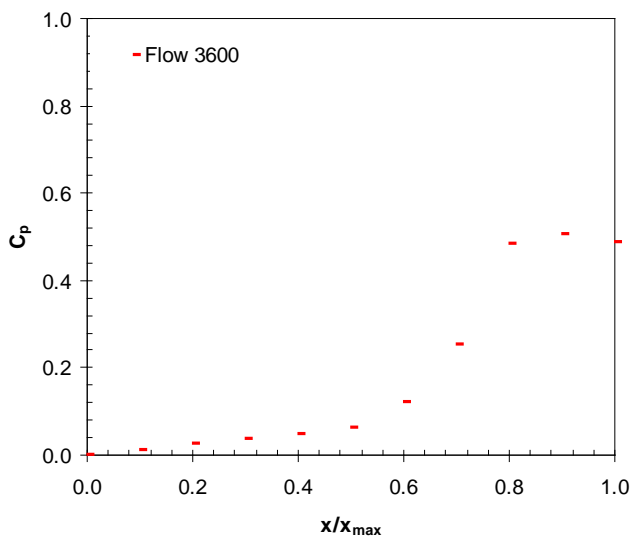
(b)



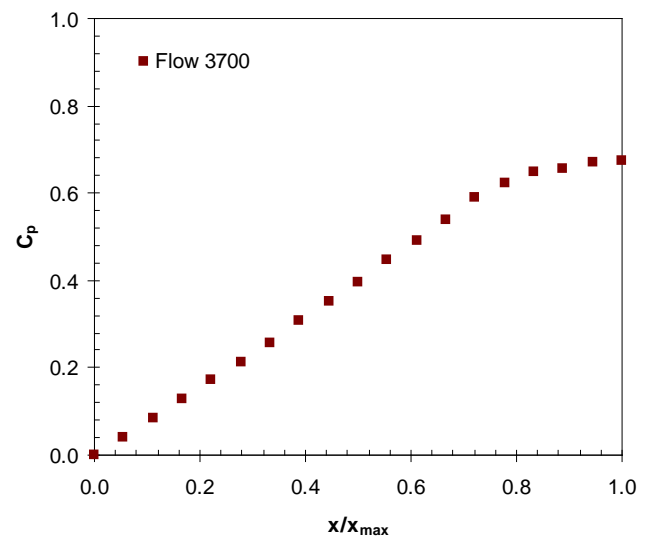
(c)



(d)



(e)



(f)

(figure continues next page)

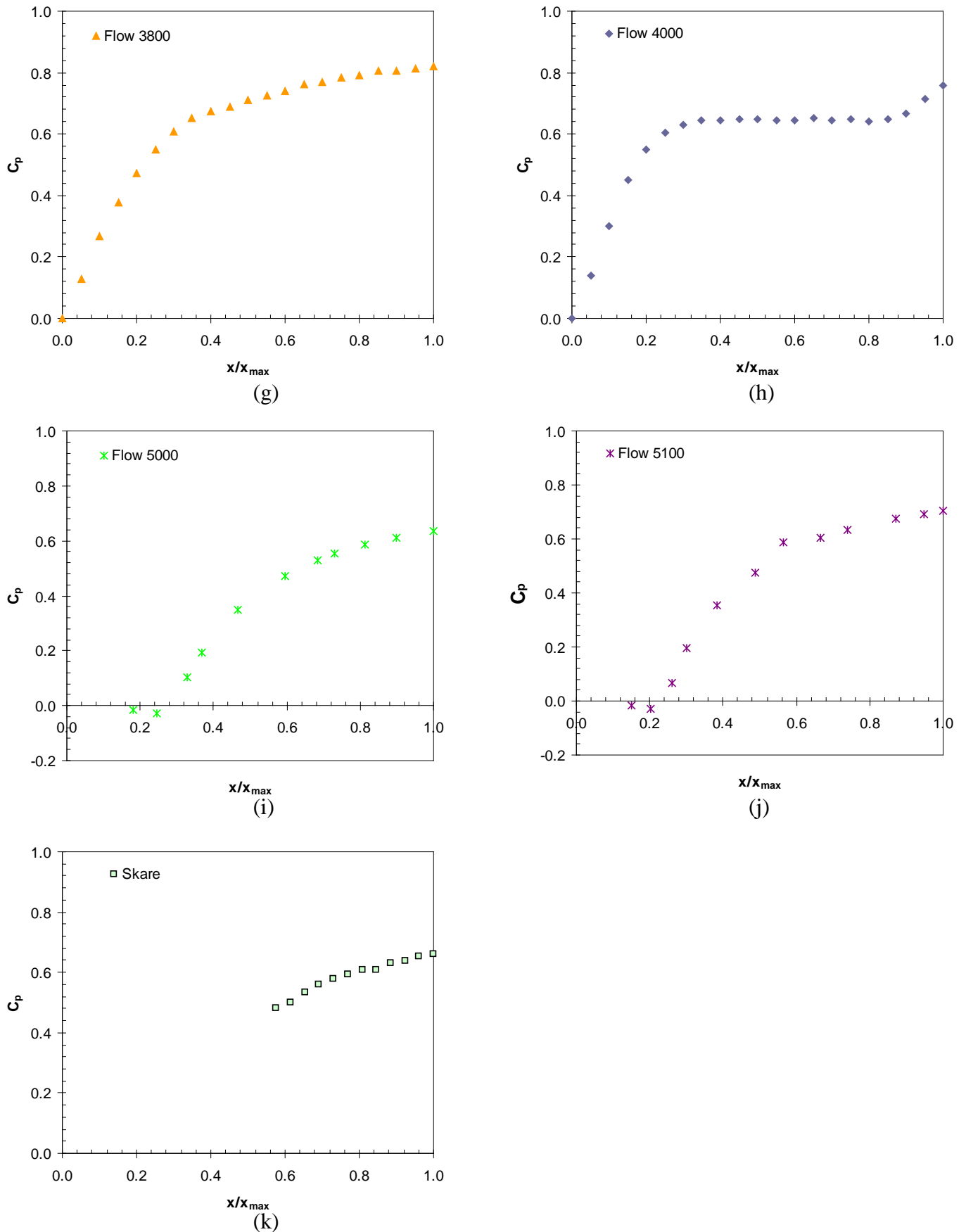


**Figure 4.31** Pressure distribution,  $C_p$  for (a) Flow 1100, (b) Flow 1200, (c) Flow 2400, (d) Flow 2900, (e) Flow 3600, (f) Flow 3700, (g) Flow 3800, (h) Flow 4000, (i) Flow 5000, (j) Flow 5100, and (k) Flow Skare.

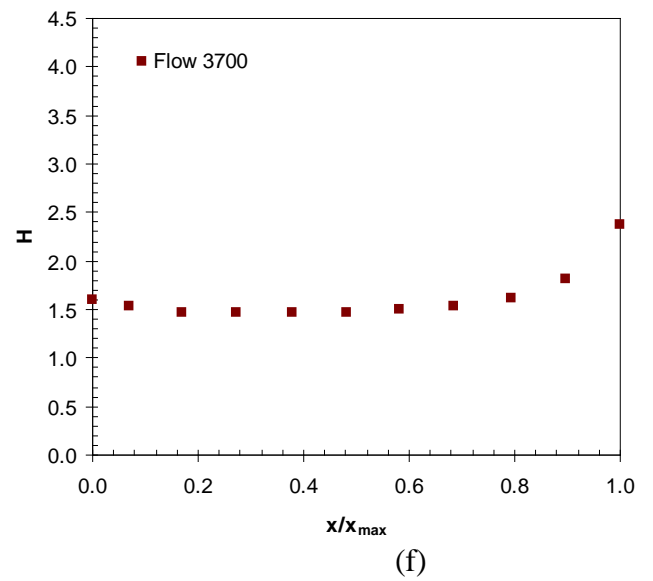
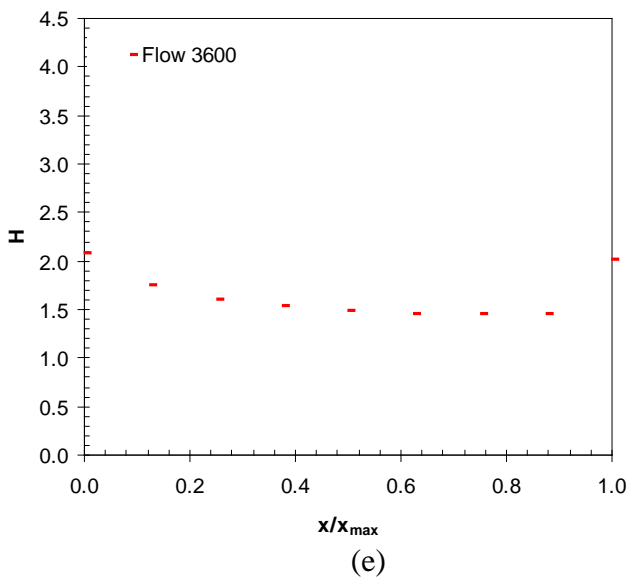
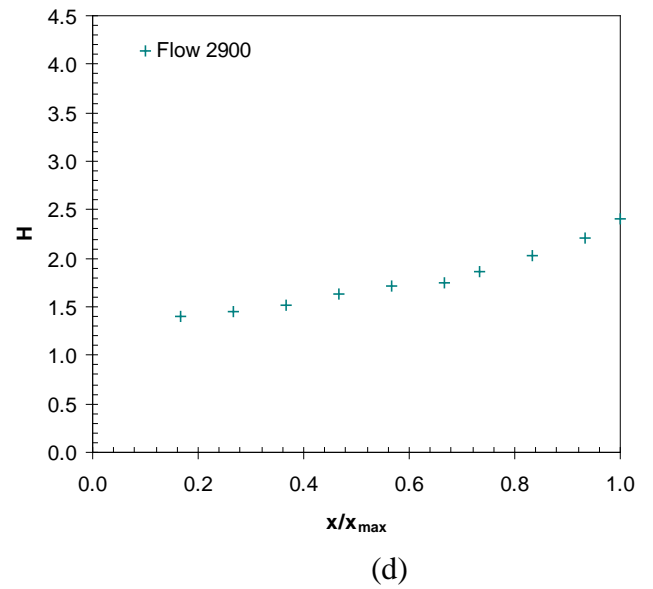
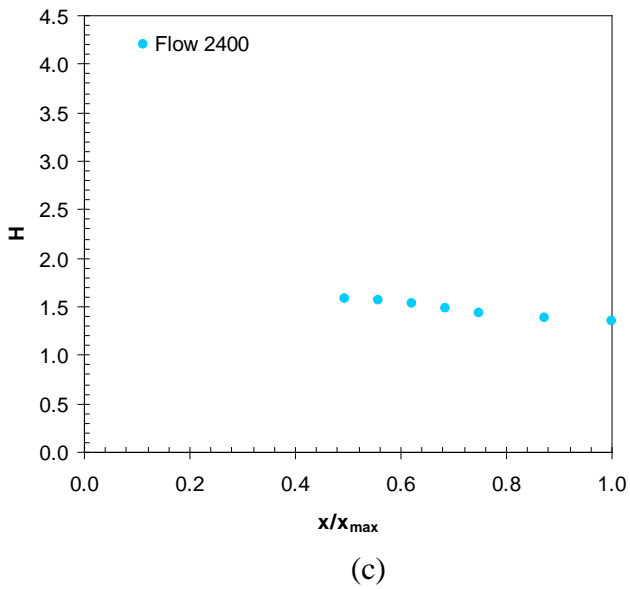
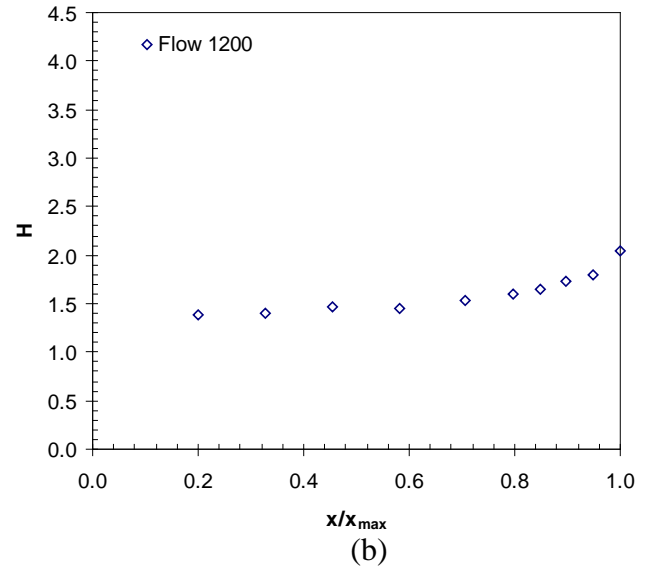
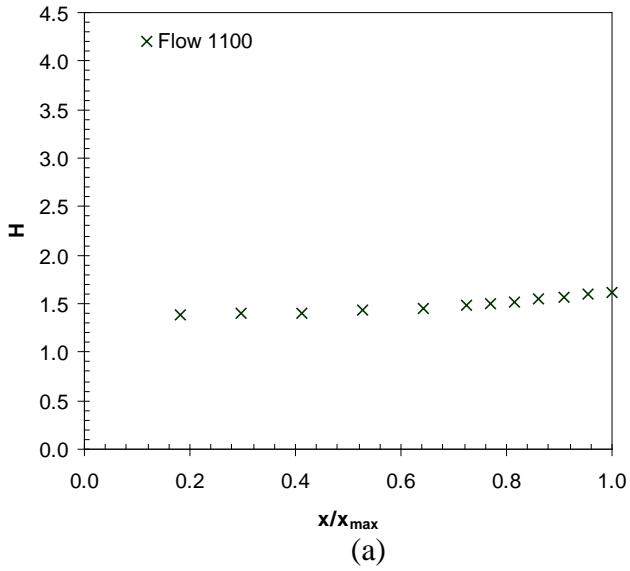


(figure continues next page)

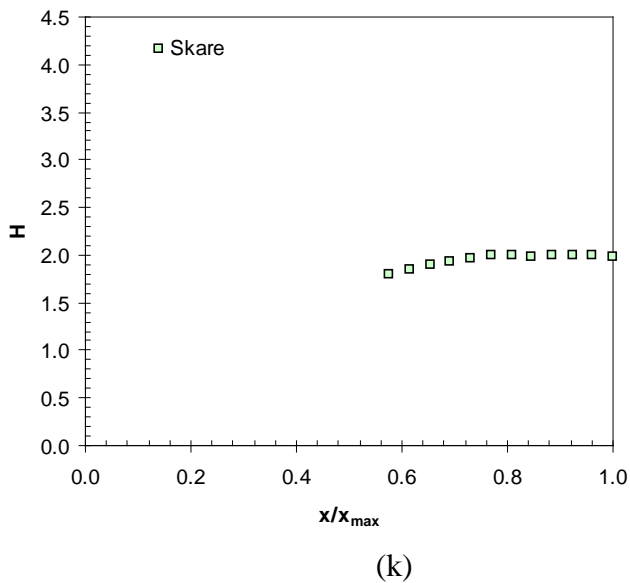
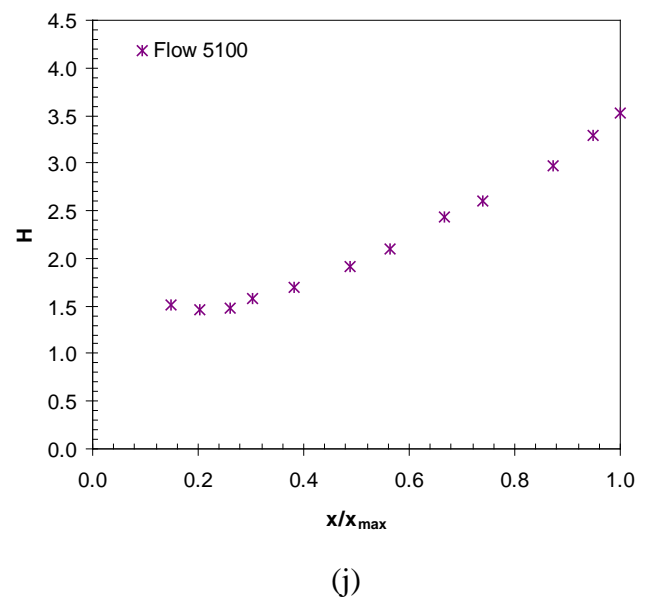
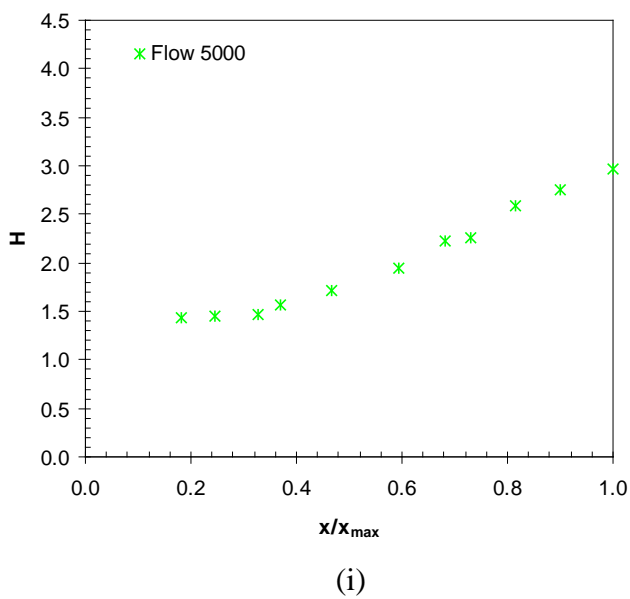
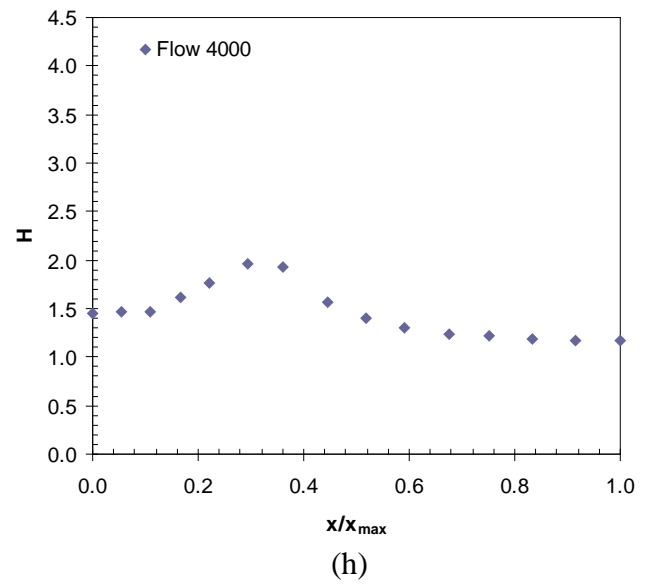
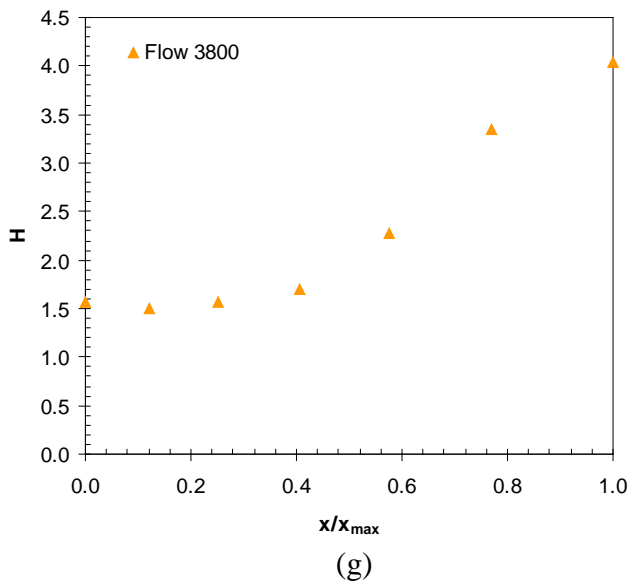
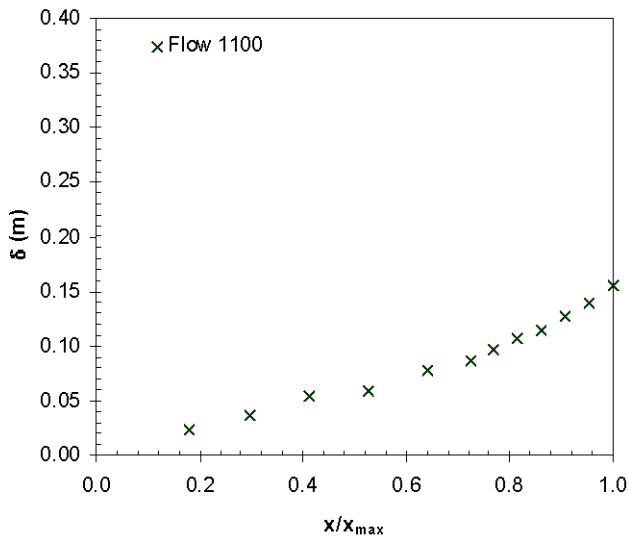
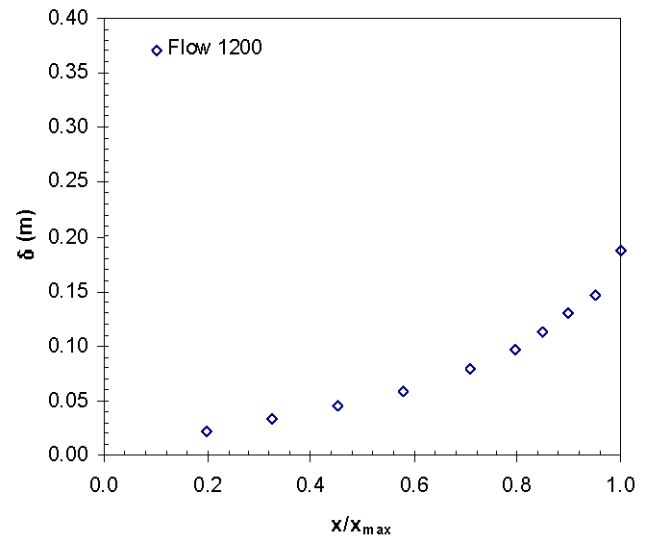


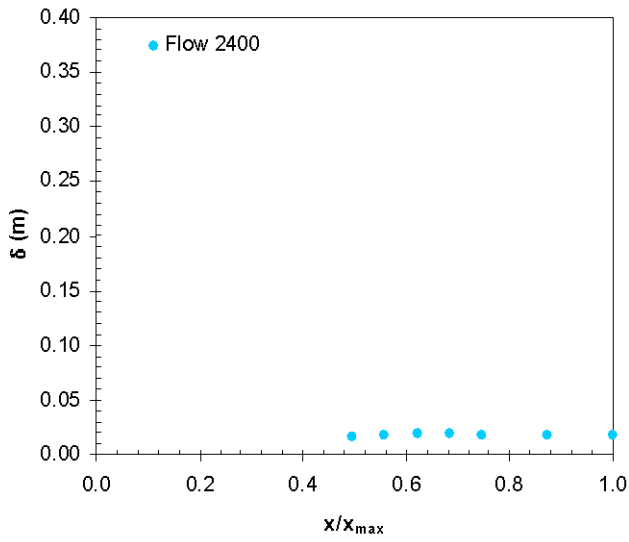
Figure 4.32 Shape factor  $H$  for (a) Flow 1100, (b) Flow 1200, (c) Flow 2400, (d) Flow 2900, (e) Flow 3600, (f) Flow 3700, (g) Flow 3800, (h) Flow 4000, (i) Flow 5000, (j) Flow 5100, and (k) Flow Skare.



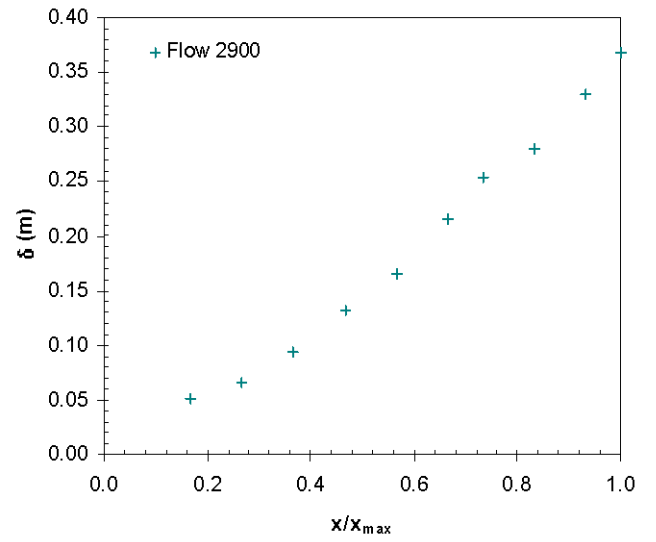
(a)



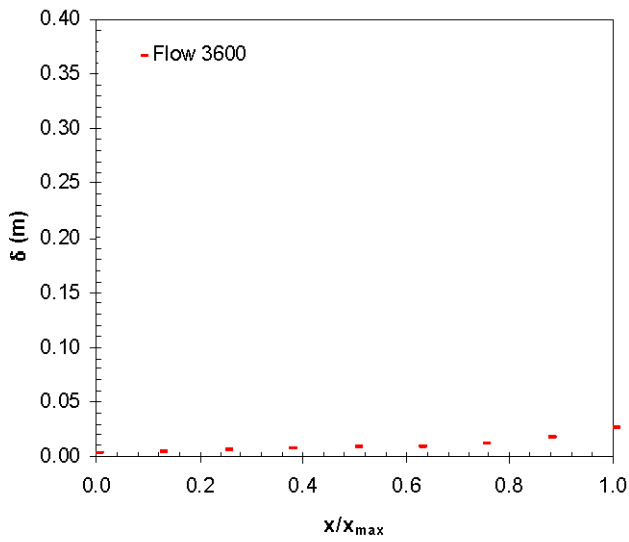
(b)



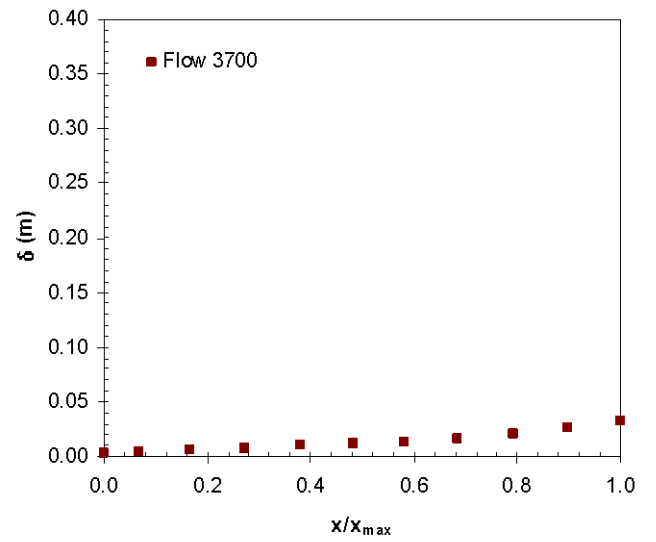
(c)



(d)



(e)



(f)

(figure continues next page)

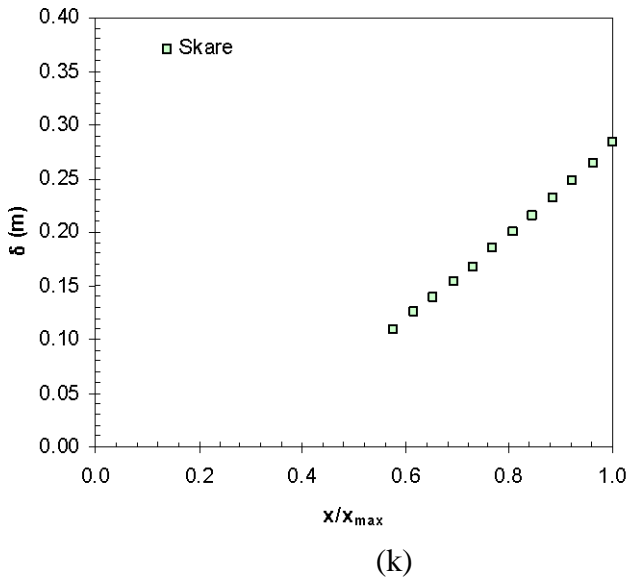
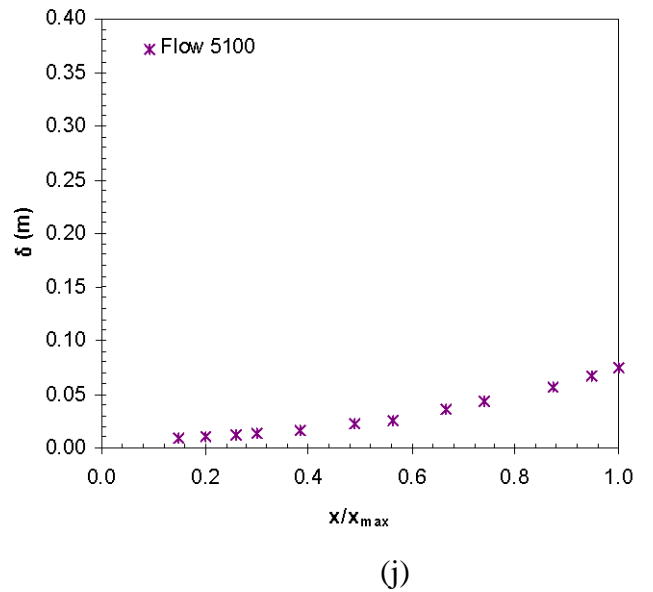
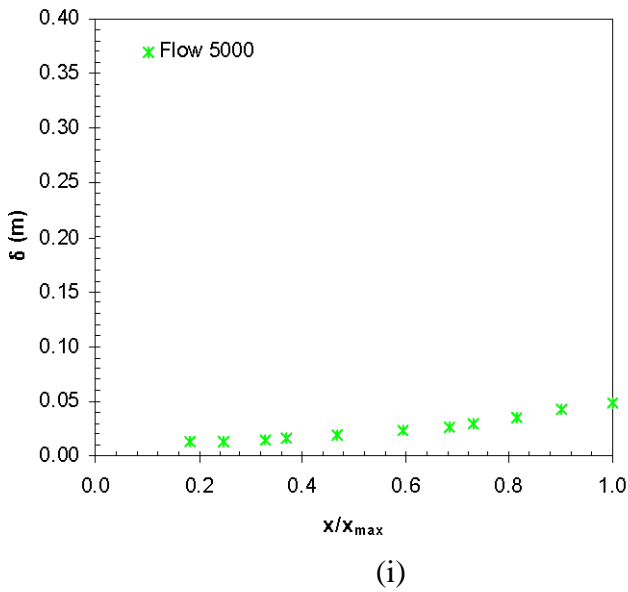
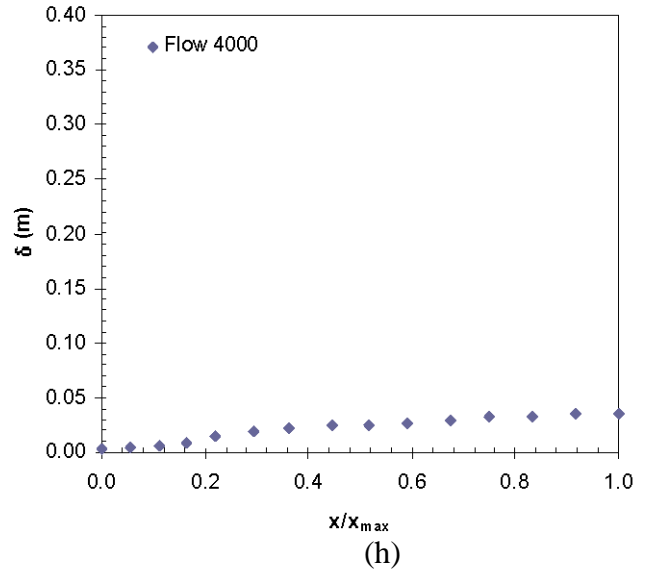
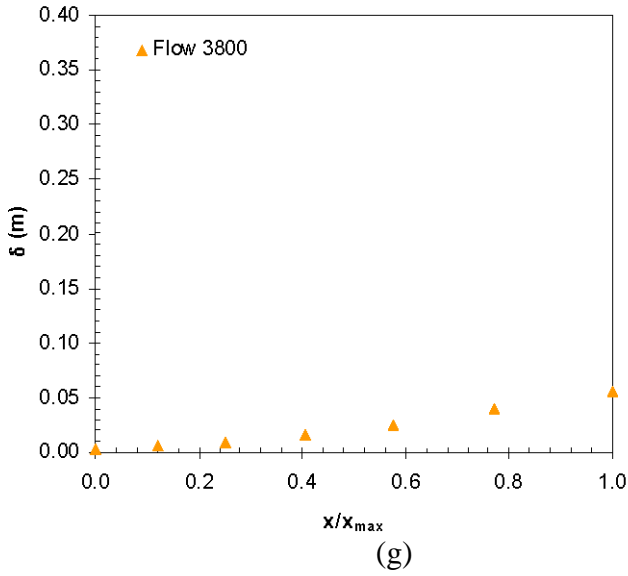
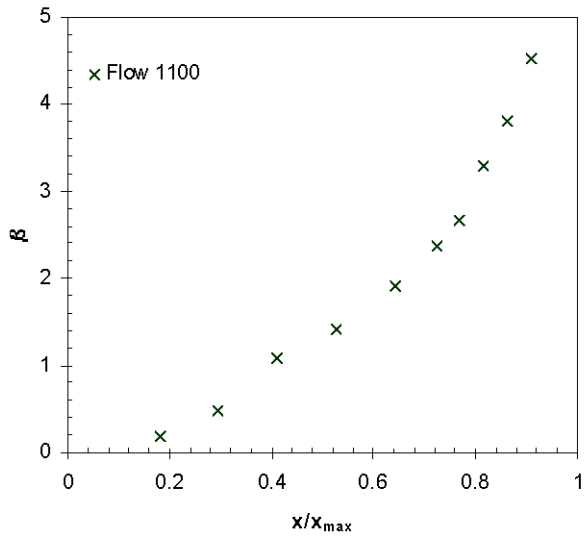
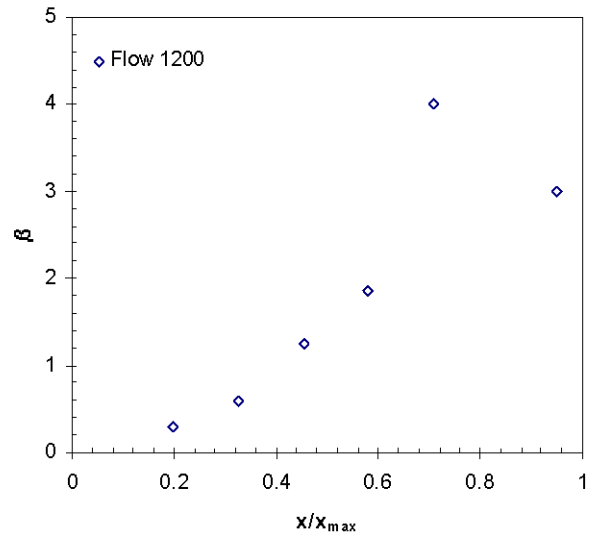


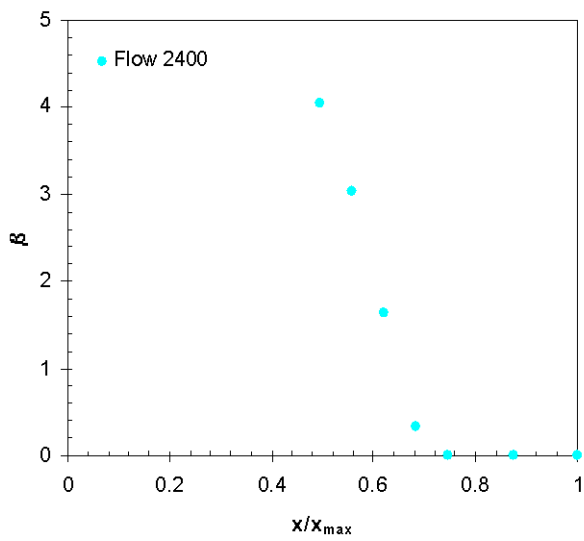
Figure 4.33 Boundary layer thickness,  $\delta$  for (a) Flow 1100, (b) Flow 1200, (c) Flow 2400, (d) Flow 2900, (e) Flow 3600, (f) Flow 3700, (g) Flow 3800, (h) Flow 4000, (i) Flow 5000, (j) Flow 5100, and (k) Flow Skare.



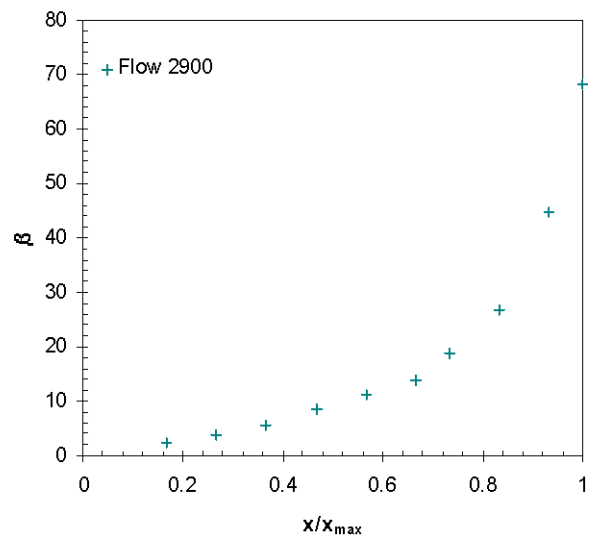
(a)



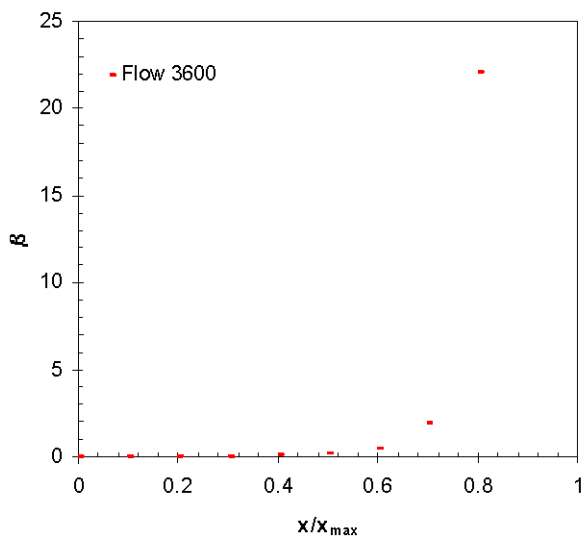
(b)



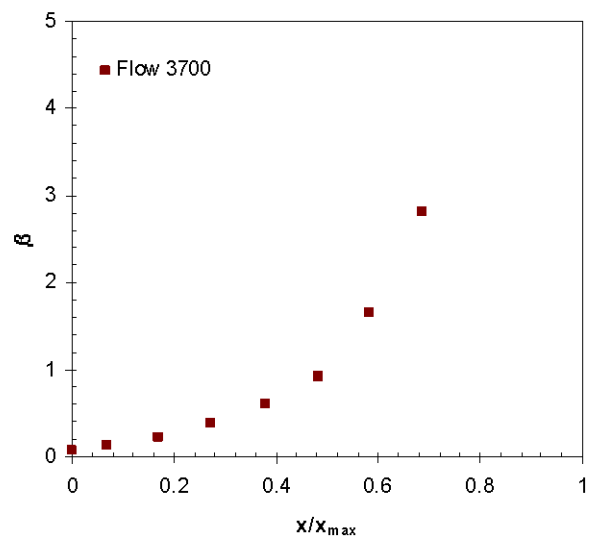
(c)



(d)



(e)



(f)

(figure continues next page)

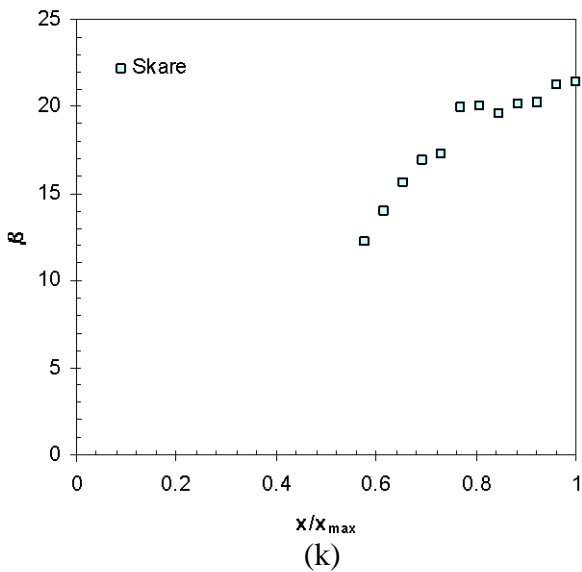
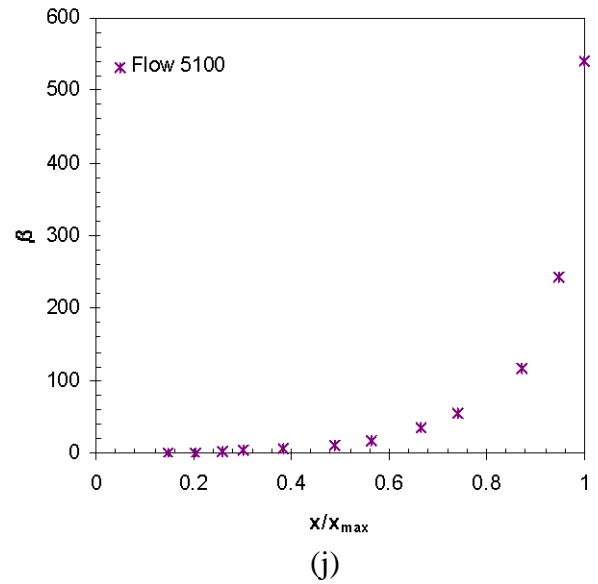
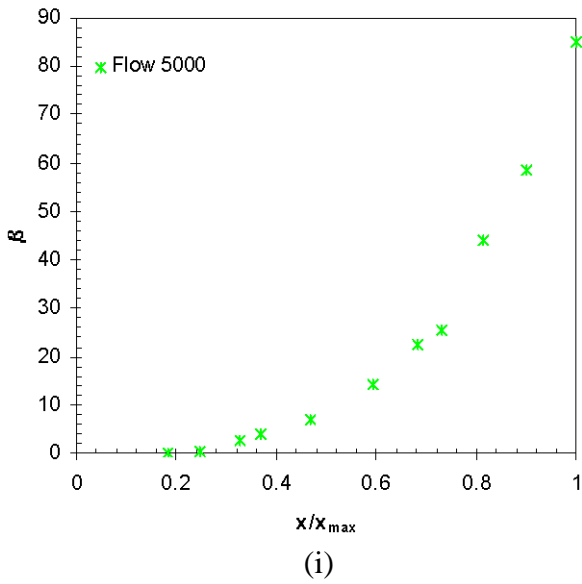
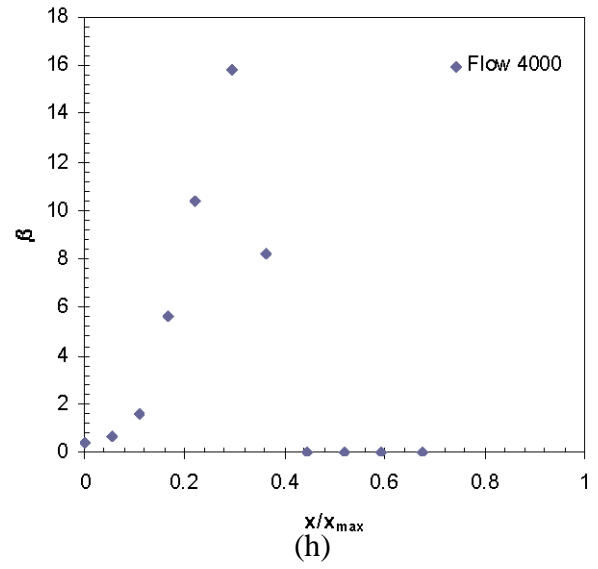
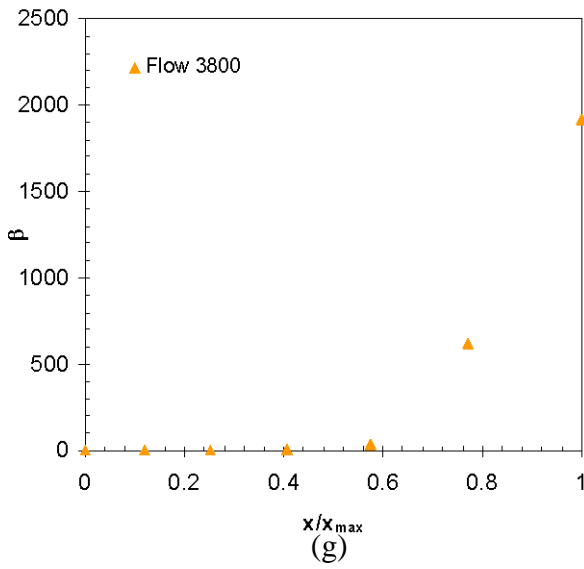
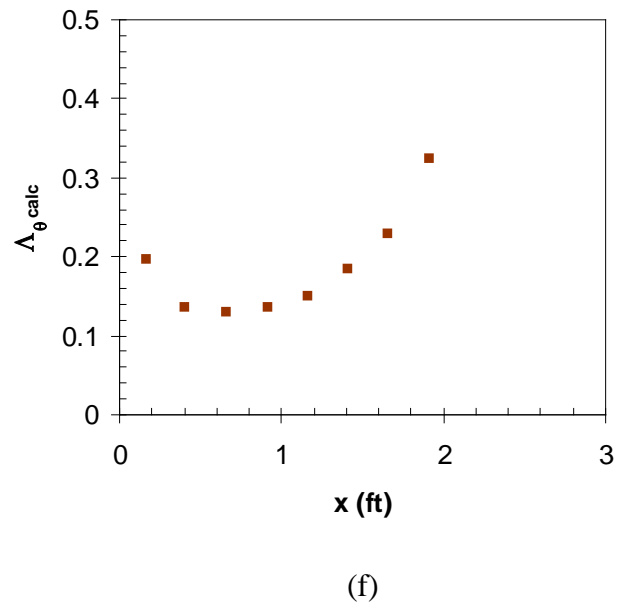
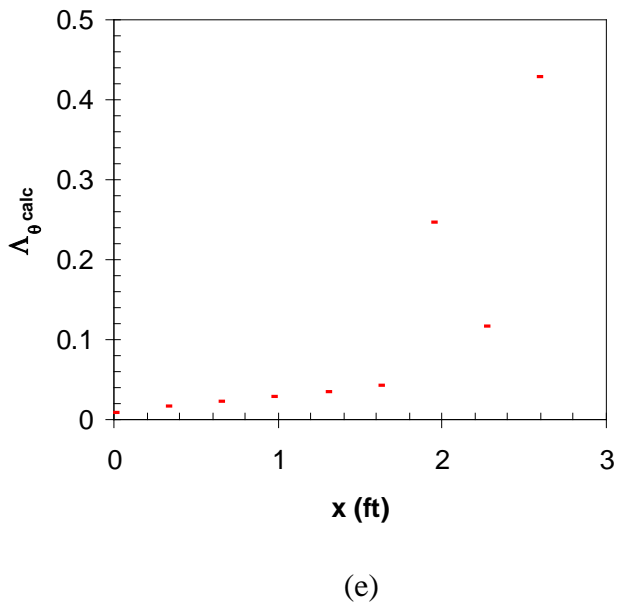
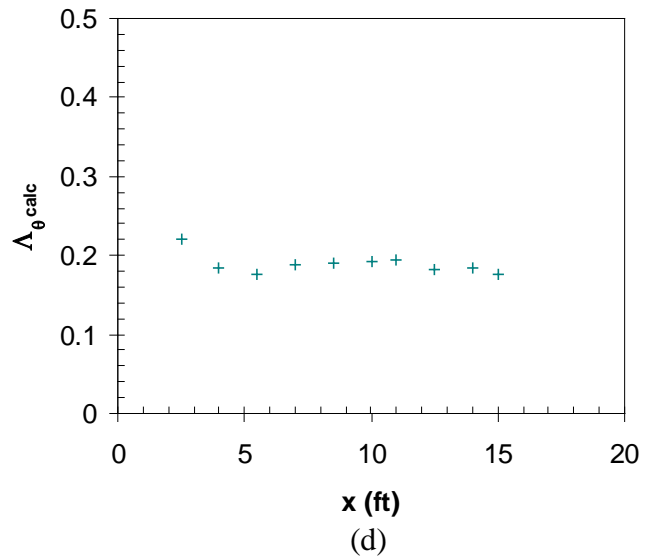
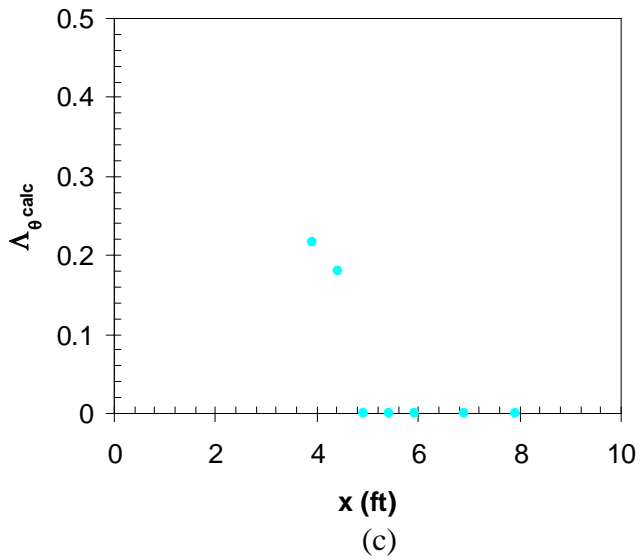
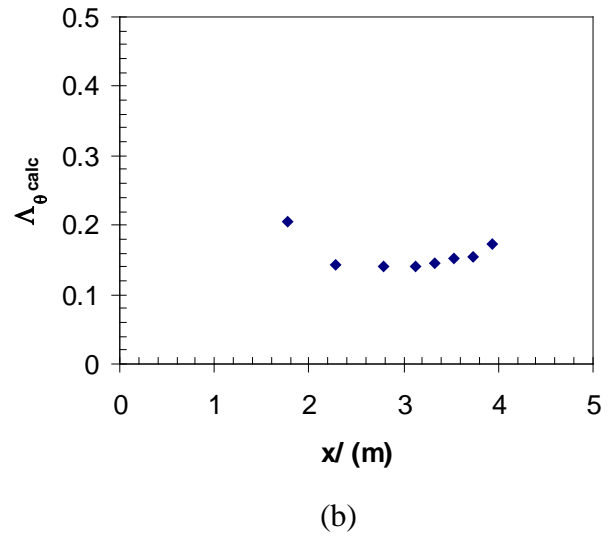
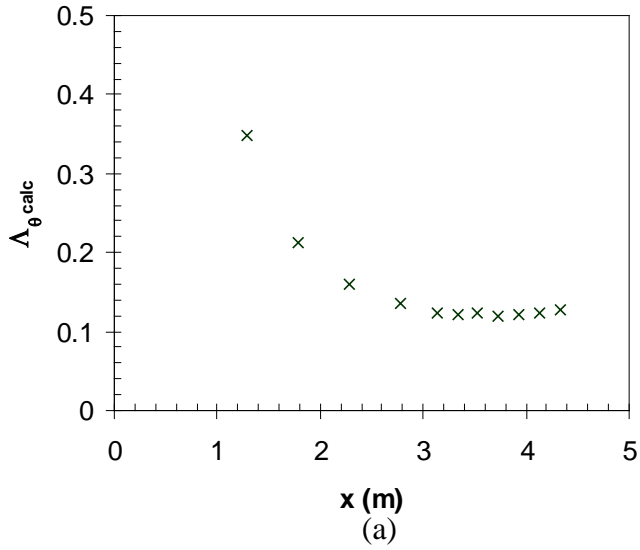


Figure 4.34 Clauser's equilibrium pressure parameter,  $\beta$  for (a) Flow 1100, (b) Flow 1200, (c) Flow 2400, (d) Flow 2900, (e) Flow 3600, (f) Flow 3700, (g) Flow 3800, (h) Flow 4000, (i) Flow 5000, (j) Flow 5100, and (k) Flow Skare. Note the varying vertical scale for each flow.



(figure continues next page)

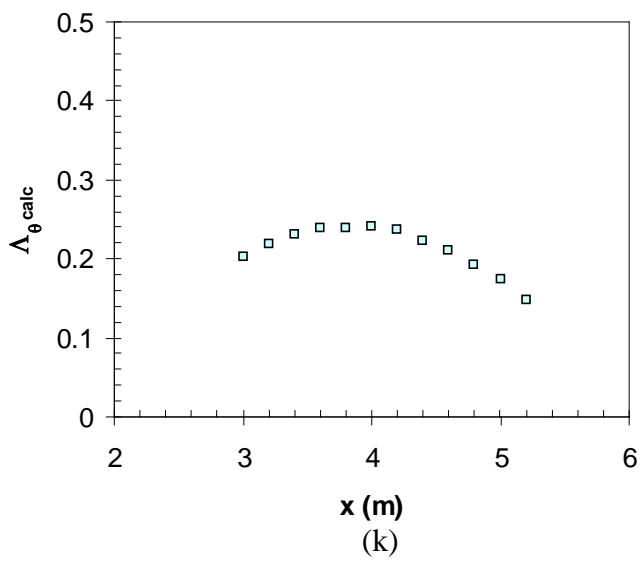
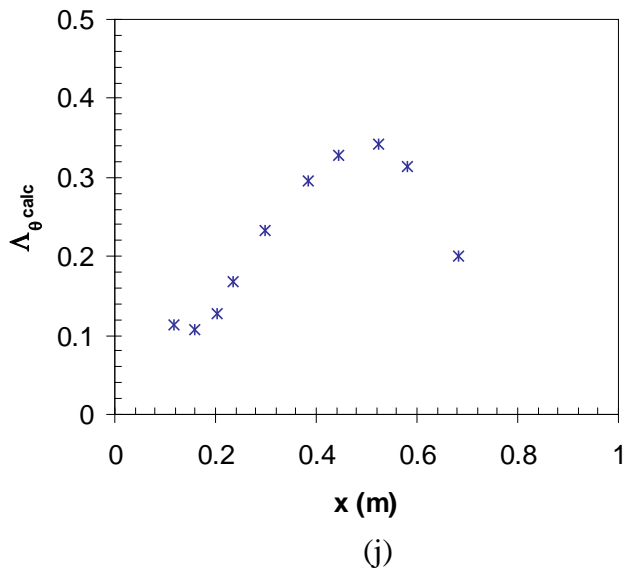
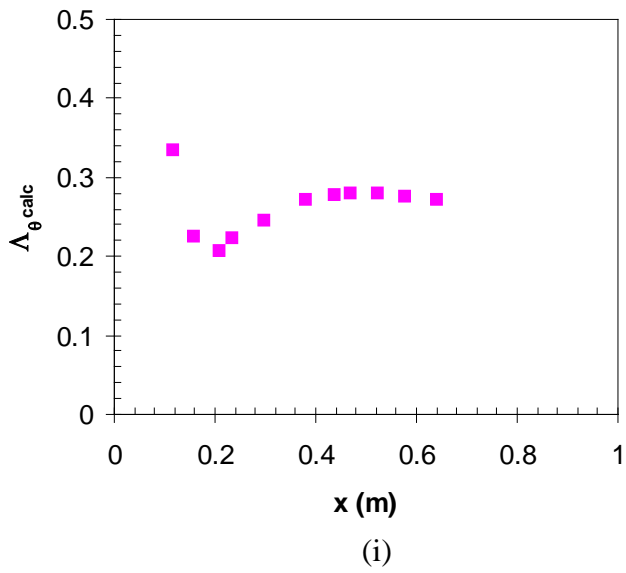
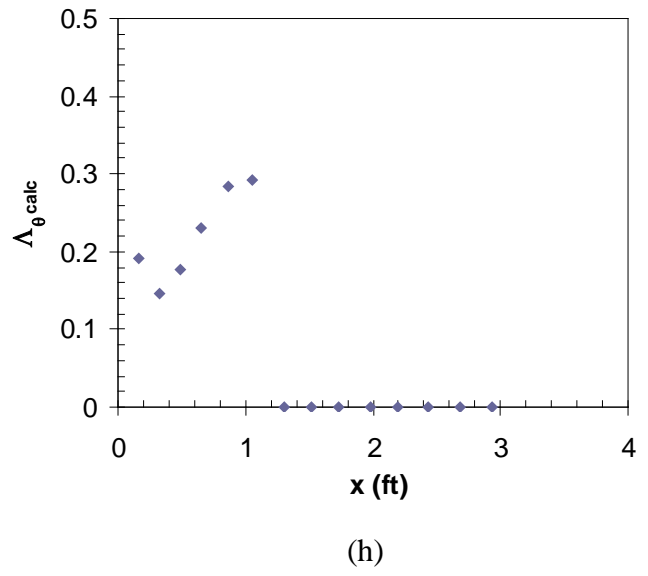
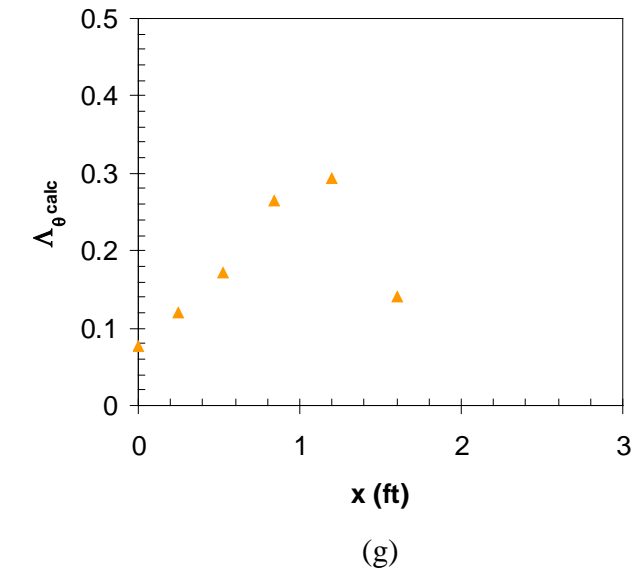


Figure 4.35 Castillo and George's pressure parameter,  $\Delta_{\theta \text{ calc}}$  for (a) Flow 1100, (b) Flow 1200, (c) Flow 2400, (d) Flow 2900, (e) Flow 3600, (f) Flow 3700, (g) Flow 3800, (h) Flow 4000, (i) Flow 5000, (j) Flow 5100, and (k) Flow Skare.

## **4.5 Conclusions**

In this chapter the basic flow details for 22 different APG flows have been given. The flow properties include  $C_p$ ,  $U_e$ ,  $\delta$ ,  $H$ ,  $u^*$ ,  $\beta$  and  $\Lambda_{\theta\text{calc}}$ . The flows are presented as 3 groups, namely the two new flows with two similar flows, the ‘classical’ flows and a broad grouping of 14 APG flows referred to as the ‘other’ flows.

The flow data has been brought together and presented in a consistent manner to allow easy comparison. These flows are referred to in subsequent chapters.

## **5           Scaling Mean Flow**

Methods for universally describing turbulent flows have long been sought with a view to improve modelling and computational accuracy. Flows with an external adverse pressure gradient have proven difficult to characterise.

In this chapter velocity deficit is presented scaled three different ways. Firstly, velocity deficit is scaled with friction velocity. Secondly, it is scaled with the Castillo/George scaling of freestream velocity, and finally with the Zagarola/Smits scaling of  $U_e\delta^*/\delta$ . Each scale is presented in a subsection with introductory explanations and review of the literature.

For each scale, the classical flows, as defined in the previous chapter, are first examined, followed by the new flows and then the 14 ‘other’ flows. For the ‘other’ flows, cases of interest are presented here whilst additional cases are contained in the appendices, as referenced in the text.

Also in this chapter, a method for quantifying the quality of collapse is given, which is useful for comparing different scaling parameters.

The Zagarola/Smits scaling of  $U_e\delta^*/\delta$ , is examined in detail in Section 5.1.5. In Section 5.1.4, a method for defining an ‘ideal’ APG Zagarola/Smits scaled profile is presented, along with a definition of a band of an acceptable collapse.

## **5.1 Velocity Deficit Profiles**

### **5.1.1 Velocity deficit scaled with friction velocity, $u_*$**

Scaling of the velocity deficit with the friction velocity,  $u_*$ , has long been used to demonstrate equilibrium of APG flows. Clauser (1954a) showed that different equilibrium APG flows collapse to a seemingly universal profile. The universality of this profile has since been challenged (Mellor and Gibson (1966)). Clauser defined equilibrium as when the pressure parameter,  $\beta = (\delta^*/\tau_o)dP/dx$  was constant. Clauser (1954a) also found that when an APG exists, it is more difficult to generate a flow with a universal collapse, due to lateral flow movement. Even with the restrictive conditions on which flows yield a universal collapse, this profile is still useful for deriving the friction velocity (Clauser (1954a), Kader and Yaglom (1978)). Utilising the universal profile in this way has made existing classical data, for which no friction velocity had been reported, available for analysis and it also provides a useful comparison for other methods of determining friction velocity.

The idea of a ‘universal’ collapse of profiles and how one might quantify an acceptable collapse and compare this with other flows are discussed in the next subsection, under the title ‘Quality of collapse’.

In Figure 5.1(a) to Figure 5.1(d), mean velocity deficit profiles are given for Flows 2200 and 2300 of Clauser, Flow 2500 of Bradshaw and Flow 3500 of Newman. These deficit profiles are scaled with  $u_*$ , and they are plotted against  $y/\delta$ . The classical flows of Clauser (Flows 2200 and 2300) and Bradshaw (Flow 2500) provide evidence of good collapse. On the other hand, profiles from Flow 3500 by Newman do not show a similar collapse. A possible explanation for this difference is the conspicuously different behaviour exhibited in the friction velocity of Flow 3500. A plot of the friction velocity for the classical flows is repeated here, as Figure 5.2, for convenience.

In Figure 5.3, the mean velocity deficit data from Flows 141, Han, A and B are scaled with the friction velocity,  $u_*$ . This scaling does not demonstrate flow equilibrium, and it does not provide a collapse of profiles for these flows. The only discernable trend is that the magnitude increases with distance in the flow direction, as illustrated with the arrows in Figure 5.3. The lack of collapse may be taken to suggest that these flows are still developing. In addition, as discussed in the previous chapter, determination of the friction velocity does have its difficulties. The debate on the

existence of log-law is ongoing and is pivotal to the extent to which friction velocity can be utilised as a scaling parameter. Therefore, a new scale with greater universality and less contention is desirable.

As a further investigation, friction velocity scaling was explored for the other published flows referred to in detail in the previous chapter. Flows L&S, A&E and N&H have a collapse of profiles, but none of the other 11 flows demonstrates a collapse. These plots are given in Appendix VIII. Interestingly, the profiles of Flows 3600, 3700 and 3800 of Moses initially do collapse, but the last profile in each flow breaks away, as presented in Figure 5.4. Note the difference in scale of this plot, which ranges to 120 units, compared with the classical and new flows, which only went to 35 units. These three flows are all boundary layers on a cylinder in axially symmetric flows.

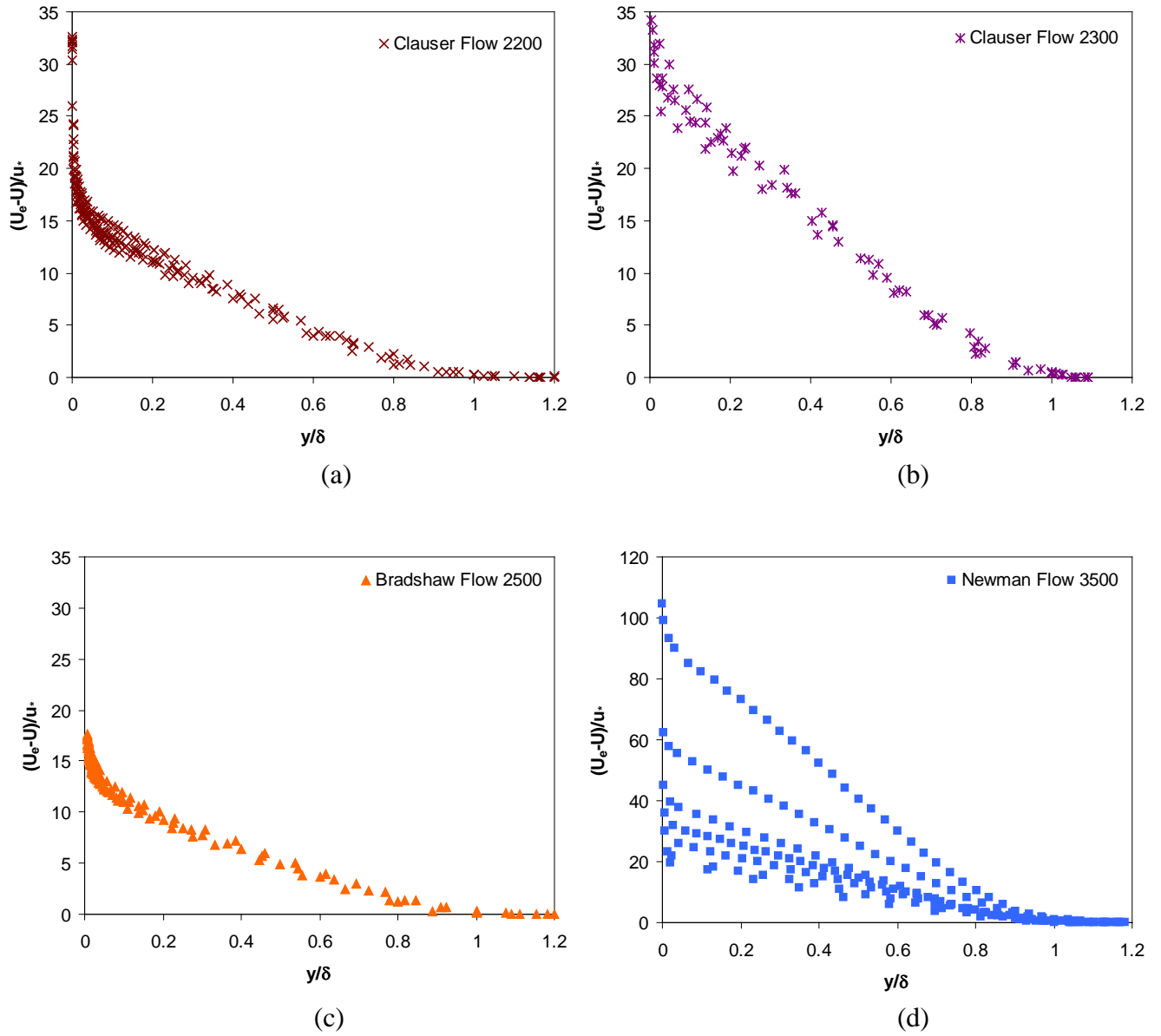


Figure 5.1 Mean velocity deficit scaled with friction velocity  $u_*$  for classical Flows (a) 2200, (b) 2300, (c) 2500 and (d) 3500

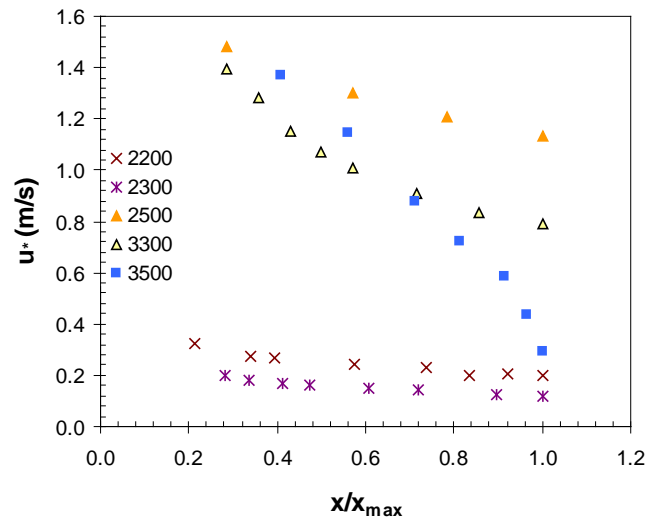


Figure 5.2 Friction velocity,  $u_*$ , for Flow 2200, Flow 2300, Flow 2500, Flow 3300 and Flow 3500. Repeat of Figure 4.29. The friction velocity for other flows is plotted in Figure 4.16 and Figure 4.22.

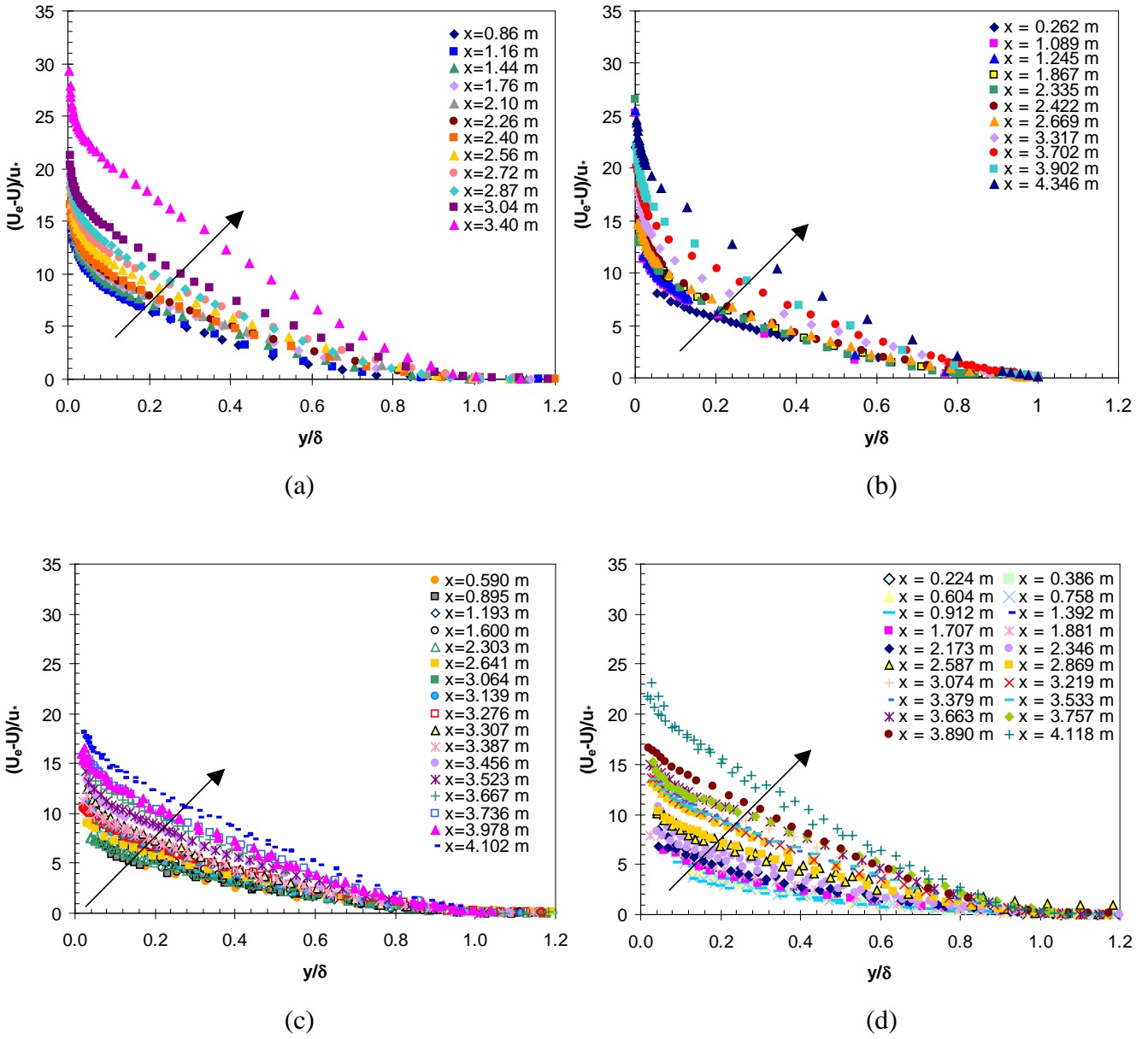
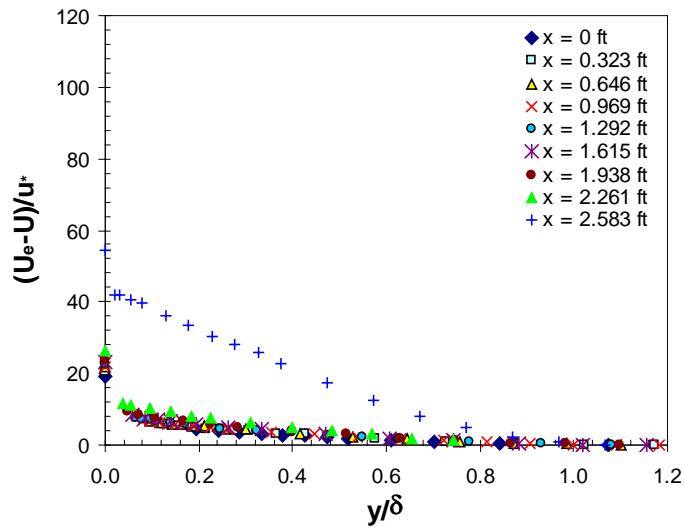
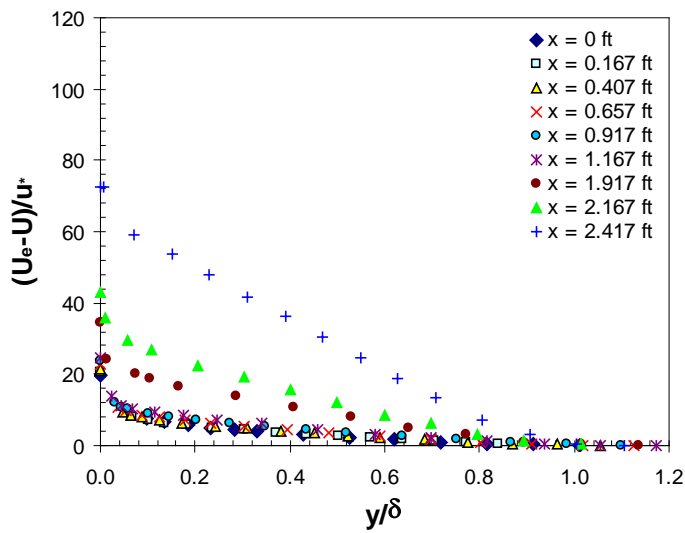


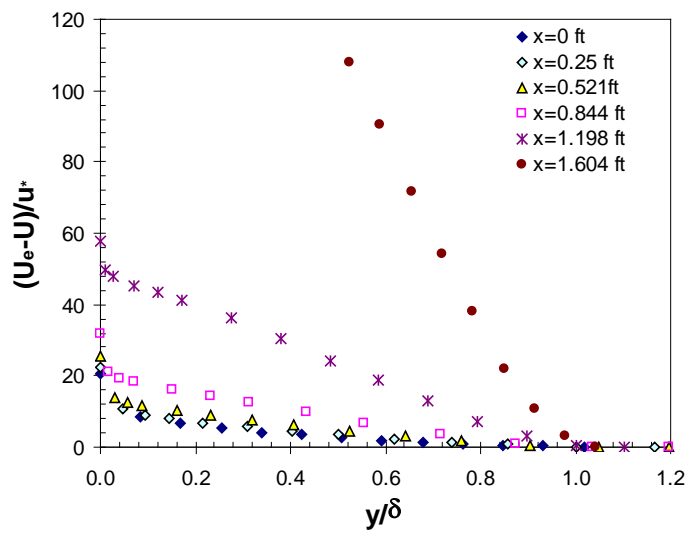
Figure 5.3 Mean velocity deficit scaled with friction velocity  $u_*$  for (a) Flow 141, (b) Flow Han, (c) Flow A and (d) Flow B. The arrow indicates flow direction.



(a)



(b)



(c)

Figure 5.4 Mean velocity deficit scaled with friction velocity  $u_*$  for (a) Flow 3600, (b) 3700, (c) Flow 3800.

### 5.1.2 Discussion on the concept of ‘Quality of Collapse’

Previously it was discussed that when using friction velocity to scale mean velocity deficit profiles, a universal collapse of profiles is expected for a flow in an equilibrium state. This leads to the question: ‘What constitutes an acceptable collapse?’ All experimental data will exhibit some degree of scatter. When data from different flows can be plotted to the same scale, it is possible to graphically assess which flows have a ‘good’ collapse and which do not. However, it is not always possible or relevant to compare flows in this manner. To enable quantification of quality of collapse the following definition is utilised:

$$\text{Quality of collapse} = 100 - \left( \frac{f_u - f_l}{f_u} \right) 100\% \quad \text{Equation 5-1}$$

where  $f_u$  is the upper bound of the set of profiles, and  
 $f_l$  is the lower bound of the set of profiles.

Thus, for a set of profiles with a ‘good’ collapse, that is if the lower bound and upper bound are close to each other, then, the Quality of collapse will be close to 100%. On the other hand, if a set of profiles does not collapse, then, the quality of collapse will be low.

This method is applied to the mean velocity deficit scaled with friction velocity profiles presented in the previous subsection, at selected  $y/\delta$  locations, as given in Table 5.1. The classical flows of Clasuer and Bradshaw are renowned for exhibiting a collapse of profiles with  $u_*$  scaling, this can be quantified such that a ‘good’ collapse has a quality of collapse of greater than 80%. All the other flows examined here have a much lower quality of collapse, ranging from 3% to 64%.

This method for determining the quality of collapse will be applied to other scaling factors in subsequent sections. Further to this concept, a band of an ‘acceptable collapse’ is defined and discussed in relation to Zagarola/Smits scaling in Section 5.1.4.

**Table 5.1 Quality of collapse data for mean velocity deficit scaled with friction velocity.**

		Flow	$y/\delta = 0.2$	$y/\delta = 0.4$	$y/\delta = 0.6$	$y/\delta = 0.8$	Average
Classical APG flows	Clauser, 1954(b)	2200	90	96	91	54	83
	Clauser, 1954(b)	2300	83	87	85	65	80
	Bradshaw, 1966	2500	90	88	88	95	90
	Newman, 1951	3500	22	22	34	30	27
New flows	Anderson	A	20	15	18	23	19
	Anderson	B	20	17	19	32	22
	Samual and Joubert	141	38	30	26	36	33
	Han	Han	46	49	40	19	39
'Other' APG flows	Ludweig and Tillmann, 1949	1100	43	35	36	97	53
	Ludweig and Tillmann, 1949	1200	21	18	19	56	29
	Bradshaw and Ferriss, 1965	2400	61	60	68	64	63
	Perry, 1966	2900	18	14	14	30	19
	Moses, 1964	3600	14	15	15	6	13
	Moses, 1964	3700	13	11	12	14	13
	Moses, 1964	3800	3	4	3	5	4
	Moses, 1964	4000	28	24	27	33	28
	Fraser, 1956	5000	6	5	4	3	5
	Fraser, 1956	5100	2	3	2	6	3
	Skare	Skare	74	69	74	37	64
	Lee and Sung, 2008	L&S					N/A
	Nagano and Houra, 2002	N&H					N/A
	Aubertine and Eaton, 2005	A&E					N/A

### 5.1.3 Velocity deficit scaled with free stream velocity, $U_e$

In Castillo and George (2001), similarity analysis of the Reynolds Averaged Navier-Stokes (RANS) equations is used to determine the scaling for the velocity profiles and Reynolds stresses, along with other constraints, for pressure gradient turbulent boundary layers. These scales have been derived from the equations of motion, only. The resulting equations are valid for large Reynolds numbers, but they become exact in the limit as the Reynolds number approaches infinity (the boundary layer approximation developed by Prandtl). Since the boundary layer equations become independent of the Reynolds number, the properly scaled velocity and Reynolds stress profiles must also become independent of the Reynolds number in this limit. This is the asymptotic invariance principle (AIP) described by George (1995). Similarity solutions for the mean velocity and Reynolds stresses are sought consisting of functions based on the variables  $\frac{y}{\delta}$ ,  $\delta^+$ ,  $\Lambda$ , and  $*$ , (defined below). Consequently, assuming a product solution between the unknown scales and these functions, it follows that:

$$U_e - U = U_{so}(x) f_o\left(\frac{y}{\delta}, \delta^+, \Lambda, *\right) \quad \text{Equation 5-2}$$

$$-\overline{uv} = R_{souv}(x) f_{uv}\left(\frac{y}{\delta}, \delta^+, \Lambda, *\right) \quad \text{Equation 5-3}$$

$$\overline{u^2} = R_{sou}(x) f_u\left(\frac{y}{\delta}, \delta^+, \Lambda, *\right) \quad \text{Equation 5-4}$$

$$\overline{v^2} = R_{sov}(x) f_v\left(\frac{y}{\delta}, \delta^+, \Lambda, *\right) \quad \text{Equation 5-5}$$

where  $f_o$  is a function for the mean velocity deficit,  
 $f_u$  and  $f_v$  are functions for the Reynolds normal stresses, and  
 $f_{uv}$  for the Reynolds shear stresses,  
 $y$  height,  
 $\delta$  boundary layer thickness,  
 $\delta^+ = \frac{\delta u_*}{\nu}$ , the Reynolds number dependence,  
 $u_*$  is friction velocity,  
 $\nu$  is kinematic viscosity,  
 $\Lambda$  pressure parameter, and

\* is any possible dependence on upstream variables.

and

$U_{so}$  is the outer scale for velocity deficit

$R_{sou}$ , and  $R_{sov}$ , are the outer scale for the Reynolds stresses, and

$R_{souv}$  is the outer scale of the Reynolds shear stress, and

$x$  is the streamwise distance.

For the particular type of equilibrium similarity, all the terms in the governing equations (outer BL equation) must maintain the same relative balance as the flow develops in the streamwise direction,  $x$ . The boundary layer equation for the outer flow as obtained from the  $x$ -momentum equation by Reynold's averaging and application of boundary conditions, after obtaining from the averaged  $y$ -momentum equation  $-P = -P_e + v^2$ :

$$U \frac{\partial U}{\partial x} + V \frac{\partial U}{\partial y} = -\frac{1}{\rho} \frac{dP_e}{dx} - \frac{\partial(\overline{uv})}{\partial y} + \frac{\partial(\overline{v^2} - \overline{u^2})}{\partial x} \quad \text{Equation 5-6}$$

According to the AIP as the Reynolds number approaches infinity, the boundary layer equations become independent of Reynolds number, thus any function or scaling parameter must also be independent of  $\delta^+$ . Therefore, the functions in Equation 5-2 to Equation 5-5 become:

As  $Re \rightarrow \infty, \delta^+ \rightarrow \infty$

$$f_o\left(\frac{y}{\delta}, \delta^+, \Lambda, *\right) \rightarrow f_{o\infty}\left(\frac{y}{\delta}, \Lambda, *\right) \quad \text{Equation 5-7}$$

$$f_{uv}\left(\frac{y}{\delta}, \delta^+, \Lambda, *\right) \rightarrow f_{uv\infty}\left(\frac{y}{\delta}, \Lambda, *\right) \quad \text{Equation 5-8}$$

$$f_u\left(\frac{y}{\delta}, \delta^+, \Lambda, *\right) \rightarrow f_{u\infty}\left(\frac{y}{\delta}, \Lambda, *\right) \quad \text{Equation 5-9}$$

$$f_v\left(\frac{y}{\delta}, \delta^+, \Lambda, *\right) \rightarrow f_{v\infty}\left(\frac{y}{\delta}, \Lambda, *\right) \quad \text{Equation 5-10}$$

where subscript  $\infty$  denotes these terms to be the infinite Reynolds number solutions.

Substituting these equations into Equation 5-6 and cancelling the  $-dP/dx$  term by the  $\rho U_e dU_e/dx$  from Euler's equation, yields:

$$\begin{aligned} & \left[ \frac{\delta}{U_{so}} \frac{dU_e}{dx} + \left( \frac{U_e}{U_{so}} \right) \frac{\delta}{U_{so}} \frac{dU_{so}}{dx} \right] f'_{o\infty} + \left[ \frac{\delta}{U_{so}} \frac{dU_{so}}{dx} \right] f'^2_{o\infty} \\ & - \left[ \frac{U_e}{U_{so}} \frac{d\delta}{dx} + \frac{\delta}{U_{so}} \frac{dU_e}{dx} \right] \frac{y}{\delta} f'_{o\infty} - \left[ \frac{d\delta}{dx} + \frac{\delta}{U_{so}} \frac{dU_{so}}{dx} \right] f'_{o\infty} \int_0^{y/\delta} f'_{o\infty} \left( \frac{y}{\delta} \right) d \left( \frac{y}{\delta} \right) \quad \text{Equation 5-11} \\ & = \left[ \frac{R_{souv}}{U_{so}^2} \right] f'_{ouv\infty} - \left[ \frac{R_{sov}}{U_{so}^2} \frac{d\delta}{dx} \right] f'_{v\infty} + \left[ \frac{R_{sou}}{U_{so}^2} \frac{d\delta}{dx} \right] f'_{u\infty} \end{aligned}$$

An equilibrium similarity solution exists only if all the square bracket terms in Equation 5-11 have the same x-dependence and are independent of  $\frac{y}{\delta}$ . As the flow develops, the bracketed terms must remain proportional to each other. Using the symbol '~' to mean 'has the same x-dependence' leads to the following statements:

$$\frac{U_e}{U_{so}} \frac{d\delta}{dx} \sim \frac{d\delta}{dx} \quad \text{Equation 5-12}$$

$$\frac{R_{souv}}{U_{so}^2} \sim \frac{d\delta}{dx} \quad \text{Equation 5-13}$$

$$\frac{R_{sou}}{U_{so}^2} \frac{d\delta}{dx} \sim \frac{d\delta}{dx} \quad \text{Equation 5-14}$$

$$\frac{R_{sov}}{U_{so}^2} \frac{d\delta}{dx} \sim \frac{d\delta}{dx} \quad \text{Equation 5-15}$$

Thus:

The outer scaling for the mean velocity,  $U_{so}$  is  $U_e$

The outer scaling for the Reynolds shear stress,  $R_{souv}$  is  $U_e^2 \frac{d\delta}{dx}$

The outer scaling for the Reynolds normal stress,  $R_{sou}$  is  $U_e^2$

The outer scaling for the Reynolds normal stress,  $R_{sov}$  is  $U_e^2$

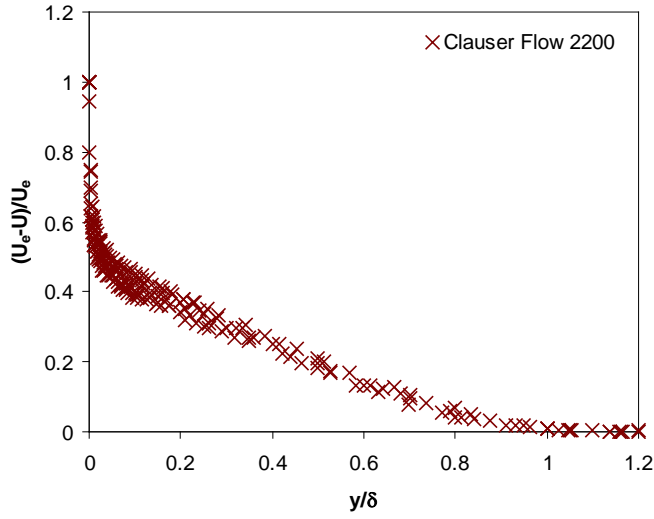
These scaling factors will be applied for mean velocity in this chapter and for the Reynolds stresses in the following chapter.

Using the Castillo and George (2001) scaling of  $U_e$ , the deficit profiles are not expected to collapse to a universal curve, rather they should converge to an asymptote in the limit of infinite local Reynolds number. The velocity deficit scaled with  $U_e$  for the classical flow data is presented in Figure 5.5. Again, the flows of Clauser (Flow 2200 and 2300) and Bradshaw (Flow 2500) demonstrate collapse but Flow 3500 differs.

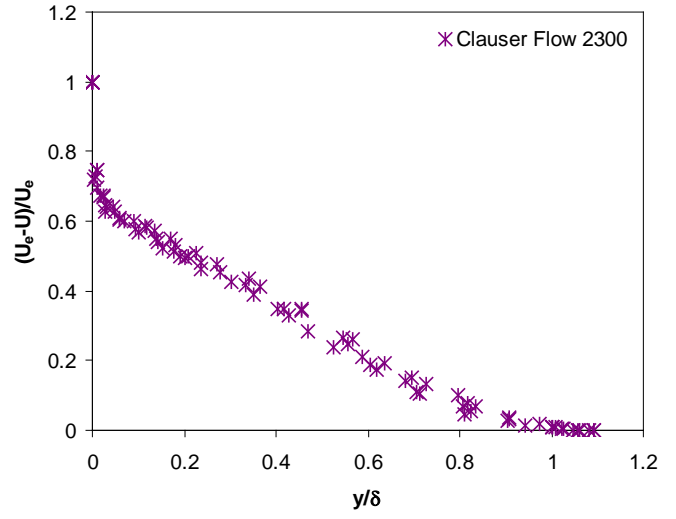
In Figure 5.6, the velocity deficit data are presented for Flows 141, Han, A and B scaled with freestream velocity,  $U_e$ . None of the flows shows an absolute collapse. A similar increase in magnitude with downstream location, as that seen with  $u_*$  scaling, is evident with this scale.

Of the other flows, Flow 3600 and Flow 3700 exhibit interesting behaviour. Similar to the behaviour seen with  $u_*$  scaling, two profiles in Flow 3600 and three profiles in Flow 3700 show a distinct variation from the others, as seen in Figure 5.7. All other flows are given in Appendix IX. The trends of deficit profiles scaled with  $U_e$  for these flows are that there is an increase in magnitude with downstream location, such that the first streamwise profile has the lowest magnitude and the profile from the last streamwise location has the largest magnitude. The only exceptions to this are Flow 4000 and Flow Skare, where initially an increase is seen with progressive profiles but then, the magnitude decreases, such that the profile from the last streamwise location does not have the largest magnitude. An examination of  $U_e$ ,  $C_p$ ,  $H$  and  $\delta$  for these two flows compared with the other flows failed to uncover any similarities or differences that would explain or predict this behaviour.

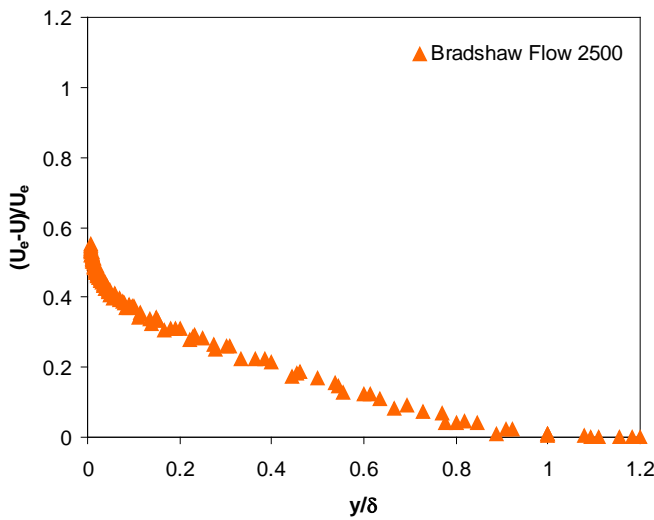
As this scaling is not expected to generate a collapse of profiles, an investigation of the quality of collapse is not done.



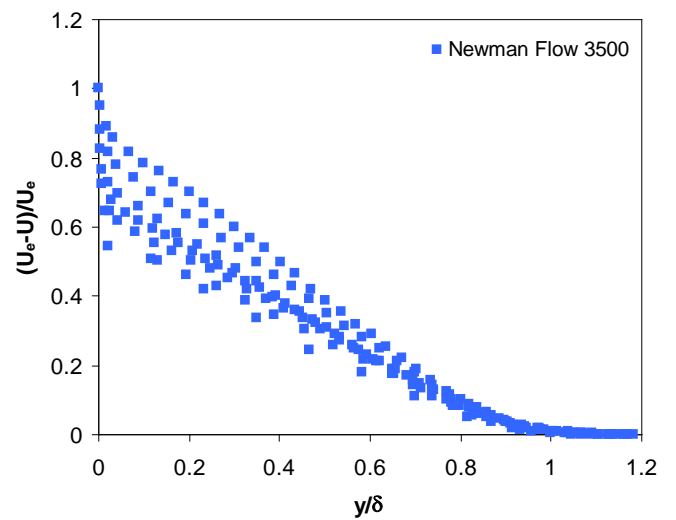
(a)



(b)



(c)



(d)

Figure 5.5 Mean velocity deficit scaled with freestream velocity  $U_e$  for classical Flows (a) 2200, (b) 2300, (c) 2500 and (d) 3500

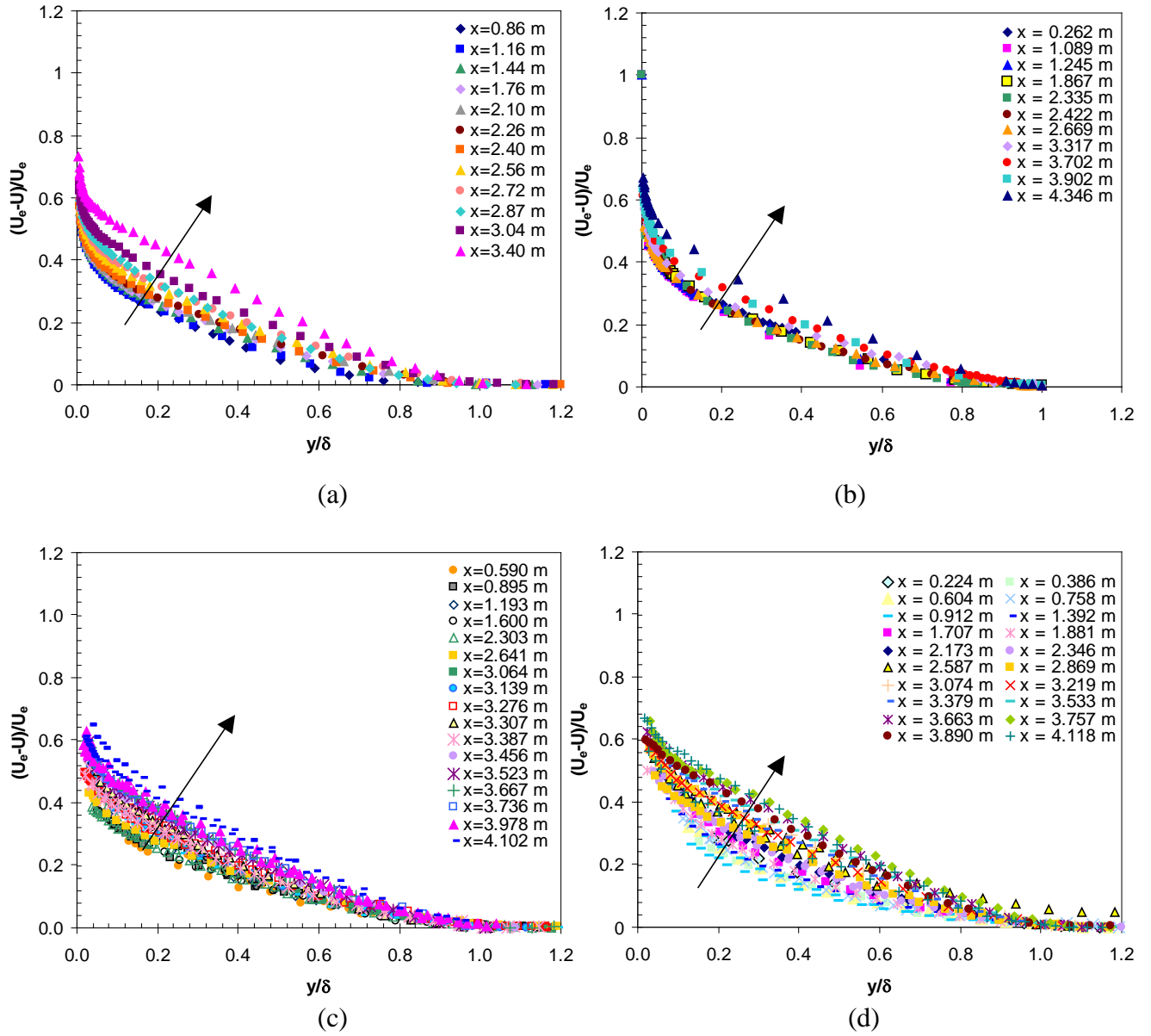


Figure 5.6 Mean velocity deficit scaled with freestream velocity  $U_e$  for (a) Flow 141, (b) Flow Han, (c) Flow A and (d) Flow B. The arrow indicates flow direction.

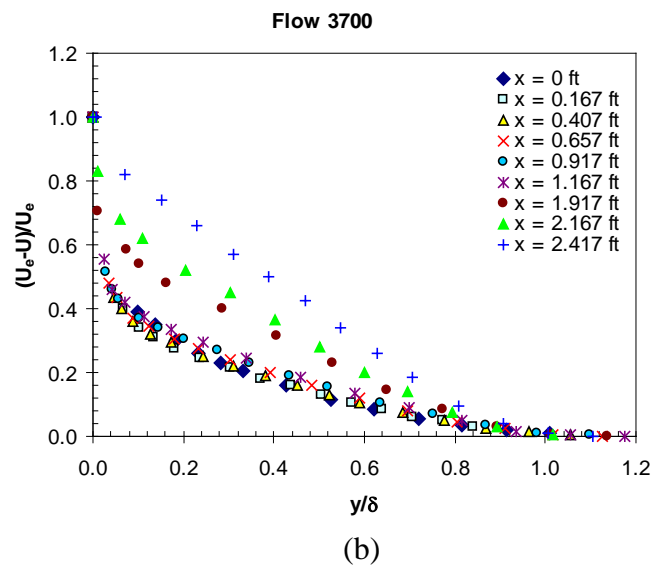
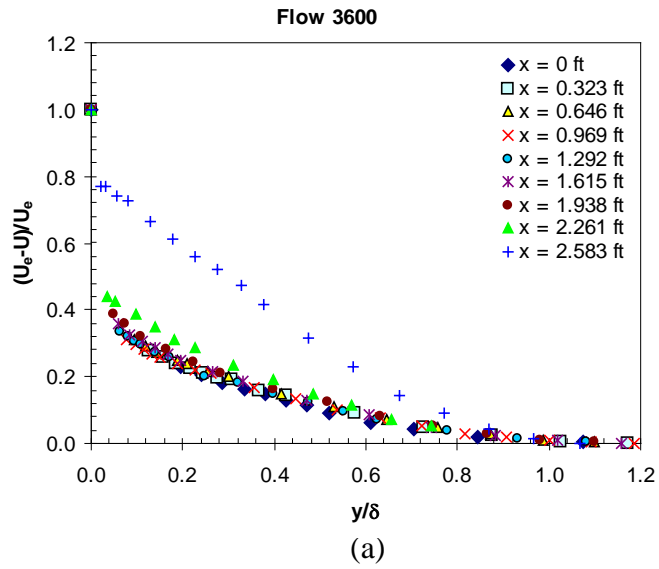


Figure 5.7 Mean velocity deficit scaled with freestream velocity  $U_e$  for (a) Flow 3600, and (b) Flow 3700.

#### **5.1.4 Zagarola/Smits scaling and definition of the ‘ideal’ APG line with a band of acceptable collapse and FPG line**

Zagarola and Smits (1998a) determined empirically a new scaling,  $U_e \delta^*/\delta$ , for the velocity deficit in the outer flow in a developing pipe or a channel flow. Later, they showed that the velocity profiles successfully collapse to one curve for a ZPG turbulent boundary layer on a smooth surface (Zagarola and Smits, 1998b) with this scaling. Using similarity analysis and the Asymptotic Invariance Principal (AIP), Castillo (2000) has shown that when the mean deficit profiles are normalized by the Zagarola and Smits (Z/S) scaling,  $U_e \delta^*/\delta$ , in pressure gradient flows, the profiles collapse to a single curve. Wosnik (2000) did the same for ZPG flows, and Castillo et al (2004) for ZPG flows with surface roughness. Contrary to the analysis of Clauser (1954a), which requires that  $u_* \sim U_e \delta^*/\delta$ , it was shown in Castillo (2000) that this is not a necessary condition to achieve self-preservation. It is further shown that  $\delta^*/\delta$  is equal to a constant in the limit of infinite Reynolds number, but the constant might depend on the initial conditions. Moreover, in the limit as the Reynolds number approaches infinity ( $\delta^+ \rightarrow \infty$ ), the Z/S scaling (i.e.  $\delta^*/\delta \rightarrow \text{const}$ ) reduces to the Castillo and George (C/G) scaling of  $U_e$ .

Castillo and Walker (2002) showed that the Z/S scaling successfully removes the Reynolds number dependence in the outer flow, and it leads to only three basic velocity profiles: one each for APG, FPG and ZPG boundary layers consistent with the results for C/G based on studies of equilibrium conditions on the pressure parameter  $\Lambda$ .

Because it has been shown that Z/S scaling of the velocity deficit produced one curve each for APG, ZPG and FPG flows (Castillo and George, 2001), it was expected here that all data should collapse to one of these curves depending on the pressure gradient. This matter is examined further next, before its implications on the overall flow development are discussed. To determine the limits of what constitutes an acceptable collapse the classical data sets of Clauser (1954b), Newman (1951) and Bradshaw (1966) were employed. These flows are regarded as fully developed APG equilibrium boundary layer flows, and have previously been used to demonstrate the collapse of Zagarola/Smits scaling (Castillo and George, 2001). By the definition

given in 5.1.2 these flows, with this scaling have an average quality of collapse of 83%.

Here, statistical means are applied to the data from these flows to define a curve representing the average collapse. This average collapse is henceforth referred to as the 'ideal APG line'. It is used as a benchmark to compare the behaviour of other APG flows.

The standard error of the curve was used to determine a bandwidth of an acceptable collapse. In Figure 5.8, the experimental data are presented of the afore mentioned flows with the ideal APG line and the upper and lower limits of the acceptable band. The best fitting equation is a 9<sup>th</sup> order polynomial, as determined using Table Curve 2D™ software. The coefficients and values of this ideal APG line are supplied in Table 5.2.

This 9<sup>th</sup> order polynomial curve can not be justified with flow physics, it is intended here only to be used in a graphical sense and possibly not in a transport equation. Although in engineering design, curve fit to experimental data has often become the norm, as in the Von Karmans profile (but for laminar flat plate boundary layer flow) and the Colebrook formulation of the Moody diagram (for a simpler turbulent flow, namely, fully developed turbulent pipe flow).

With the APG band hence defined, it is possible to demonstrate flow development to an equilibrium state. This is an important discovery, which will be further explored in chapter 6 with an analysis of the Reynolds stresses.

For the sake of comparison, it is also necessary to examine the favourable pressure gradient case. To define the ideal FPG behaviour, the arithmetic average of Flow 1300 (Ludweig and Tillmann, 1949) velocity profiles are used, Figure 5.9.

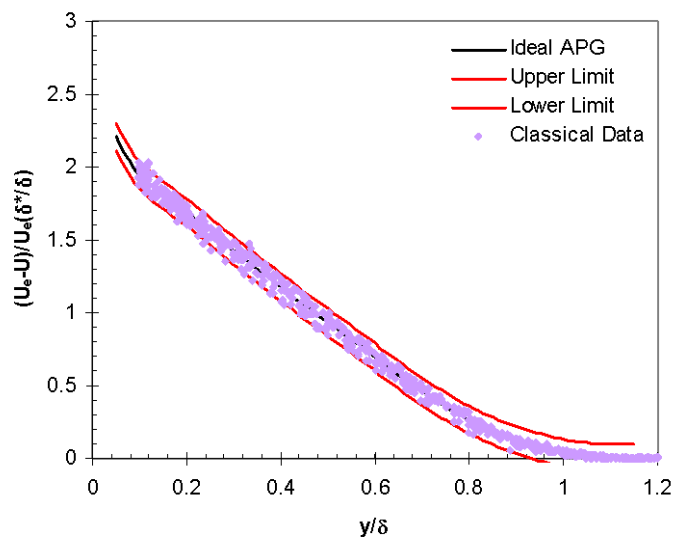


**Figure 5.8** Classical data of Newman, Clauser and Bradshaw, Flows 2200, 2300, 2500 and 3500. Illustrated with the determined curve fit for ‘ideal’ APG behaviour and the upper and lower limits of the acceptable range.

**Table 5.2 Coefficients for the 10th order polynomial fit to define bandwidth of acceptable APG equilibrium collapse.**

Coefficient	Value
a <sub>0</sub>	2.8
a <sub>1</sub>	-18.3
a <sub>2</sub>	160.0
a <sub>3</sub>	-856.8
a <sub>4</sub>	2691.9
a <sub>5</sub>	-5199.5
a <sub>6</sub>	6238.9
a <sub>7</sub>	-4526.0
a <sub>8</sub>	1816.8
a <sub>9</sub>	-309.8
Sum of the mean square difference of data from the fit	0.094

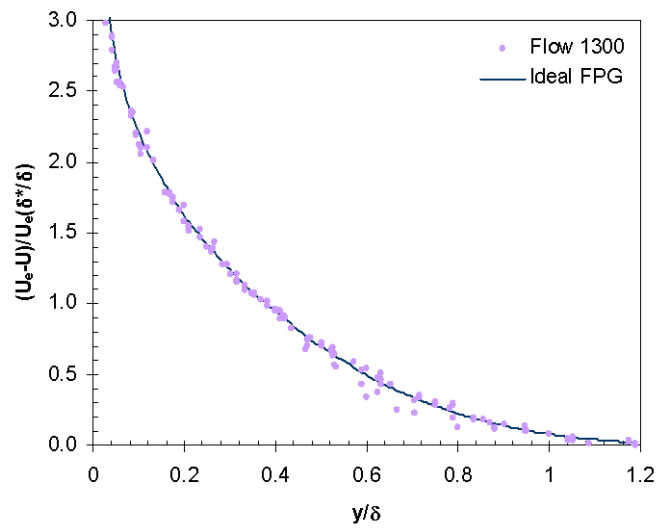


**Figure 5.9** Favourable pressure gradient Flow 1300 velocity deficit with Zagarola/Smits scaling. Illustrated with the determined arithmetic average for ‘ideal’ FPG behaviour.

### 5.1.5 Velocity deficit scaled with Zagarola/Smits scale ( $U_e\delta^*/\delta$ )

In Figure 5.10, the Z/S scaling of  $U_e\delta^*/\delta$  is presented for the velocity deficit of Flow 141. Two solid lines are also included in Figure 5.10. The top line (in the mid region) is the ideal APG line given in the previous sub-section. This line represents the expected or ‘ideal’ APG flow behaviour. The lower line represents the expected FPG behaviour, given here to demonstrate the extent that the profiles deviate from the expected APG behaviour.

For Flow 141, based on pressure parameter,  $C_p$ , measurements are reported only in the APG region, thus it is expected that all profiles from this flow would match the APG line. It is evident in Figure 5.10 that this is not the case, when velocity deficit is scaled with  $U_e\delta^*/\delta$ , some profiles are clearly falling below the ideal APG line.

To determine which profiles are acceptably close to the expected APG behaviour, the bandwidth determined earlier using the classical flow data is applied to the data presented in Figure 5.10. In Figure 5.11, the ideal APG line with the bandwidth of the acceptable collapse is presented. To explore which part of the flow has APG behaviour, only those profiles that lie within the band are given. The streamwise location of the first profile to fall within the acceptable band is  $x = 2.10$  m ( $x/x_{\max} = 0.5$ ). Profiles before this streamwise location are behaving more like an FPG flow.

To explain this behaviour the pressure parameter  $\Lambda_\theta$ , is utilised, due to its use to define flow equilibrium. For completeness, a plot of  $\Lambda_\theta$  is repeated here as Figure 5.12. Based on  $\Lambda_{\theta\text{calc}}$ , as described in Section 4.1.5, the flow equilibrium was determined to have occurred at a streamwise distance of  $x = 2.10$  m ( $x/x_{\max} = 0.5$ ) for Flow 141. This is the same location as the onset of the fully-developed APG behaviour based on the Z/S scale.

The same analysis was applied to the other new flows, namely Flows A, B and Han. Firstly, the Zagarola/Smits scaling was applied and compared with the ideal APG line and the ideal FPG line, as presented in Figure 5.13. Secondly, the ideal APG line and the bandwidth of acceptable collapse were used to determine which profiles are in a

fully-developed APG state, as shown in Figure 5.14. Thirdly, the location of the first profile to fall within this band was taken, as listed in Table 5.3. In all four cases, the onset of the equilibrium flow condition determined this way, corresponds exactly with that determined by the pressure parameter  $\Lambda_{0\text{calc}}$ .

The velocity deficit profiles for these flows do not demonstrate a unique collapse to either APG or FPG lines. A progressive development between the states is evident by the velocity profiles that are between the average lines for APG and FPG behaviour. Hence,  $Z/S$  scaling used in conjunction with the pressure distribution,  $C_p$ , is not enough to scale a developing flow. Neither the shape factor nor Clauser's equilibrium pressure parameter can predict which profiles will scale.

Using the ideal APG line and the bandwidth of an acceptable collapse, flow development to an equilibrium state can be demonstrated for these flows. This corresponds to the equilibrium state as defined by the pressure parameter  $\Lambda_0 \sim \text{constant}$ .

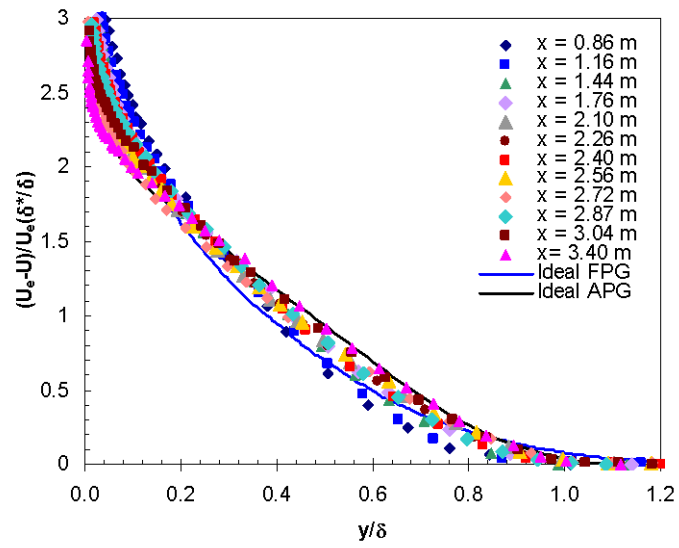
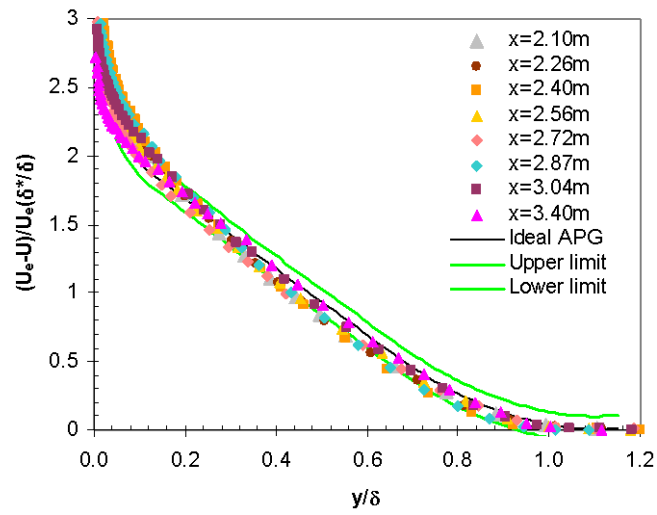


Figure 5.10 Mean velocity deficit scaled with Zagarloa/Smits scale  $U_e(\delta^*/\delta)$  for Flow 141. The two solid lines represent ideal APG behaviour and the ideal FPG behaviour.



**Figure 5.11 Mean velocity deficit scaled with Zagarloa/Smits scale  $U_e(\delta^*/\delta)$  for Flow 141. Ideal APG line and the bandwidth of acceptable collapse are also given. Profiles falling outside the acceptable band have been removed.**

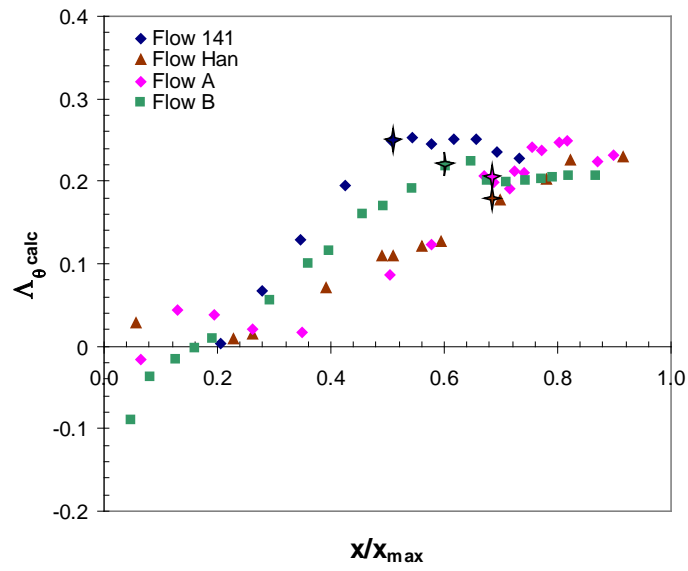
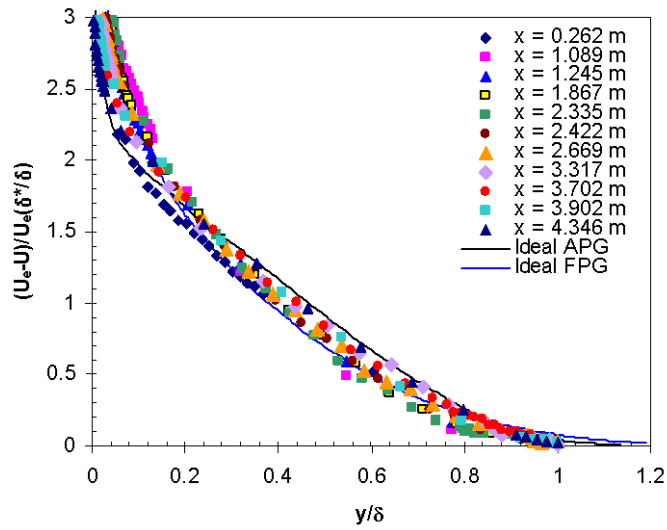
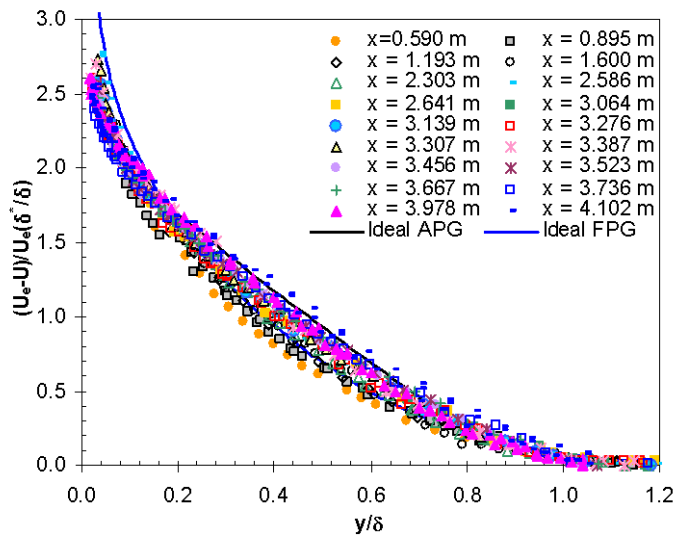


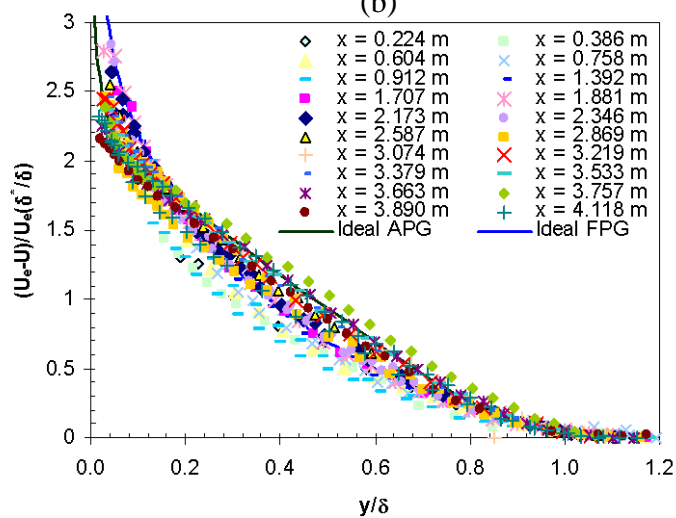
Figure 5.12 Pressure parameter  $\Delta\theta_{calc}$ , for Flow A, Flow B, Flow Han and Flow 141



(a)

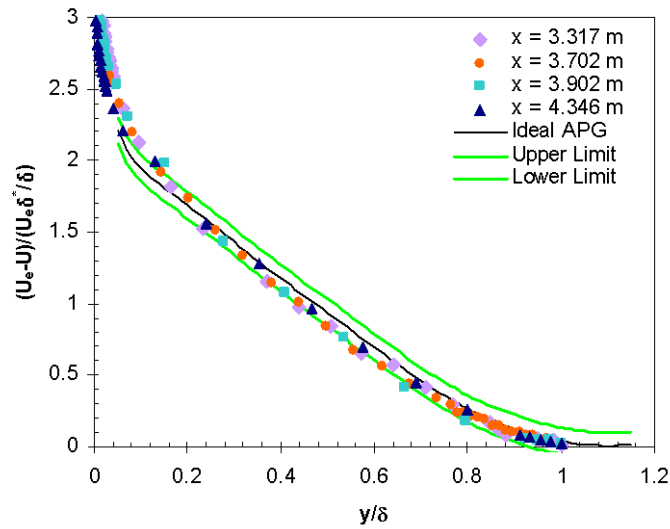


(b)

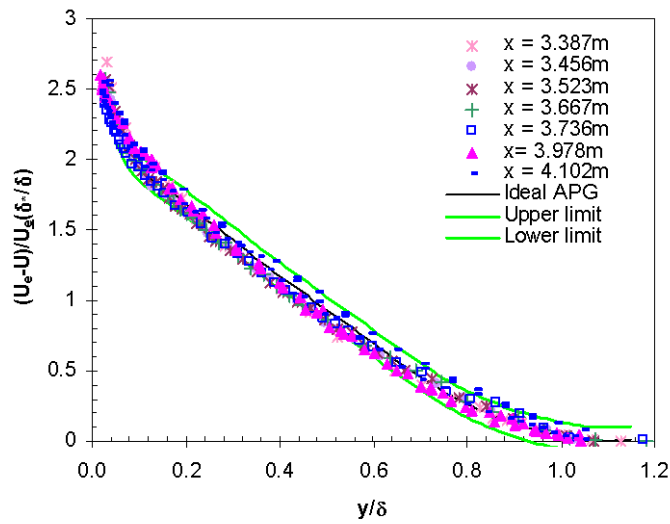


(c)

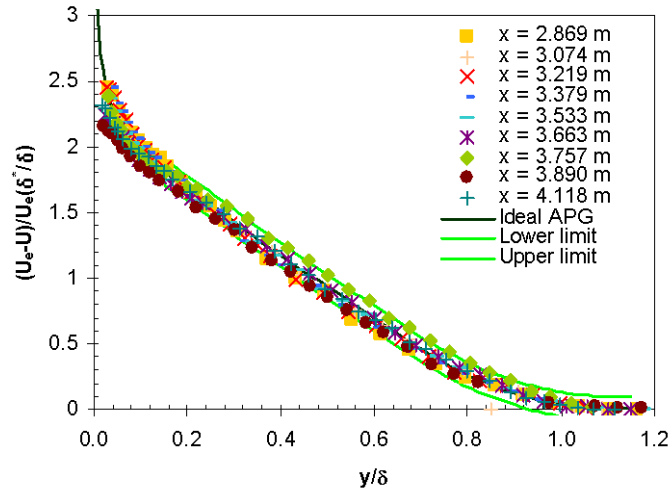
Figure 5.13 Mean velocity deficit scaled with Zagarloa/Smits scale  $U_e(\delta^*/\delta)$  for (a) Flow Han, (b) Flow A, and (c) Flow B. The two solid lines represent ideal APG and FPG behaviour.



(a)



(b)



(c)

Figure 5.14 Mean velocity deficit scaled with Zagarloa/Smits scale  $U_e(\delta^*/\delta)$  for (a) Flow Han, (b) Flow A, and (c) Flow B. Ideal APG line and the bandwidth of acceptable collapse are also given. Profiles falling outside the acceptable band have been removed.

**Table 5.3 Location of the first velocity deficit profile to fall within the APG equilibrium band.**

<b>Flow</b>	<b>Location of first acceptable profile</b>
141	2.10 m ( $x/x_{\max} = 0.5$ )
Han	3.32 m ( $x/x_{\max} = 0.7$ )
A	3.39 m ( $x/x_{\max} = 0.7$ )
B	2.87 m ( $x/x_{\max} = 0.6$ )

## 5.2 The ideal APG band and $\Lambda_{\theta_{calc}}$ for 'other' flows

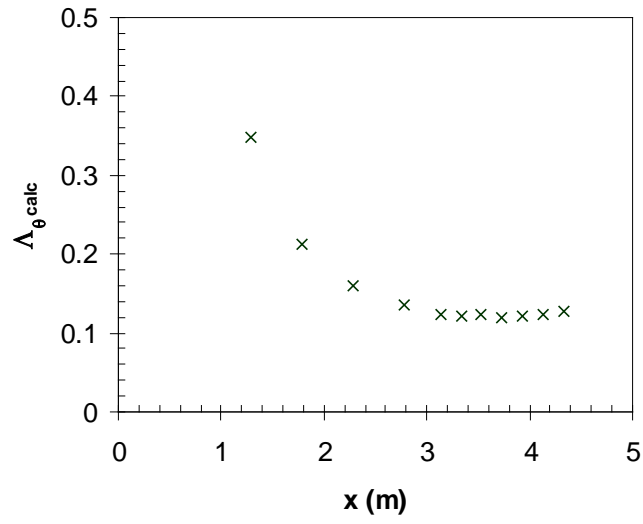
To explore the relationship between the APG equilibrium region as defined by the ideal APG band, and  $\Lambda_{\theta_{calc}}$ , the 14 'other' flows are examined. In Figure 5.15 to Figure 5.25 three plots are presented for each flow. The first plot, (a), is  $\Lambda_{\theta_{calc}}$  to show which flows have a region of equilibrium. The second plot, (b), is the mean velocity deficit profile scaled with  $U_e(\delta^*/\delta)$ , this is repeated in the third plot, (c), with only the profiles which are inside the ideal band.

Four flows, as given in Table 5.4, exhibit a region of constant  $\Lambda_{\theta_{calc}}$ , the streamwise location of the onset of this equilibrium is given in the table. The mean velocity deficit profiles scaled with  $U_e(\delta^*/\delta)$  which fall within the ideal APG band agree with this equilibrium region. This demonstrates that the ideal APG band and  $\Lambda_{\theta_{calc}}$  can be used together or independently to define a region of flow equilibrium.

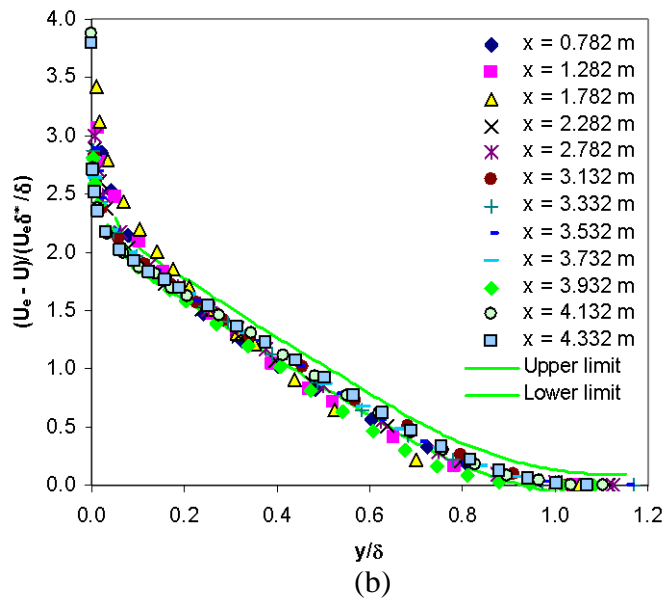
Flow 3600 and Flow 5100 do not exhibit a region of constant  $\Lambda_{\theta_{calc}}$  and as expected, the mean velocity deficit profiles scaled with  $U_e(\delta^*/\delta)$  do not fall within the ideal APG band.

To calculate  $\Lambda_{\theta_{calc}}$ , it is necessary to determine the streamwise derivative of freestream velocity,  $\frac{dU_e}{dx}$ . This presents a problem for two of the flows under review here, namely Flow 2400 and Flow 4000 which both have long regions of steady freestream velocity, thus a zero rate of change and a zero  $\Lambda_{\theta_{calc}}$ . Profiles from within this zero pressure gradient region should not fall within the ideal APG band, which is the case with Flow 4000. However, for Flow 2400 all profiles are clearly within the band. The first few profiles are from an APG region and would be expected to fall within the band but even when the pressure gradient has decreased to zero, the mean velocity deficit profiles are still behaving as though they are experiencing APG conditions. This result must be due to the flow taking some distance downstream to start showing the effect of the zero pressure gradient.

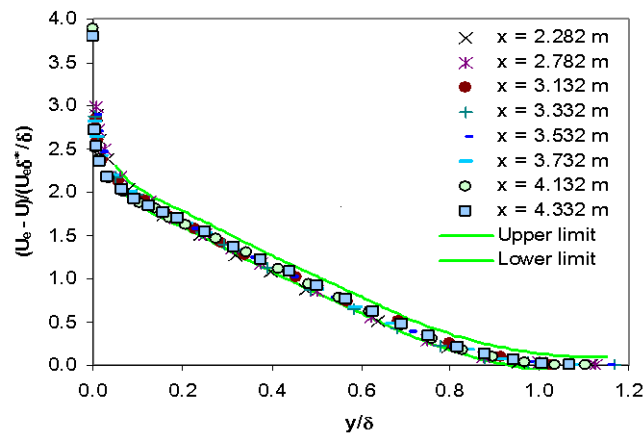
For three flows, namely L&S, N&H and A&E data was not available to calculate  $\Lambda_{\theta_{calc}}$ .



(a)



(b)



(c)

Figure 5.15 Flow 1100 (a)  $\Delta_{\theta,calc}$ , (b) mean velocity deficit profiles scaled with  $U_e^2 \delta^*/\delta$ , (c) only the profiles within the ideal APG band

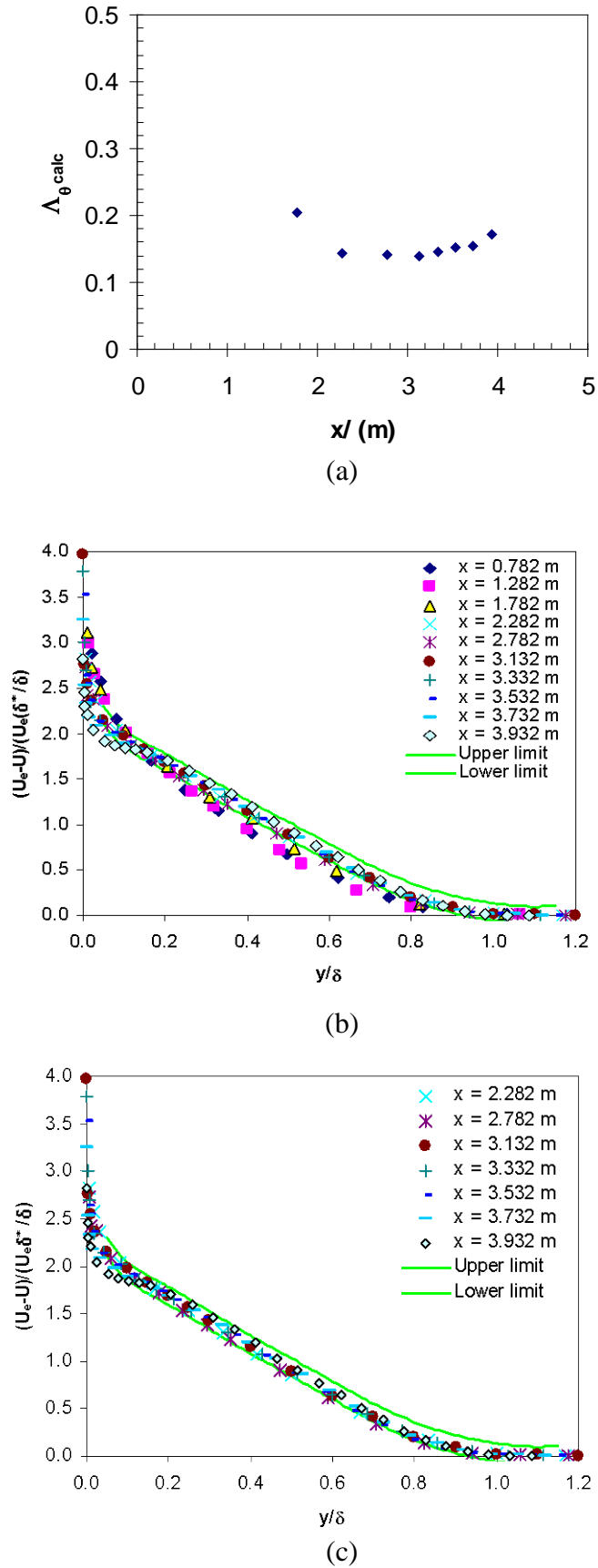


Figure 5.16 Flow 1200 (a)  $\Delta\theta_{calc}$ , (b) mean velocity deficit profiles scaled with  $U_e^2 \delta^* / \delta$ , (c) only the profiles within the ideal APG band

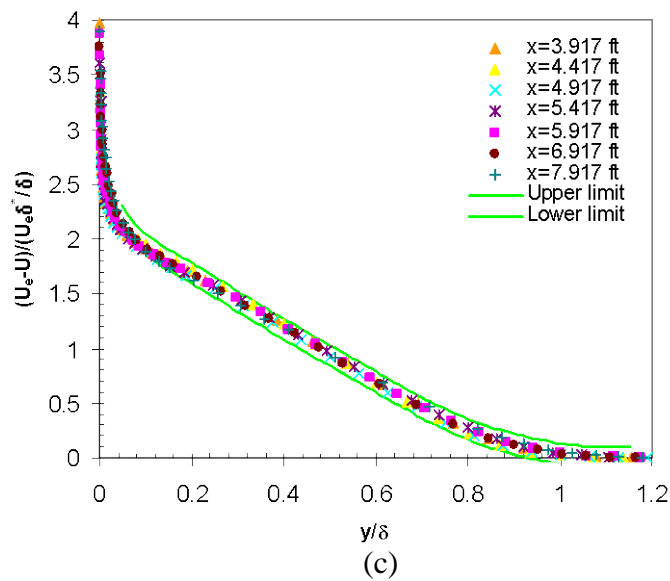
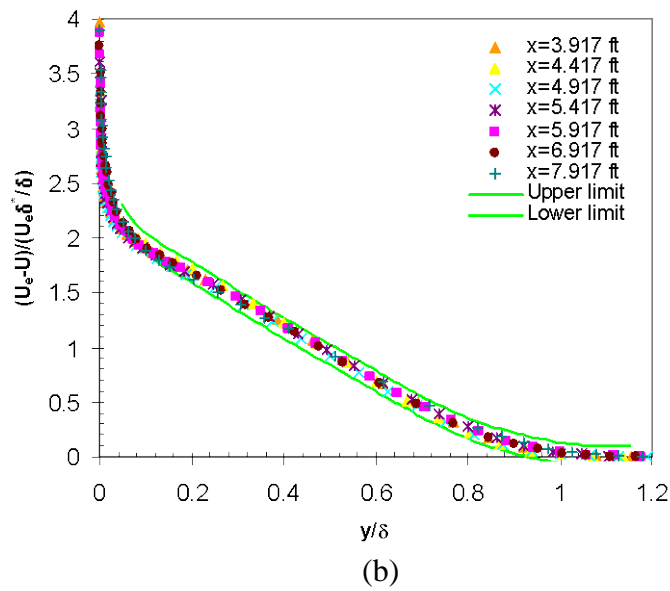
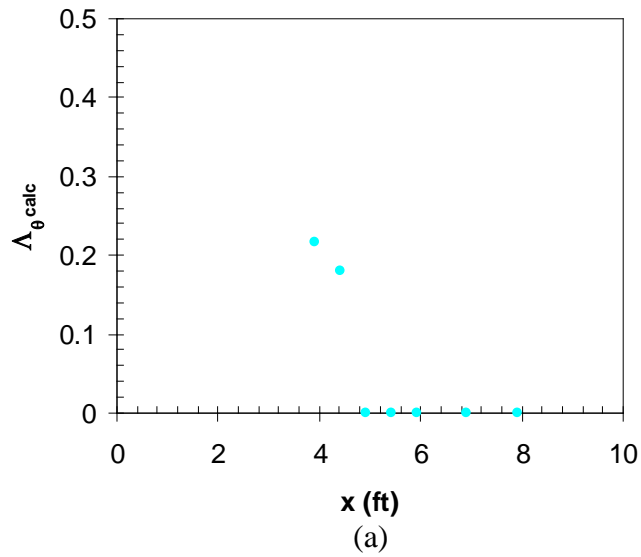
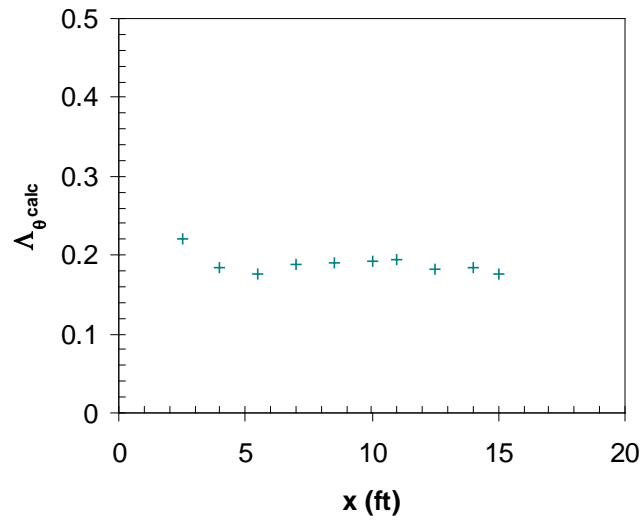
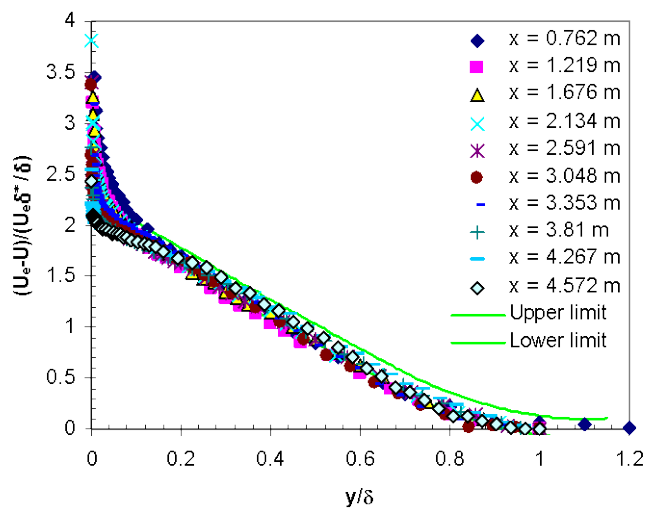


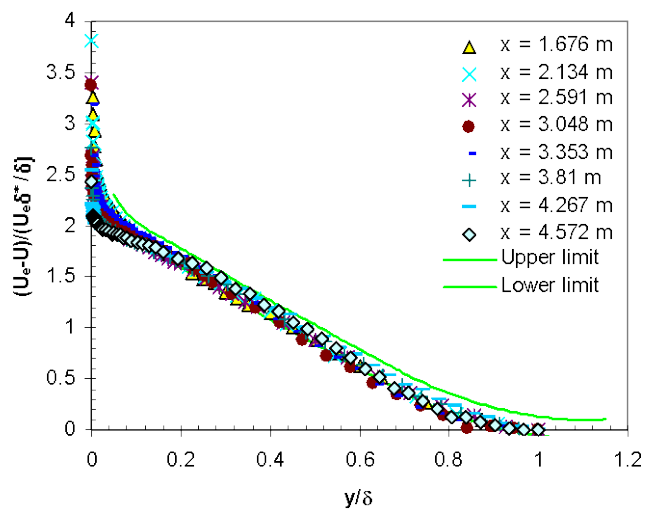
Figure 5.17 Flow 2400 (a)  $\Lambda_{\theta, calc}$ , (b) mean velocity deficit profiles scaled with  $U_e^2 \delta^* / \delta$ , (c) only the profiles within the ideal APG band



(a)

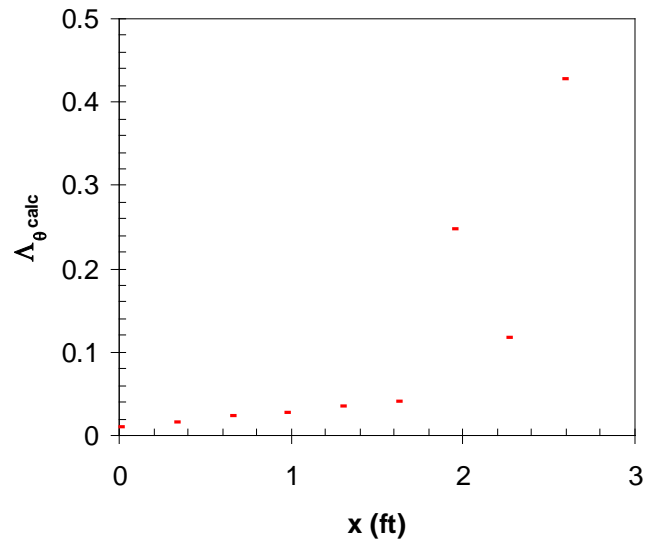


(b)

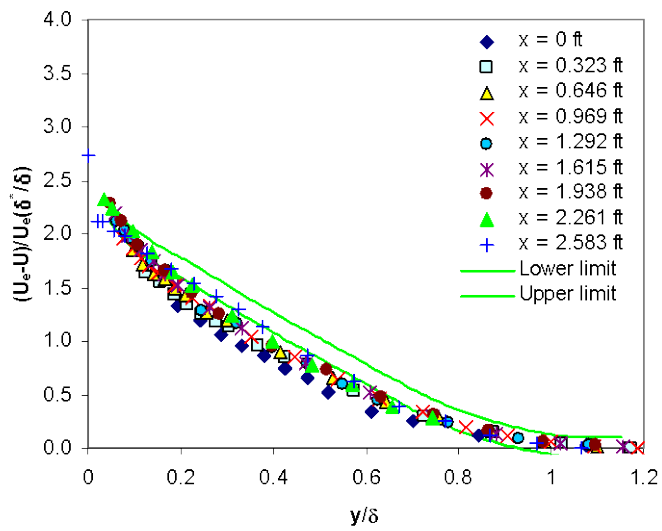


(c)

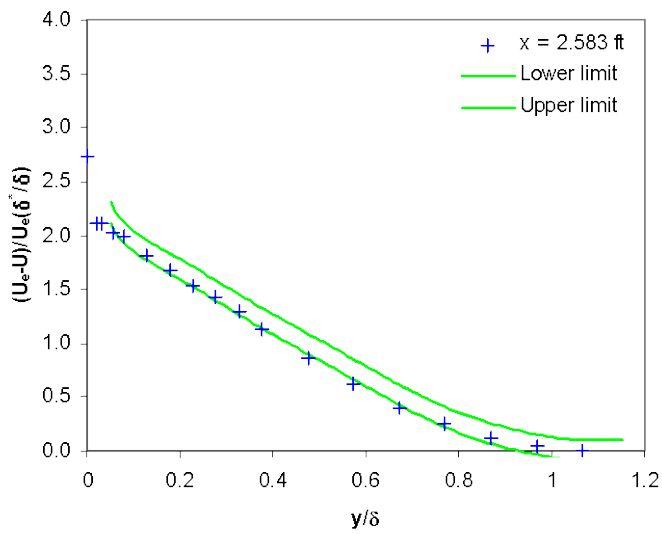
Figure 5.18 Flow 2900 (a)  $\Lambda_{\theta calc}$ , (b) mean velocity deficit profiles scaled with  $U_e^2 \delta^* / \delta$ , (c) only the profiles within the ideal APG band



(a)

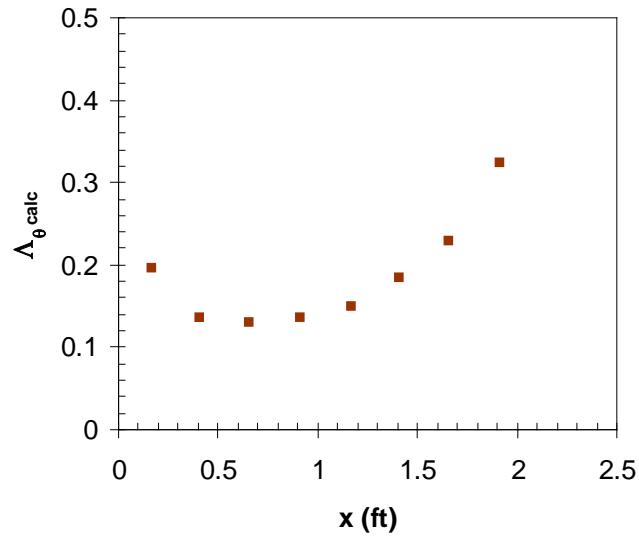


(b)

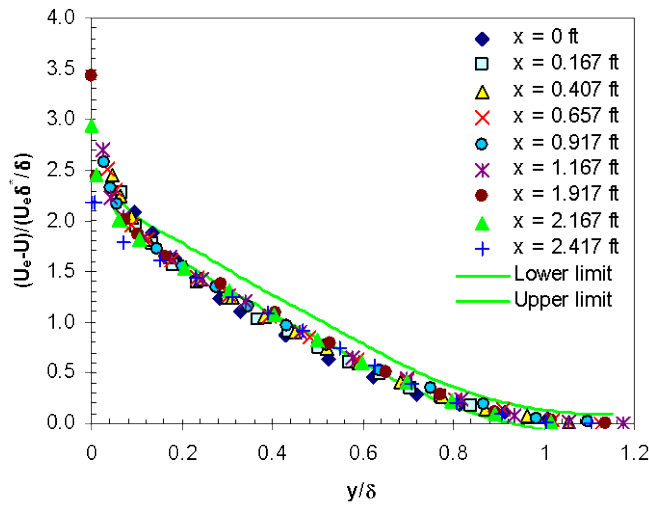


(c)

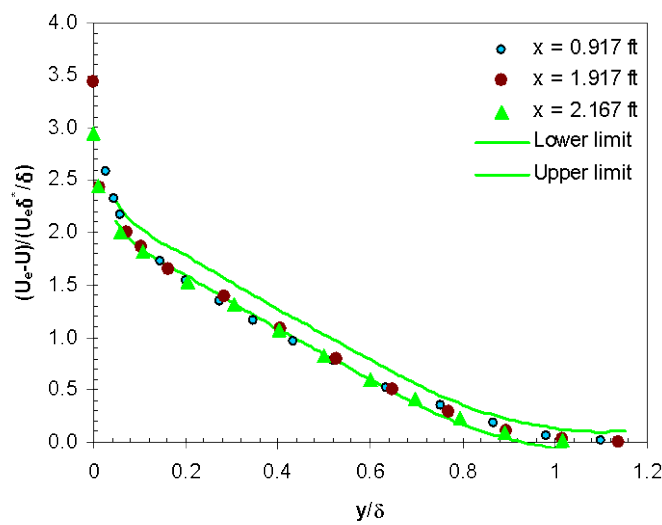
Figure 5.19 Flow 3600 (a)  $\Delta\theta_{calc}$ , (b) mean velocity deficit profiles scaled with  $U_e^2 \delta^* / \delta$ , (c) only the profiles within the ideal APG band



(a)



(b)



(c)

Figure 5.20 Flow 3700 (a)  $\Delta\theta_{calc}$ , (b) mean velocity deficit profiles scaled with  $U_e^2 \delta^*/\delta$ , (c) only the profiles within the ideal APG band

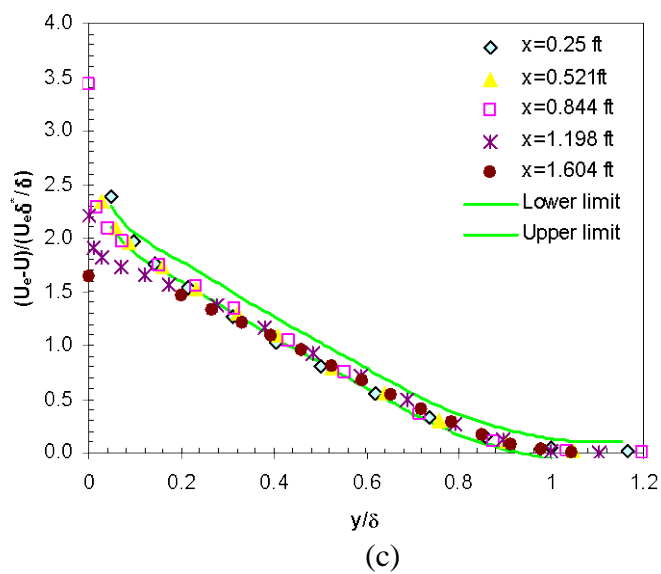
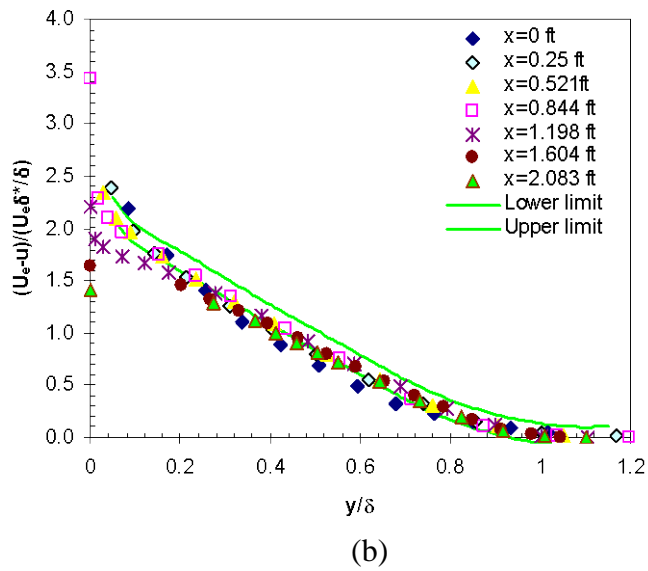
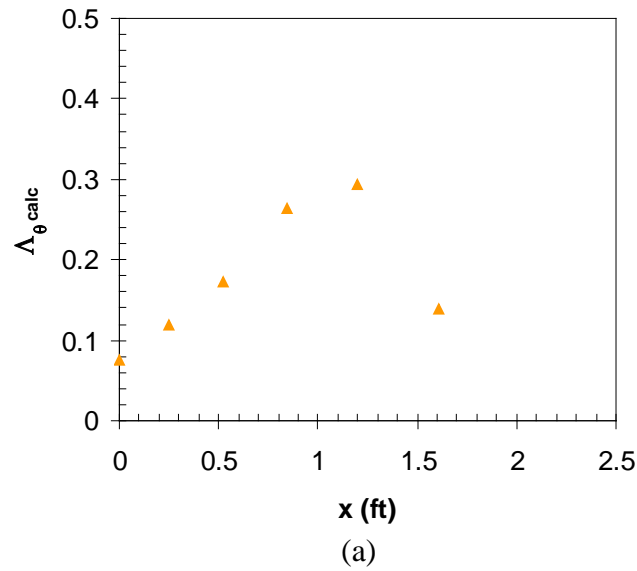
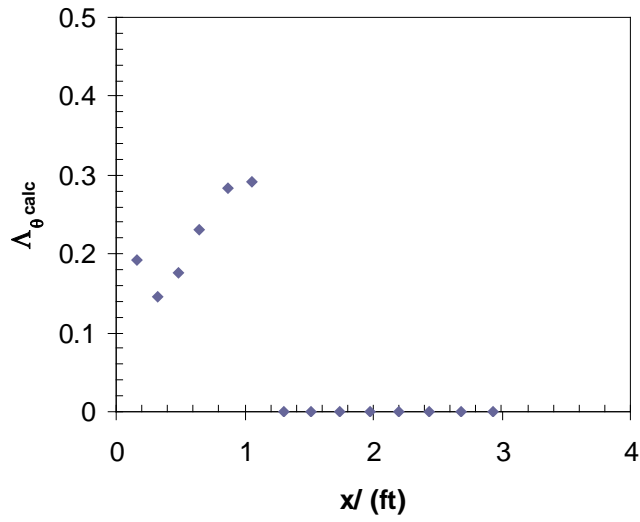
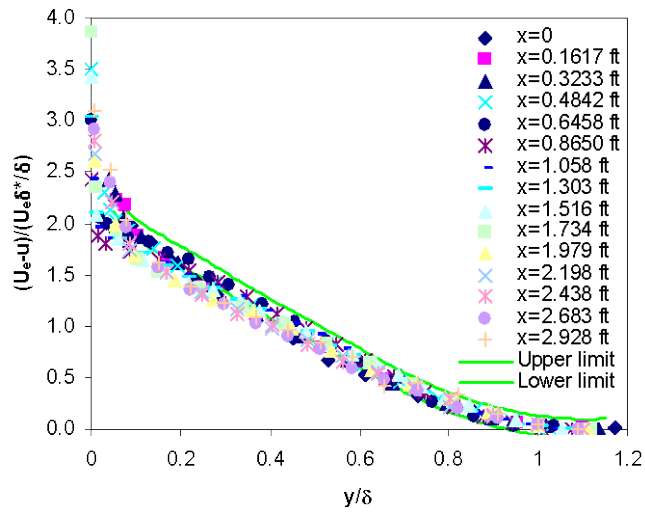


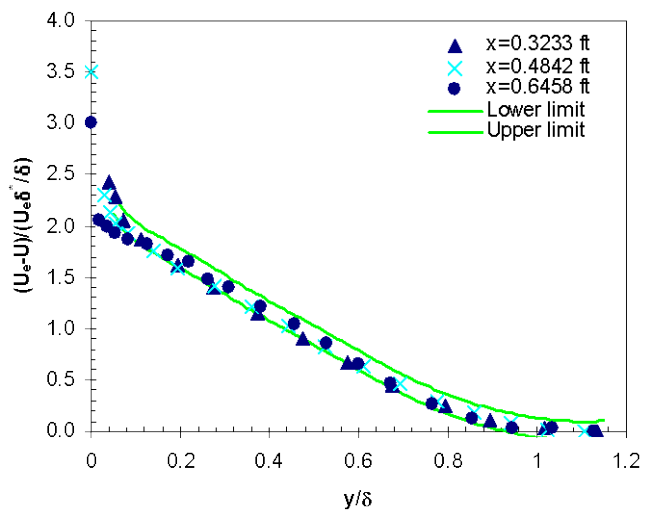
Figure 5.21 Flow 3800 (a)  $\Delta\theta_{calc}$ , (b) mean velocity deficit profiles scaled with  $U_e^2 \delta^*/\delta$ , (c) only the profiles within the ideal APG band



(a)

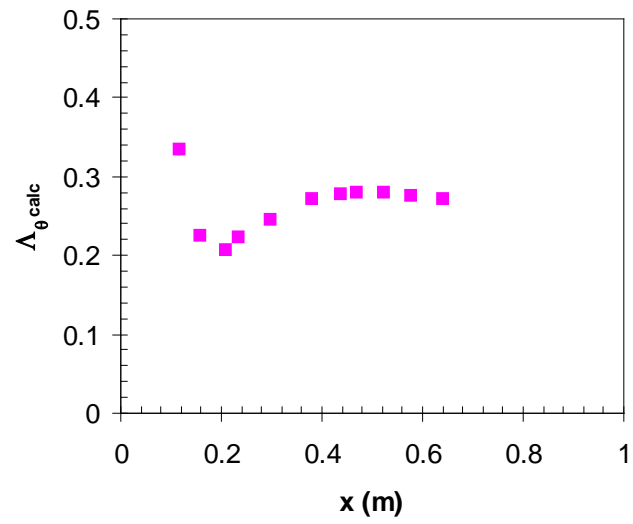


(b)

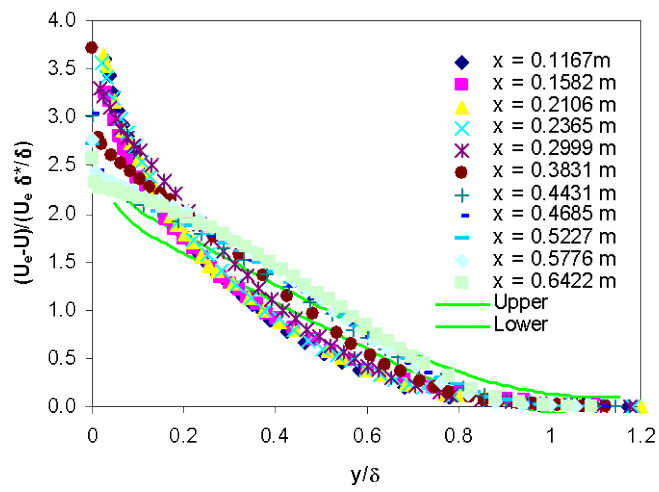


(c)

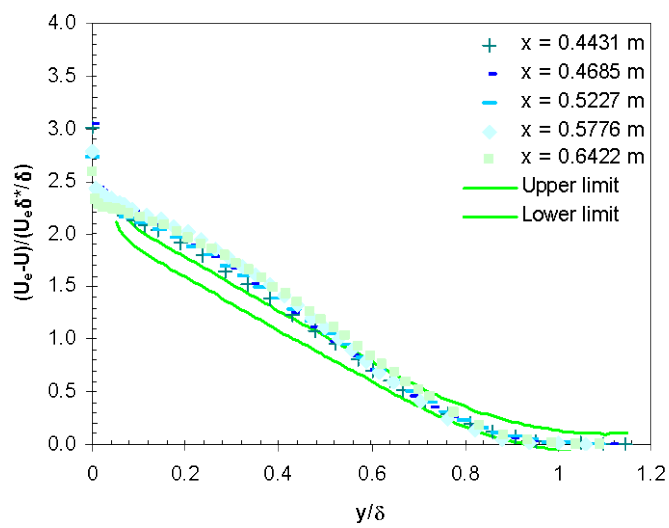
Figure 5.22 Flow 4000 (a)  $\Delta\theta_{calc}$ , (b) mean velocity deficit profiles scaled with  $U_e^2 \delta^*/\delta$ , (c) only the profiles within the ideal APG band



(a)

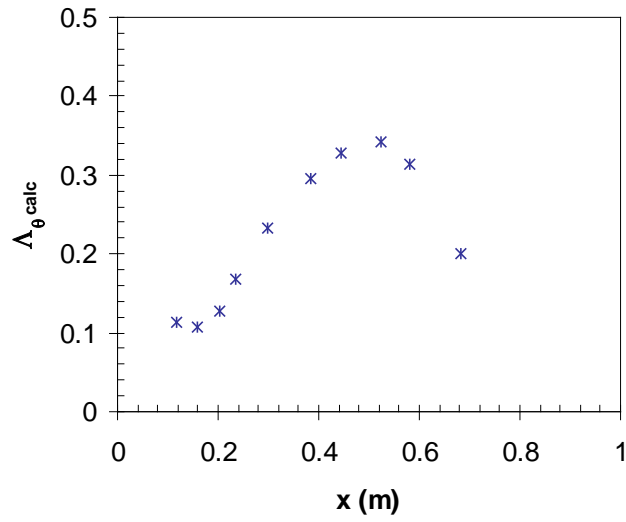


(b)

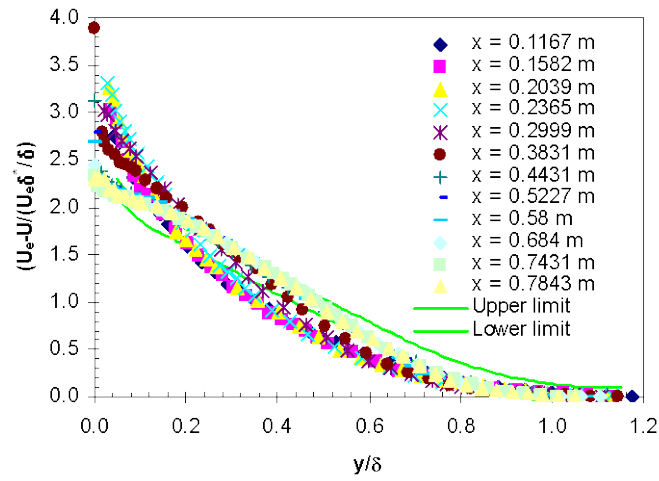


(c)

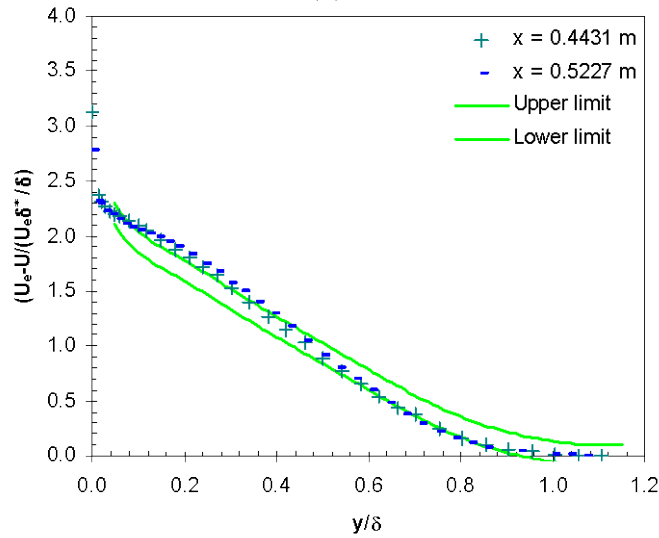
Figure 5.23 Flow 5000 (a)  $\Delta\theta_{calc}$ , (b) mean velocity deficit profiles scaled with  $U_e^2 \delta^*/\delta$ , (c) only the profiles within the ideal APG band



(a)



(b)



(c)

Figure 5.24 Flow 5100 (a)  $\Delta\theta_{calc}$ , (b) mean velocity deficit profiles scaled with  $U_e^2 \delta^*/\delta$ , (c) only the profiles within the ideal APG band

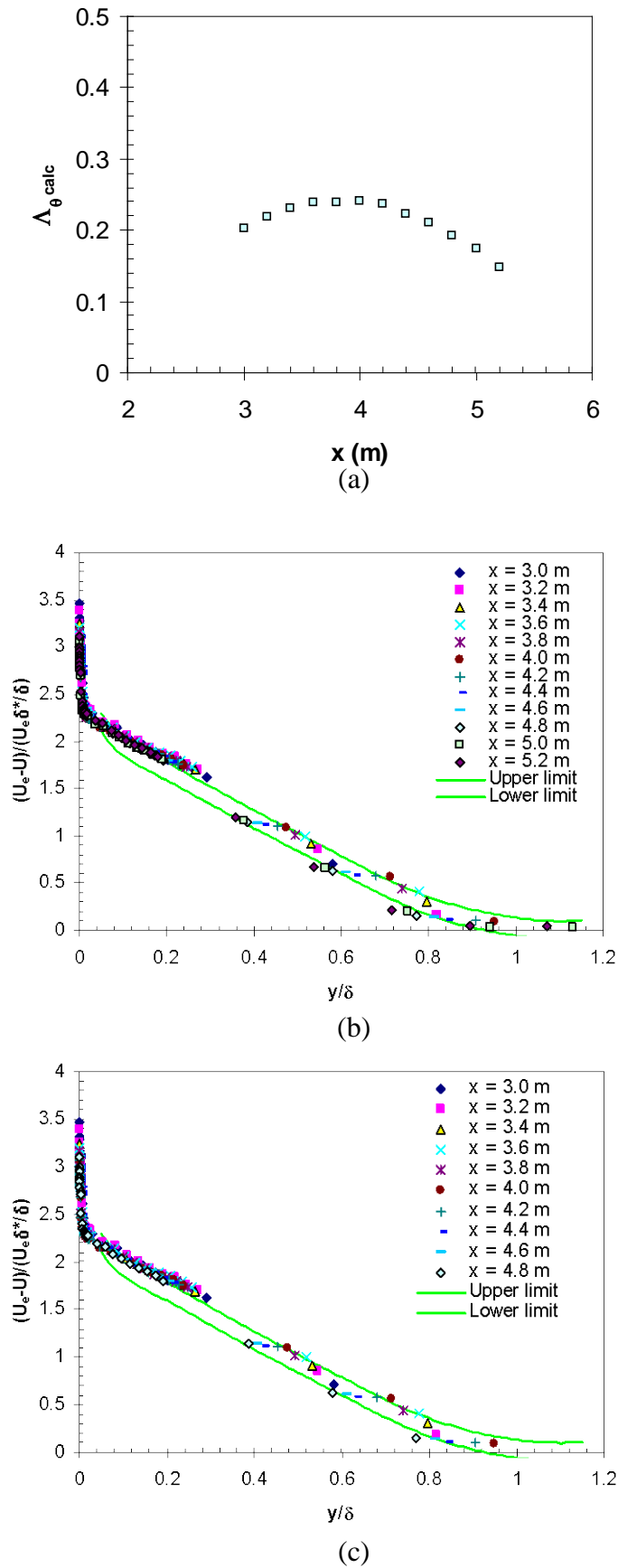


Figure 5.25 Flow Skare (a)  $\Lambda_{\theta, calc}$ , (b) mean velocity deficit profiles scaled with  $U_e^2 \delta^*/\delta$ , (c) only the profiles within the ideal APG band

**Table 5.4 Onset of equilibrium as defined by  $\Lambda_{\theta_{calc}}$  and first profile to fall within ideal APG band**

Flow	Onset of $\Lambda_{\theta_{calc}}$ equilibrium	First profile to fall in ideal APG band
1100	2.78 m	2.28 m
1200	2.28 m	2.28 m
2900	1.22 m	1.67 m
Skare	3.0 m	3.0 m

### **5.3 Conclusions**

Using friction velocity to scale mean velocity deficit is expected to generate a collapse of profiles for equilibrium flows. However, this is only evident for the classical flows. These flows are in equilibrium in the strict sense of Clauser, as defined by  $\beta \sim \text{constant}$ . Profiles from Flows 141, Han, A and B do not collapse, a streamwise increase in magnitude is seen. Only 3 of the 14 ‘other’ flows demonstrate a collapse of profiles, these are Flows L&S, A&E and N&H.

The Castillo/George scaling of  $U_e$  was applied to all the examined flows to observe the level of collapse of profiles. Similar to  $u_*$  scaling, the classical flows collapse but again, it is not the case for the other, more realistic APG flows.

A new scale of  $U_e \delta^*/\delta$  for mean velocity deficit has been empirically determined by Zagarola and Smits (1998a). It was shown that, compared to using friction velocity or freestream velocity this scale yielded a significantly better collapse of profiles (Zagarola and Smits, 1998b). An advantage of this scaling parameter is that compared to friction velocity it is easily defined or measured. This scale was applied to all the examined flows.

The profiles for the classical flows did collapse when scaled with  $U_e \delta^*/\delta$ . This collapse was used to define the ‘ideal’ APG profile, Table 5.2. A bandwidth for an acceptable collapse was also determined. This ideal line and band of collapse can be used to demonstrate flow development to an equilibrium state.

Furthermore, the ideal APG line and band are in agreement with the onset of equilibrium defined by  $\Lambda_{\theta \text{calc}} \sim \text{constant}$ . This was demonstrated by finding the profiles that fall within the ideal APG band and comparing them with  $\Lambda_{\theta \text{calc}}$ .

Zagarola and Smits (1998b) were able to show that this scale successfully collapses profiles from many turbulent boundary layer flows. It has been shown in this chapter that  $U_e \delta^*/\delta$  does not universally collapse all turbulent APG boundary layer flows. Pressure parameter,  $C_p$ , increasingly or decreasingly APG, shape factor,  $H$ , nor

Clauser's equilibrium pressure parameter,  $\beta$  can predict which profiles will scale. However, it is shown, that the existence of equilibrium, as re-defined here by modifying Castillo/George's idea of  $\Lambda_{\theta_{calc}} \sim \text{constant}$ , corresponds to this band for the more realistic, new APG flows.

The ideal APG band and  $\Lambda_{\theta_{calc}}$  can be used together or independently to define a region of flow equilibrium. This equilibrium region corresponds to a state of predictable streamwise growth, and it should be applicable to all APG flows, even when  $\beta$  is not constant.

## 6 Reynolds Stresses and Higher Order Moments

In this chapter, second order correlations (the Reynolds stresses), are presented with various scales and analysed with respect to the previously defined APG equilibrium region, defined by  $\Lambda_{\theta\text{calc}} \sim \text{constant}$ . The scaling factors examined here are the friction velocity scaling,  $u_*^2$ , and the freestream velocity scale,  $U_e^2$ , and the Castillo/George scaling of  $U_e d\delta/dx$ , along with the Zagarola/Smits scale of  $U_e^2(\delta^*/\delta)$ .

As discussed before, the scaling of the Reynolds stresses with the square of the friction velocity represents the classical scaling corresponding to  $U^+ = U/u_*$ . The freestream velocity scaling of the Reynolds normal stresses with  $U_e^2$  follows from the mean flow scaling of Castillo and George (2001). The equivalent scale for the Reynolds shear stress is  $U_e^2 d\delta/dx$ , as discussed in 5.1.3. The Zagarola/Smits mean deficit scaling of  $U_e^2(\delta^*/\delta)$  inspired the use here of the scale  $U_e^2(\delta^*/\delta)$  for the Reynolds normal stress.

Published data for Reynolds stresses are limited. The flows by Skare (1993), Nagano et al (1992), Nagano and Haoura (2002), Lee and Sung (2008) and Aubertine and Eaton (2006) are examined, along with Flows A and B. Other flows examined so far could not be included, because Reynolds stress data were not available.

It is shown in this chapter that the behaviour of Flows A and B is consistent with other reported flows, for scaling with friction velocity and freestream velocity. It is also shown that the Zagarola/Smits scaling yields a collapse of profiles for  $\overline{u^2}$  and  $\overline{v^2}$  in the APG equilibrium region.

Differences in the profiles within the APG equilibrium region and those before are apparent for  $\overline{uv}$ ,  $\overline{u^2}$ ,  $\overline{v^2}$ ,  $\overline{u^3}$ ,  $\overline{v^3}$ ,  $\overline{uv^2}$  and  $\overline{u^2v}$ . This result is further evidence that the APG equilibrium band, as defined in Section 5.1.4 can be used to identify when a flow has reached an equilibrium condition.

Higher order moments are also examined in preparation for energy budgets.

## 6.1 Reynolds Stresses

Turbulent flow is made up of eddy motions in three dimensions. A rotating fluid particle can be considered the smallest of these eddies, and the largest eddy is limited only by the flow geometry. The three dimensional nature of these eddies mean that at any point, the flow experiences movement in all three dimensions. For the flows examined here, including the two generated for this study, Flow A and Flow B, the bulk transport occurs in the x direction, and the instantaneous velocity in this direction is defined as  $u$ . The flow also experiences instantaneous velocity in the y direction defined as  $v$ , and perpendicular to the x-y plane in the z direction, defined as  $w$ .

By its nature, a turbulent flow can be randomly fluctuating. This presents a mathematical challenge, as velocity components and pressure are rapidly varying with space,  $x$ ,  $y$  and  $z$  and time,  $t$ . In 1895, Osborne Reynolds applied a time-averaging concept to the turbulent variables of the continuity equation.

Looking at a characteristic time trace of a turbulent function  $U$ , which varies as a function of  $(x, y, z, t)$ , and it has rapid random fluctuations, the time-averaged value is defined:

$$U = \frac{1}{T} \int_0^T u dt \quad \text{Equation 6-1}$$

where  $U$  is the time averaged velocity in the streamwise direction, [m/s]  
 $T$  is the time period, [s], and  
 $u$  is the instantaneous velocity in the streamwise direction, [m/s].

This definition has already been used in the derivation of Equation 5-5. The time period  $T$ , must be greater than any significant period of the fluctuations themselves. For the hot wire anemometry measurements in Flows A and B, a sampling period of 26 seconds was used. This was the maximum time period that could be recorded with the available hardware. Experiments with shorter averaging times showed that the results became independent of the averaging time as 26 seconds were approached.

Returning to the time trace, the fluctuating component  $u'$  is defined as the difference between the instantaneous value and the average:

$$u' = u - U \quad \text{Equation 6-2}$$

where  $u'$  is the fluctuating component of the streamwise velocity, [m/s]  
 $u$  is the instantaneous velocity in the streamwise direction, [m/s]  
 $U$  is the time (ensemble) averaged velocity in the stream wise direction, [m/s]

Therefore,  $u$  consists of the mean plus the fluctuating component. Of course, each velocity component and pressure can be written this way, as suggested by Reynolds.

$$\begin{aligned} u &= U + u' \\ v &= V + v' \\ w &= W + w' \\ p &= P + p' \end{aligned} \quad \text{Equation 6-3}$$

where  $U$  refers to velocity in the streamwise, or  $x$  direction, [m/s],  
 $V$  refers to velocity in the  $y$  direction, [m/s],  
 $W$  refers to velocity in the cross-stream, or  $z$  direction, [m/s], and  
 $P$  refers to the pressure, [N/m<sup>2</sup>].

Substituting these equations into the momentum equation and taking the time average, generates mean values and 6 mean products of fluctuating velocities. These mean products or ‘correlations’ are called the turbulent stresses, or Reynolds stresses. They are  $-\overline{\rho u^2}$ ,  $-\overline{\rho v^2}$ ,  $-\overline{\rho w^2}$ ,  $-\overline{\rho uv}$ ,  $-\overline{\rho vw}$ , and  $-\overline{\rho uw}$ . The additional terms come from the three convective acceleration terms. They have the same units and a similar effect on the flow as viscous forces per fluid volume.

An  $x$ -wire probe can simultaneously measure the flow velocity in two directions, as discussed in Chapter 3. With the probe aligned in its ‘proper’ position, the wires sense  $u$  and  $v$  components, and as such, the correlations  $\overline{u^2}$ ,  $\overline{v^2}$ , and  $\overline{uv}$  can be determined. By rotating the probe on its axis by 90°, the wires sense the  $u$  and  $w$

velocity components, hence  $\overline{u^2}$ ,  $\overline{w^2}$ , and the  $\overline{uw}$  correlation. For Flow A and Flow B, the probe was aligned to measure  $u$  and  $v$  velocity components. A small number of experiments were also conducted with the probe rotated by 90 degrees to measure  $u$  and  $w$  behaviour. The correlation  $\overline{vw}$  could not be measured with the current equipment.

In this chapter, the effects of different scaling parameters for Reynolds stresses are examined. The parameters used include friction velocity and extensions of the Castillo/George and Zagarola/Smits scales. The results from Flow A and B are compared with those from the literature for which Reynolds stress data are available.

### 6.1.1 Scaling shear stress, $\overline{uv}$ with $u_*^2$ , $uv_{\max}$ and $U_e^2 \frac{d\delta}{dx}$

In this sub-section, different approaches to scale  $uv$  are presented. The scales are, the classical  $u_*^2$  scaling,  $uv_{\max}$  and  $U_e^2 \frac{d\delta}{dx}$  corresponding to the Castillo/George scaling of the mean velocity deficit.

The most commonly accepted non-dimensional scaling for the Reynolds stresses is to use friction velocity, as recommended by Townsend (1956). This scaling for  $\overline{uv}$  is given for Flow A and Flow B in Figure 6.1(a) and Figure 6.2(a), respectively. Frame (b) in these figures contain the profiles that fall before the APG equilibrium region, whilst frame (c) contains only APG equilibrium profiles, as defined in f 5.1.4 with the ideal APG band.

A change is evident between the groups of profiles before the APG equilibrium region and those within it. For Flow A, before equilibrium, the peak value increases in magnitude and moves away from the wall, (excluding the first measurement location), in Figure 6.1(b). However, within the APG equilibrium region the  $y/\delta$  location of the peak has stabilised at  $y/\delta \approx 0.4$ , in Figure 6.1(c). This is consistent with the behaviour reported by Skare (Thesis, p 50, 1993) where the  $y$  location of the peak increases before the APG equilibrium region, then stabilises within it. This behaviour is also seen in Flow B, but it is not as obvious, with the last profile in each frame defying the trend. In the APG equilibrium region, in Figure 6.2(c), the peak has stabilised at  $y/\delta \approx 0.4$ , (excluding the last measurement location,  $x = 3.757$  m).

The strong APG flow of Lee and Sung (2008) was obtained by direct numerical simulation (DNS). The results for  $u_{\text{rms}}$ ,  $v_{\text{rms}}$  and  $\overline{uv}$  compare favourably with the experimental work of Nagano et al (1992). In both cases,  $\overline{uv}$  scaled with friction velocity demonstrated the same shift in the location of the peak, as seen with Flows A and B before the APG equilibrium region. Figure 6.3 is a reproduction of Figure 11 from Lee and Sung (2008). An arrow is used to highlight the progression of the peak. This figure contains both DNS data of Lee and Sung and the experimental data of Nagano et al (1992). These two flows are revisited in Sections 6.1.2 and 6.1.3, when

discussing the scaling of  $\overline{u^2}$  and  $\overline{v^2}$  respectively. As stated in Section 5.2, it was not possible to estimate  $\Lambda_{\theta\text{calc}}$  for the data of Lee and Sung.

For Flow 141, it is difficult to draw conclusions about the shear stress data scaled with friction velocity, given in Figure 6.4. Only four profiles are available, one of which exhibits anomalous behaviour near the wall, as such it is difficult to determine the location of the peak magnitude. The two profiles that are within the APG equilibrium region ( $x > 2.1$  m) both have a peak magnitude at  $y/\delta \approx 0.25$ , which is consistent with the afore mentioned flows which also exhibited a steady  $y/\delta$  location of the peak magnitude for profiles within the APG equilibrium region.

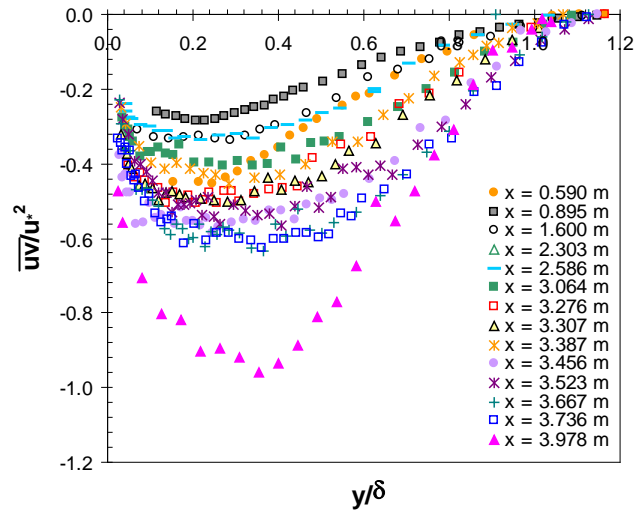
Another simple way to scale  $\overline{uv}$  is to use its own local maximum, as presented in Figure 6.5 and Figure 6.6 for Flow A and Flow B, respectively. Again, frame (b) contains data profiles before the APG region and frame (c) contains data profiles within the APG equilibrium region. The disparity between these two regions is even more apparent with this scaling, particularly with Flow B.

In Chapter 5, the Castillo and George scaling of  $U_e$  was used for the mean velocity deficit. The equivalent scaling for  $\overline{uv}$ , as shown in Castillo and George (2001) and in 5.1.3 is  $U_e^2 \frac{d\delta}{dx}$  where  $\frac{d\delta}{dx}$  is the growth rate of the boundary layer. Amongst the chosen scaling parameters, this scaling yields the best collapse of profiles within the APG equilibrium region for Flows A and B, as evident in Figure 6.7(c) and Figure 6.8(c).

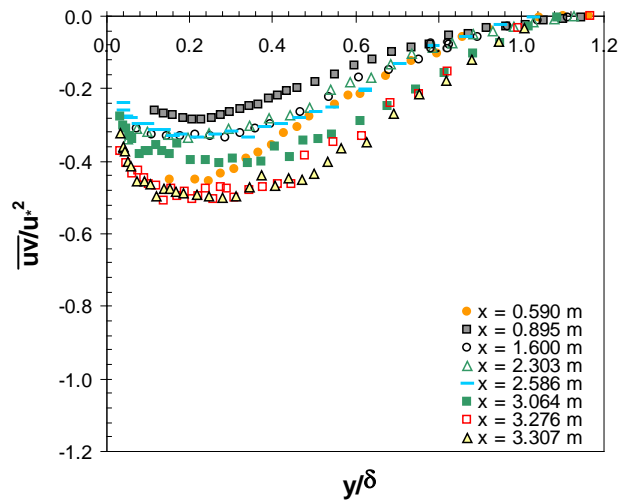
The profiles were analysed for quality of collapse using the method established in the Chapter 4. The results for quality of collapse are given in Table 6.1. Consistently, with both  $u_*$  or  $U_e^2 \frac{d\delta}{dx}$  scaling, the quality of collapse is greater in the APG equilibrium region. For example, Flow B  $\overline{uv}$  scaled  $U_e^2 \frac{d\delta}{dx}$  has a quality of collapse of 70% within the APG equilibrium region, compared with a 23% quality of collapse over the entire flow.

Comparing the two scales,  $U_e^2 \frac{d\delta}{dx}$  yields a better collapse of profiles. Using friction velocity,  $u_*$ , the quality of collapse within the APG equilibrium region, for Flow A and B is 47% and 57% respectively, whereas using  $U_e^2 \frac{d\delta}{dx}$  it is 65% and 70% respectively.

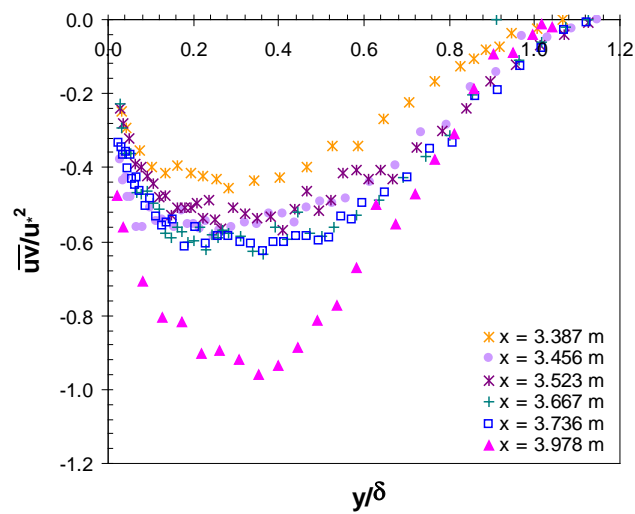
In conclusion, comparing the group of profiles within the APG equilibrium region, (frame (c) in each figure) with the group of profiles before (frame (b) in each figure), differences are observed with friction velocity,  $u_{v_{max}}$  and  $U_e^2 \frac{d\delta}{dx}$  scales, particularly for Flow B. Examination of the flow geometry, or pressure distribution,  $C_p$ , or shape factor,  $H$ , or boundary layer thickness,  $\delta$ , or Clausers equilibrium pressure parameter,  $\beta$ , does not yield an explanation for this behaviour. However, the behaviour can be categorised using the ideal APG band previously defined here by the Zagarola/Smits scaling, corresponding to  $\Lambda_{\theta_{calc}} \sim \text{constant}$ . This is further evidence that these two criteria define a universal equilibrium condition in the mean flow with an APG.



(a)

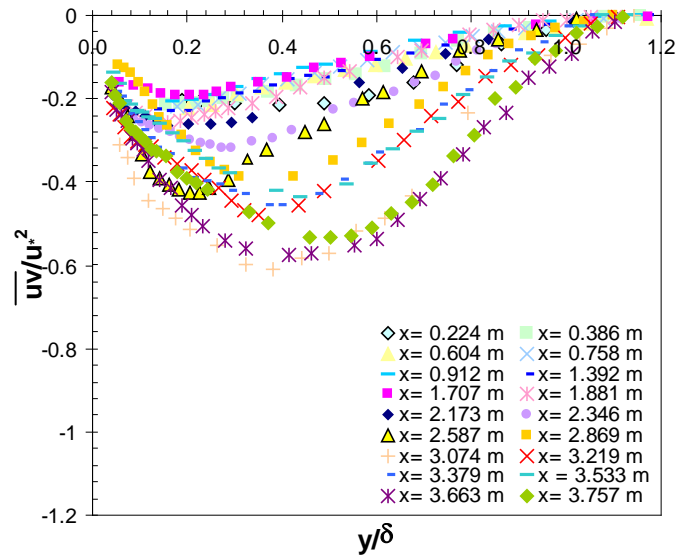


(b)

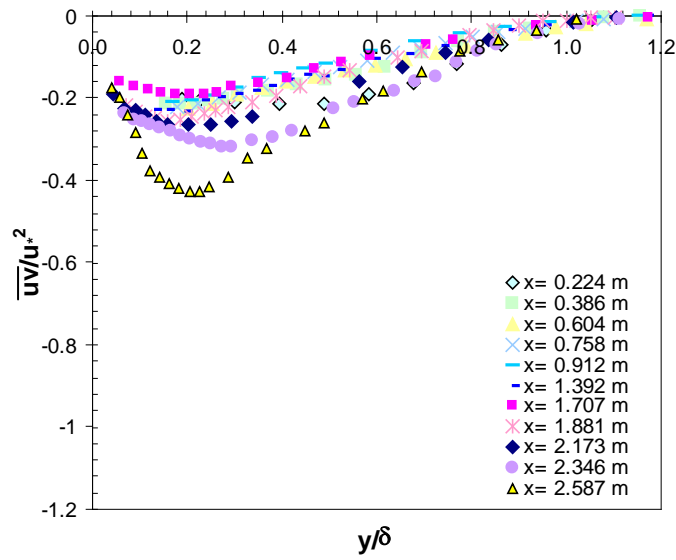


(c)

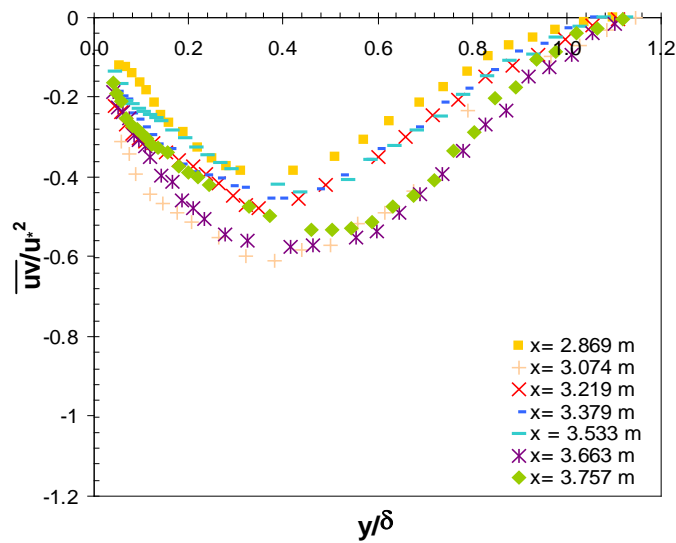
Figure 6.1 Shear stress  $-\overline{uv}$  scaled with friction velocity  $u_s^2$  for Flow A. (a) All stations, (b) before APG equilibrium region, and (c) APG equilibrium region.



(a)



(b)



(c)

Figure 6.2 Shear stress  $\overline{uv}$  scaled with friction velocity  $u_*^2$  for Flow B. (a) All stations, (b) before APG equilibrium region, and (c) APG equilibrium region.

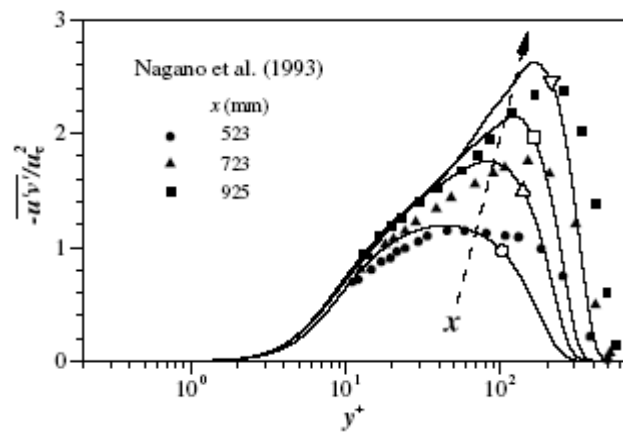


**Figure 6.3** Shear stress  $uv$  scaled with friction velocity  $u_*^2$ . The solid lines are the DNS results of Sung and Lee (2008). The symbols present the experimental data of Nagano et al (1992). The arrow indicates the streamwise direction and highlights the shift in the  $y$  location of the peak. (Figure 11 of Lee and Sung, 2008, p 574)

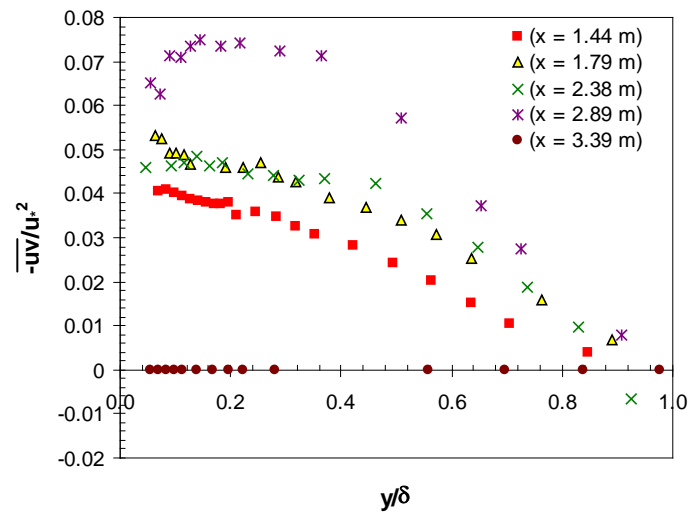
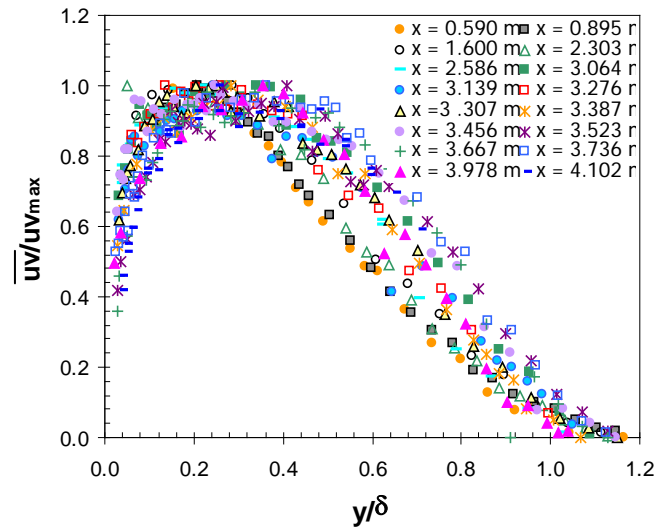
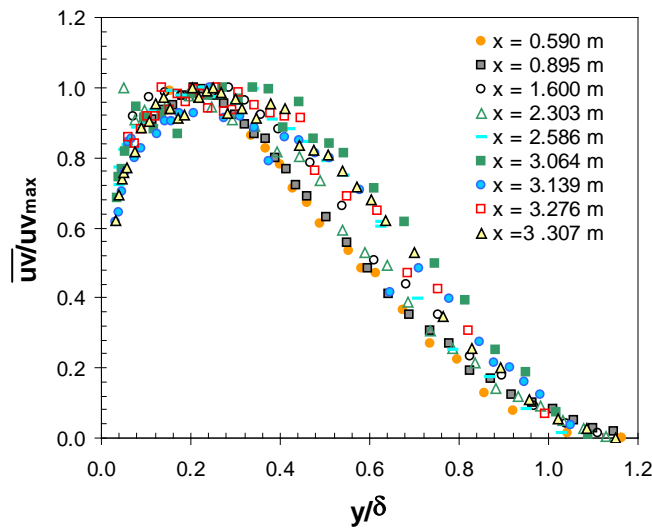


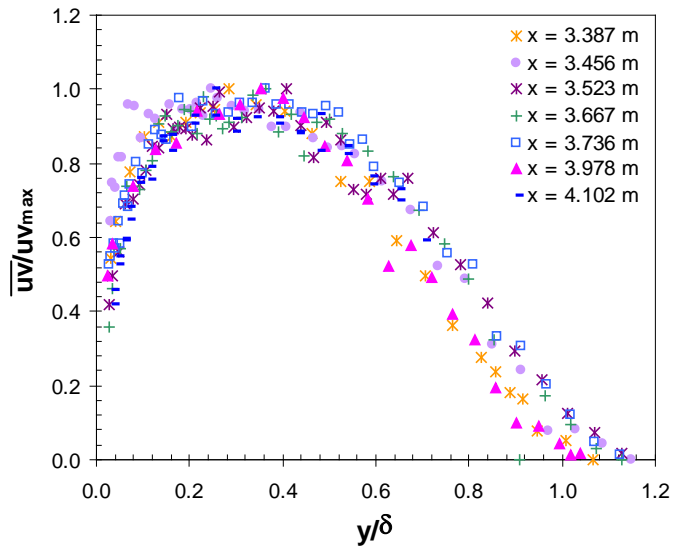
Figure 6.4 Flow 141,  $\overline{-uv}$  scaled with friction velocity. (Onset of equilibrium occurs at  $x = 2.1$  m)



(a)



(b)



(c)

Figure 6.5 Shear stress  $\overline{uv}$  scaled with the maximum shear stress  $uv_{\max}$  for Flow A. (a) All stations, (b) before APG equilibrium region, and (c) APG equilibrium region.

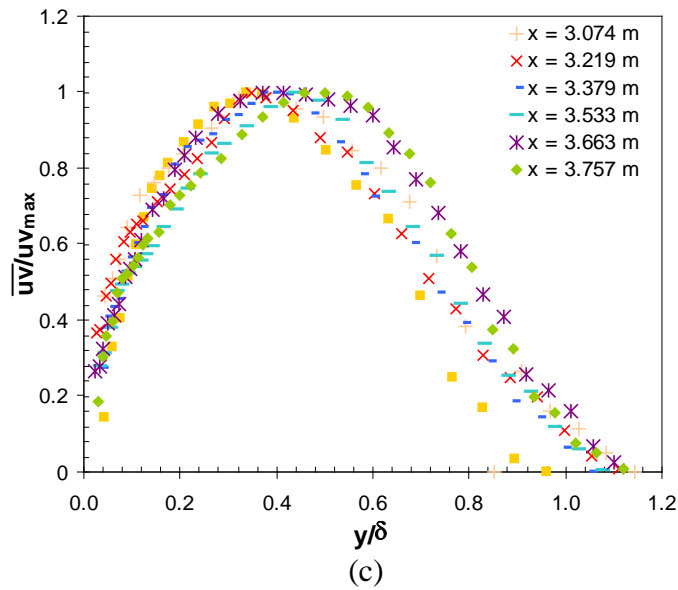
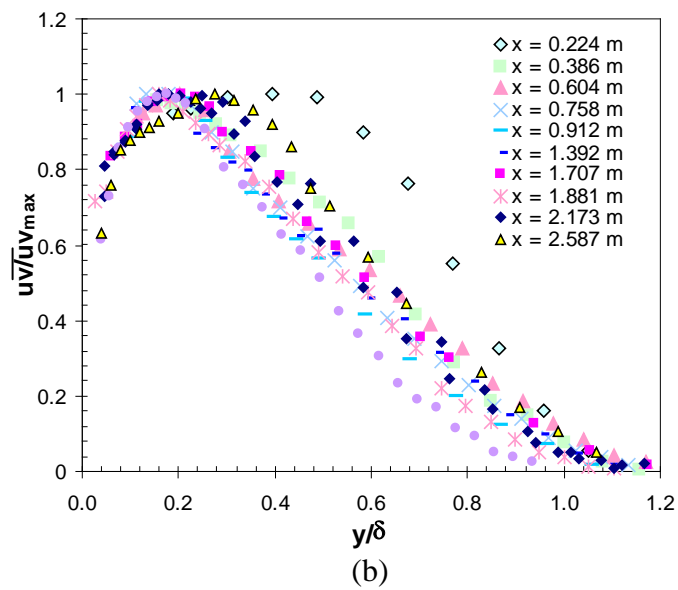
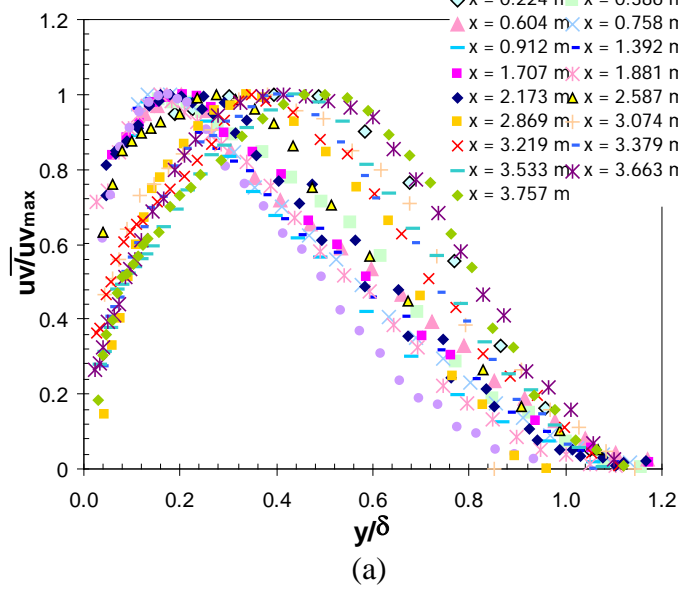


Figure 6.6 Shear stress  $\overline{uv}$  scaled with the maximum shear stress  $uv_{max}$  for Flow B. (a) All stations, (b) before APG equilibrium region, and (c) APG equilibrium region.

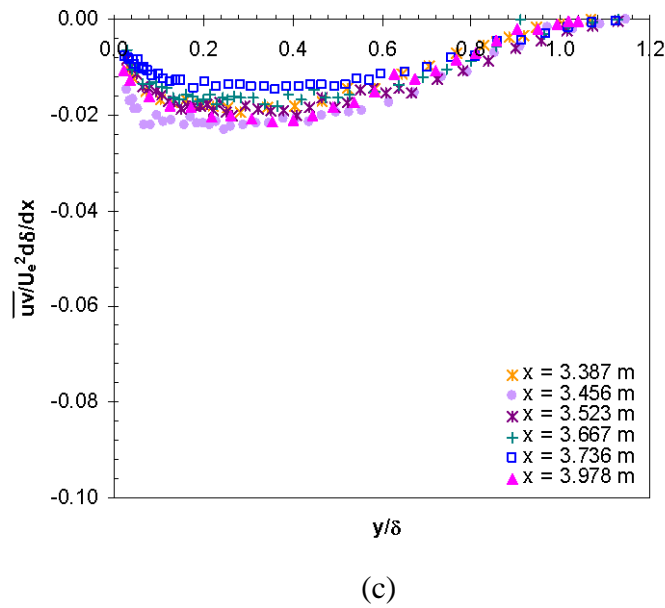
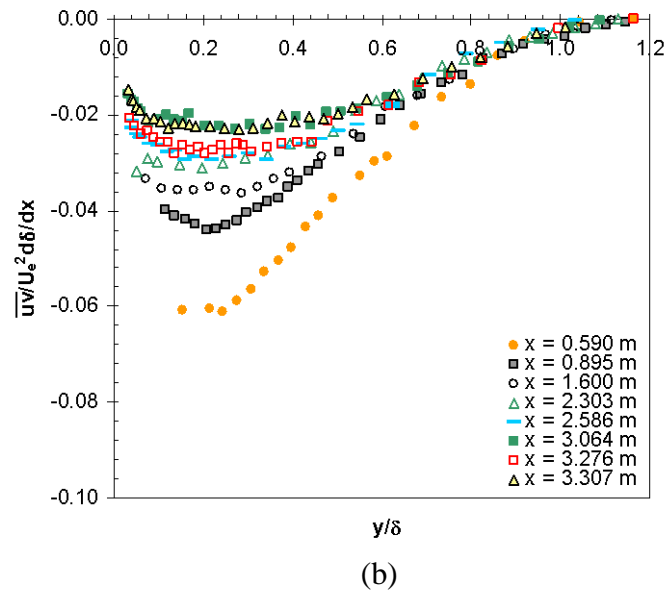
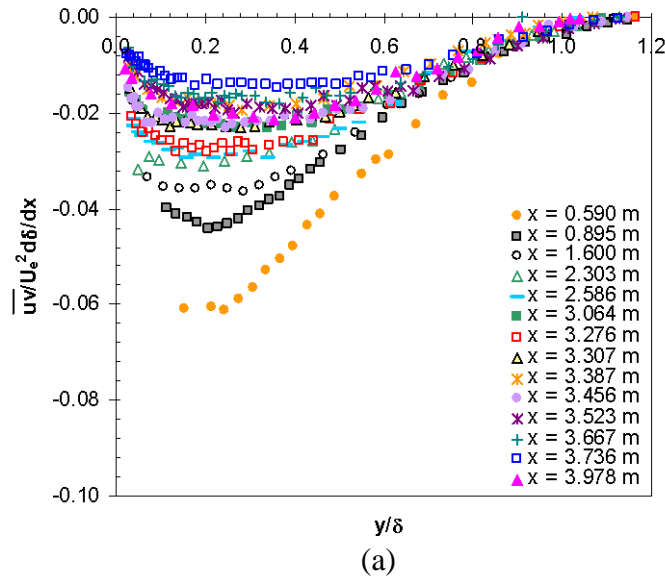
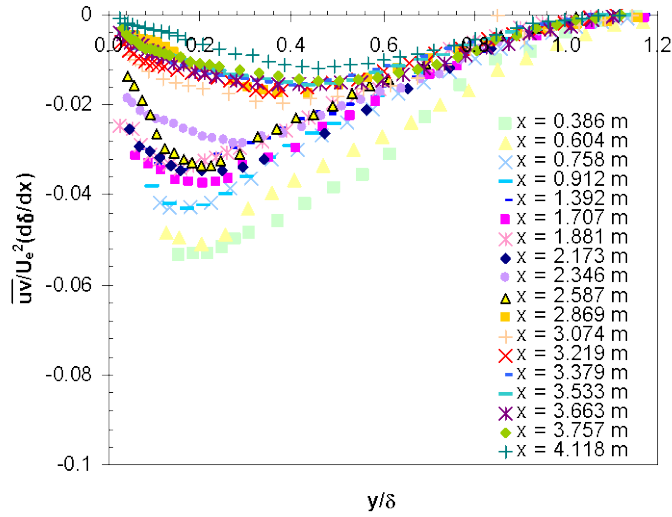
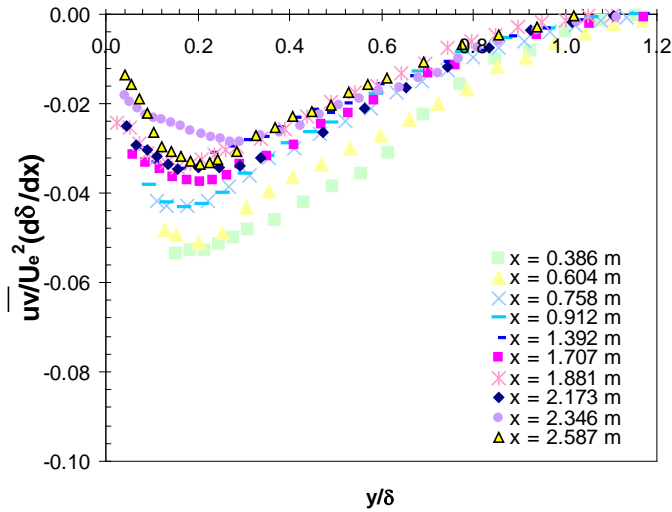


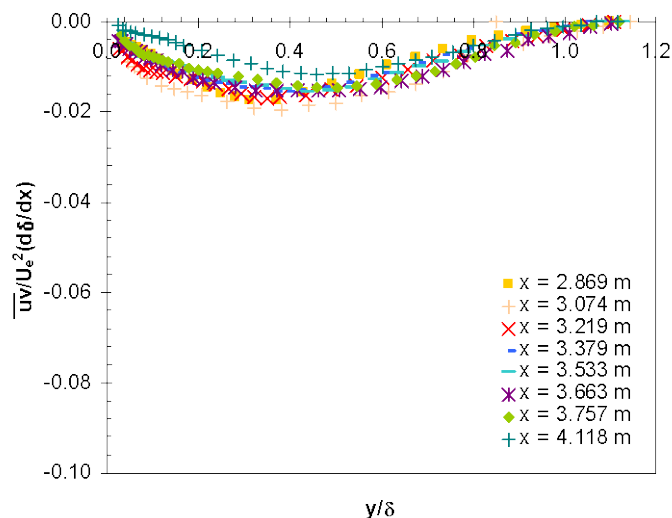
Figure 6.7 Shear stress  $uv$  scaled with  $U_e^2(d\delta/dx)$  of Castillo/George for Flow A. (a) All stations, (b) before APG equilibrium region, and (c) APG equilibrium region.



(a)



(b)



(c)

Figure 6.8 Shear stress  $-\overline{uv}$  scaled with  $U_e^2(d\delta/dx)$  of Castillo/George for Flow B. (a) All stations, (b) before APG equilibrium region, and (c) APG equilibrium region.

**Table 6.1 Quality of collapse (Average from  $y/\delta = 0.2, 0.4$  and  $0.6$ )**

		All profiles	APG equilibrium region
$\overline{uv}/u_*^2$	Flow A	28 %	47 %
$\overline{uv}/u_*^2$	Flow B	27 %	57 %
$\overline{uv}/U_e^2(d\delta/dx)$	Flow A	23 %	65 %
$\overline{uv}/U_e^2(d\delta/dx)$	Flow B	23 %	70 %

### 6.1.2 Scaling normal stress in the x direction, $\overline{u^2}$ , with $u_*^2$ , $U_e^2$ and $U_e^2 \delta^*/\delta$

In Figure 6.9 and Figure 6.10, the profiles for the normal stress component  $\overline{u^2}$  are presented scaled with friction velocity  $u_*^2$ . The profiles do not demonstrate a better collapse in the APG equilibrium region, as opposed to the ‘non-equilibrium’ region for Flows A and B. This result is expected, since with  $u_*$  scaling, the velocity deficit profiles did not show a collapse as discussed in Section 5.1.1.

In the DNS results of Lee and Sung (2008), two peaks exist in  $u_{rms}$  scaled with friction velocity. As seen in Figure 6.11, collapse of profiles occurs in the near wall peak, at  $y/\delta \cong 0.04$ , as expected, since  $u_*$  is a near wall scale. However, the profiles of the outer peak do not collapse. They increase in magnitude and exhibit a shift in the  $y$  location, similar to that in  $\overline{uv}/u_*^2$ . These results are consistent with the experiments of Nagano and Houra (2002) and Nagano et al (1992), also plotted in Figure 6.11. Whilst with Flows A and B, the existence of two peaks is not obvious, the profile of the outer peak and its shift in location in the streamwise direction ( $x$ ) is the similar to that shown in Lee and Sung (2008) and Nagano and Houra (2002). The DNS results can be more accurate in the wall vicinity than the actual x-wire measurements.

The equivalent Castillo/George scaling for  $\overline{u^2}$  is freestream velocity,  $U_e^2$ , as shown in Castillo, Seo et al, 2002 and in Section 5.1.3. This is applied to Flow A in Figure 6.12 and Flow B in Figure 6.13. Whilst it is difficult, with these results, to definitively say that  $U_e^2$  generates a better collapse in the APG equilibrium region, it is clear that there is a difference between those profiles before and those within the APG equilibrium region. Particularly evident when observing frame (a) in each figure is that two groupings of profiles are distinguishable. This occurs because the  $y$  location of the peak value is shifting away from the wall with the downstream location.

Before the equilibrium region for Flows A and B, the maximum normal stress occurs at a  $y/\delta \approx 0.1$ , as evident by the peak in Figure 6.12(b) and Figure 6.13(b). However, in the APG equilibrium region this peak is not as sharp and it has shifted further away

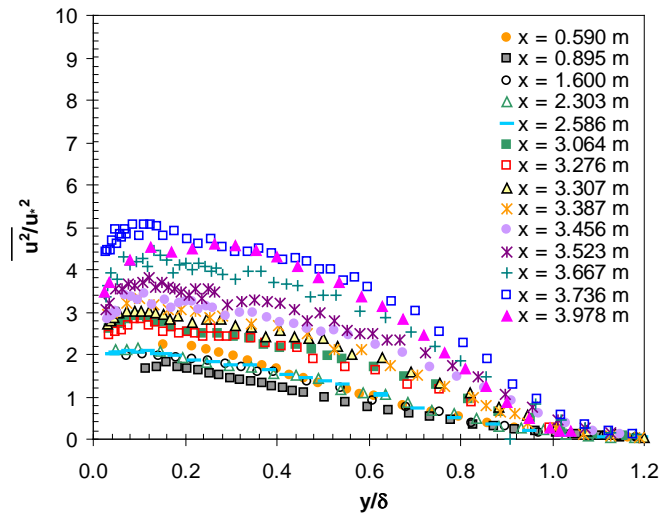
from the wall for both Flows A and Flow B, as seen in Figure 6.12(c) and Figure 6.13(c).

To scale  $\overline{u^2}$ , for flat plate boundary layer flows, Degraff and Eaton (2000) use  $u_{\tau_{\text{ref}}} U_{e_{\text{ref}}}$ , where the subscript refers to a reference location. Aubertine and Eaton (2006) applied this scale to an APG flow. They observed an inner peak and a plateau. In the flow direction, this plateau increased relative to the peak, and the inner peak decreased in magnitude. In Aubertine and Eaton (2005), the local values of freestream velocity, and friction velocity ( $U_e u_\tau$ ) are also used to scale  $\overline{u^2}$ , as seen in Figure 6.14. Here, a collapse of profiles is seen in the inner region for APG locations. This is similar to the pattern seen with Flows A and B with  $U_e^2$  scaling, particularly in Figure 6.12(c) and Figure 6.13(c), within the APG equilibrium region. The plateau clearly increases in the flow direction.

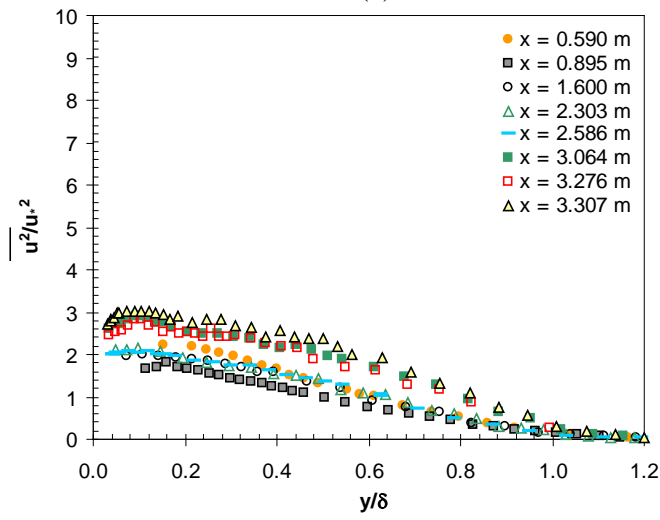
The Castillo/George method for determining the outer scale for mean velocity deficit was presented in Section 5.1.3. The outer scale for mean deficit being defined as  $U_{\text{so}} = U_e$  leads to the scaling factor for shear stress,  $\overline{uv}$ , to be  $U_e^2 \frac{d\delta}{dx}$  and normal stresses,  $\overline{u^2}$ ,  $\overline{v^2}$  to be  $U_e^2$ . If the same methodology is applied with the Zagarola/Smits scale of  $U_{\text{so}} = U_e \frac{\delta^*}{\delta}$  as the starting point, then  $U_e^2 \frac{d\delta}{dx} \left(\frac{\delta^*}{\delta}\right)^2$  would be the scale for Reynolds shear stress and  $U_e^2 \left(\frac{\delta^*}{\delta}\right)^2$  for normal stresses. However, to scale Reynolds normal stress,  $U_e^2 \left(\frac{\delta^*}{\delta}\right)$  was intuitively selected. The experimental results supported this choice, as  $U_e^2 \left(\frac{\delta^*}{\delta}\right)$  yielded a greater quality of collapse than  $U_e^2 \left(\frac{\delta^*}{\delta}\right)^2$  for  $\overline{u^2}$  and  $\overline{v^2}$ . As a result, only  $U_e^2 \left(\frac{\delta^*}{\delta}\right)$  scale is presented here, for Reynolds stresses.

Using  $U_e^2 \left( \frac{\delta^*}{\delta} \right)$  to scale  $\overline{u^2}$  with the Flow A and Flow B data, yields good results. A collapse of profiles is achieved in the APG equilibrium region, as seen in Figure 6.15(c) and Figure 6.16(c). The increase in magnitude in the flow direction seen with the other scaling factors is no longer present.

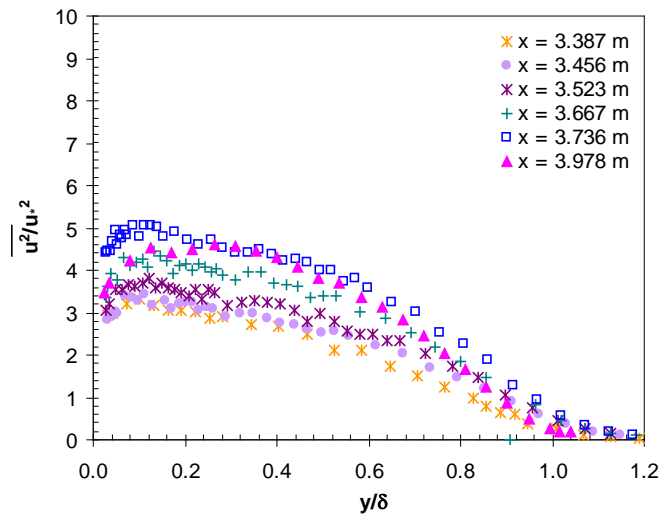
The results for quality of collapse are given in Table 6.2. Consistently, with any of the three scales,  $u_*^2$ ,  $U_e^2$  or  $U_e^2(\delta^*/\delta)$ , the quality of collapse is greater in the APG equilibrium region. Comparing the three scales,  $U_e^2(\delta^*/\delta)$  yields the best collapse of profiles. This result adds to the strength of the previously defined APG equilibrium concept. Within the APG equilibrium region the quality of collapse for Flow A is 89% and Flow B is 77%. Recalling that we earlier defined a ‘good’ collapse based on the classical flows as 80%, the results for this scale are encouraging.



(a)



(b)



(c)

Figure 6.9 Normal stress  $\overline{u^2}$  scaled with the friction velocity  $u_*$  for Flow A. (a) All stations, (b) before APG equilibrium region, and (c) APG equilibrium region.

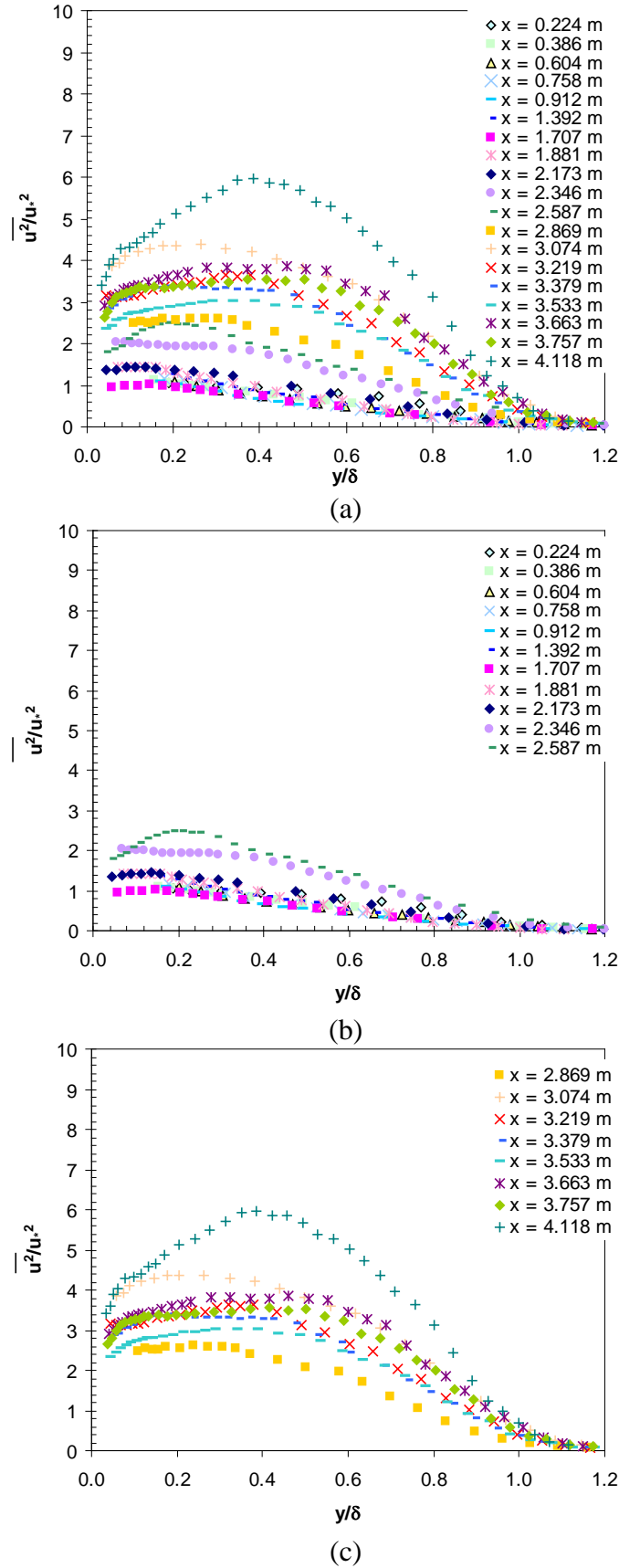


Figure 6.10 Normal stress  $\overline{u^2}$  scaled with the friction velocity  $u_*^2$  for Flow B. (a) All stations, (b) before APG equilibrium region, and (c) APG equilibrium region.

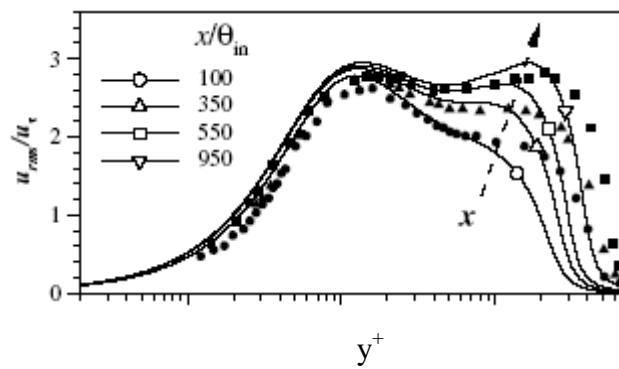


Figure 6.11 DNS results of Sung and Lee (solid line) and experimental results of Nagano et al (1992) (solid symbols) for  $u_{rms}$  scaled with  $u_*$ . The arrow indicates the streamwise direction and highlights the shift in the  $y$  location of the peak. (Figure 10a of Lee and Sung, 2008, p 573)

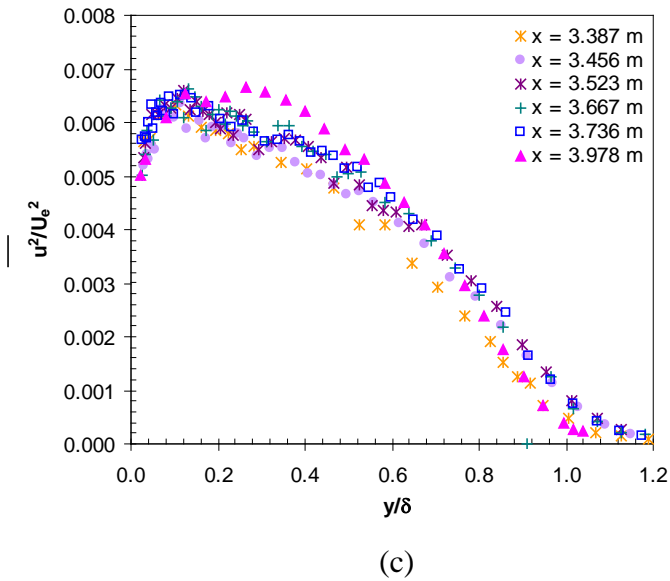
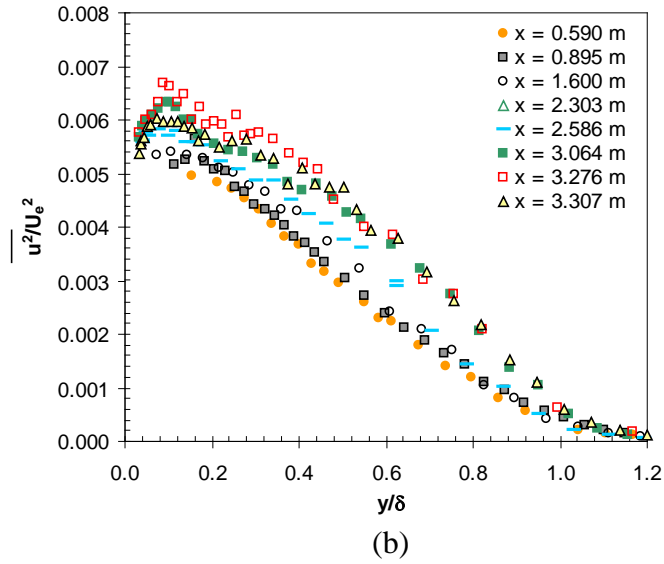
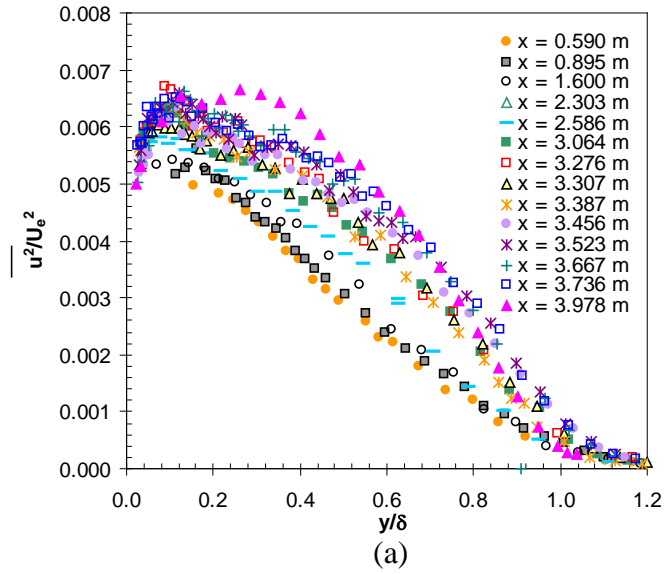


Figure 6.12 Normal stress  $\overline{u^2}$  scaled with the Castillo/George scaling, freestream velocity  $U_e^2$  for Flow A. (a) All stations, (b) before APG equilibrium region, and (c) APG equilibrium region.

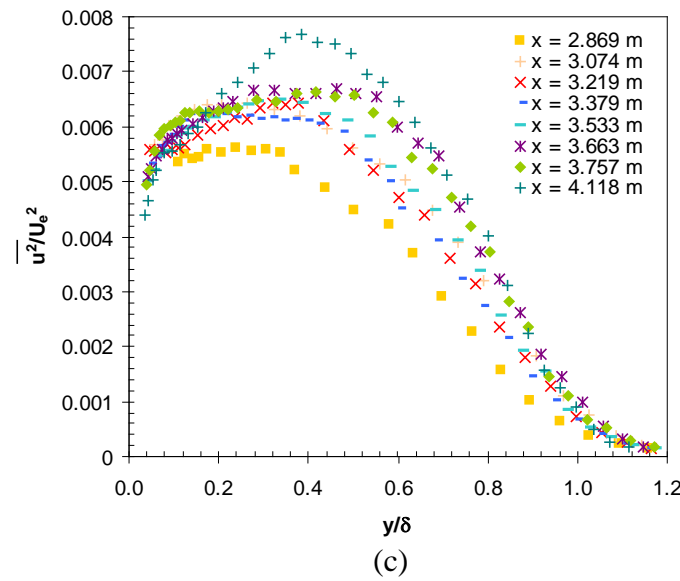
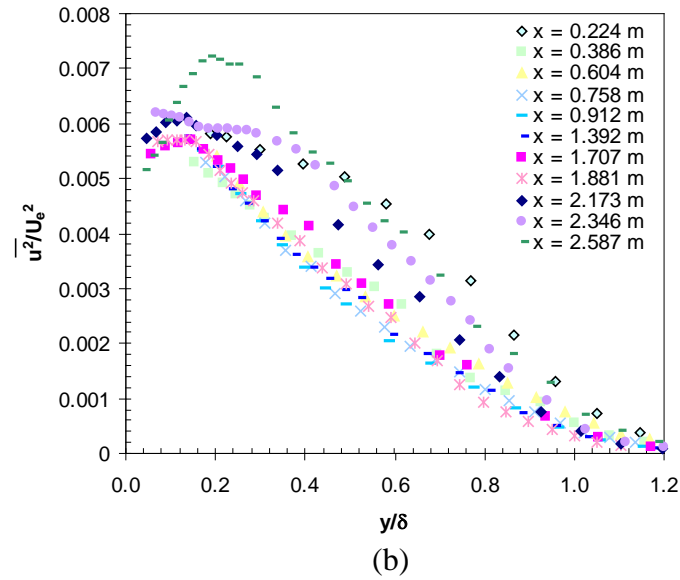
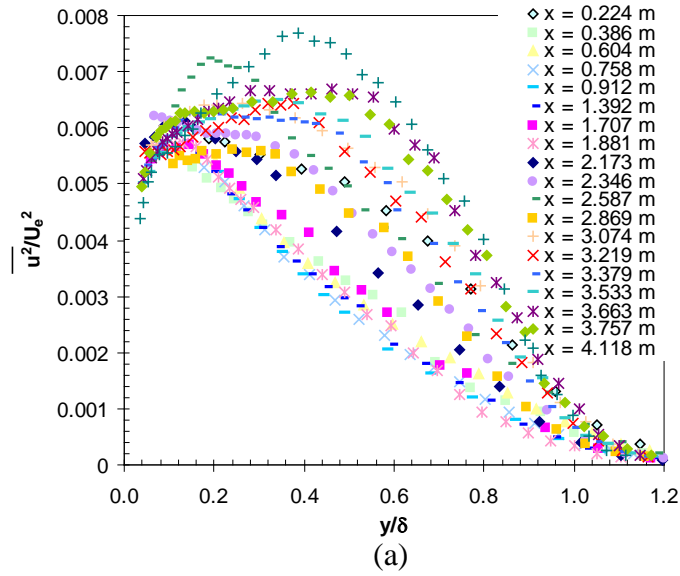


Figure 6.13 Normal stress  $\overline{u^2}$  scaled with the Castillo/George scaling, the freestream velocity  $U_e^2$  for Flow B. (a) All stations, (b) before APG equilibrium region, and (c) APG equilibrium region.

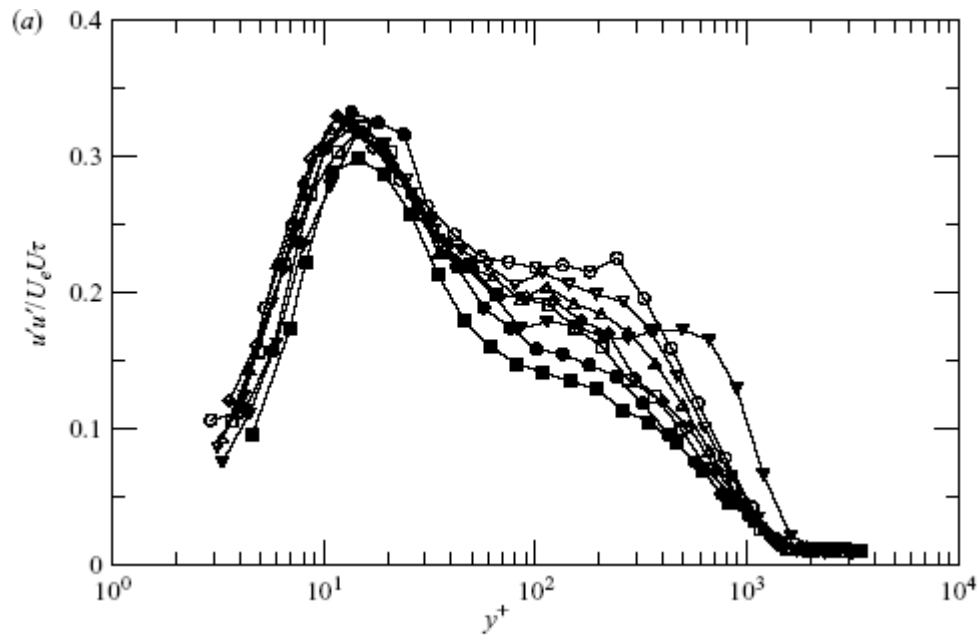
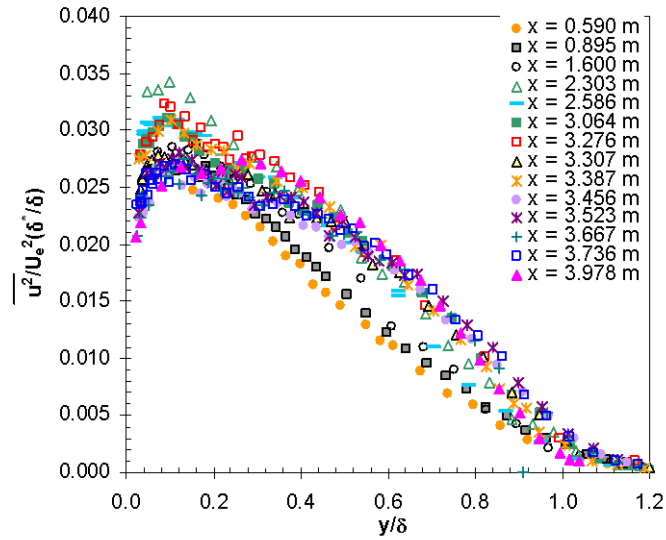
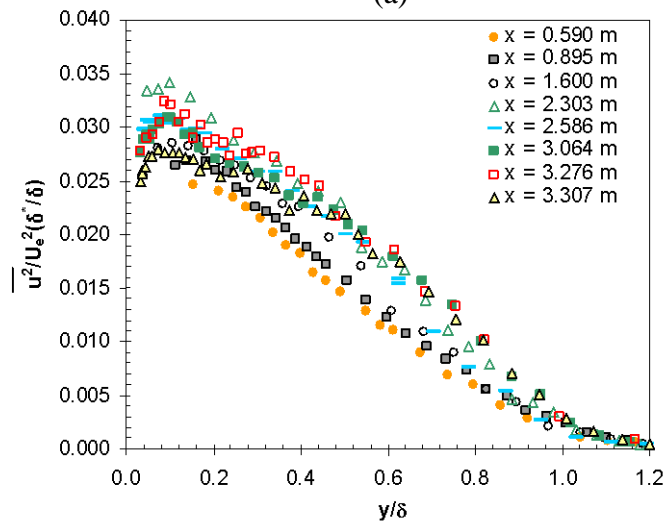


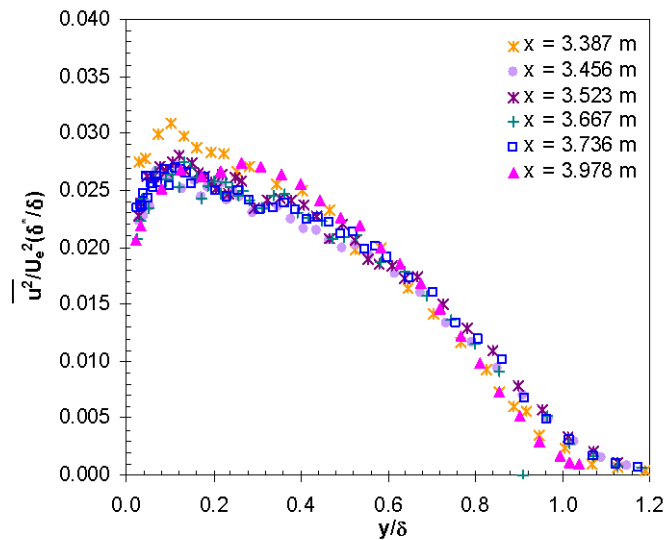
Figure 6.14 Reynolds stress  $\overline{u'u'}$  scaled with  $U_e u_\tau$  (Figure 7(a) of Aubertine and Eaton (2005))



(a)

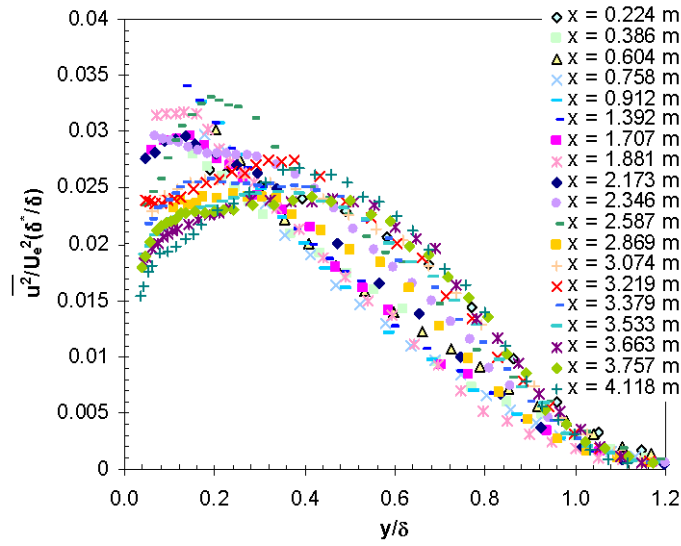


(b)

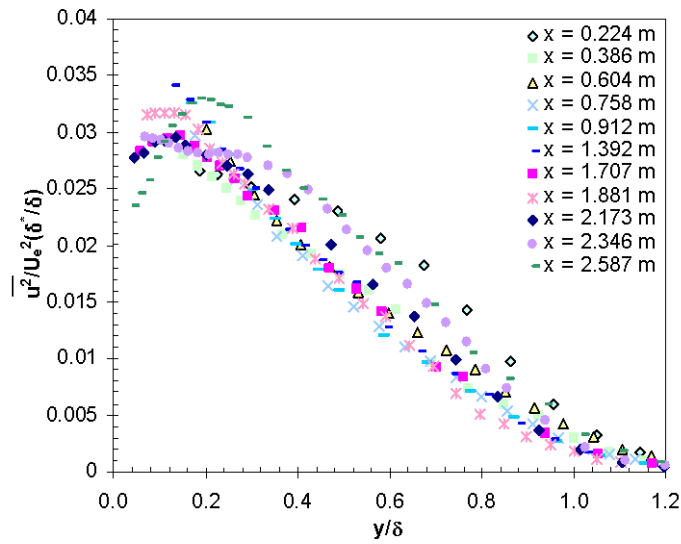


(c)

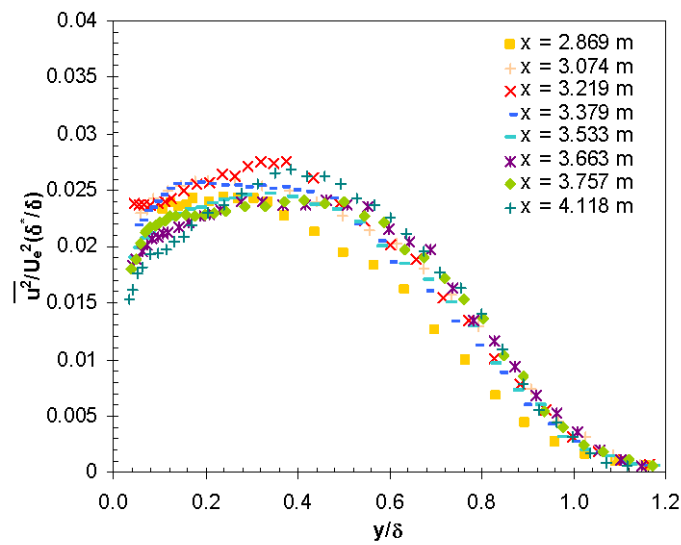
Figure 6.15 Normal stress  $\overline{u^2}$  scaled with the Zagarola/Smits scaling,  $U_e^2(\delta^*/\delta)$  for Flow A. (a) All stations, (b) before APG equilibrium region, and (c) APG equilibrium region.



(a)



(b)



(c)

Figure 6.16 Normal stress scaled  $\overline{u^2}$  with the Zagarola/Smits scaling,  $U_e^2(\delta^*/\delta)$  for Flow B. (a) All stations, (b) before APG equilibrium region, and (c) APG equilibrium region.

**Table 6.2** Quality of collapse for  $\overline{u^2}$  (Average from  $y/\delta = 0.2, 0.4, 0.6$  and  $0.8$ )

		All profiles	APG equilibrium region
$\overline{u^2}/u_*^2$	Flow A	26 %	58 %
$\overline{u^2}/u_*^2$	Flow B	13 %	52 %
$\overline{u^2}/U_e^2$	Flow A	50 %	79 %
$\overline{u^2}/U_e^2$	Flow B	42 %	72 %
$\overline{u^2}/U_e^2(\delta^*/\delta)$	Flow A	64 %	89 %
$\overline{u^2}/U_e^2(\delta^*/\delta)$	Flow B	54 %	77 %

### 6.1.3 Scaling normal stress in the y direction, $\overline{v^2}$ , with $u_*^2$ , $U_e^2$ and $U_e^2 \delta^*/\delta$

In this sub-section, the scaling of the normal stress in the y-direction,  $\overline{v^2}$  is discussed. The scaling parameters used are the same as those applied in the previous section for  $\overline{u^2}$ . The friction velocity,  $u_*^2$ , the Castillo/George scaling of freestream velocity,  $U_e^2$  and the Zagarola/Smits scaling of  $U_e^2 \delta^*/\delta$  are applied to Flow A and Flow B. The results are discussed in comparison to other published normal stress data.

Lee and Sung (2008) found that when  $\sqrt{\overline{v^2}}$  was scaled with the local friction velocity, the peak value increased in magnitude. In addition, the y location of the peak moved away from the wall in the streamwise direction, as indicated by the arrow in Figure 6.17. The data of Nagano et al (1992) are also supplied in this figure demonstrating the agreement between the DNS results and experimentally obtained values of  $\sqrt{\overline{v^2}}$ . The results of Aubertine and Eaton (2006) also demonstrate a peak that increases in magnitude and moves away from the wall.

For Flow A and B,  $\overline{v^2}$  scaled with  $u_*^2$  is presented in Figure 6.18 and Figure 6.19, respectively. The vertical scale is the same as that used for  $\overline{u^2}$  to demonstrate the reduced magnitude here. The profiles before the APG equilibrium region behave the same way as the flows reported above, in that the peak magnitude increases in the flow direction, (as represented by arrows in Figure 6.18(b) and Figure 6.19(b)). With the APG equilibrium region the peak magnitude increases, but it remains steady in relation to the wall at approximately  $y/\delta = 0.3$  for Flow A and  $y/\delta = 0.35$  for Flow B, as shown in Figure 6.18(c) and Figure 6.19(c) respectively. A steady peak is also reported by Skare (1993) at  $y/\delta = 0.45$  who also claims the small degree of separation of the profiles constitutes a collapse and demonstrates equilibrium.

Similar traits are evident when Flows A and B are scaled with the Castillo/George scale of freestream velocity, namely that before the APG equilibrium region, the peak increases in magnitude and moves away from the wall. Within the APG equilibrium

region, the peak is still increasing in magnitude but its location in relation to the wall has stabilised, as shown in Figure 6.20 and Figure 6.21.

When Z/S scaling  $,U_e^2\delta^*/\delta$  is applied to Flows A and B, a collapse is achieved in the equilibrium region, as shown in Figure 6.22 and Figure 6.23. It is no longer possible to perceive a succession in the profiles related to the streamwise direction.

The results are summarised in Table 6.3 where the quality of collapse values are given. Consistently with all scaling parameters, a better collapse of profiles is evident within the APG equilibrium region. Again here, as with  $\overline{u^2}$  the Zagarola/Smits scaling yields the best quality of collapse, In the APG equilibrium region the quality of collapse for  $\overline{v^2}/U_e^2(\delta^*/\delta)$  for Flow A is 92% and for Flow B is 87%.

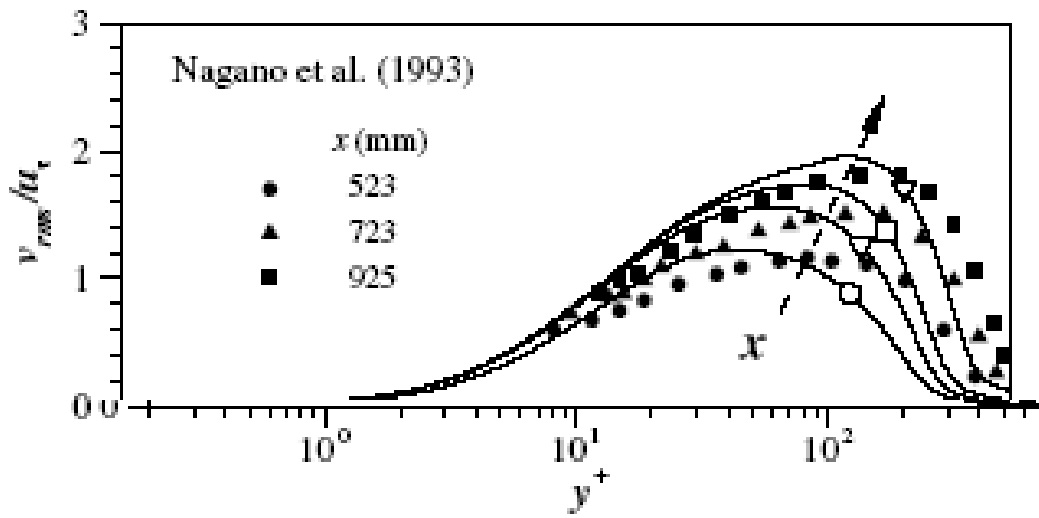


Figure 6.17  $v_{rms}$  scaled with friction velocity. The symbols represent the data of Nagano et al (1992) while the solid lines are the DNS results of Lee and Sung (2008). The arrow indicates the streamwise direction. (Figure 10(a) of Lee and Sung, 2008, p 573)

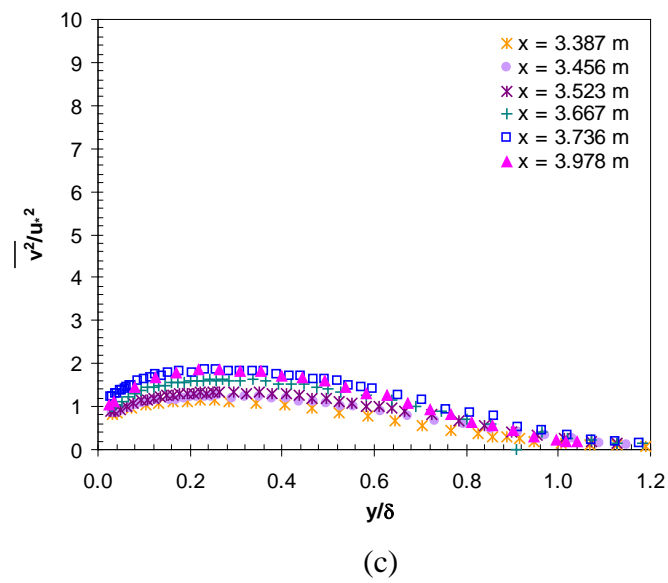
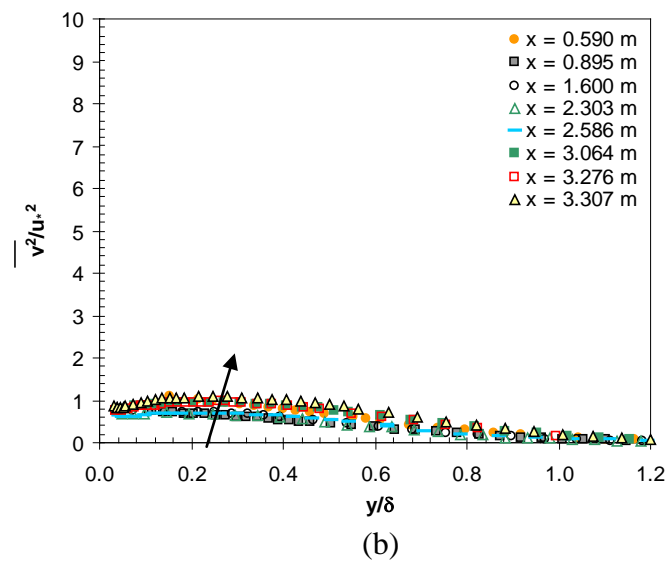
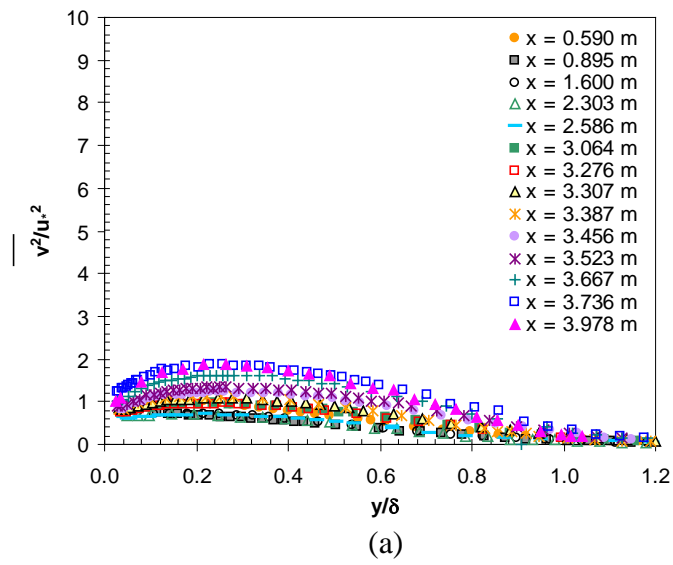


Figure 6.18 Normal stress  $\overline{v^2}$  scaled with the friction velocity,  $u_*^2$  for Flow A. (a) All stations, (b) before APG equilibrium region, and (c) APG equilibrium region.

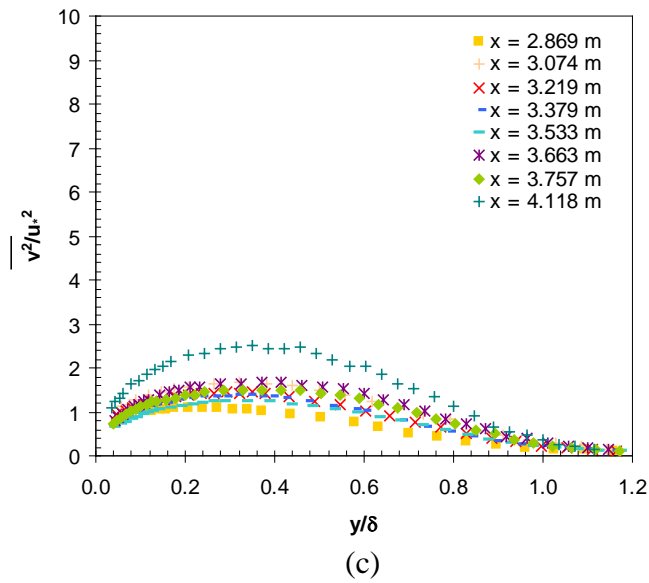
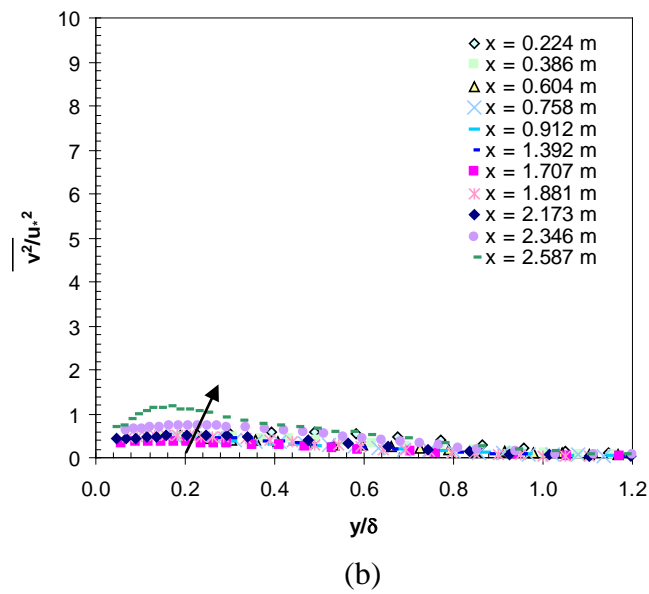
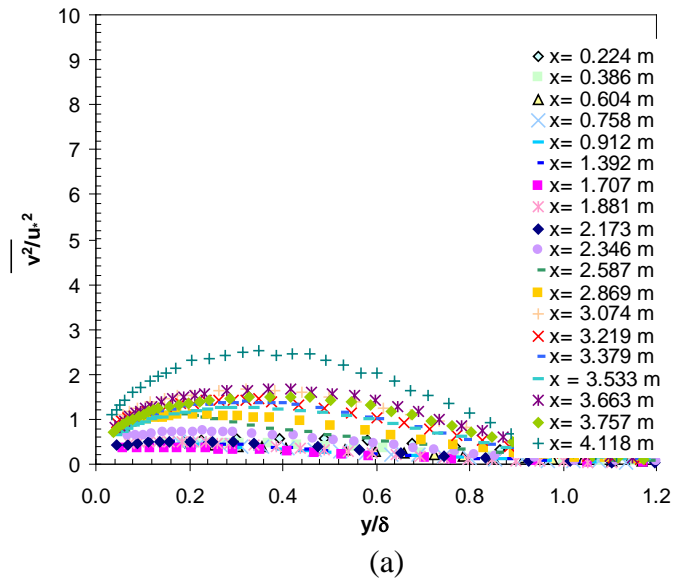
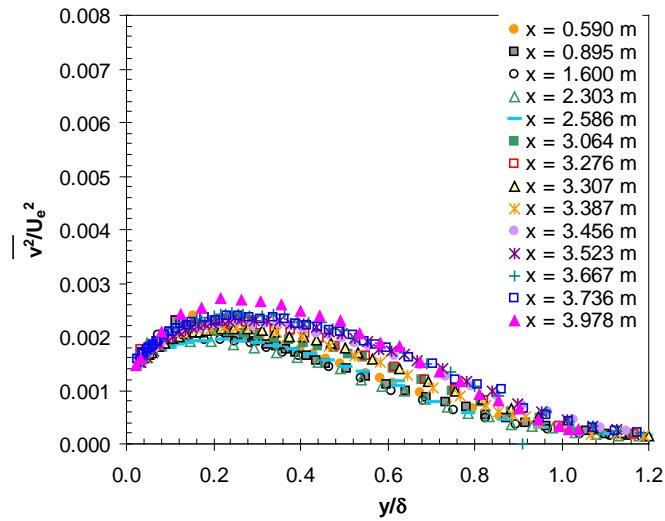
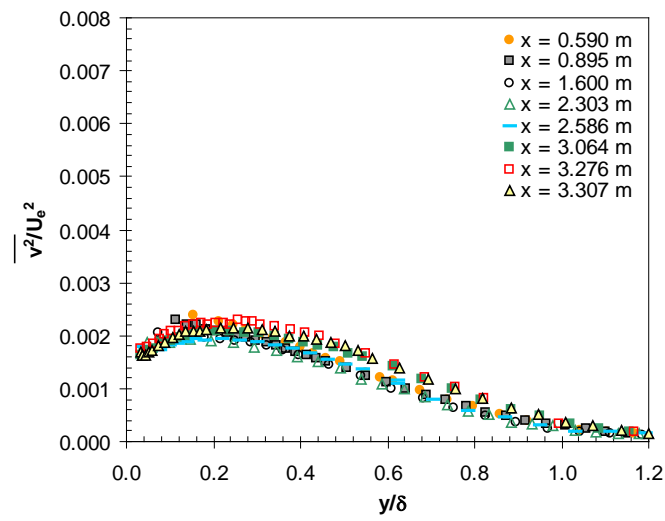


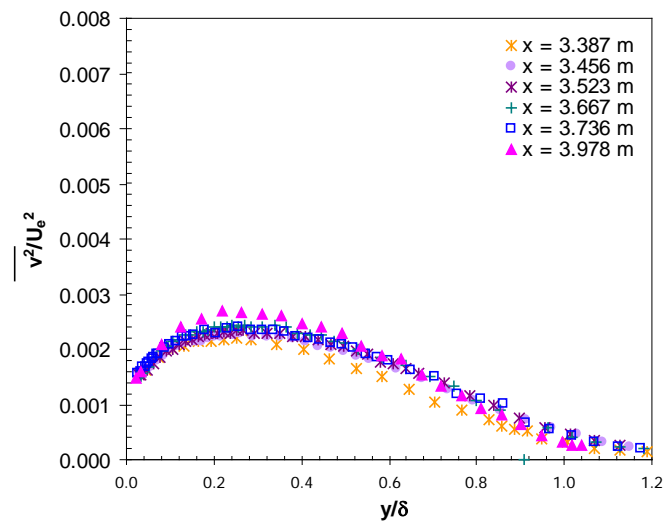
Figure 6.19 Normal stress  $\overline{v^2}$  scaled with the friction velocity,  $u_*^2$  for Flow B. (a) All stations, (b) before APG equilibrium region, and (c) APG equilibrium region.



(a)



(b)



(c)

Figure 6.20 Normal stress  $\overline{v^2}$  scaled with the freestream velocity,  $U_e^2$  for Flow A. (a) All stations, (b) before APG equilibrium region, and (c) APG equilibrium region.

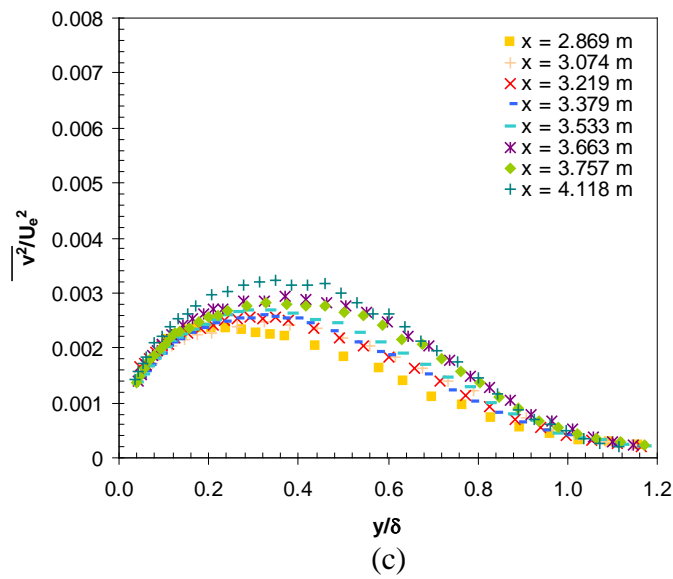
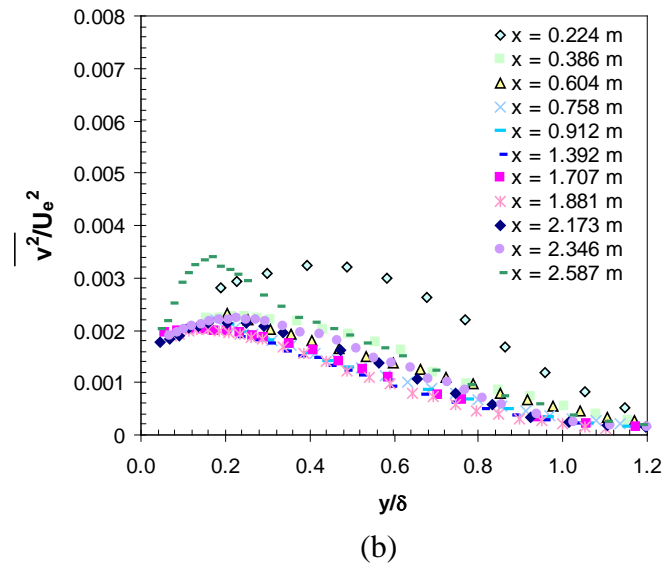
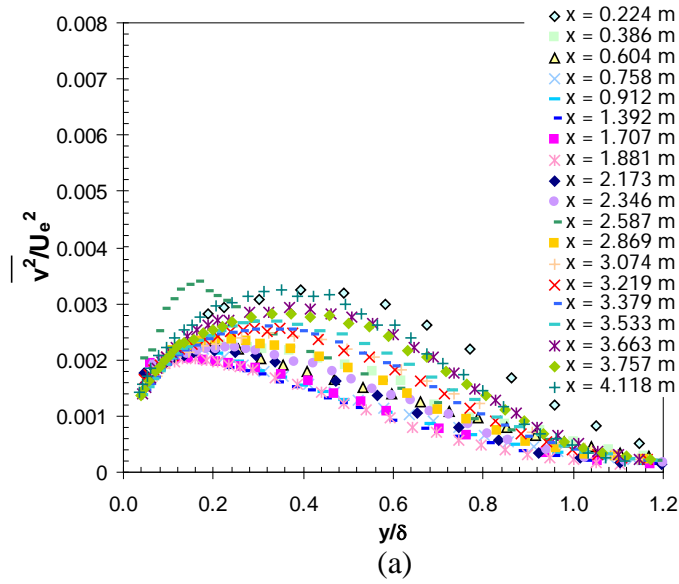
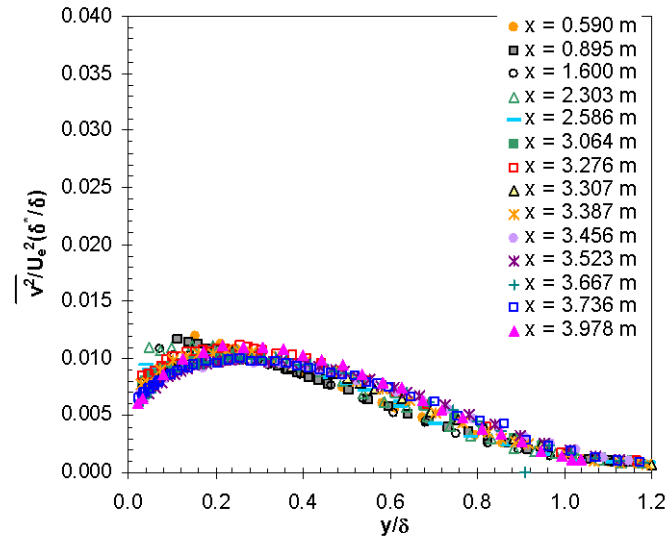
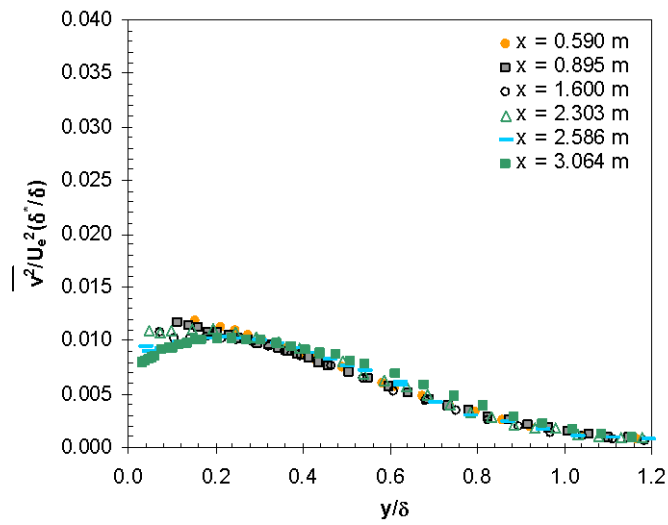


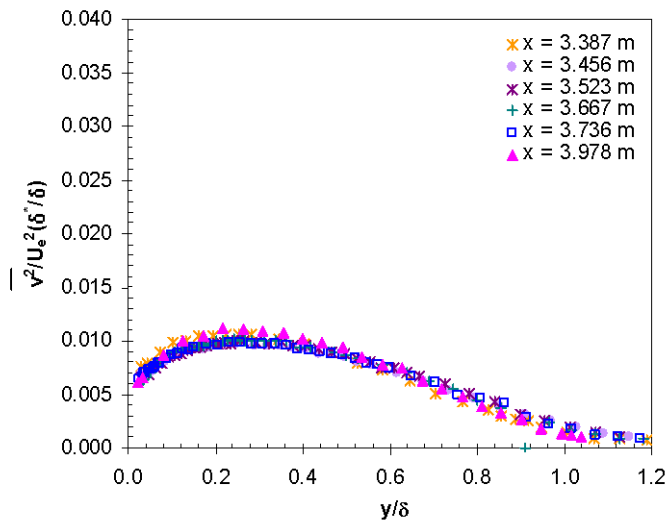
Figure 6.21 Normal stress  $\overline{v^2}$  scaled with the freestream velocity,  $U_e^2$  for Flow B. (a) All stations, (b) before APG equilibrium region, and (c) APG equilibrium region.



(a)

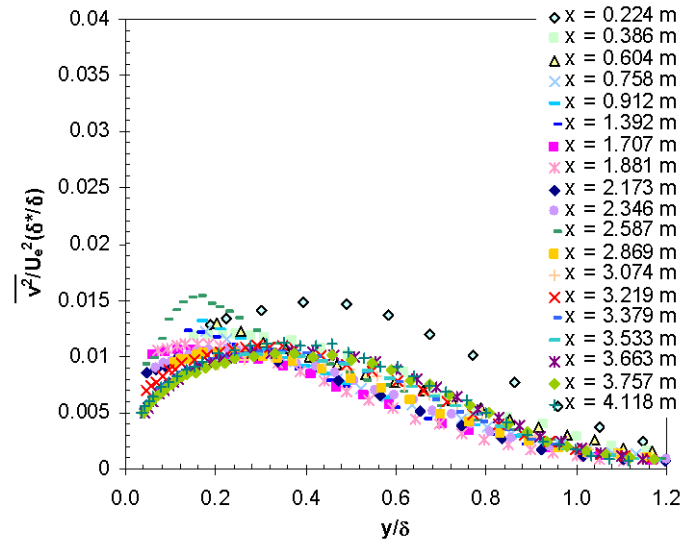


(b)

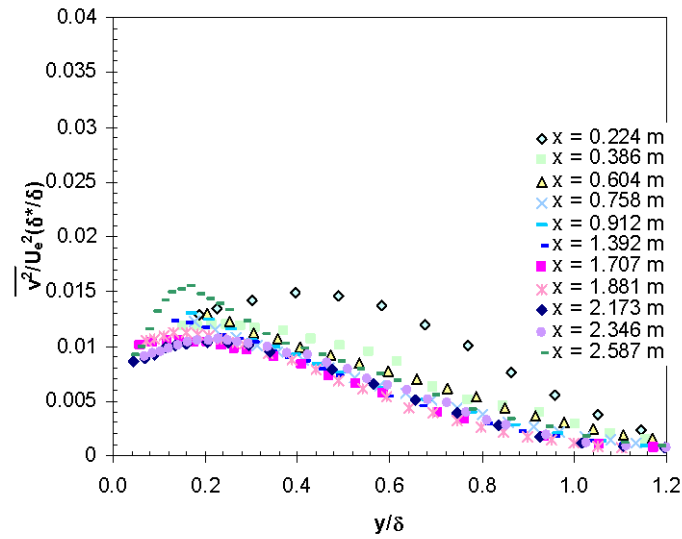


(c)

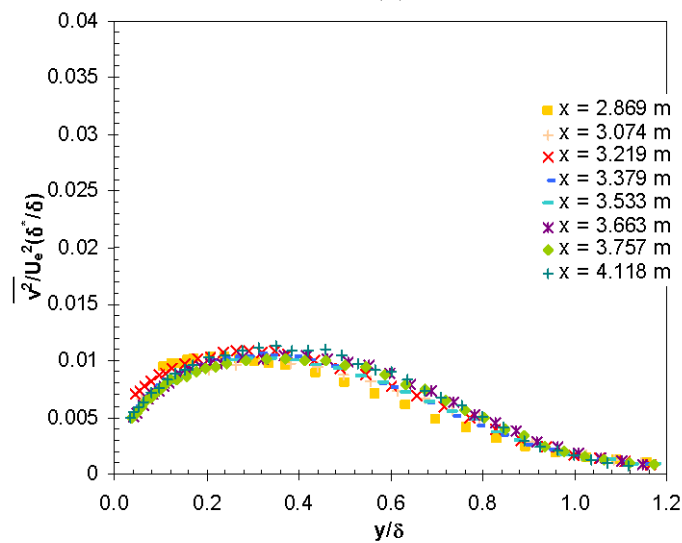
Figure 6.22 Normal stress  $\overline{v^2}$  scaled with Zagarola/Smits scaling,  $U_e^2(\delta^*/\delta)$  for (a) Flow A, (b) Before APG equilibrium region, (c) APG equilibrium region.



(a)



(b)



(c)

Figure 6.23 Normal stress  $\overline{v^2}$  scaled with Zagarola/Smits scaling,  $U_e^2(\delta^*/\delta)$  for Flow B. (a) All stations, (b) before APG equilibrium region, and (c) APG equilibrium region.

**Table 6.3** Quality of collapse for  $\overline{v^2}$  (Average from  $y/\delta = 0.2, 0.4, 0.6$  and  $0.8$ )

		All profiles	APG equilibrium region
$\overline{v^2}/u_*^2$	Flow A	32 %	65 %
$\overline{v^2}/u_*^2$	Flow B	21 %	66 %
$\overline{v^2}/U_e^2$	Flow A	64 %	78 %
$\overline{v^2}/U_e^2$	Flow B	42 %	71 %
$\overline{v^2}/U_e^2(\delta^*/\delta)$	Flow A	77 %	92 %
$\overline{v^2}/U_e^2(\delta^*/\delta)$	Flow B	50 %	87 %

#### 6.1.4 Scaling normal stress in the z direction, $\overline{w^2}$

Little information is available on  $\overline{w^2}$  in the literature. Of the 22 flows examined here, only Flow 141, Skare and L&S have published  $\overline{w^2}$  data. In general,  $\overline{w^2}$  exhibits a similar profile to  $\overline{v^2}$  with a slightly higher magnitude.

As with  $\overline{v^2}$  scaled with friction velocity, a collapse of profiles with some scatter, peaking at  $y/\delta \cong 0.45$ , is reported by Skare (1993). Likewise, Lee and Sung (2008) found similar behaviour between  $\overline{v^2}$  and  $\overline{w^2}$ , scaled with friction velocity. For both quantities, the peak increased in magnitude and moved away from the wall.

For Flow 141, the  $\overline{w^2}$  behaviour is between the two previously mentioned flows in that when scaled with the local freestream velocity, the first 3 profiles collapse. Then, the peak increases in magnitude and moves away from the wall, as shown in Appendix X, Figure 10.7.

For Flow A, two profiles of  $\overline{w^2}$  scaled with  $u_*^2$  are given in Figure 6.24. They exhibit the general behaviour of being similar in shape to  $\overline{v^2}$  with slightly higher magnitude. With only two profiles, it is not possible to draw conclusions about collapses or shifting peaks. They are given here for thoroughness and to confirm estimates used for calculating the energy budgets.

#### 6.1.4.1 Estimating $\overline{w^2}$ , $\overline{uw^2}$ and $\overline{vw^2}$ for energy budgets

The normal stress in the z direction,  $\overline{w^2}$ , was not measured for all stations in these experiments. However,  $\overline{w^2}$  is required when calculating advection and dissipation. Commonly,  $\overline{w^2}$  is modelled as  $\overline{w^2} = K(\overline{u^2} + \overline{v^2})$  (Cutler and Johnston, 1989) where  $K = 0.5$ . Skare found  $K = 0.4$  to be a better estimate. In Figure 6.25  $\overline{w^2}$  is plotted measured with a rotated x-wire probe, compared with  $K(\overline{u^2} + \overline{v^2})$ . In this case,  $K = 0.3$  gives a good match. This is also the case with  $\overline{uw^2}$  which is well modelled by  $K(\overline{u^3} + \overline{uv^2})$  with  $K = 0.3$ , as presented in Figure 6.26.

To calculate the turbulent kinetic energy balance the term,  $\overline{vw^2}$  is also required. This term could not be measured, but it is often modelled by  $\overline{vw^2} = K(\overline{u^2v} + \overline{v^3})$ . The recommended value of  $K$  is again 0.5. However, Anderson and Eaton (1989) report that this value tends to over estimate  $\overline{vw^2}$ . As  $K = 0.3$  gave a better representation in the previously two mentioned cases, it is again applied here.

Skare applied the gradient diffusion hypothesis suggested by Daly and Harlow (1970) where the correlation is modelled as follows:

$$\overline{u_i u_j u_k} = -C_s \frac{k}{\varepsilon} \left( \overline{u_k u_i} \frac{\partial \overline{u_j}}{\partial x_i} \right) \quad \text{Equation 6-4}$$

where  $\overline{u_i u_j u_k}$  is an un-measurable triple correlation of velocity components,  $C_s$  is a constant taken to be 0.22, and  $\varepsilon$  is the rate of dissipation, [ $m^2/s^3$ ].

For  $\overline{uv^2}$  Equation 6-4 becomes:

$$\overline{uv^2} = -C_s \frac{k}{\varepsilon} \left( \overline{u^2} \frac{\partial \overline{v^2}}{\partial x} + \overline{uv} \frac{\partial \overline{v^2}}{\partial y} \right) \quad \text{Equation 6-5}$$

where  $u$  refers to velocity in the x direction, [m/s],  
 $v$  refers to velocity in the y direction, [m/s],

x is the streamwise distance, [m] , and

y is the height, [m].

Skare used this method to estimate the measurable term  $\overline{uv^2}$  . The dissipation rate,  $\varepsilon$ , used was determined from the isotropic turbulence assumption and from the inertial sub-range. In both cases  $\overline{uv^2}$  was over estimated by a factor of 2 to 3.

To avoid applying an estimate that relies on the calculation of the dissipation rate, the more conventional  $\overline{vw^2} = K(\overline{u^2v} + \overline{v^3})$  is used here with  $K = 0.3$ .

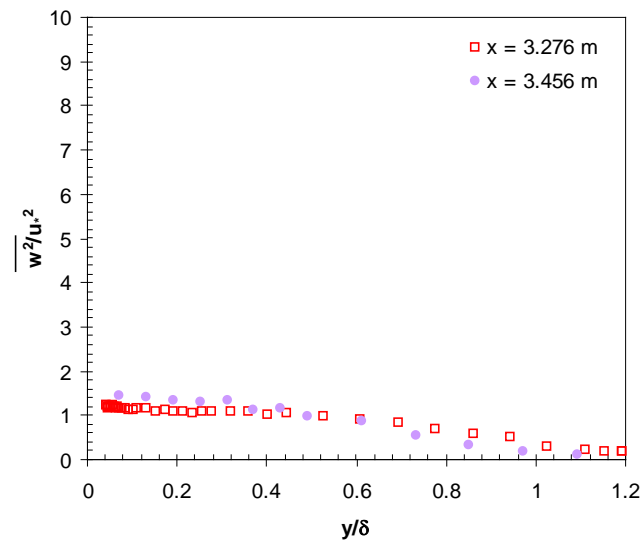


Figure 6.24 Normal stress  $\overline{w^2}$  scaled with friction velocity,  $u_*^2$  for 2 locations in Flow A.

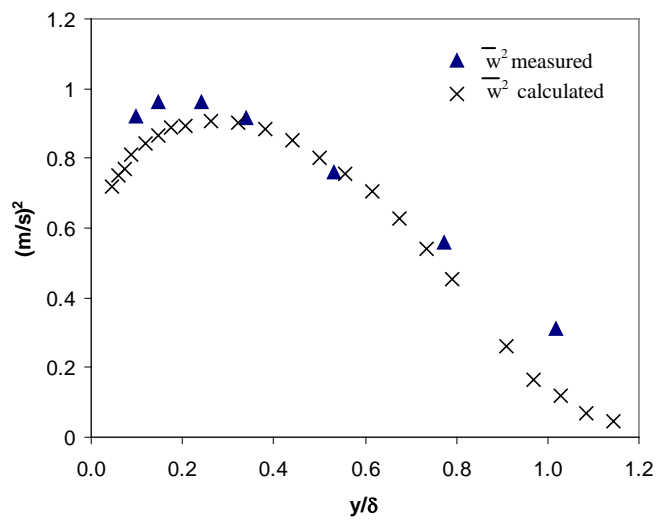


Figure 6.25 Comparison between measured  $\overline{w^2}$  and the estimate  $\overline{w^2} = 0.3(\overline{u^2} + \overline{v^2})$ .

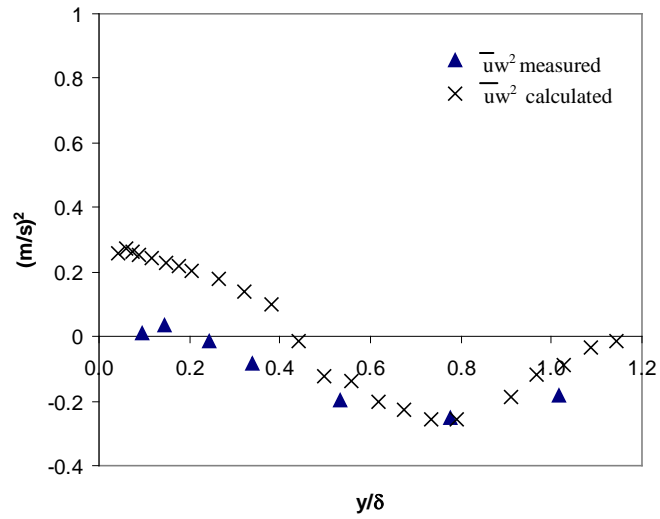


Figure 6.26 Comparison between measured  $\overline{uw^2}$  and the estimate  $\overline{uw^2} = 0.3(\overline{u^3} + \overline{uv^2})$ .

### 6.1.5 Scaling shear stress, $\overline{uw}$ with $u_*^2$

The lateral shear stress  $\overline{uw}$  should be zero in a 2-dimensional flow. However, experimentally, it is expected to be small, due to the difficulty in measuring a zero quantity, and that in reality a flow is rarely completely 2-dimensional. Skare found scatterly results with the value of  $\overline{uw}$  being approximately 20% of  $\overline{uv}$ .

To measure lateral shear stress an x-wire probe was rotated, on its axis, by 90 degrees. Vertical traverses were performed at two streamwise locations for Flow A. These results, scaled with friction velocity,  $u_*^2$  are given in Figure 6.27. The values are scattered but close to zero, at the peak  $\frac{\overline{uw}}{u_*^2}$  for one station ( $x = 3.276$  m) is 16% of  $\frac{\overline{uv}}{u_*^2}$  and 50% for the other station ( $x = 3.456$  m).

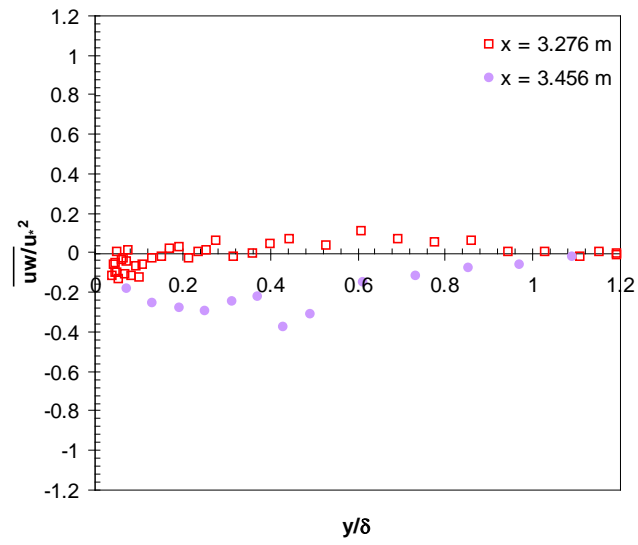


Figure 6.27 Lateral shear stress  $\overline{uw}$  scaled with friction velocity,  $u_*^2$  for 2 locations of Flow A.

## 6.2 Higher order moments.

The measured triple correlations in the xy plane are  $\overline{u^3}$ ,  $\overline{v^3}$ ,  $\overline{uv^2}$  and  $\overline{u^2v}$ . All triple correlations exhibit a harmonic variation with transverse distance, with zero values at the wall, within the boundary layer and returning to zero at the boundary layer edge. The individual patterns reported here are in agreement with the results reported by Skare.

A comparison between Skare's flow and Flows A and B is given in Appendix XI, and it is summarised briefly here. Flow Skare is an equilibrium boundary layer in a strong APG. The skin friction coefficient is kept constant. This is the most significant difference between Flows A and B and Flow Skare. The freestream velocity is of a similar magnitude. The published triple order correlations for Flow Skare provide a useful frame of reference.

$\overline{u^3}$  is the transport of the normal stress  $\overline{u^2}$  in the x direction. In Figure 6.28,  $\overline{u^3}$  is presented scaled with friction velocity,  $u_*^3$  for Flows A and B. There is a distinct difference between the shape of the curve before the APG equilibrium region (Figure 6.28(c) and Figure 6.28(d)) and in the APG region (Figure 6.28(e) and Figure 6.28(f)). The waveform is more pronounced and of a higher magnitude in the APG region.

In Figure 6.29,  $\overline{u^3}$  is presented scaled with freestream velocity,  $U_e^3$  which is the scale that Skare uses. Skare reports that  $\overline{u^3}$  values are larger than three times those of the other triple correlations (Skare, p98, 1993). This observation is consistent with the results for Flows A and B. Again, a marked difference is observed before the APG equilibrium region and within it.

$\overline{v^3}$  represents the transport of the Reynolds stress  $\overline{v^2}$  away from the wall. In Figure 6.30 and Figure 6.31,  $\overline{v^3}$  is presented as scaled with  $u_*^3$  and  $U_e^3$ , respectively. This quantity does not behave as expected. Based on Flow Skare (and others), it was anticipated that  $\overline{v^3}$  would have a waveform passing through zero at the wall, at the location of maximum stress and at the edge of the boundary layer. In both Flows A

and  $\overline{v^3}$  scaled with  $u_*$  or  $U_e$  does have a waveform, but it is displaced vertically upwards from the horizontal axis.

$\overline{uv^2}$  is the turbulent transport of  $\overline{uv}$  perpendicular to the wall. This quantity exhibits similar waveform behaviour to  $\overline{u^3}$ , as expected. In Figure 6.32 and Figure 6.33,  $\overline{uv^2}$  is presented scaled with  $u_*$  and  $U_e$ , respectively. These results are consistent with the findings of Skare. The results of Nagano and Houra (2002) demonstrate how the profiles change in the x-direction. Early in the flow, the second peak is small, almost flat, as shown in frames (c) and (d). This increases markedly downstream, as shown in frames (e) and (f). Frames (c) and (d) in Figure 6.32 and Figure 6.33 correspond to the stations before the APG equilibrium region in Flows A and B. The APG equilibrium region results are given in frames (e) and (f). The profiles of the former are flat. In the latter, the peaks have increased magnitude.

The last of the triple correlations presented here is  $\overline{u^2v}$ , which is the turbulent transport of  $\overline{u^2}$  perpendicular to the wall. In Figure 6.34 and Figure 6.35,  $\overline{u^2v}$  plots are presented scaled with  $u_*^3$  and  $U_e^3$ . This quantity also exhibits similar waveform behaviour to  $\overline{u^3}$ ; however, the sign of the peaks is reversed. In this case, a negative peak occurs in the inner half of the boundary layer, and a positive peak occurs in the outer half. This result is consistent with the findings of Lee and Sung (2008) whose results display a similar increase in magnitude of the outer peak with increasing adverse pressure gradient.

In conclusion, the higher order moments behave as expected, they will be utilised in the next chapter to calculate the energy budgets.

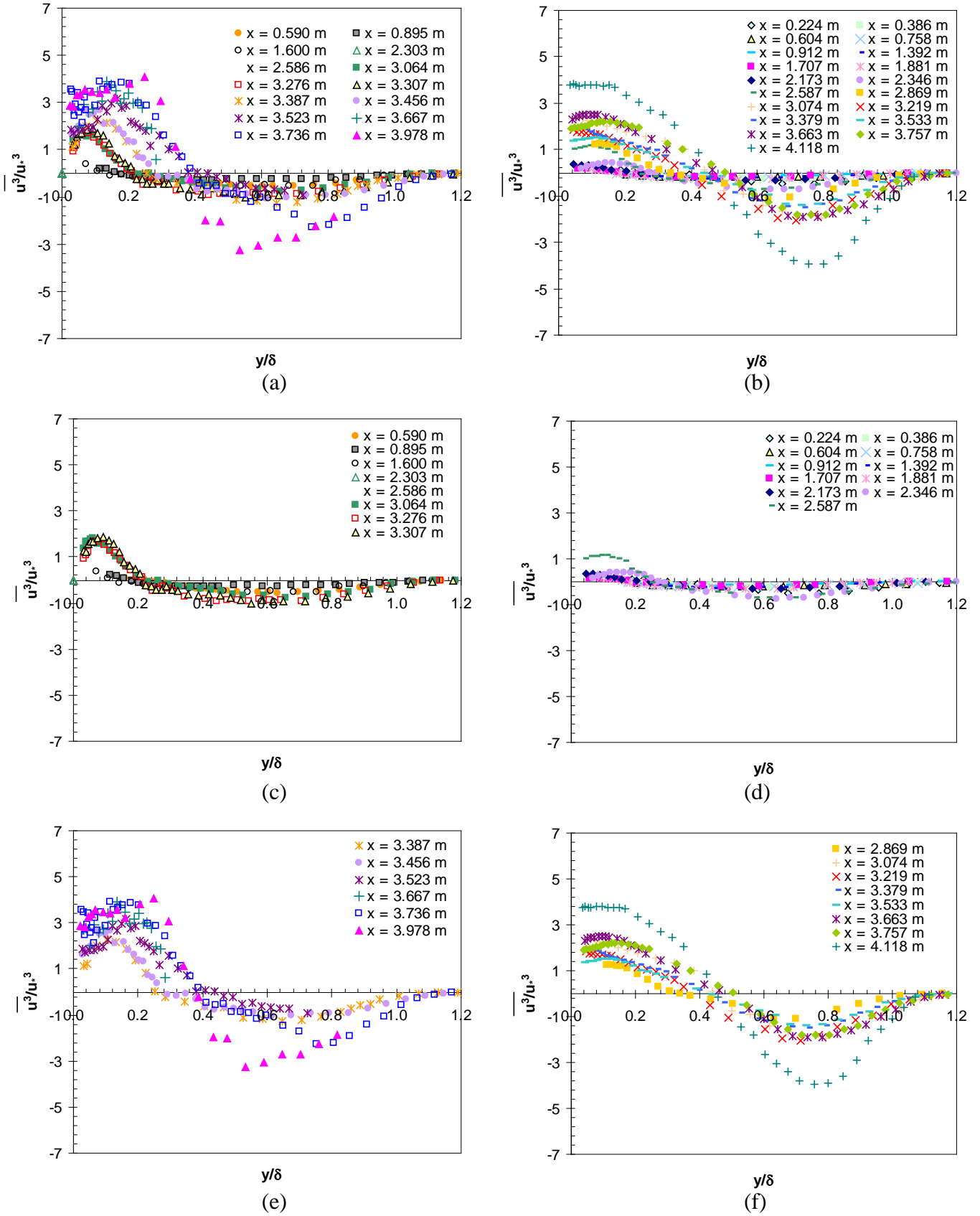


Figure 6.28  $\overline{u^3}$  scaled with friction velocity  $u_*^3$  for Flow A (left column) and Flow B (right column). (a) and (b), All stations; (c) and (d), before APG equilibrium region; (e) and (f), within the APG equilibrium region.

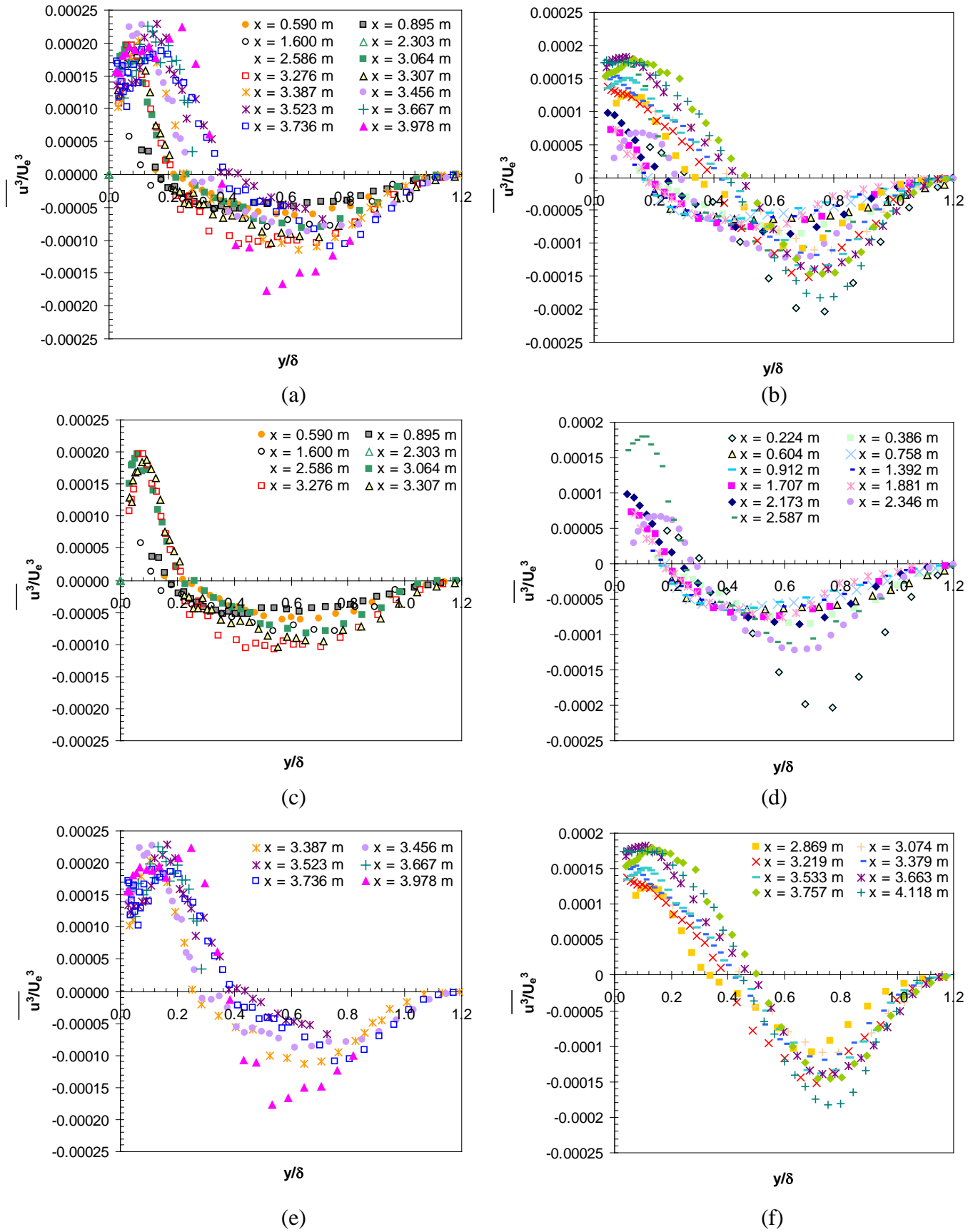


Figure 6.29  $\overline{u^3}$  scaled with freestream velocity  $U_e^3$  for Flow A (left column) and Flow B (right column). (a) and (b), All stations; (c) and (d), before APG equilibrium region; (e) and (f), within the APG equilibrium region.

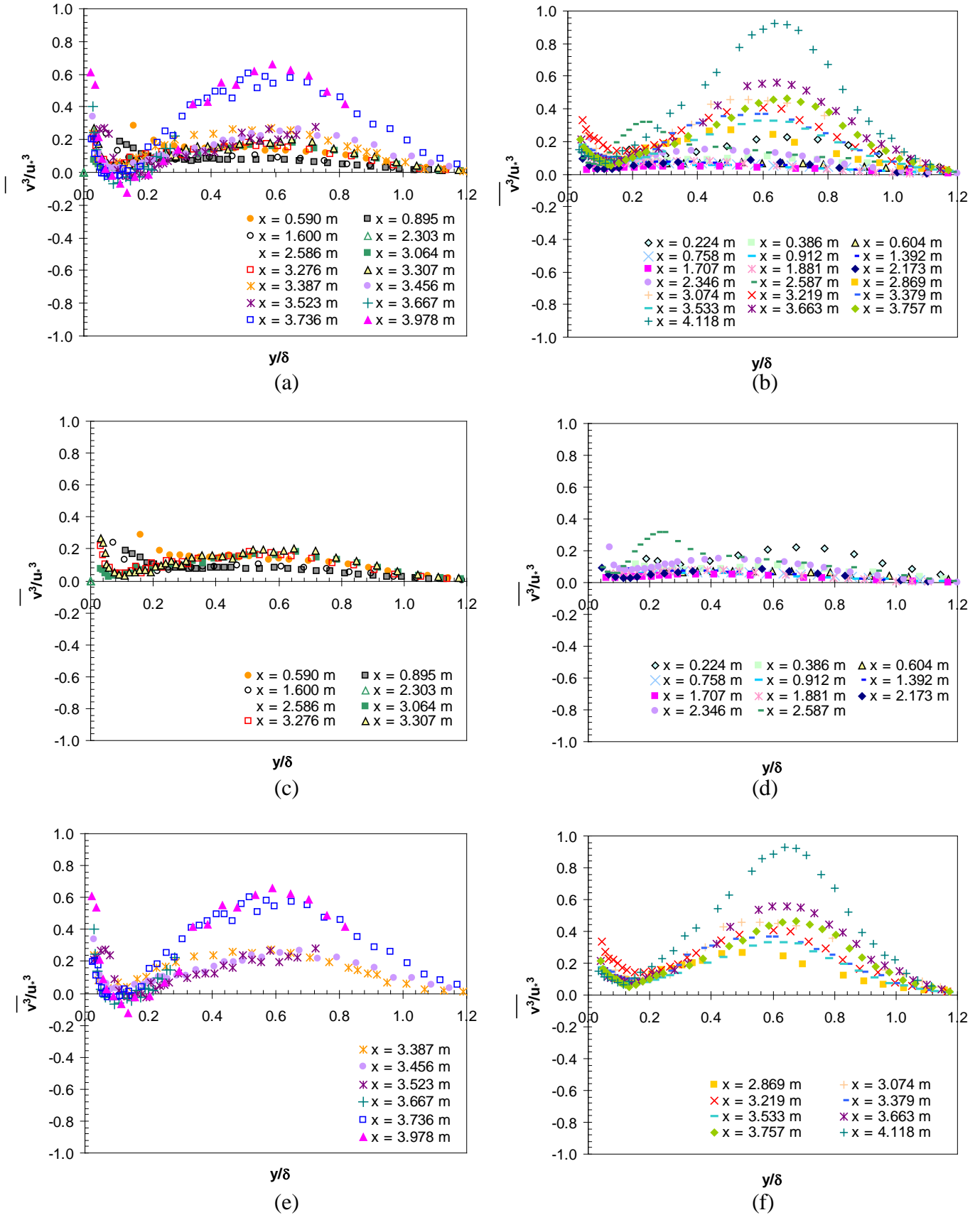


Figure 6.30  $\overline{v^3}$  scaled with friction velocity  $u_*^3$  for Flow A (left column) and Flow B (right column). (a) and (b), All stations; (c) and (d), before APG equilibrium region; (e) and (f), within the APG equilibrium region.

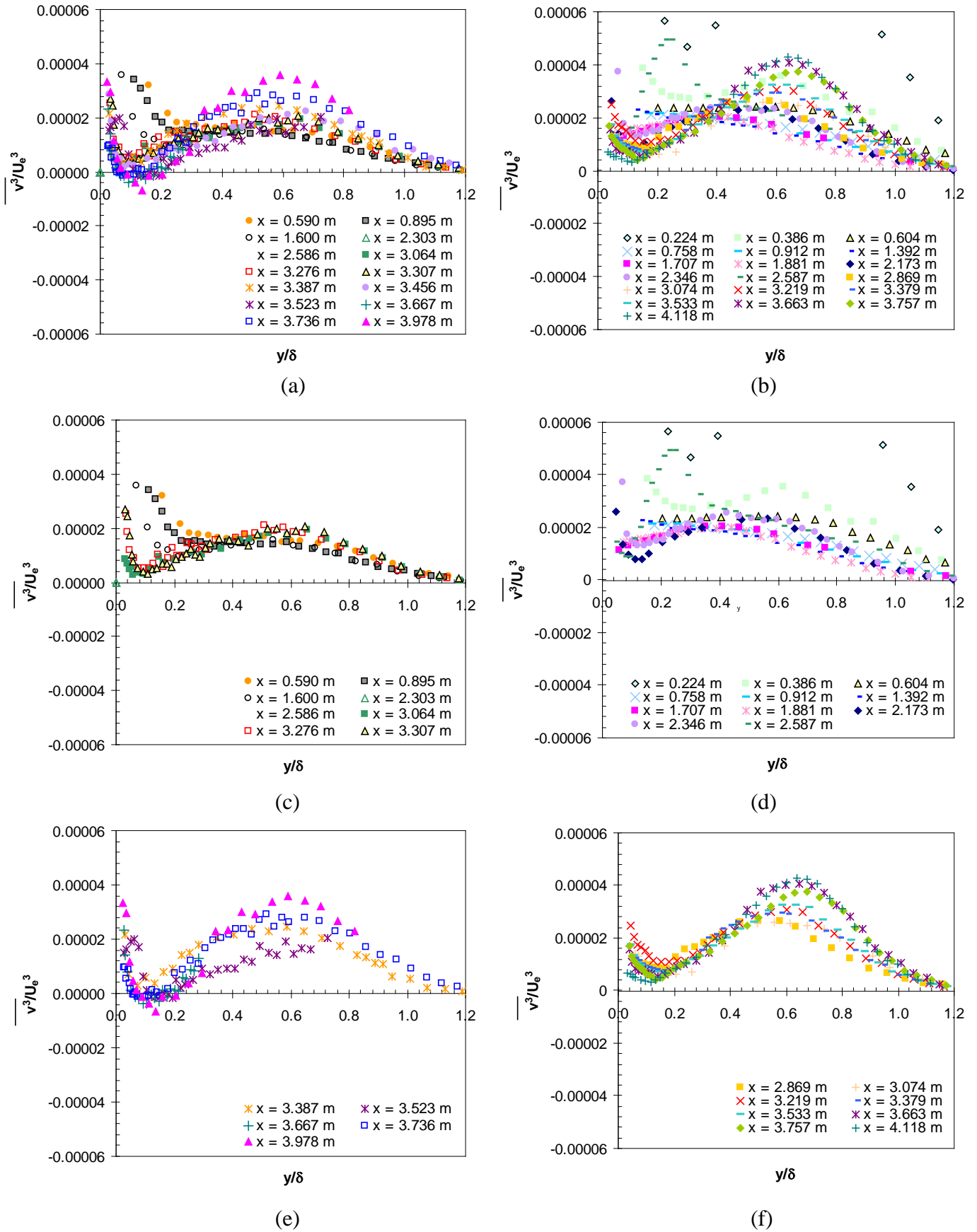


Figure 6.31  $\overline{v^3}$  scaled with freestream velocity  $U_e^3$  for Flow A (left column) and Flow B (right column). (a) and (b), All stations; (c) and (d), before APG equilibrium region; (e) and (f), within the APG equilibrium region.

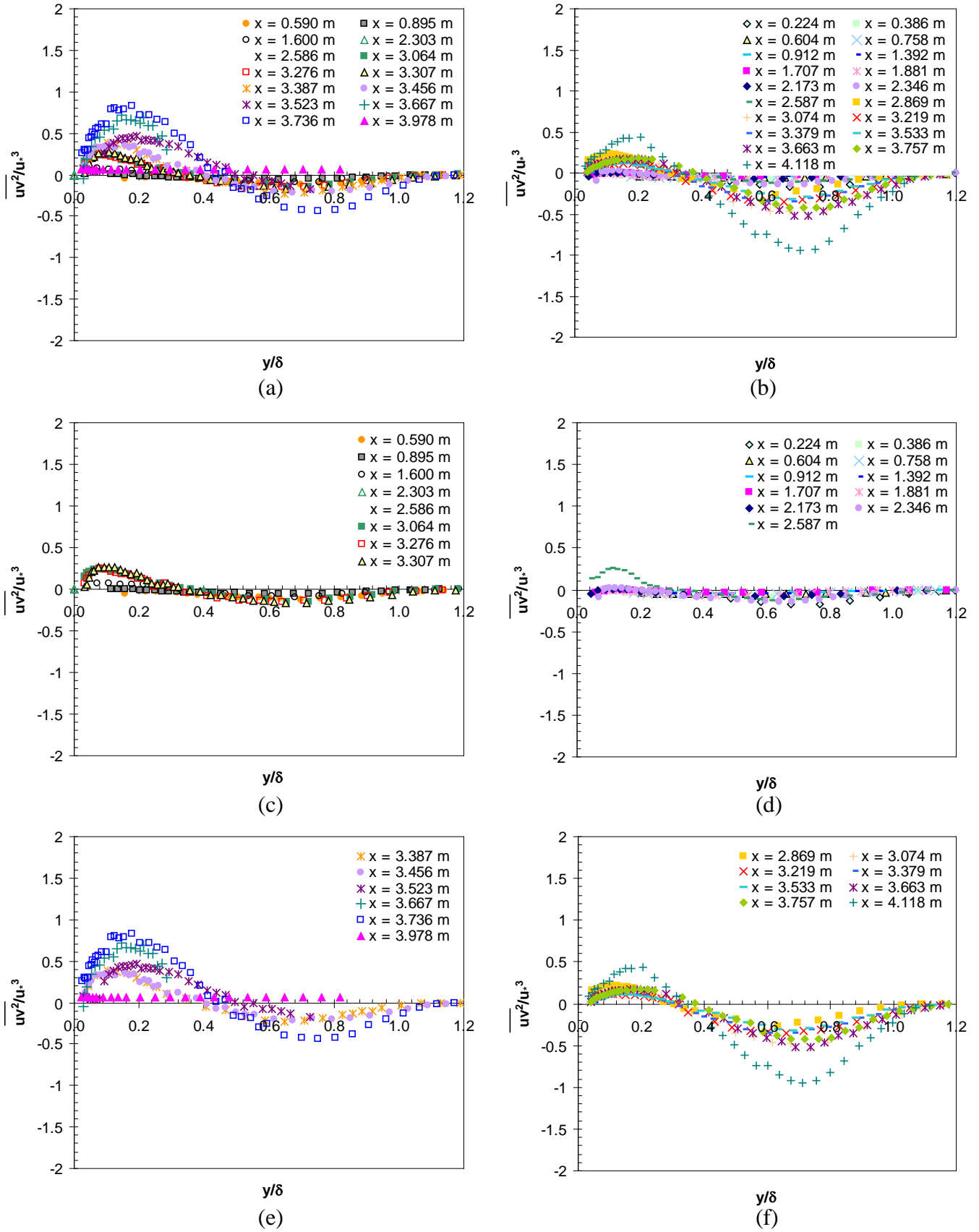


Figure 6.32  $\overline{uv^2}$  scaled with friction velocity  $u_*^3$  for Flow A (left column) and Flow B (right column). (a) and (b), All stations; (c) and (d), before APG equilibrium region; (e) and (f), within the APG equilibrium region.

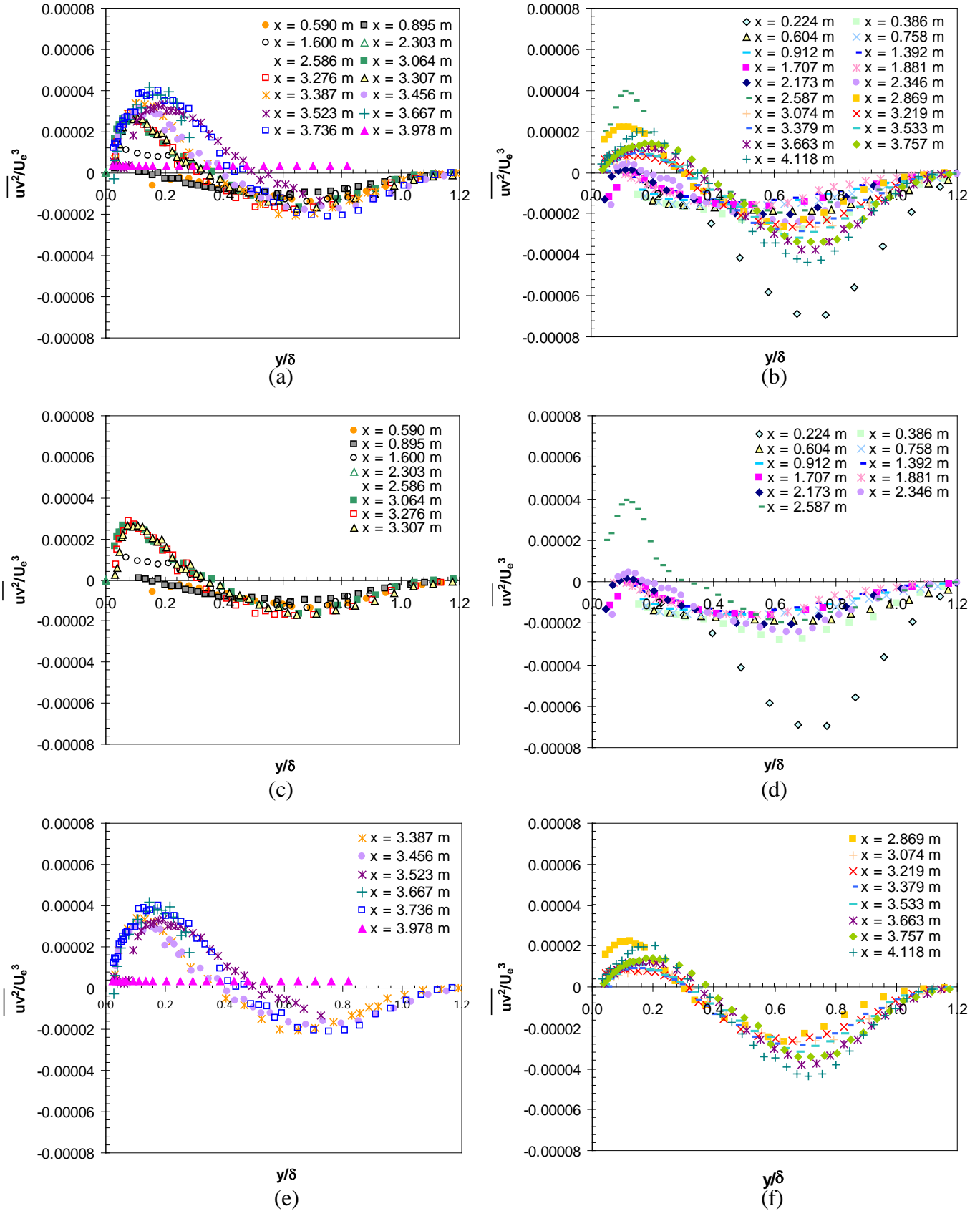


Figure 6.33  $\overline{uv^2}$  scaled with freestream velocity  $U_e^3$  for Flow A (left column) and Flow B (right column). (a) and (b), All stations; (c) and (d), before APG equilibrium region; (e) and (f), within the APG equilibrium region.

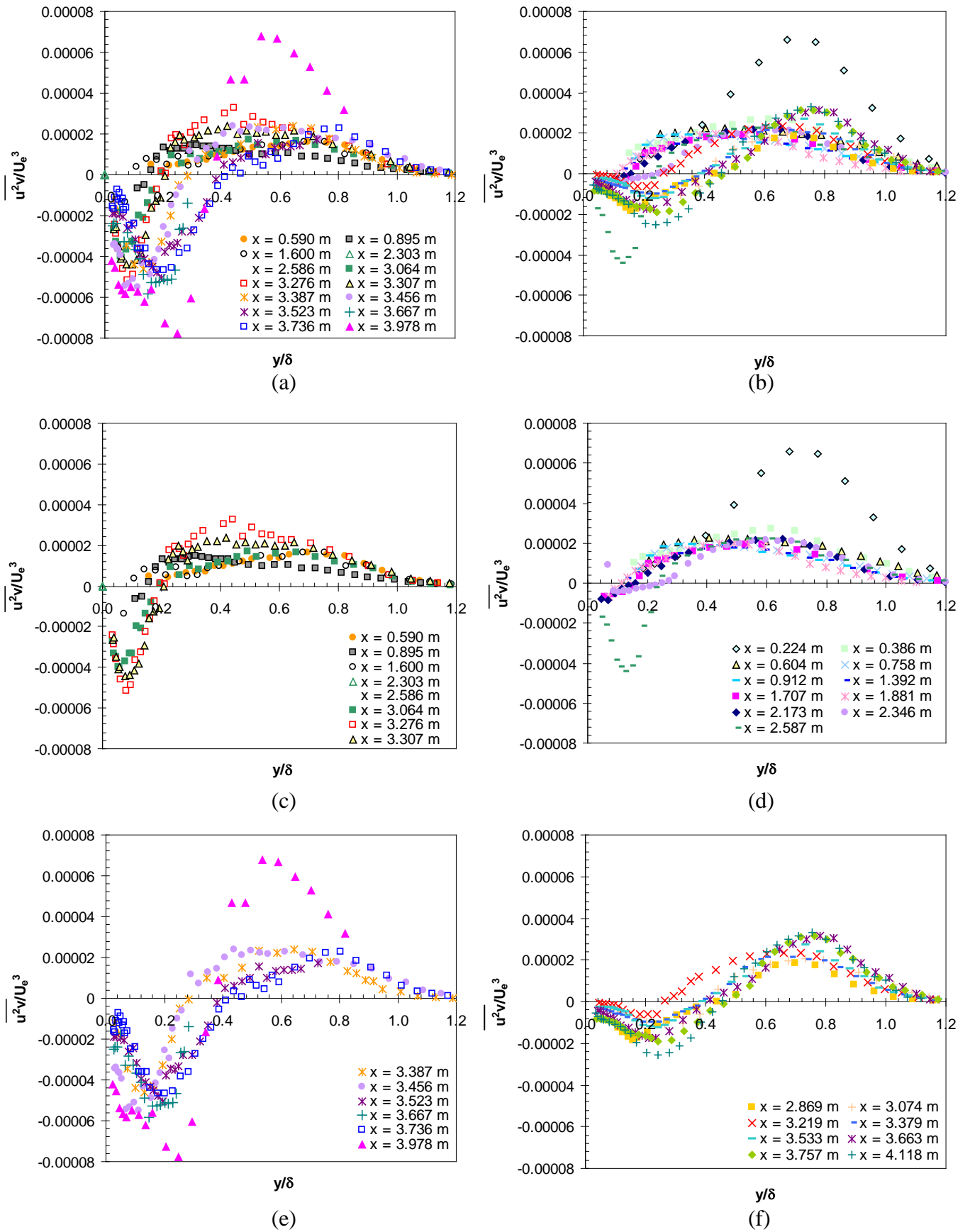


Figure 6.34  $\overline{u^2v}$  scaled with freestream velocity  $U_e^3$  for Flow A (left column) and Flow B (right column). (a) and (b), All stations; (c) and (d), before APG equilibrium region; (e) and (f), within the APG equilibrium region.

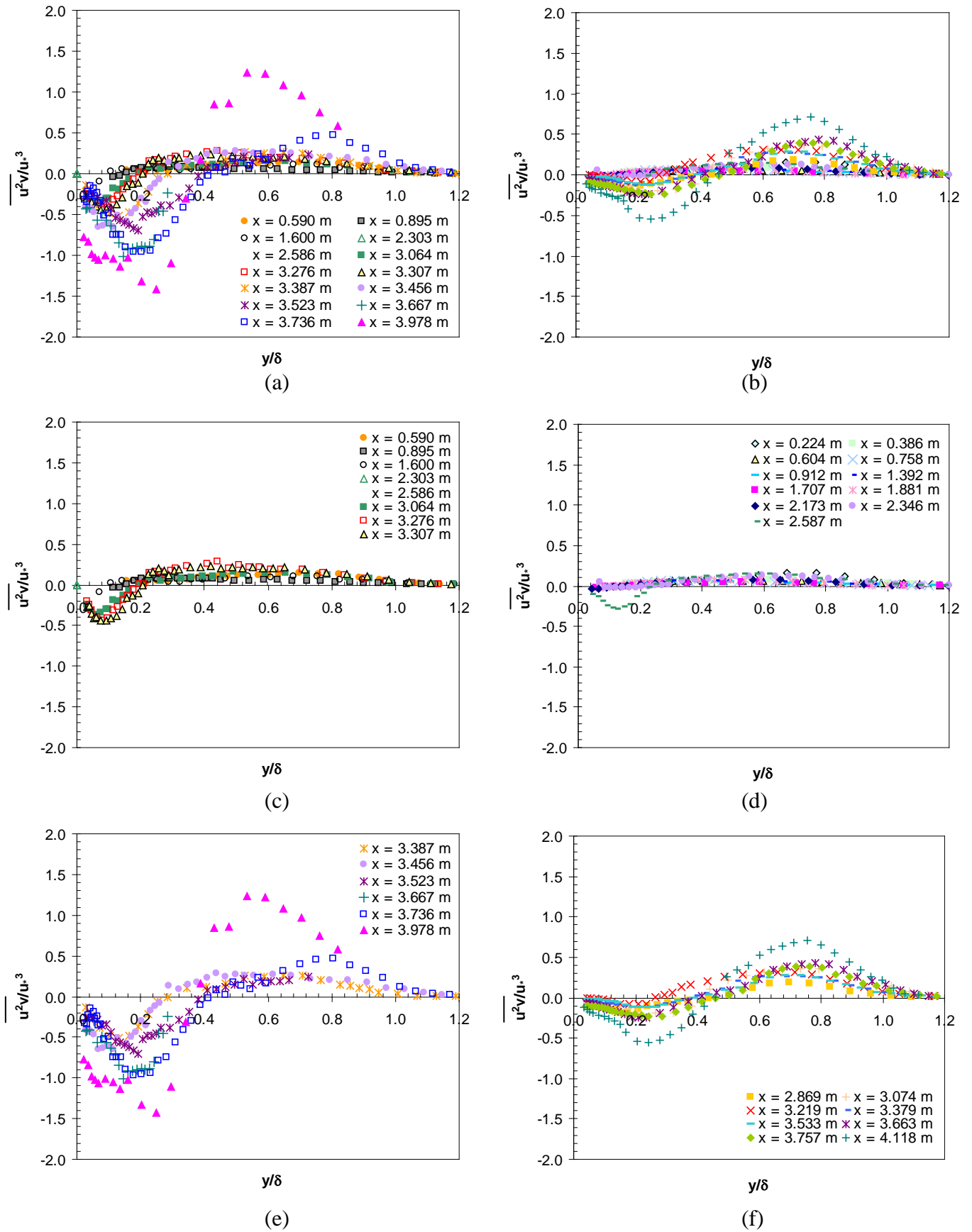


Figure 6.35  $\overline{u^2v}$  scaled with friction velocity  $u_*^3$  for Flow A (left column) and Flow B (right column). (a) and (b), All stations; (c) and (d), before APG equilibrium region; (e) and (f), within the APG equilibrium region.

### 6.3 Conclusions

None of the scaling parameters used for  $\overline{uv}$  provided a universal collapse of profiles. The best scaling parameter was the Castillo/George scale of  $U_e^2 \frac{d\delta}{dx}$  which yielded the best quality of collapse within the APG equilibrium region.  $\overline{v^2}$

The normal stresses in the x and y directions,  $\overline{u^2}$ ,  $\overline{v^2}$ , are not successfully scaled by either friction velocity or the Castillo/George scale of  $U_e^2$ . The Zagarola/Smits scale of  $U_e^2 \frac{\delta^*}{\delta}$  does successfully collapse profiles for both Flow A and B within the APG equilibrium region.

The definition of an APG equilibrium region based on the ideal APG line from Zagarola/Smits scaling of mean velocity, given in the previous chapter, was examined in relation to Reynolds stresses. For all the Reynolds stresses, a distinction is seen between profiles within the APG equilibrium region and those before it. A better collapse of profiles is evident within the APG equilibrium region.

Examination of the flow geometry, pressure distribution,  $C_p$ , shape factor, H, boundary layer thickness,  $\delta$ , or Clausers equilibrium pressure parameter,  $\beta$ , does not indicate a reason for division of profiles. Scrutinizing the pressure distribution indicates that all profiles come from within the APG region and that the change from 'increasing' to 'decreasing' adverse pressure gradient does not coincide with the grouping of profiles.

The higher order moments were presented and were found to be suitably comparable with other flows from the literature. They will be used in the next chapter to determine the energy budgets.

## 7 Energy Budgets

In this chapter, turbulence kinetic energy balances are presented for Flow B. The objective is to examine the flow development especially within the APG equilibrium region defined previously in 5.1.4. For this purpose, the contribution to the turbulence kinetic energy balance of the advection and diffusion of turbulence kinetic energy is studied along with the more dominant production and viscous dissipation terms. Three different methods are used here to calculate the rate of dissipation. The results are discussed in relation to other published flows, including Skare (1993) and Lee and Sung (2008). The energy budgets show a difference between locations within the APG equilibrium region and those before it.

### 7.1 Introduction

All turbulent flows are dissipative. The kinetic energy of turbulence is lost to deformation work that results from viscous shear stresses. If no energy is supplied, turbulence decays rapidly. Also, diffusion of fluid particles and their turbulent kinetic energy occurs. Thus, as described by Hinze (1975), an equilibrium state corresponds to the balance amongst the supply of kinetic energy to the turbulent motion, mean transport, diffusion and viscous dissipation.

The general transport equation for Reynolds stress in a steady 2-dimensional boundary layer is:

Equation 7-1

$$\underbrace{\frac{D}{Dt} \frac{\overline{u_i u_i}}{2}}_{A_{Tk}} = - \underbrace{\frac{\partial}{\partial x_i} \frac{1}{\rho} \overline{p U_i}}_{\text{Pressure work}} - \underbrace{\frac{\partial}{\partial x_j} \overline{u_j \frac{u_i u_i}{2}}}_{\text{Turbulent transport}} - \underbrace{\overline{u_i u_j} \frac{\partial U_i}{\partial x_j}}_{\text{Production}} + \underbrace{v \frac{\partial}{\partial x_j} \overline{u_i \left( \frac{\partial u_i}{\partial x_j} + \frac{\partial u_i}{\partial x_i} \right)}}_{\text{Viscous diffusion}} - \underbrace{v \left( \frac{\partial u_i}{\partial x_j} + \frac{\partial u_j}{\partial x_i} \right) \frac{\partial u_i}{\partial x_j}}_{\text{Dissipation}}$$

$A_{Tk}$                        $D_{Tk}$                        $P_{Tk}$                        $\varepsilon_{Tk}$

For formulation of this equation, see Hinze (Chap. 1, 1975), Townsend (Chap. 2, 1956) and Tritton (Chap. 11, 1988).

The interaction between pressure and velocity fluctuations, defined above as the pressure work term, could not be measured. However, it is considered to have an insignificant contribution to diffusion, an assumption supported by the DNS results of Lee and Sung (2008). They also found that viscous diffusion can be considered negligible; its only contribution is in a region very close to the wall.

Knowing that in a 2-dimensional boundary layer  $\frac{\partial}{\partial z} \approx 0$ ,  $W \approx 0$ , and  $uw \approx 0$ , along with the expression for continuity  $\frac{\partial U}{\partial x} + \frac{\partial V}{\partial y} = 0$ , by using  $i = 1, 2, 3$  and  $j = 1, 2, 3$  we obtain:

$$A_{TK} = -D_{TK} - P_{TK} - \epsilon_{TKE} \quad \text{Equation 7-2}$$

where

$$A_{TK} = U \frac{\partial}{\partial x} \left( \frac{\overline{u^2 + v^2 + w^2}}{2} \right) + V \frac{\partial}{\partial y} \left( \frac{\overline{u^2 + v^2 + w^2}}{2} \right) \quad \text{Equation 7-3}$$

$$D_{TK} = \frac{\partial}{\partial x} \left( \frac{\overline{u^3 + uv^2 + uw^2}}{2} \right) + \frac{\partial}{\partial y} \left( \frac{\overline{u^2v + v^3 + vw^2}}{2} \right) \quad \text{Equation 7-4}$$

$$P_{TK} = \left( \overline{u^2} - \overline{v^2} \right) \frac{\partial U}{\partial x} + \overline{uv} \frac{\partial U}{\partial y} + \overline{uv} \frac{\partial V}{\partial x} \quad \text{Equation 7-5}$$

Each of these terms is calculated from the x-wire results for Flow B and is discussed in more detail below. Once Flow A and B were examined to show that the location of transition from increasing APG to decreasing APG had no relation to which mean velocity deficit and Reynolds stress profiles collapsed, there was no need to do the turbulence kinetic energy balances for both flows. Therefore, only Flow B is examined further here.

## 7.2 Advection

Advection,  $A_{Tk}$ , as derived from the general transport equation is:

$$A_{Tk} = U \frac{1}{2} \frac{\partial(\overline{u^2} + \overline{v^2} + \overline{w^2})}{\partial x} + V \frac{1}{2} \frac{\partial(\overline{u^2} + \overline{v^2} + \overline{w^2})}{\partial y} \quad \text{Equation 7-6}$$

To calculate advection, it is necessary to find the derivatives of  $\overline{u^2}$ ,  $\overline{v^2}$  and  $\overline{w^2}$  in both the x and y directions. The  $\overline{w^2}$  term was not simultaneously measured so the approximation  $\overline{w^2} = K(\overline{u^2} + \overline{v^2})$ , as discussed in Section 6.1.4.1, is applied. The resultant equation is given in Equation 7-7.

$$A_{Tk} = U \frac{1}{2} \frac{\partial(1.3\overline{u^2} + 1.3\overline{v^2})}{\partial x} + V \frac{1}{2} \frac{\partial(1.3\overline{u^2} + 1.3\overline{v^2})}{\partial y} \quad \text{Equation 7-7}$$

Before calculating the derivatives, an interpolation method was applied to the raw data to generate values with a regular  $y = 1$  mm spacing. Some smoothing was required before forward differencing could be used to find the derivatives. The same process was also applied to all other terms required to calculate diffusion, dissipation and production. A five-point moving average was applied to smooth the results and reduce the data. This process might have lowered the amplitude, but it should not have affected the slopes appreciably. Such averaging was essential to generate the differential terms.

When advection is expected to be zero, the first and second term in Equation 7-6 are equal but opposite in sign. An example from location  $x = 3.663$  m is a good demonstration of this occurrence. In Figure 7.1 the individual advection terms are presented; whilst the resultant advection is shown in Figure 7.2.

The oscillations observed in Figure 7.2, and others throughout this chapter, are errors as a result of differentiating discrete experimental data points.

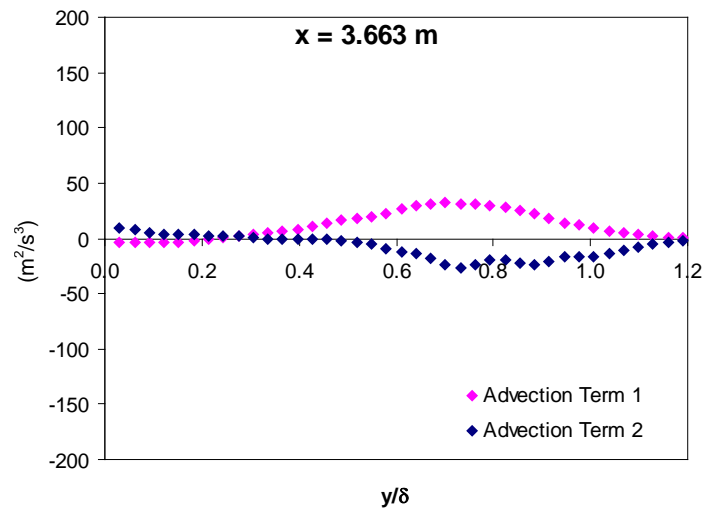


**Figure 7.1** Advection terms from location  $x = 3.663$  m demonstrating their equal but opposite nature. Where Term 1 is  $U \frac{1}{2} \frac{\partial \overline{(1.3u^2 + 1.3v^2)}}{\partial x}$ , and Term 2 is  $V \frac{1}{2} \frac{\partial \overline{(1.3u^2 + 1.3v^2)}}{\partial y}$ .

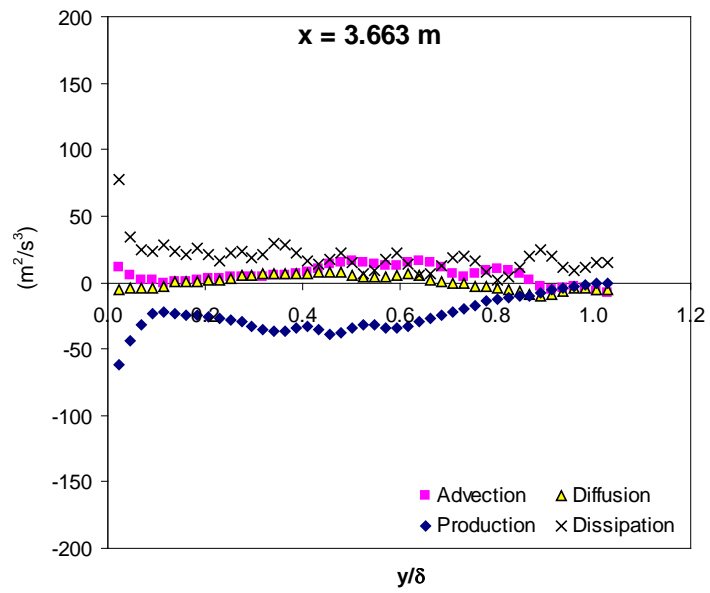


Figure 7.2 Advection, production, dissipation and diffusion terms at location  $x = 3.663$  m.

### 7.3 Production

The production of turbulent kinetic energy, in a 2-dimensional turbulent boundary layer as derived in Section 7.1 is repeated here:

$$P_{Tk} = \left( \overline{u^2} - \overline{v^2} \right) \frac{\partial U}{\partial x} + \overline{uv} \frac{\partial V}{\partial x} + \overline{uv} \frac{\partial U}{\partial y} \quad \text{Equation 7-8}$$

By investigation,  $dV/dx$  yields a negligible contribution, and it is not plotted here.

The biggest contribution comes from the  $\overline{uv} \frac{\partial U}{\partial y}$  term, which is expected. The term

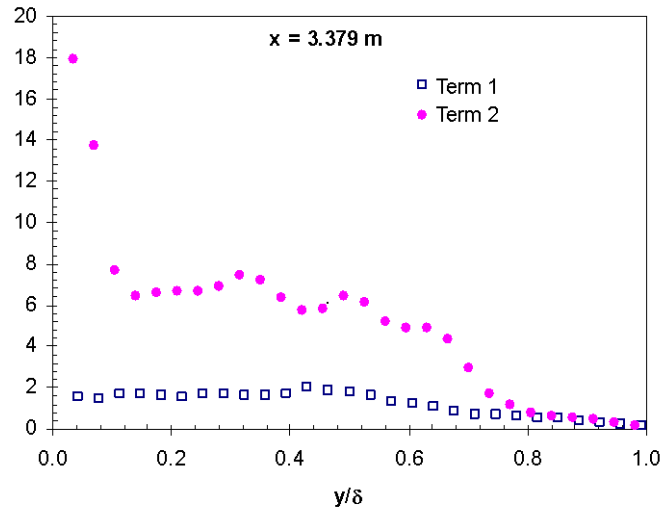
$\left( \overline{u^2} - \overline{v^2} \right) \frac{\partial U}{\partial x}$  is often neglected, it has negligible contribution in ZPG flows.

However, in APG flows its significance increases as found here and also in Skare (1993). Skare found that the term contributed 10% to the total production, here at  $x=3.379$  m the contribution was 20% and at  $x = 3.663$  m was 28%.

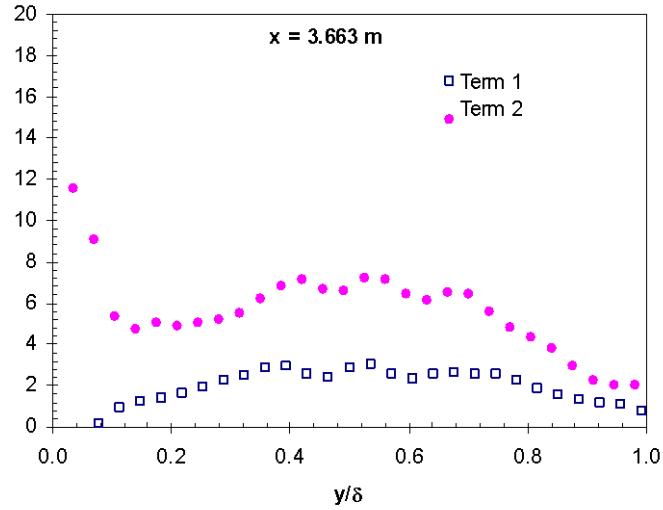
Data from two sample stations are presented in Figure 7.3 scaled with  $\delta/u_*^3$ . It is observed that a peak in production occurs in the outer flow ( $y/\delta = 0.5$ ). This outer peak does not occur in ZPG flows, it is a result of the adverse pressure gradient. The location of this peak does not coincide with the peak in individual stress components, listed in Table 7.1. The peak in production has moved further away from the wall. This is indicative of the importance of these terms in APG flows.

**Table 7.1 Location of the peak value of stresses for Flow B in the APG equilibrium region.**

$\overline{uv}$	$y/\delta = 0.4$
$\overline{u^2}$	$y/\delta = 0.3 - 0.4$
$\overline{v^2}$	$y/\delta = 0.3$



(a)



(b)

**Figure 7.3** Production terms non-dimensionalised with  $\delta/u_*^3$  at locations (a)  $x = 3.379$  m and (b)  $x = 3.663$  m for Flow B. Both locations are within the ideal APG band. The terms are defined as

Term 1:  $-\left(\overline{u^2} - \overline{v^2}\right) \frac{dU}{dx}$ , Term 2:  $-\overline{uv} \frac{dU}{dy}$ .

## 7.4 Diffusion

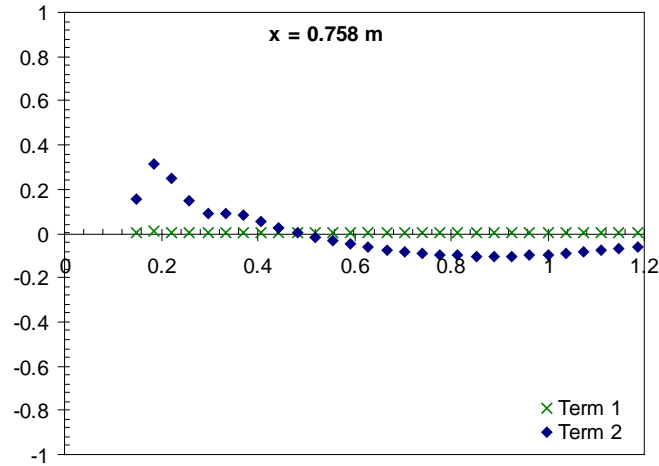
The turbulent transport of the Reynolds stresses, is the diffusion of turbulent kinetic energy, as derived earlier:

$$D_{Tk} = -\frac{\partial}{\partial x} \frac{(\overline{u^3} + \overline{uv^2} + \overline{uw^2})}{2} - \frac{\partial}{\partial y} \frac{(\overline{u^2v} + \overline{v^3} + \overline{vw^2})}{2} \quad \text{Equation 7-9}$$

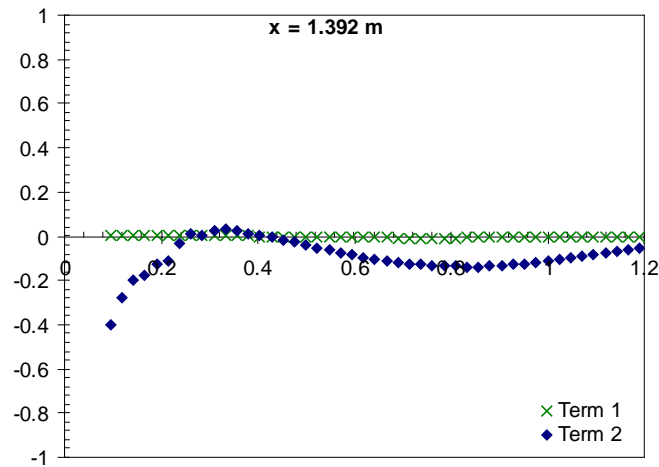
As discussed in Section 6.1.4.1, it is necessary to implement approximations for  $\overline{uw^2}$  and  $\overline{vw^2}$  which further reduces the above equation:

$$D_{Tk} = \frac{1}{2} \frac{\partial}{\partial x} (1.3\overline{u^3} + 1.3\overline{uv^2}) + \frac{1}{2} \frac{\partial}{\partial y} (1.3\overline{u^2v} + 1.3\overline{v^3}) \quad \text{Equation 7-10}$$

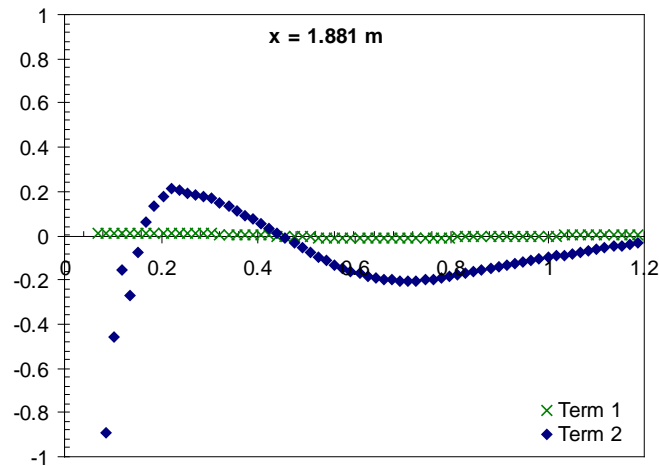
Plotting each term, scaled with  $\delta$  and  $u_*^3$ , it is evident that the second term,  $\frac{\partial}{\partial y} (1.3\overline{v^3} + 1.3\overline{u^2v})$  is the dominant one. Term 1 is often neglected (Skare, 1993, Krogstad and Skare, 1995). In Figure 7.4, the diffusion terms are plotted for locations prior to the APG equilibrium region, where the contribution of term 1 is close to zero. However, within the APG equilibrium region, the significance of term 1 increases dramatically, as seen in Figure 7.5. The magnitude of term 2 has also increased, as indicated by the change of scale between Figure 7.4 and Figure 7.5. The results of Skare (1993) also indicate that term 1 has significant contribution, 10-15% of total diffusion. This result may be due to increased turbulence activity and that the mean flow may be approaching separation.



(a)



(b)



(c)

Figure 7.4 Diffusion terms, non-dimensionalised with  $\delta/u_*^3$  for Flow B at 3 locations before the APG equilibrium region, namely a)  $x = 0.758$  m, b)  $x = 1.392$  m, and c)  $x = 1.881$  m. The terms are defined as Term 1:  $\frac{\partial}{\partial x} (1.3\overline{u^3} + 1.3\overline{uv^2})$  and Term 2:  $\frac{\partial}{\partial y} (1.3\overline{v^3} + 1.3\overline{u^2v})$ .

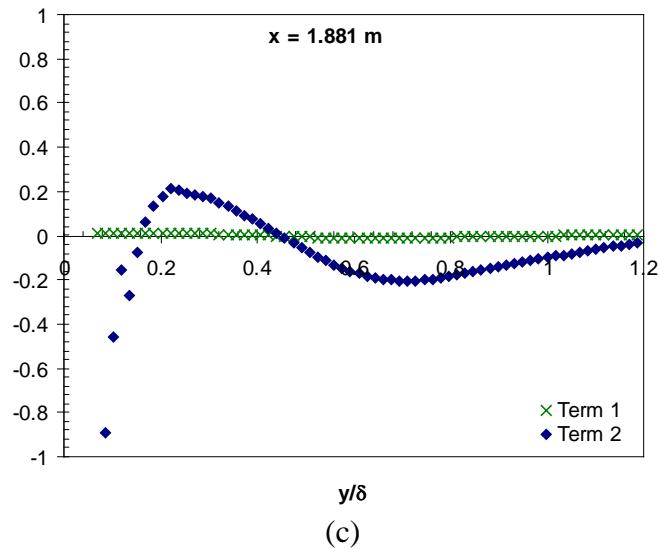
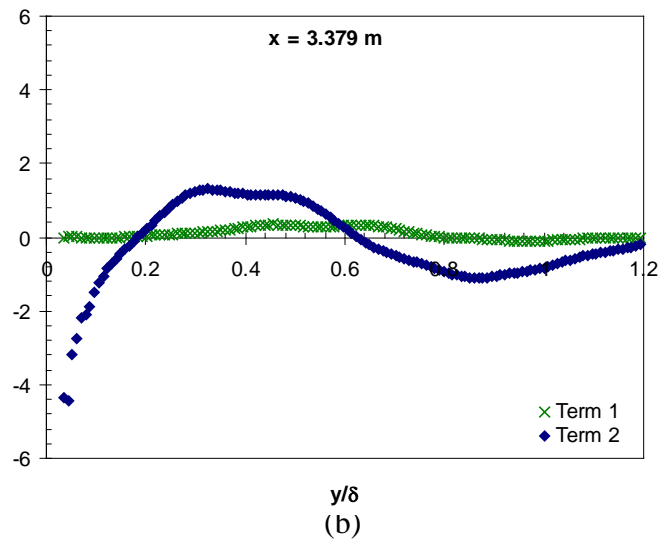
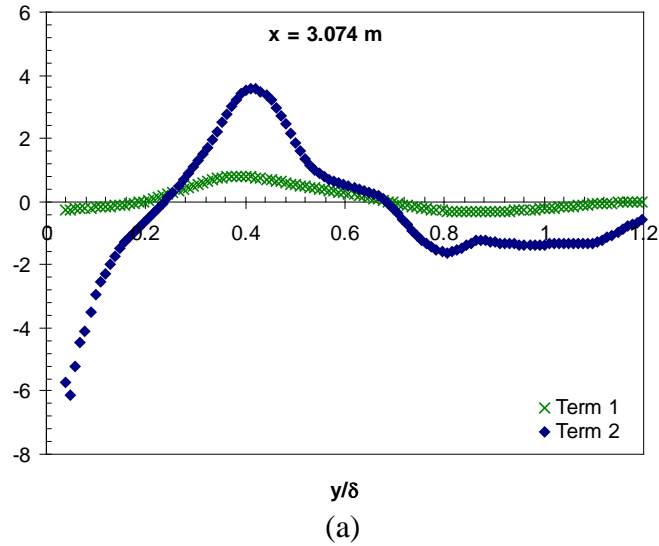


**Figure 7.5** Diffusion terms, non-dimensionalised with  $\delta/u_*^3$  for Flow B at 3 locations in the APG equilibrium region, a)  $x = 3.074$  m, b)  $x = 3.379$  m, and c)  $x = 3.663$  m. The terms are defined as

**Term 1:**  $\frac{\partial}{\partial x} (1.3\overline{u^3} + 1.3\overline{uv^2})$  and **Term 2:**  $\frac{\partial}{\partial y} (1.3\overline{v^3} + 1.3\overline{u^2v})$ .

## 7.5 Dissipation

Dissipation of turbulent kinetic energy is given by

$$\varepsilon = \nu \overline{\left( \frac{\partial u_i}{\partial x_j} + \frac{\partial u_j}{\partial x_i} \right) \frac{\partial u_i}{\partial x_j}} \quad \text{Equation 7-11}$$

To measure dissipation, one must obtain spatial derivatives of fluctuating velocities in three directions. This can be achieved by using an array of x-wire probes. It is not without difficulty, including problems related to flow blockage, spatial resolution and noise contamination, (Antonia, 2003). Other techniques include the zero-wire length method proposed by Azad and Kassab (1985, 1989) and developed further by Turan and Azad (1993). Alternative techniques only require the use of a single hot-wire probe and others that require an x-wire probe. Three such techniques are utilized here.

### 7.5.1 Isotropy

One method widely used experimentally is to assume isotropy. The resulting rate of dissipation expression is given in Equation 7-12.

$$\varepsilon_{\text{iso}} = 15\nu \overline{\left( \frac{\partial u}{\partial x} \right)^2} \quad \text{Equation 7-12}$$

The experimental evaluation of this equation requires data from a single hot wire probe. Other more complicated experimental techniques exist for direct measurement of dissipation, for example, Zhou, Antonia and Chua (2002) use an arrangement of four x-wire probes. Generally, calculating dissipation based on isotropy is expected to be an underestimate (Turan, 1988). However, it is still a useful order of magnitude exercise, because it is a quick source for comparison with other techniques.

Using the single wire measurements of Flow B, a fast Fourier transform (fft) was performed on the streamwise fluctuating velocity component. The Matlab code for this process is given in Appendix XII along with detailed descriptions and plots. The signal was first divided into 10 segments so that an average auto spectrum could be calculated. The auto spectrum was scaled such that the area under the graph was equal to the mean square of the velocity fluctuations. By using Equation 7-13 the

frequency axis of the auto spectrum is scaled to one-dimensional longitudinal wave number,  $k_1$ .

$$k_1 = \frac{2\pi f}{U} \quad \text{Equation 7-13}$$

where  $k_1$  is the longitudinal wave number,  
 $f$  is the frequency of the velocity fluctuations [Hz] and  
 $U$  is the streamwise mean velocity, [m/s]

The one-dimensional power spectrum is defined such that:

$$\overline{u^2} = \int_0^{\infty} E_1(k_1) dk_1 \quad \text{Equation 7-14}$$

where  $\overline{u^2}$  is the mean square average of the velocity fluctuation, [(m/s)<sup>2</sup>].

Thus, the rate of dissipation as determined from the assumption of isotropy, (Hinze, 1975) is obtained by:

$$\varepsilon_{iso} = 15\nu \int_0^{\infty} k_1^2 E_1(k_1) dk_1 \quad \text{Equation 7-15}$$

where  $\nu$  is the kinematic viscosity, [m<sup>2</sup>/s],  
 $E_1(k_1)$  as defined in Equation 7-14, [m<sup>3</sup>/s<sup>2</sup>] and  
 $k_1$  longitudinal wave number as defined in Equation 7-13, [m<sup>-1</sup>].

Two examples of the isotropic rate of dissipation for Flow B are given in Figure 7.6. As expected, this estimation is seen to be lower in magnitude than those obtained with the other two methods used here to determine the rate of dissipation. The two other alternative techniques are discussed below.

### 7.5.2 Kolmogorov's 5/3rds law

Another method for determining the rate of dissipation is by using the Kolmogorov spectral law, given in Equation 7-16.

$$E_1(k_1) = Ck_1^{-\frac{5}{3}}\varepsilon^{\frac{2}{3}} \quad \text{Equation 7-16}$$

where  $E_1(k_1)$  as defined in Equation 7-14, [ $\text{m}^3/\text{s}^2$ ],  
 $C$  is a constant,  
 $k_1$  longitudinal wave number as defined in Equation 7-13, [ $\text{m}^{-1}$ ], and  
 $\varepsilon$  is the rate of dissipation.

With the equilibrium regime in isotropic turbulence, a range exists where the turbulence is statistically in equilibrium, and it is governed only by the rate of dissipation and viscosity. When Reynolds number is high enough, a sub-range must exist, even when the flow is not isotropic, where the dissipation rate is small, compared to the effects of energy transfer by inertia. Then it is expected that, turbulence is determined only by dissipation, and it is independent of viscosity.

Bradshaw (1967) determined  $C = 0.5 \pm 10\%$  for boundary layer flows. This value is supported by others, and it is applied here. The power spectrum is used to determine the rate of dissipation. Two samples from  $x = 2.587$  m and  $x = 3.553$  m are provided in Figure 7.6. The results have some scatter, but are in general agreement with the dissipation rate as calculated from the balance of the turbulence kinetic energy equation, as discussed below.

### 7.5.3 Turbulent kinetic energy balance

The final method used here is to determine the rate of dissipation as the remainder of the turbulent kinetic energy balance. In previous sections, the calculation of advection, production and diffusion have been discussed. Hence the last term of Equation 7-6, the rate of dissipation, can be determined as the balance:

$$-\varepsilon_{\text{TKE}} = A_{\text{Tk}} + D_{\text{Tk}} + P_{\text{Tk}} \quad \text{Equation 7-17}$$

$$-\varepsilon_{\text{Tk}} = U \frac{1.3}{2} \frac{\partial(\overline{u^2} + \overline{v^2})}{\partial x} + V \frac{1.3}{2} \frac{\partial(\overline{u^2} + \overline{v^2})}{\partial y} + \frac{1.3}{2} \frac{\partial(\overline{u^3} + \overline{uv^2})}{\partial x} + \frac{1.3}{2} \frac{\partial(\overline{u^2v} + \overline{v^3})}{\partial y} + (\overline{u^2} - \overline{v^2}) \frac{\partial U}{\partial x} + \overline{uv} \frac{\partial U}{\partial y} \quad \text{Equation 7-18}$$

The shortcoming of this method is that any errors in determining the other components cumulate here. Furthermore, any effect of the pressure-velocity term, which has previously been neglected, is added here. The result of these errors is estimated by Cutler and Johnston (1989) to be as much as  $\pm 30\%$ .

#### **7.5.4 Discussion of dissipation results**

The rate of dissipation scaled with  $\delta/u_*^3$  is given in Figure 7.6 for one location before the APG equilibrium region and one within the APG equilibrium region. The former exhibits behaviour similar to a ZPG flow, with a steadily decaying profile.

In the APG equilibrium region, the rate of dissipation develops a ‘hump’ around  $y/\delta = 0.5$  which is consistent with the findings of Skare (1993) and Lee and Sung (2008).

The three methods used here to determine the rate of dissipation give reasonably similar results before the APG equilibrium region, as shown in Figure 7.6(a). However, in the APG equilibrium region, as shown in Figure 7.6(b), the results are noticeably different.

Outside of APG, isotropy and Kolmogorov’s law hold more effectively than within the band, because they’re closer to the closing term  $\varepsilon$ . As expected, isotropy and the assumptions leading to the  $5/3^{\text{rds}}$  law do not hold within the band.

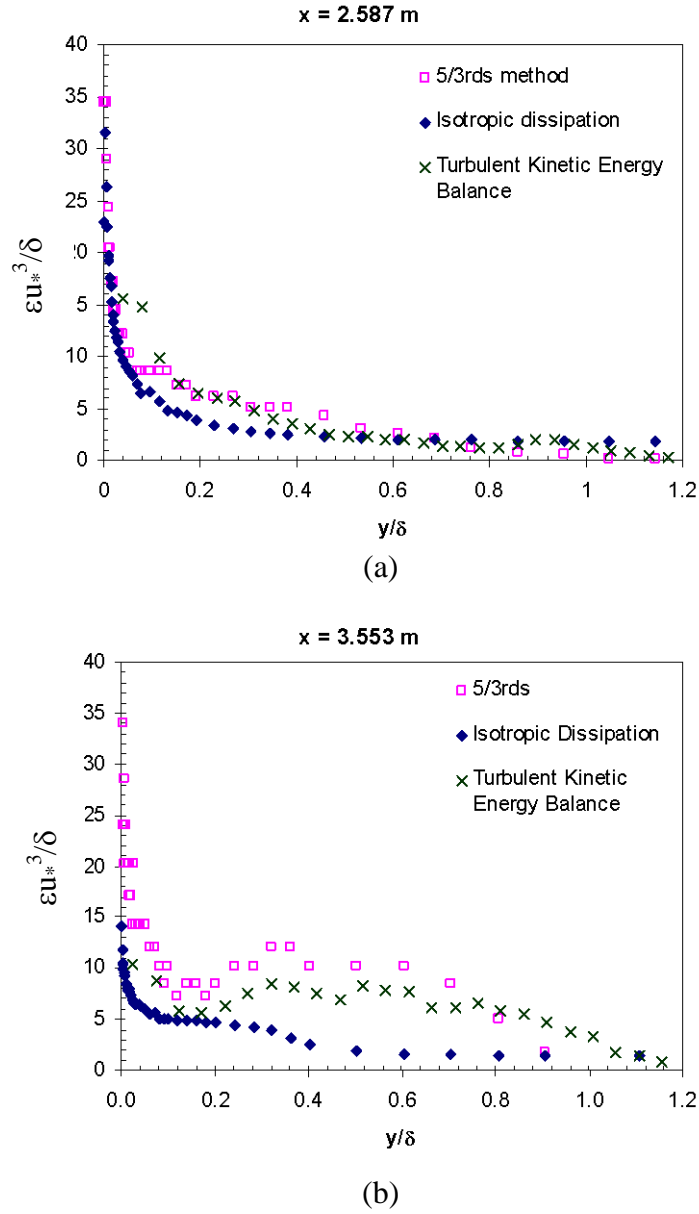


Figure 7.6 Comparison plots for 3 different ways off determining the rate of dissipation of turbulent kinetic energy, namely, dissipation based on isotropy, dissipation based on the Kolmogorov's 5/3rds law and dissipation as the remainder of the turbulent kinetic energy balance. At two locations for Flow B, (a)  $x = 2.587 \text{ m}$  before APG equilibrium and (b)  $x = 3.553 \text{ m}$ , within APG equilibrium region

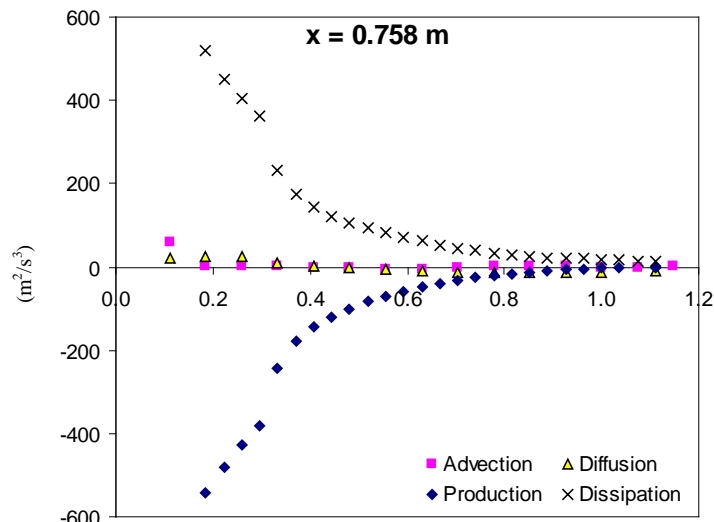
## **7.6 Turbulent Kinetic Energy Budget**

Three samples of the turbulent kinetic energy budget for locations before the APG equilibrium region are given in Figure 7.7. Advection and diffusion are almost zero over the entire boundary layer. Production is balanced by dissipation, and both have a similar shape.

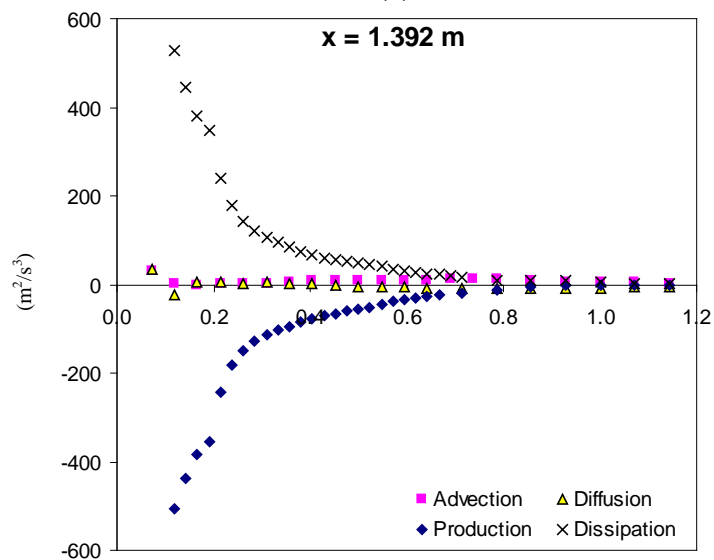
The turbulent kinetic energy budget for three locations within the APG equilibrium region is given in Figure 7.8. In contrast to Figure 7.7, the magnitude has decreased and the shape of the production and dissipation profiles has changed, a hump is now evident at  $y/\delta = 0.4 \sim 0.5$ .

Lee and Sung (2008) found that in the near wall region, the terms in the energy budget of an APG flow were qualitatively similar to, or smaller than that of a ZPG system. Furthermore, they found that this was not the case in the outer region, ( $y/\delta > 0.2$ ). For instance, Lee and Sung found a peak in production which occurs at  $y/\delta = 0.5$ , as discussed earlier, and so did Skare. This is also the case for Flow B in Figure 7.8.

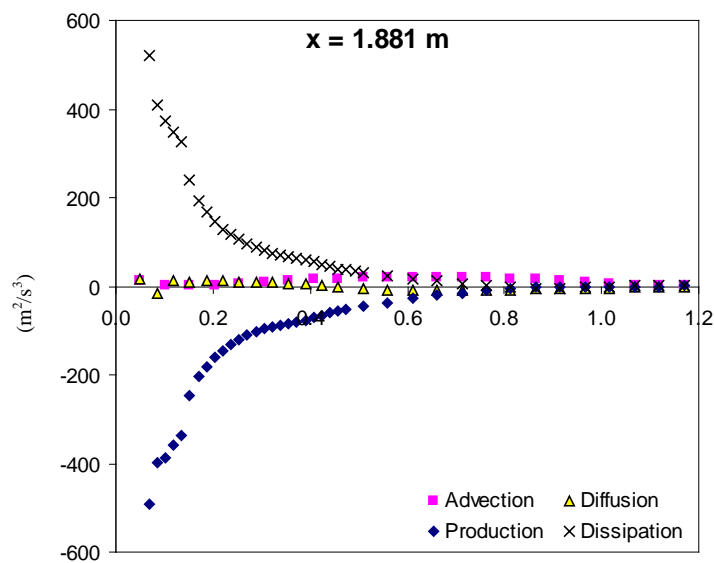
The differences between the profiles may be best judged by observing the dissipation or production terms in isolation. In Figure 7.9, the streamwise development is shown of the rate of dissipation. In Figure 7.10, the streamwise development of production is given, where an arrow is used to indicate the streamwise direction. The first three locations are before the APG equilibrium region and the last three profiles are within the APG equilibrium region. The rate of production of turbulent kinetic energy is stabilising in the APG equilibrium region, as evident by the collapse of profiles for  $y/\delta > 0.2$ .



(a)

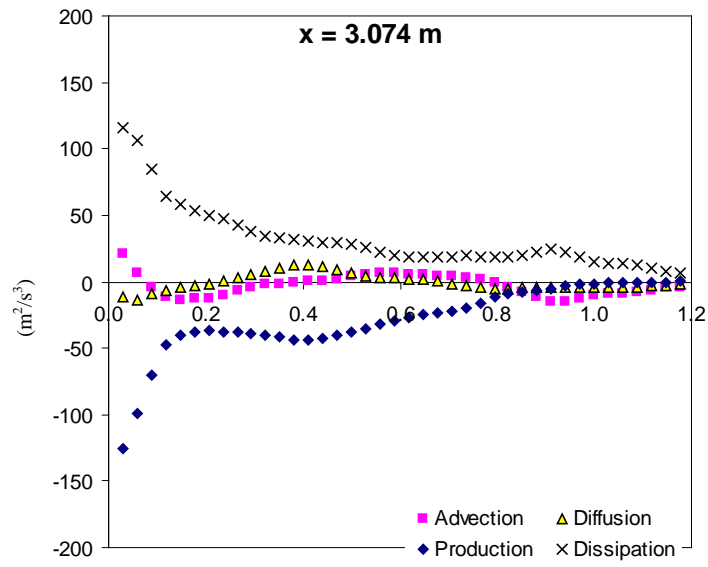


(b)

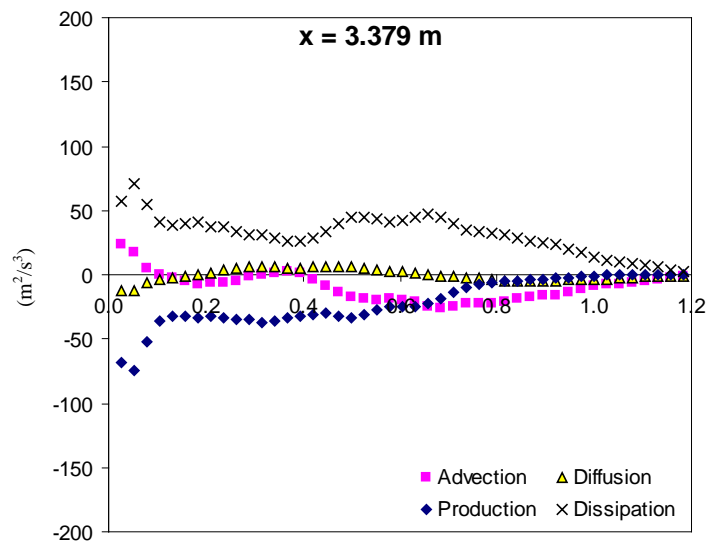


(c)

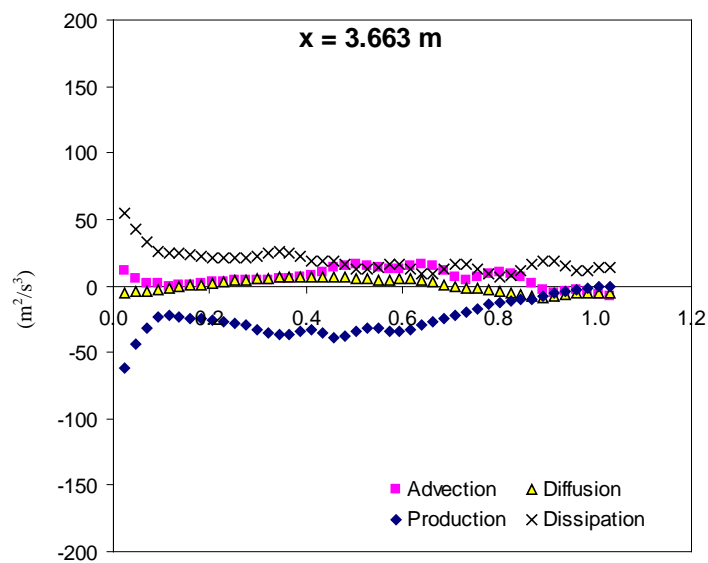
Figure 7.7 Turbulent kinetic energy budget for three locations before the APG equilibrium region, for Flow B. The horizontal scale is  $y/\delta$ .



(a)



(b)



(c)

Figure 7.8 Turbulent kinetic energy budget for three locations within the APG equilibrium region, for Flow B. The horizontal scale is  $y/\delta$ .

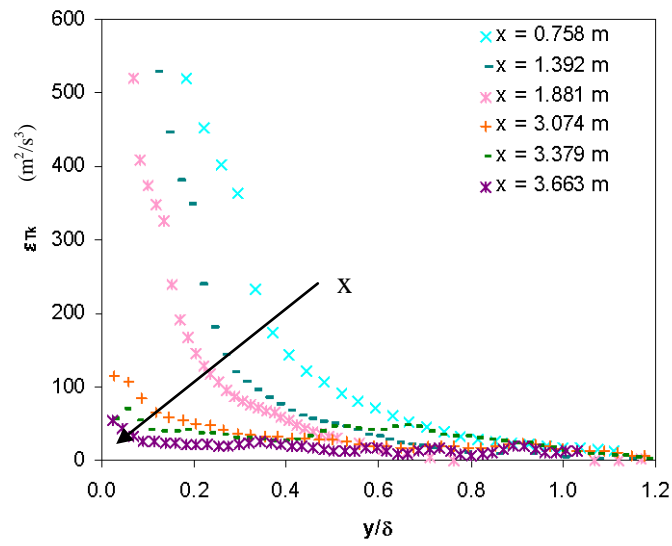


**Figure 7.9** Streamwise development of the rate of dissipation for Flow B. The arrow indicates the flow direction. The first three locations are before the APG equilibrium region and the last three profiles are within the APG equilibrium region.

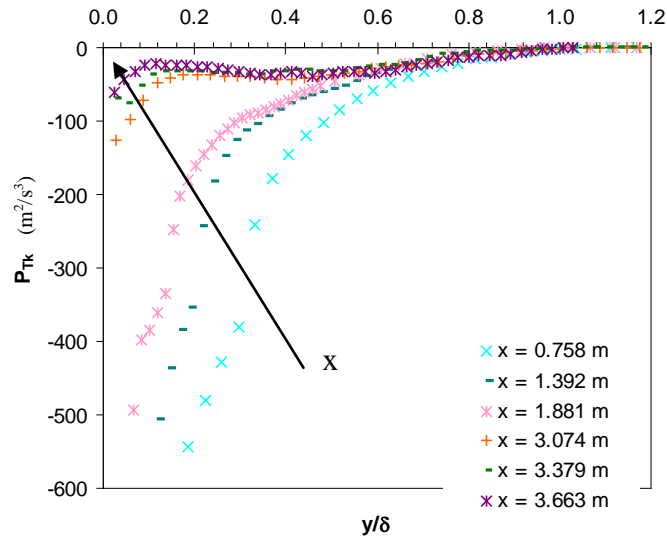


**Figure 7.10** Streamwise development of the turbulent kinetic energy production rate for Flow B. The arrow indicates the flow direction. The first three locations are before the APG equilibrium region and the last three profiles are within the APG equilibrium region.

## 7.7 Conclusions

The term  $(\overline{u^2} - \overline{v^2})\frac{\partial U}{\partial x}$ , from the expression for production of turbulent kinetic energy, and the term  $\frac{\partial}{\partial x}(1.3\overline{u^3} + 1.3\overline{uv^2})$  from the expression for diffusion cannot be assumed to have negligible contributions. For the APG equilibrium region of the flow, both these terms have a significant contribution.

Within the APG equilibrium region the magnitude of production and dissipation has decreased, whilst the significance of advection and diffusion increases.

In the APG equilibrium region, the rate of production of turbulent kinetic energy and its rate of dissipation appear to have attained quasi-steady behaviour.

Three techniques have been compared to determine the rate of dissipation, namely by the assumption of isotropy, by Kolmogorov's  $5/3^{\text{rds}}$  law and as the remainder of turbulent kinetic energy balance. Before the APG equilibrium region, all three methods give similar results, however, as expected, within the APG equilibrium region, the isotopic dissipation rate is much lower than the others.

## **8 Conclusions**

Two new, increasingly adverse pressure gradient flows were generated. Velocity components and correlations for  $u$  and  $v$  were measured extensively using an  $x$ -wire probe, and some  $u$  and  $w$  correlations were also measured. Static pressure data and friction velocity were also recorded. Flow parameters such as boundary layer thickness, momentum thickness, shape factor, equilibrium pressure parameter and turbulence intensity were determined.

The scaling parameters of friction velocity, freestream velocity, as well as that of Zagarola/Smits  $U_e \delta^*/\delta$  were applied to mean flow. The appropriate equivalent scaling factors were applied to Reynolds stresses along with higher order moments. The mean velocity scale of Zagarola/Smits was modified to  $U_e^2 \delta^*/\delta$  and applied to Reynolds stresses.

By examining the two new flows along with other flows from the literature, it was shown that velocity deficit scaled with friction velocity does not generate a universal collapse of profiles for APG flows.

Using the Zagarola/Smits scale of  $U_e \delta^*/\delta$  for mean velocity deficit only yielded a collapse of profiles for the 'classical' flows. This collapse led to the definition of an 'ideal APG line' and a bandwidth for an acceptable collapse. It was shown that this line can be used to determine when a flow has reached an equilibrium state. This prediction cannot be made by using pressure distribution or shape factor. The definition of this equilibrium region is consistent with the pressure parameter  $\Lambda_{\theta_{calc}} \approx \text{constant}$ . This is a significant finding of this research.

When  $uv$  is scaled with friction velocity, the peak value increases in magnitude and moves away from the wall for subsequent stations in the streamwise direction. However, within the APG equilibrium region, the  $y/\delta$  location stabilises but the magnitude still increases. Scaling  $\overline{uv}$  with the Castillo/George scaling of  $U_e^2 (d\delta/dx)$  yields a collapse of profiles in the 'ideal' APG equilibrium region.

For  $\overline{u^2}$  scaled with friction velocity or freestream velocity, the peak value increases in magnitude and moves away from the wall for subsequent stations in the streamwise direction. This is also the case for  $\overline{v^2}$  scaled with friction velocity or freestream velocity at locations prior to the APG equilibrium region. Within the ‘ideal’ APG equilibrium region the peak still increases in magnitude, but it is steady in relation to its  $y/\delta$  location. Using the modified Zagarola/Smits scaling of  $U_e^2 \delta^*/\delta$  for  $\overline{u^2}$  or  $\overline{v^2}$  yields a collapse of profiles within the ‘ideal’ APG equilibrium region.

Differences in the profiles within the APG equilibrium region and those before exist when scaling  $\overline{u^3}$ ,  $\overline{v^3}$ ,  $\overline{uv^2}$  or  $\overline{u^2v}$  with friction velocity or freestream velocity. The waveform is more pronounced and of a higher magnitude in the ‘ideal’ APG region.

It was shown that when calculating production of turbulent kinetic energy for a flow subjected to an APG, the term  $\left(\overline{u^2} - \overline{v^2}\right) \frac{\partial U}{\partial x}$  is not negligible. Nor is the term,  $\frac{\partial}{\partial x} \left(1.3\overline{u^3} + 1.3\overline{uv^2}\right)$  from the expression for diffusion. Both these terms are often assumed to have a negligible contribution, however it has been shown here that for APG flows this is not the case.

For the turbulent kinetic energy budget, differences are evident between locations within the ideal APG equilibrium region, and those before it. Before APG equilibrium, advection and diffusion are almost zero. Production is balanced by dissipation. However, within the ideal APG equilibrium region, the magnitude of production and dissipation has decreased and the profile shape has changed. Also, advection and diffusion now have an increased contribution.

In the APG equilibrium region, the rate of production of turbulent kinetic energy and its rate of dissipation decrease in the streamwise direction, until the APG equilibrium region, where both appear to stabilise.

The difference in behaviour exhibited within the ideal APG equilibrium region by velocity components, velocity correlations and the energy budgets for these flows is

evidence that the ideal APG equilibrium band can be used to identify when a flow has reached an equilibrium condition. This knowledge is expected to enhance the ability to predict how such a flow will develop.

## 9 References

- Anderson, C.M., Turan, Ö.F., Brzek, B. and Castillo, L., “An Adverse Pressure Gradient Turbulent Boundary Layer: New Measurements and Outer Scaling”, Poster presentation, AIAA, 2004
- Anderson, C.M., Turan, Ö.F., Brzek, B. and Castillo, L., “Adverse Pressure Gradient Turbulent Boundary Layer Flows, Part 1: Flow Development,” Fifteenth Australasian Fluid Mechanics Conference, Sydney, NSW, Australia, December 13-17. Paper No. AFMC15-259. 2004
- Anderson, C.M., Turan, Ö.F., Brzek, B. and Castillo, L., “Scaling laws and measurements on adverse pressure gradient turbulent boundary layers” 43<sup>rd</sup> AIAA Fluid Dynamics Conference, Reno, Nevada, January 10-13. Paper No. AIAA 2005-0111. 2005
- Anderson S. D. and Eaton J.K., “Reynolds stress development in pressure-driven three-dimensional turbulent boundary layers.” *J. Fluid Mech.*, Vol.202, pp. 263:294, 1989.
- Antonia, R. A., “On estimating mean and instantaneous turbulent energy dissipation rates with hot wires”, *Exp. Thermal and Fluid Science*, Vol 27, pp 151-157, 2003
- Andreopoulos, J and Rodi, W., “Experimental investigation of jets in a crossflow.”, *J. Fluid Mech.* Vol 138, pp 93–127, 1984.
- Aubertine, C. D. and Eaton, J. K., “Reynolds number scaling in a non-equilibrium turbulent boundary layer with mild adverse pressure gradient”, *Int. J. Heat and Fluid Flow*, Vol 27, pp 566:575, 2006
- Aubertine, C. D. and Eaton, J. K., “Turbulence development in a non-equilibrium turbulent boundary layer with mild adverse pressure gradient”, *J. Fluid Mech.*, Vol 532, pp 345:364, 2005
- Azad, R. S., and Kassab, S. Z., “Dissipation of energy in turbulent flow” University of Manitoba Report METR-9, 1985
- Azad, R. S., and Kassab, S. Z., “New method of obtaining turbulence dissipation”, *Exp. in Fluids*, Vol. 7, pp 81-87, 1989
- Barenblatt, G. I. And Chorin, A. J., “Scaling of the intermediate region in wall-bounded turbulence: the power law.” *Phys Fluids*, Vol 10, pp 1043:1044, 1998

- Bradshaw, P., "The Turbulence Structure of Equilibrium Boundary Layers" NPL Aero. Rep. 1184, 1966
- Bradshaw, P., "The turbulent structure of equilibrium turbulent boundary layers", *J. Fluid Mech.*, Vol 29, pp 625:645, 1967
- Bradshaw, P., "An introduction to turbulence and its measurements", Pergamon Press, 1971
- Bradshaw, P., and Ferriss, D., "The Response of a retarded Equilibrium Turbulent Boundary Layer to the Sudden Removal of Pressure Gradient" NPL Aero. Rep. 1145, 1965
- Browne, L. W. B., Antonia R. A. and L. P. Chua., "Calibration of X-probes for turbulent flow measurements.", *Exp. Fluids*, Vol 7, pp 201:208, 1989
- Brunn, H. H., "Hot – wire Anemometry: Principles and signal analysis", Oxford University Press, USA, 1995
- Brunn, H. H., "Interpretation of a hot-wire signal using a universal calibration law." *J. Phys. E Sci. Instrum.* Vol 4, pp 225:231, 1971
- Brzek, B., "Development and Characterization of an Increasing Adverse Pressure Gradient Turbulent Boundary Layer", M. Sci. Thesis, Rensselaer Polytechnic Institute, 2004
- Brzek, B., Castillo L, Anderson, C.M. and Turan, Ö.F., 2004, "Adverse Pressure Gradient Turbulent Boundary Layer Flows, Part 2: Scaling of Reynolds Stresses," Fifteenth Australasian Fluid Mechanics Conference, Sydney, NSW, Australia, December 13-17. Paper No. AFMC15-260.
- Brzek, B., Turan, Ö.F., Anderson, C.M., and Castillo, L., 2005, "Outer scaling in Turbulent Boundary Layers" 35<sup>th</sup> AIAA Fluid Dynamics Conference and Exhibit, Toronto, Canada, June 6-9. Paper No. AIAA 2005-4814.
- Castillo, L., "Application of Zagarola/Smits Scaling in Turbulent Boundary Layers with Pressure Gradient", *Advances in Fluids Mechanics 3*, Canada, 2000
- Castillo, L. and George, W.K., "Similarity Analysis for Turbulent Boundary Layer with Pressure Gradient: Outer Flow", *AIAA Journal*, Vol. 39 No. 1, pp41:47, 2001
- Castillo, L., and Seo, J., "Experimental investigation of the initial conditions in turbulent boundary layers at high Reynolds number.", Paper 2002-0577, AIAA Aerospace sciences meeting and exhibit, 14-17<sup>th</sup> January 2002

- Castillo, L., Seo, J., Hangan, H., and Johnson, T. G., "Smooth and rough turbulent boundary layers at high Reynolds number." *Exp. In Fluids*, Vol 36, pp759:774, 2004
- Castillo, L. and Walker, D., "The Effects of the Upstream Conditions on the Outer Flow of Turbulent Boundary Layers," *AIAA Journal*, Vol. 40(7), pp. 1292:1299, 2002
- Castillo, L. and Wang, X., "Similarity Analysis for Non-equilibrium turbulent Boundary Layers", 32<sup>nd</sup> AIAA Fluid Dynamics Conference and Exhibit, 2002
- Castillo, L. George, W.K. and Wang, X. "Characterizing Turbulent Boundary Layers Subject to Strong Adverse Pressure gradient with Eventual Separation', ASME Fluids Eng. Division, S-315 FEDSM paper 2001:18112, 2001b)
- Champagne, F.H., Sleicher, C.A., and Wehrmann, O.H., "Turbulence measurements with inclined hot-wires. Part 1: Heat transfer experiments with inclined hot-wire." *J. Fluid Mech.* Vol 28, pp 153:175, 1967.
- Clauser, F.H., "The Turbulent Boundary Layer", *Advances in Applied Mechanics*, Vol. 4, pp 1:51, 1954a
- Clauser, F.H., "Turbulent Boundary Layers in Adverse Pressure Gradients", *J. Aero. Sci.*, Vol.21, No. 2, pp. 91-108, 1954b. Tabulated data reproduced in 'Proceedings Computation of Turbulent Boundary Layers –1968 AFOSR-IFP-Stanford Conference' as 'Flow 2200'.
- Coles, D.E. and Hirst, D.E., "Proceedings, Computation of Turbulent Boundary Layers – 1968 AFSOR-IFP-Stanford Conference", Volume II. Mech Eng Dept, Stanford University, 1969
- Cuttler, A. D. and Johnston, J. P., "The relaxation of a turbulent boundary layer", *J. Fluid Mech.* Vol 200, pp 367:387, 1989
- Daly, B. J. and Harlow, F. H., "Transport equations in turbulence." *Phys. of Fluids*, Vol 13, pp 2634:2649, 1970
- Degraff, D. B. and Eaton, J. K., "Reynolds number scaling of the flat plate turbulent boundary layer", *J. Fluid Mech.* Vol 422, pp 319:346, 2000
- Driver, D. M., "Application of oil-film interferometry skin-friction measurements to large wind tunnels", *Exp. Fluids*, Vol. 34, pp717-725, 2003
- Fraser, H. R., "Study of an incompressible turbulent boundary layer in a conical diffuser", *Ph. D. Thesis, Uni. Ill.* 1956

- Frei, D. and Thomann, H., "Direct measurements of skin friction in a turbulent boundary layer with a strong adverse pressure gradient", *J. Fluid Mech.*, Vol 101 part 1, pp 19:95, 1980
- George, W. K., "Some new ideas for similarity of turbulent shear flows," *Turbulence, Heat and Mass Transfer*, Lisbon 1994, edited by K. Hanjalic and J. C. F.Pereira, Begell House, New York, 1995, pp 24:49.
- George, W. K. and Castillo, L., "Zero-pressure-gradient turbulent boundary layer", *Applied Mech. Reviews.* Vol 50 pp 689:729, 1997
- Han, J. Y., "Pressure signature in Adverse-Pressure Gradient Wall Bounded Turbulent Flows", M. Eng Thesis, Victoria University, 2000
- Hinze, J. O., "Turbulence", McGraw-Hill 2<sup>nd</sup> ed, Ch 7, 1975
- John J. and Schobeiri, T., "A simple and accurate method of calibrating X-probes", *ASME*, Vol 115, pp 148:152, 1993.
- Johnson, F. D. and Eckelmann, H., "A variable angle method of calibration for X-probes applied to wall-bounded turbulent shear flow.", *Exp fluids*, Vol 2, pp 121:130, 1984
- Kader, B. A., and Yaglom, A. M., "Similarity treatment of moving-equilibrium turbulent boundary layers in adverse pressure gradients", *J. Fluid Mech.*, Vol. 89 part 1, pp. 305:342, 1978
- King, L. V. "On the convection of heat from small cylinders in a stream of fluid", *Phil. Trans. R. Soc.* 214A, 373, 1914
- Kline, S. J., Cantwell, B. J. and Liley, G. M., "1980-81 AFOSR-HTTM Stanford Conference on Complex Turbulent Flows" Volume 1, second printing 1983
- Kline, S. J., and McClintock, F. A., "Describing Uncertainties in Single-sample Experiments", *Mech. Eng.*, p. 3, 1953, Reference [1], pp 44-51 in Holman, J. P., "Experimental Methods for Engineers", McGraw Hill, 1978
- Krogstad P. A, and Skare, P. E., "Influence of a strong adverse pressure gradient on a turbulent boundary layer", *Phys. Fluids*, Vol. 7, No 8, pp. 2014-2024, 1995
- Lee, J.-H. and Sung, H. J., "effects of an adverse pressure gradient on a turbulent boundary layer" *Int. J. Heat and Fluid Flow*, Vol 29, pp 568:578, 2008

- Ludweig and Tillmann, “Investigations of the Wall Shearing Stress in Turbulent Boundary Layers”, *Ing-Arch.*, 17, 1949. Tabulated data reproduced in ‘Proceedings Computation of Turbulent Boundary Layers –1968 AFOSR-IFP-Stanford Conference’ as ‘Flow 1300’.
- Lueptow, R. M., Breuer K. S. and Haritonidis, J. H., “Computer-aided Calibration of X-probes Using a Look-up Table”, *Experiments in Fluids* 6, pp115:118, 1988
- Mellor, G. L. and Gibson, D. M., “Equalibrium turbulent boundary layers”, *J. Fluid Mech.*, Vol 24, pp 225-253, 1966
- Moses, H. L., “The behavior of turbulent boundary layers in adverse pressure gradients” MIT Gas Turbine Lab. Rept. No 73, 1964
- Nagano, Y. and Houra, T., “Higher order moments and spectra of velocity fluctuation in adverse pressure gradient turbulent boundary layer.” *Exp. In Fluids*, Vol 33, pp 22:30, 2002
- Nagano, Y., Tagawa, M. and Tsujo, T., “Effects of adverse pressure gradients on mean flows and turbulence statistics in a boundary layer” From Durst F., Friedrich R., Launder B. E., Schmidt F. W., Schumann U., Whitelaw J. H. (Editors) “Turbulent Shear Flows”, Vol 8. Springer, Berlin Heidelberg New York, pp 7–21, 1992
- Naughton, J. W. and Sheplak, M. “Modern skin friction measurement techniques, description, use and what to do with the data”, *AIAA Paper*, pp 2000:2521, 2000
- Newman, B. G., “Some Contributions to the Study of the Turbulent Boundary Layer Near Separation”, *Austr. Department Supply Rept. ACA-53*, 1951. Tabulated data reproduced in *Proceedings, Computation of Turbulent Boundary Layers –1968 AFSOR-IFP-Stanford Conference* as ‘Flow 3500’
- Patel, V. C., “Calibration of the Preston tube and limitations on its use in pressure gradients”, *Journal Fluid Mechanics*, Vol 23, Part 1, pp 185:208, 1965
- Perry, A. E., “Turbulent boundary layers in decreasing adverse pressure gradients”, *J. Fluid Mech.*, Vol. 26, part 3, pp. 481:506, 1966
- Preston, J. H., “Three-Quarter Radius Pitot Tube Flow Meter”, *The Engineer*, October, pp 400:402, 1950
- Reichert, J. K. and Azad, R.S., “Wall shear stress measurement with a hot–film probe in variable temperature flow.”, *Rev. Sci. Instr.*, Vol 48 pp 341 – 345 1977

- Samuel, A.E. and Joubert, P.N., “A boundary layer developing in an increasingly adverse pressure gradient.” *J. Fluid Mech.*, vol. 66, part 3, pp. 481:505, 1974 Tabulated data reproduced in ‘Proceedings Computation of Turbulent Boundary Layers –1980 AFOSR-IFP-Stanford Conference’ as ‘Flow 141’.
- Schlichting, H., “Boundary Layer Theory” 7<sup>th</sup> Ed. McGraw Hill, New York, 1979
- Schubauer, G. B. and Klebanoff, P. S., “Investigation of separation of the turbulent boundary layer.” NACA Report 1030, NACA Technical Note 2133, 1951
- Siddall, R. G. and Davies, T. W., “An Improved Response Equation for Hot-Wire Anemometry”, *Int. J. Heat and Mass Transfer*, Vol 15, pp 367:368, 1972
- Skåre P.E., “Experimental Investigation of Equilibrium Boundary Layer in Strong Adverse Pressure Gradient”. Dr. Ing Thesis. Thermo- and Fluid Dynamics Department of Applied Mechanics, Norwegian Institute of Technology, pp49:98, 1993
- Tennekes, H. and Lumley, J. L., “A First Course in Turbulence”, The Massachusetts Institute of Technology Press, ch. 1 & 5, 1972
- Townsend, A.A, “The Structure of Turbulent Shear Flow”, Cambridge University Press, pp. 150:158, 1956
- Tritton, D. J., “Physical Fluid Dynamics”, 2<sup>nd</sup> Edition, Oxford University Press, Ch.11, 1988
- Turan, Ö. F. and Azad, R. S., “Comparison of the Zero-Wire-Length Dissipation Technique with Spectral Corrections and the Effect of High Turbulence Intensity”, *Experimental Thermal and Fluid Science*, Vol 6, pp. 292:308, 1993
- Turan, Ö. F. “Further study of a new method of evaluating turbulence dissipation” Ph.D. Thesis, University of Manitoba, 1988
- Wei, T., Schmidt, R., McMurtry, p., “ Comment on the Clauser chart method for determining the friction velocity”, *Experiments in Fluids*, Vol 38, pp 695:699, 2005
- Willmarth, W. W., and Bogar, T. J., “Survey and new measurements of turbulent structure near the wall.”, *Physics of Fluids*, Vol 20, pp 59:521, 1977
- Wosnik, M., “On Wall-Bounded Turbulent Shear Flows”, Ph.D Thesis, U. of Buffalo, 2000

- Zagarola, M.V., Perry, A. E, and Smits, A.J., “log laws or power laws: the scaling overlap region”, *Phys Fluids*, Vol 9, pp 2024-2100, 1997
- Zagarola, M.V. and Smits, A.J., “ Mean-flow scaling of turbulent pipe flow”, *J. Fluid Mech.*, Vol. 373, pp. 33:79, 1998a)
- Zagarola, M.V. and Smits, A.J., “A New Mean Velocity Scaling for Turbulent Boundary Layers”, *Proceedings of FEDSM’98*, Washington D.C., 1998b)
- Zilberman, M., “On the interaction of transitional spots and generation of a synthetic turbulent boundary layer. Ph.D. Thesis, Tel-Aviv University, 1981
- Zhou, T., Antonia, R. A., and Chua, L. P., “Performance of a probe for measuring turbulent energy and temperature dissipation rates”, *Exp. In Fluids*, Vol 33, pp 334:345, 2002

## **10 Appendices**

## Appendix I Step-by-step instructions for producing the x-wire calibration look-up table.

Step 1. Gather the data.

Using the stand and equipment described in Section 3.4, for any given angle a series of voltage readings is gathered for different wind tunnel velocities.

The raw data collected are:

Velocity,  $Q$ ,  
Wire 1 voltage,  $E_1$ ,  
Wire 2 voltage,  $E_2$ ,  
Pitch Angle,  $\gamma$ .

Step 2. Average the voltage reading.

A sampling rate of 10 KHz was used to record 65,532 samples of voltage.

Determine the arithmetic average for each wire  $E_1$  and  $E_2$ , at each point.

Step 3. Plot  $E_1$  versus  $E_2$ .

Determine the linear relationship between  $E_1$  and  $E_2$  for each yaw angle.

Step 4. Generate new  $E_2$  values.

Using the equations determined in Step 3 generate new  $E_2$  values for a regularly spaced series of  $E_1$  values. The number of points in the final look-up table is determined by the spacing of the new  $E_1$  and new  $E_2$  values.

Step 5. Plot  $E_1$  versus velocity,  $Q$ .

Use polynomial regression to fit a cubic for  $Q$  as a function  $E_1$  at a given angle. Using the same regularly spaced  $E_1$  values as before determine the corresponding new  $Q$  values. Now each of these 'new' data points has  $E_1$ ,  $E_2$  and  $Q$  for each angle.

Step 6. Plot  $E_2$  versus angle for constant  $E_1$

Fit an equation and generate new angles for regularly spaced  $E_2$ .

Step 7. Plot  $E_2$  versus  $Q$  for constant  $E_1$

Fit a cubic for  $Q$  in terms of  $E_2$  for constant  $E_1$ . Generate new  $Q$  values for regular spacing of  $E_2$ . Now each of these 'new' data points has  $E_1$ ,  $E_2$ ,  $Q$  and angle,  $\gamma$ .

Step 8. Produce the look-up table.

Using the above data with the relationships  $u = Q\cos\gamma$  and  $v = Q\sin\gamma$  the look-up table is completed. All the data is stored in a table to be used for calibration conversion. Now any  $E_1$ ,  $E_2$  voltage pair within the calibration range, can be translated to velocity components  $u$  and  $v$ .

## Appendix II Matlab® calibration and conversion code.

```

%      Written by Catherine Anderson
%      This program is for the calibration of x-wire probes using the method outlined
%      by Lueptow et al in Experiments in Fluids V6 pp115-118 1988

clear all;
close all;
clc;

increment = 0.01;
f=1;
a = 1;
% Read in Calibration data from excel.%%%%%%%%%%
% The Excel file must be open, the data should be arranged in columns as follows:
% D     E           F           G           H           I
% Angle, Cone Pressure, Core Velocity(mmH20), Velocity(m/s), Wire 1 Voltage, Wire 2 Voltage

% Read in columns D G H I
% Sets up link with excel
channel = ddeinit('excel', 'newyaw.xls');

% Reads from Excel
angle = ddereq(channel, 'r6c2:r150c2');
vel = ddereq(channel, 'r6c5:r150c5');
e1 = ddereq(channel, 'r6c6:r150c6');
e2 = ddereq(channel, 'r6c7:r150c7');

% Terminates the channel to Excel
ddeterm(channel);
%%%%%%%%%%
%Plot E1 vs E2
% For each angle set, E1 vs E2 plots as a straight line
% Low velocity occurs at the lower left of the plot and velocity increases to a maximum at the top right

figure(f);
plot(e1, e2, 'bx');
xlabel('E1 (volts)')
ylabel('E2 (Volts)')
title('E1 vs E2 for all angles')
hold on;
f = f+1;

%Plot E1 vs velocity
%For each angle set, E1 vs velocity plots as a cubic curve
figure(f);
plot(e1,vel,'bx');
xlabel('E1 (volts)')
ylabel('Velocity (m/s)')
title('E1 vs Velocity for all angles')
hold on;
%%%%%%%%%%

%need to find the index locations where each new angle set starts.
index(1) = 1; %sets the first value of index to 1
a=2; %control of position in the index matrix
for i = 1:(length(angle) -1)
    if angle(i+1)~= angle(i)
        index(a) = i+1;
        a = a+1;
    end
end

```

```

    end % of if data..
end %of for i =1:...

%create a list of all used angles
angles = angle(index);

%num is the number of measured angles
num = length(angles);

%Add to the list of index locations the index of the last position
index(length(index)+1)=length(angle);

%find the voltage range for each angle set
% for i = 1:num
%   minvoltse1(i) = min(e1(index(i):(index(i+1)-1)));
%   maxvoltse1(i) = max(e1(index(i):(index(i+1)-1)));
%   minvoltse2(i) = min(e2(index(i):(index(i+1)-1)));
%   maxvoltse2(i) = max(e2(index(i):(index(i+1)-1)));

%   newE1a(i,:) = linspace(minvoltse1(i), maxvoltse1(i));
% end

for z= 1:num
    %Fit a linear equation to get E2 = aE1 + b
    coefe2= polyfit(e1(index(z):index(z+1)-1),e2(index(z):index(z+1)-1),1);
    coefs((1:2),z) =coefe2';
    %Fit a quadratic to get Q = ae1^2 + bE1 + c
    coefQ((1:3),z) = (polyfit(e1(index(z):index(z+1)-1),vel(index(z):index(z+1)-1),2))';
end %of for z=1...

%%%%%%%%%%%%%%%%%%%%%%%%%%%%%%%%%%%%%%%%%%%%%%%%%%%%%%%%%%%%%%%%%%%%%%%%
%Calculate new E2 and Q values based on fit obtained above

%This loop determines newQ and newE2 over the e1 voltage applicable to each angle set
%for k = 1:num
%   newQ(k,:) = spline(e1(index(k):(index(k+1)-1)),vel((index(k):(index(k+1)-1))), newE1a(k,:));
%   figure(f)
%   plot(newE1a(k,:),newQ(k,:), 'r');
%   hold on;
%   title('Fit shows new Q values');

%   newE2(k,:) = polyval(coefs(:,k), newE1a(k,:));
%   figure(f-1)
%   plot(newE1a(k,:), newE2(k,:), 'r')
%end

newE1 = [round(min(e1)):increment:3.5];
% round(max(e1))+4*increment];
npts = length(newE1);
for j = 1:num
    newQ(j,:) = polyval(coefQ(:,j),newE1);
    newE2(j,:) = polyval(coefs(:,j), newE1);

    figure(f)
    plot(newE1, newQ(j,:), 'r')
    hold on;

    figure(f-1)

```

```

    plot(newE1, newE2(j,:), 'r')
end

%To see the quality of these fits the curve are plotted for new E1 values.

f = f+1;

%%%%%%%%%%%%%%%%%%%%%%%%%%%%%%%%%%%%%%%%%%%%%%%%%%%%%%%%%%%%%%%%%%%%%%%%
%Now fit a curve to get angle = aE2 -b and Q =ae2^3 + bE2^2 + cE2 + d for a constant E1

for h = 1:npts
    figure(f)
    plot(newE2(:,h), angles, 'rx')
    hold on;
    xlabel('newE2');
    ylabel('angles');

    figure(f+1)
    plot(newE2(:,h), newQ(:,h), 'rx')
    xlabel('newE2');
    ylabel('newQ');
    hold on;

    coefs2= polyfit(newE2(:,h), angles, 3);
    coefA((1:4),h) = coefs2';
    coefQ2((1:4),h)= (polyfit(newE2(:,h), newQ(:,h),3))';

end % of for h 1...

%Now solve the above to equations for regular spacing of E2 for each set E1
regE2 = [round(min(e1)):increment:3.5];
        %round(max(e1))+4*increment];

for i = 1:length(regE2)
    newAngle(i,:) = polyval(coefA(:,i), regE2);
    figure(f)
    plot(regE2, newAngle(i,:), 'r')
    hold on
    plot(newE2(:,i) ,angles, 'bx')
    %pause;

    %axis([min(regE2),max(regE2),-50,50]);

    newQ2(i,:) = polyval(coefQ2(:,i), regE2);
    figure(f+1)
    plot(regE2, newQ2(i,:), 'r')
    hold on
    plot(newE2(:,i),newQ(:,i), 'bx')
    %pause

    %axis([min(regE2),max(regE2),0,30]);

    %Calculate u an v
    U(i,:) = newQ2(i,:).*cos(newAngle(i,:)*pi/180);
    V(i,:) = newQ2(i,:).*sin(newAngle(i,:)*pi/180);
end
f = f+2;
j=1;

```

```

% This loop was a test to see which data sets were viable
%for i= 1:npts
% figure(f+i+2)
% plot(newE2(:,i),newAngle(:,i), 'b.')
% pause(1)
%end

for a = 1:npts
    datas((j:j+npts-1),1) = newE1(a);% E1
    j = j+npts;
end

counter = 0;
while counter <= npts*npts-npts
    for a = 1:npts
        datas((counter+a), 2) = regE2(a);

        end % of for a = ...
        counter = counter + npts;
    end %of while loop

k=1;

for a = 1:npts

    datas((k:k+npts-1),3) = (newQ2(a,:))'; %Q2
    datas((k:k+npts-1),4) =(newAngle(a,:))'; % angle
    k = k+npts;

end

%E2
%Angle
% datas((j:j+npts-1),5) = datas(i,3).*cos(datas(i,4)*pi/180); %U

    k = 1;

    while k <= npts *npts
        for a = 1: npts
            % datas(k,3) = polyval(coefQ2(:,a), datas(k,2)); %Q

            datas(k,5) = datas(k,3).*cos(datas(k,4)*pi/180); %U
            datas(k,6) = datas(k,3).*sin(datas(k,4)*pi/180); %V
            end

            k = k + 1;
        end

figure(f)
plot3(datas(:,1), datas(:,2), datas(:,5),'b. ');
% axis([1.2,3,1.2,3,0,3]);
title('New U velocities');
xlabel('e1');
ylabel('e2');
zlabel('U m/s');
f = f+1;

figure(f)

```

```

plot3(datas(:,1), datas(:,2), datas(:,6),'b. ');
title('New V velocities');
xlabel('e1');
ylabel('e2');
zlabel('V m/s');

f = f+1;

%figure(2)
%plot(newE1,newE2)

%figure(7)
%5for i=1:length(newE1)
% plot(newE2(:,i),angles,'b. ');
% hold on;
% plot(regE2,newAngle(i,:),'r');
%end

%for i=1:length(newE1)
% figure(9)
% plot(regE2, newAngle(i,:))
% hold on;
% xlabel('regE2')
% ylabel('new Angle')

% figure(10)
% plot(regE2, newQ2(i,:))
% hold on;
% xlabel('Reg E2')
% ylabel('new Q2')

% figure(3)
% plot(newE1(i),newE2(:,i));
% hold on;
% for a = 1:num
% %plot3(newE1(i),regE2(i),U(i,:));
% figure(4)
% %plot(newE1(a),newE2(i,:));
% end % of for a= ...
%plot3(newE1(i),newE2(i,:),U(i,:));
%end % of for i=..

%create a new data set which has the first column as E1
%values the 2nd col as E2 3rd as Q and 4th as angle
%for k = 1:length(newE1*6)

% for j = 1:length(newE1)
%     for i=1:length(newE1)
%         data(k,1) = newE1(i);
%             data(k,2) = regE2(j);
%                 data(k,3) = U(j,i);
%                     data(k,4) = V(j,i);
% figure(4);
% plot3(data(:,1),data(:,2),data(:,3),'r. ')
% hold on;
% axis([1.2,3,1.2,3,0,30]);
% figure(99)
% plot3(data(:,1),data(:,2),data(:,4),'r. ')

```

```

% hold on;
% axis([1.2,3,1.2,3,0,30]);

% end %of for i=1...

% end % of for j = 1...
%end % of for k

a =1;

% while 1
% k=menu('Choose An Operation','Plot raw E1 vs E2','Plot raw E1 vs Velocity',...
% 'Plot interpolated values of E2','Plot interpolated values of Velocity','Run calibration on selected
data file','Finished and save');
% if k==1
% figure(f - (f-1))
% elseif k==2
% figure(f - (f-2))

% elseif k==3
% figure(f - (f-3))
% elseif k==4
% figure(f -1)
% elseif k==5
close all;
%%%%%%%%%%%%%%%%%%%%%%%%%%%%%%%%%%%%%%%%%%%%%%%%%%%%%%%%%%%%%%%%%%%%%%%%
% END OF CALIBRATION SECTION
%%%%%%%%%%%%%%%%%%%%%%%%%%%%%%%%%%%%%%%%%%%%%%%%%%%%%%%%%%%%%%%%%%%%%%%%

%%%%%%%%%%%%%%%%%%%%%%%%%%%%%%%%%%%%%%%%%%%%%%%%%%%%%%%%%%%%%%%%%%%%%%%%
% START OF CONVERSION SECTION
%%%%%%%%%%%%%%%%%%%%%%%%%%%%%%%%%%%%%%%%%%%%%%%%%%%%%%%%%%%%%%%%%%%%%%%%

%%%%%%%%%%%%%%%%%%%%%%%%%%%%%%%%%%%%%%%%%%%%%%%%%%%%%%%%%%%%%%%%%%%%%%%%
%file acuqisition: In this example the raw data files are saved with file names 'r03bb' indicating
location 'R' in the tunnel, traverse heights 03 through to 40, flow B, repeated traverse b
%%%%%%%%%%%%%%%%%%%%%%%%%%%%%%%%%%%%%%%%%%%%%%%%%%%%%%%%%%%%%%%%%%%%%%%%
files = ['r03bb'
'r04bb'];
'r05bb'
'r06bb'
'r07bb'
'r08bb'
'r09bb'
'r10bb'
'r11bb'
'r12bb'
'r13bb'
'r14bb'
'r15bb'
'r16bb'
'r17bb'
'r18bb'
'r19bb'
'r20bb'
'r21bb'
'r22bb'

```

```

'r23bb'
'r24bb'
'r25bb'
'r26bb'
'r27bb'
'r28bb'
'r29bb'
'r30bb'
'r31bb'
'r32bb'
'r33bb'
'r34bb'
'r35bb'
'r36bb'
'r38bb'
'r39bb'
'r40bb'];

fid2 = fopen('results12.txt','w');

for i = 1:length(files)
    fname = [files(i,:), '.txt'];
    load(fname);
    data = eval(files(i,:));

    e1d = data(:,2); % all the e1 data from the measurement
    e2d = data(:,3); % all the e2 data from the measurement
    points = length(data);

    clear data;
    fname = [files(i,:)];
    clear([fname])
    clear fname;
i

%%%%%%%%%%%%%%%%%%%%%%%%%%%%%%%%%%%%%%%%%%%%%%%%%%%%%%%%%%%%%%%%%%%%%%%%
for j= 1:points

    for w = 1:npts
        if e1d(j) >= newE1(w)
            idx = w;
        end % of if e1d

        if e2d(j) >= regE2(w)
            idx2 = w;
        end %of if e2d

        if idx == npts
            idx = idx-1;
        end
        if idx2 == npts
            idx2 = idx2-1;
        end

% Now find the 4 rows in the datas matrix which %
% correspond to the lower and upper points for E1, E2 %
r1 = datas(((idx-1)*npts+idx2),(5:6));
r2 = datas(((idx-1)*npts+idx2+1),(5:6));
r3 = datas((idx*npts)+idx2,(5:6));
r4 = datas((idx*npts)+idx2+1,(5:6));

```

```

end % of for w =

% Average the 4 values found for U velocity and V velocity, there are other ways to do this such as
% interpolation but averaging was chosen for its simplicity and speed.
% With an initial calibration increment of 0.02 averaging is adequate.

Ucal(j,a) = mean([r1(1),r2(1),r3(1),r4(1)]);
Vcal(j,a) = mean([r1(2),r2(2),r3(2),r4(2)]);
end % FOR J = ..

UcalMean(a) = mean(Ucal(:,a));
VcalMean(a) = mean(Vcal(:,a));

fluctU(:,1) = Ucal(:,a) - UcalMean(a);
fluctV(:,1) = Vcal(:,a) - VcalMean(a);
uv(:,a) = (sum(fluctU(:,1).*fluctV(:,1)))/points;

uprime(a) = sqrt(mean(fluctU(:,1).*fluctU(:,1)));
vprime(a) = sqrt(mean(fluctV(:,1).*fluctV(:,1)));

u2(a)= mean(fluctU(:,1).*(fluctU(:,1)));
v2(a) = mean(fluctV(:,1).*(fluctV(:,1)));
v3(a) =mean(fluctV(:,1).*fluctV(:,1).*(fluctV(:,1)));
uv2(a) =mean(fluctU(:,1).*fluctV(:,1).*(fluctV(:,1)));
u3(a) = mean(fluctU(:,1).*fluctU(:,1).*(fluctU(:,1)));
vu2(a) =mean(fluctV(:,1).*fluctU(:,1).*(fluctU(:,1)));
    clear e1d
    clear e2d
    clear fluctU
    clear fluctV

    fprintf(fid2,'%3.4f\t %3.4f\t %3.4f\t %3.4f\t %3.4f\t %3.4f\t %3.4f\t %3.4f\t %3.4f\r\n',
UcalMean(a), VcalMean(a), uv(a), uprime(a), vprime(a), u3(a), v3(a), vu2(a), uv2(a));

    a =a +1
    end %of for loop
fclose(fid2);

% elseif k == 6
save rbbFluctU
%     break;

% end; %end of if

%end; %of while

```

### Appendix III Use of Siddall and Davies technique for calibrating single wire probe

The relationship between voltage and velocity is:

$$E^2 = A + BU_e^{1/2} + CU_e$$

Where  $U_e$  is the effective cooling velocity acting on the wire and  $E$  is the wire voltage.

This equation is rearranged to make velocity the subject, this is done by making a substitution for velocity to allow the equation to be treated as a quadratic, as shown below;

$$E^2 = A + B U_e^{0.5} + CU$$

$$\text{let } U_e = X^2, \Rightarrow \sqrt{U_e} = X$$

$$E^2 = A + BX + CX^2$$

$$0 = CX^2 + BX + A - E^2$$

Solving the quadratic :

$$x = \frac{-B \pm \sqrt{B^2 - 4(A - E^2)C}}{2C}$$

Substituting for x :

$$U_e = \left[ \frac{-B \pm \sqrt{B^2 - 4(A - E^2)C}}{2C} \right]^2$$

Using a least squares technique with the recorded voltage and velocity data, the coefficients A, B, and C.

## Appendix IV      Matlab® code for converting voltage readings from a single wire probe.

```
% Program to convert voltages to velocities for a single wire probe.

clear all;
close all;

% Calibration constants
a1= -0.014;
b1= 0.824;
c1= 1.613;

files = ['ao100'
        'ao102'
        'ao103'
        'ao104'
        'ao105'
        'ao106'
        'ao107'
        'ao108'
        'ao109'
        'ao110'];

%USE A LOOP TO LOAD DATA FILES

for i = 1:length(files)
    fname = [files(i,:), '.txt'];
    load(fname);
    data = eval(files(i,:));

    E = data(:,2); % all the voltage data from the measurement

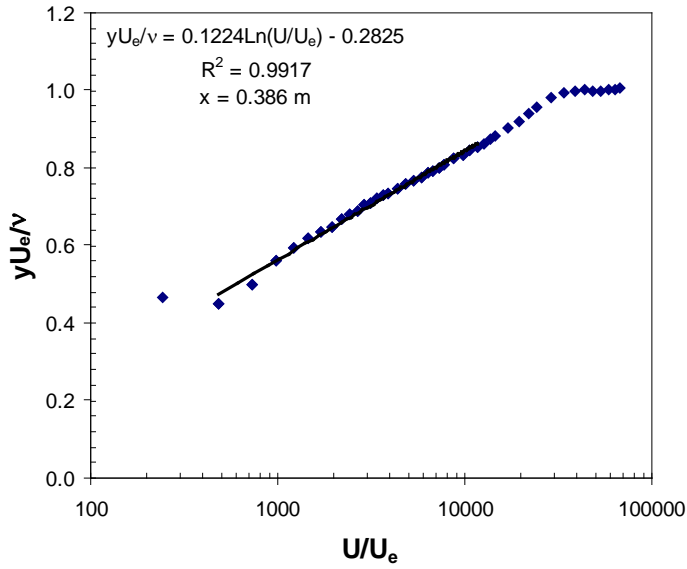
    points = length(data);

    clear data;
    fname = [files(i,:)];
    clear([fname]) %Clears the actual loaded file from the memory
    clear fname; %Clear the variable 'fname'

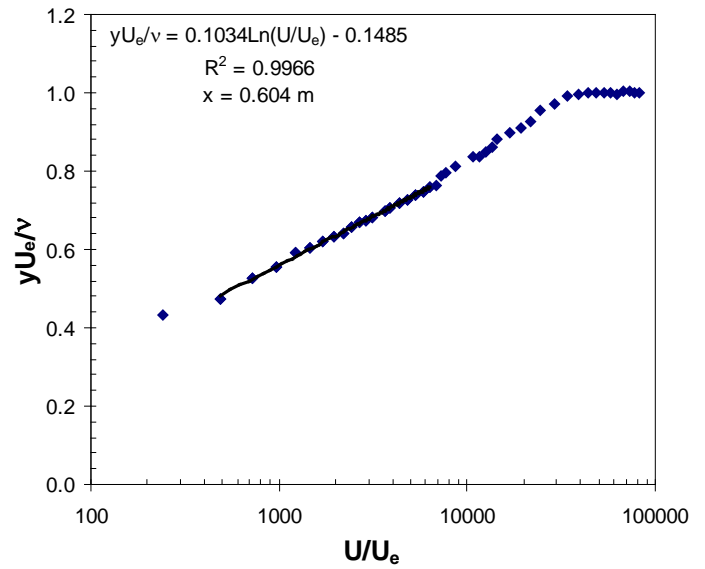
    vel = ((-b1 + sqrt((b1^2) - 4*(a1)*(c1-E.^2)))/(2*a1)).^2;

    aveV(i) = mean(vel);
    fluctU(:,i) = vel - aveV(i);
    uprime(i) = sqrt(mean(fluctU(:,i).*fluctU(:,i)));
end
```

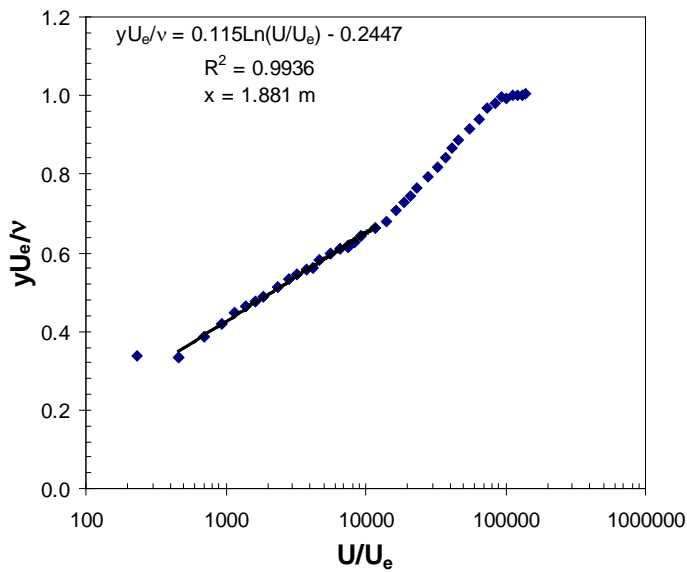
## Appendix V Clauser Charts for Flow B.



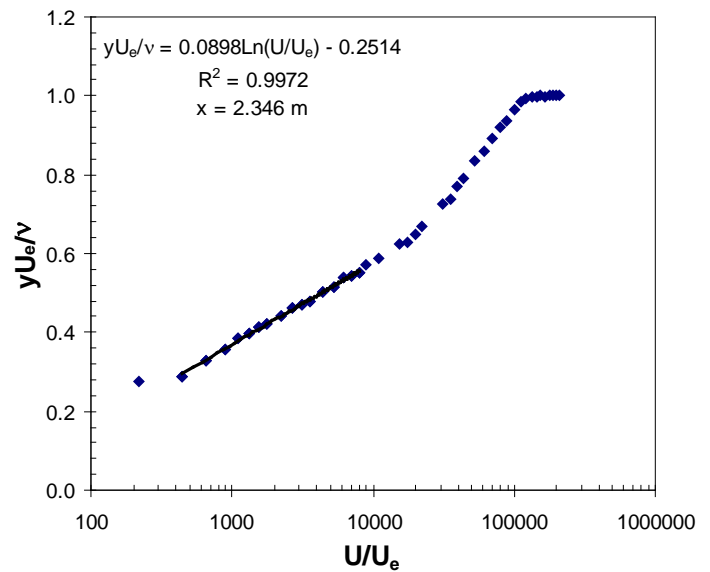
(a)



(b)

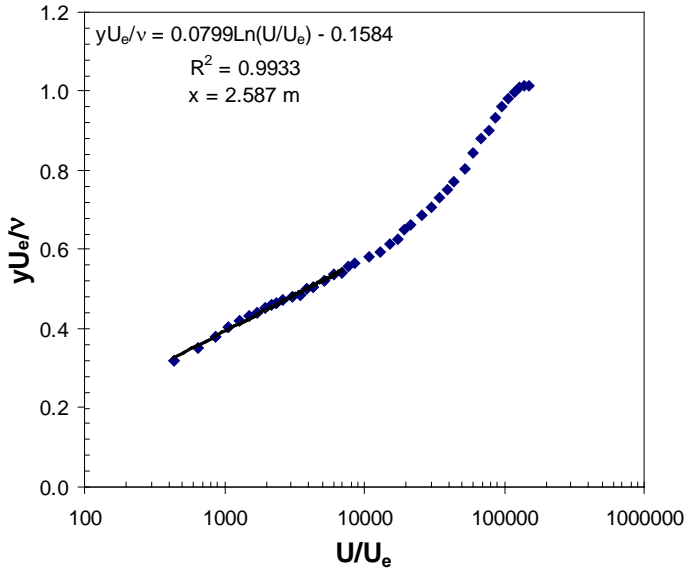


(c)

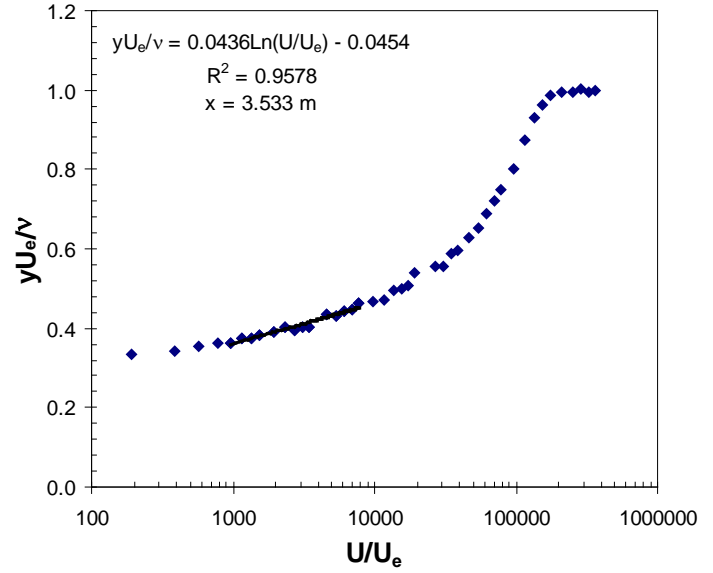


(d)

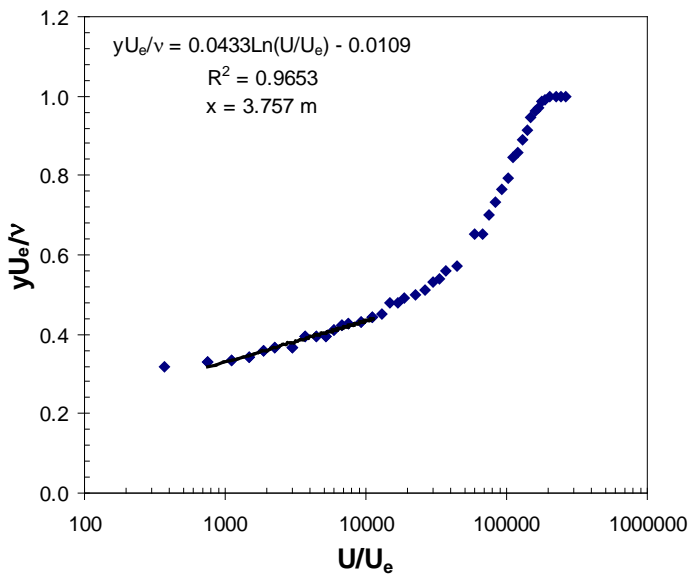
(figure continues next page)



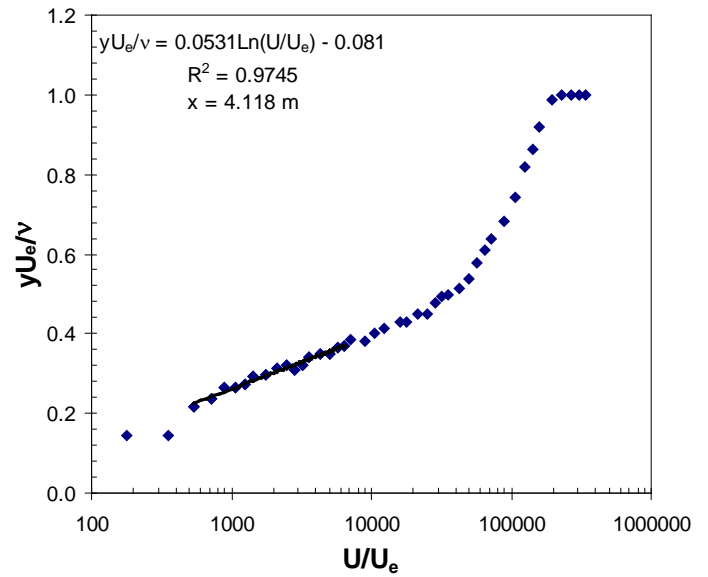
(e)



(f)



(g)



(h)

(figure continues next page)

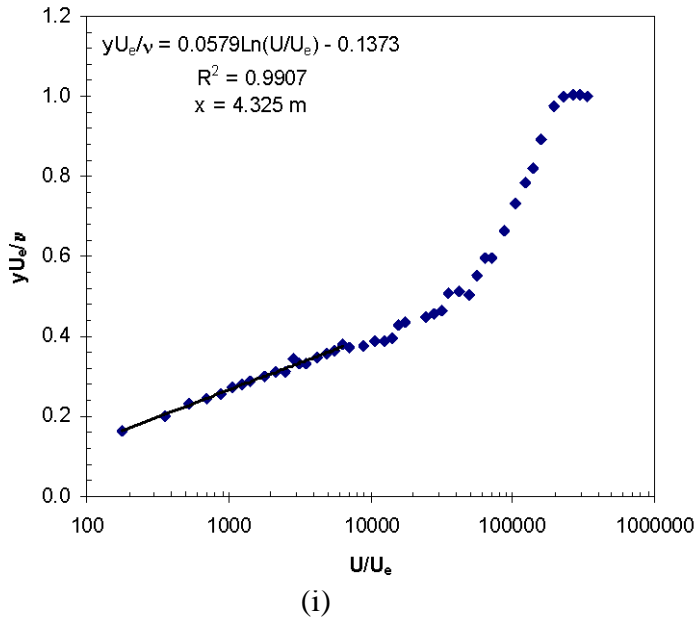


Figure 10.1 Cluser charts for Flow B. Single wire probe data. Each plot a) to i) is labelled with the gradient which is used to determine the friction velocity  $u_*$ , the  $R^2$  value which is an indication of the quality of fit, and  $x$  the stream wise location. See Chapter 4.1.6 for more details.

## Appendix VI Steps to convert Log-Law

Refer back to Sub-section 4.1.7.2.

Starting with the log-law:

$$\frac{U}{u_*} = \frac{1}{\kappa} \ln\left(\frac{yu_*}{v}\right) + B \quad \text{Equation 10-1}$$

Multiply by  $u_*$

$$U = \frac{u_*}{\kappa} \ln\left(\frac{yu_*}{v}\right) + Bu_* \quad \text{Equation 10-2}$$

Re-write log

$$U = \frac{u_*}{\kappa} \left( \ln\left(\frac{y}{v}\right) + \ln(u_*) \right) + Bu_* \quad \text{Equation 10-3}$$

Divide by  $U_e$

$$\frac{U}{U_e} = \frac{u_*}{U_e \kappa} \left( \ln\left(\frac{y}{v}\right) + \ln(u_*) \right) + \frac{Bu_*}{U_e} \quad \text{Equation 10-4}$$

Inside bracketed expression add and subtract  $\ln(U_e)$

$$\frac{U}{U_e} = \frac{u_*}{U_e \kappa} \left( \ln\left(\frac{y}{v}\right) + \ln(u_*) + \ln(U_e) - \ln(U_e) \right) + \frac{Bu_*}{U_e} \quad \text{Equation 10-5}$$

$$\frac{U}{U_e} = \frac{u_*}{U_e \kappa} \left( \ln\left(\frac{yU_e}{v}\right) + \ln(u_*) - \ln(U_e) \right) + \frac{Bu_*}{U_e} \quad \text{Equation 10-6}$$

$$\frac{U}{U_e} = \frac{u_*}{U_e \kappa} \ln\left(\frac{yU_e}{v}\right) + \frac{u_*}{U_e \kappa} \ln\left(\frac{u_*}{U_e}\right) + \frac{Bu_*}{U_e} \quad \text{Equation 10-7}$$

General form equation of a straight line

$$y = m x + c$$

$$\frac{U}{U_e} = \frac{u_*}{\kappa U_e} \ln\left(\frac{yU_e}{v}\right) + C \quad \text{Equation 10-8}$$

In a plot of  $\frac{U}{U_e}$  versus  $\ln\left(\frac{yU_e}{v}\right)$  the gradient,  $m$ , of the resulting straight line is  $\frac{u_*}{U_e \kappa}$ .

This allows the calculation of friction velocity,  $u_* = m\kappa U_e$

**Appendix VII Tabulated data for the Classical flows 2200, 2300, 2500, 3300, and 3500**

Flow		2200			
$x/x_{max}$	$U_e$ (ft/s)	$\delta$ (inch)	H	$u_*$ (ft/s)	$\Lambda_{\theta calc}$
0.21	32.5	2.50	1.67	1.07	-0.19
0.34	29.1	3.90	1.60	0.90	-0.27
0.40	28	4.40	1.64	0.87	-0.28
0.58	25.2	6.00	1.53	0.79	-0.28
0.74	23.6	8.60	1.51	0.75	-0.30
0.83	22.5	9.50	1.50	0.66	-0.33
0.92	21.8	10.00	1.51	0.68	-0.32
1	21.2	11.42	1.51	0.65	-0.31

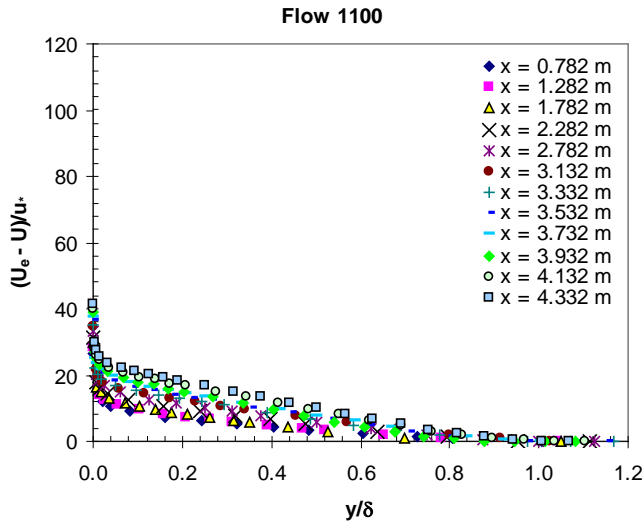
Flow		2300			
$x/x_{max}$	$U_e$ (ft/s)	$\delta$ (in)	H	$u_*$ (ft/s)	$\Lambda_{\theta calc}$
0.28	26.1	3.60	1.79	0.66	-0.18
0.34	24.8	4.40	1.84	0.60	-0.21
0.41	23.5	5.50	1.80	0.55	-0.23
0.48	22.8	6.67	1.79	0.53	-0.24
0.61	21.3	9.90	1.76	0.49	-0.26
0.72	20.2	11.90	1.77	0.47	-0.25
0.90	18.9	17.00	1.76	0.41	-0.20
1.00	18.1	21.00	1.76	0.38	-0.16

Flow		2500			
$x/x_{max}$	$U_e$ (ft/s)	$\delta$ (in)	H	$u_*$ (ft/s)	$\Lambda_{\theta calc}$
0.29	143.40	1	1.42	4.87	-0.21
0.57	129.10	1.8	1.39	4.26	-0.18
0.79	123.50	2.2	1.39	3.96	-0.18
1.00	119.00	2.6	1.40	3.72	-0.17

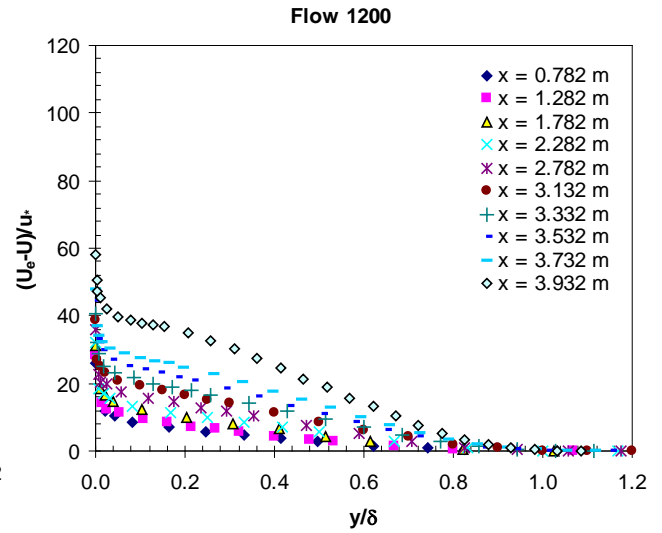
Flow 3300					
$x/x_{max}$	$U_e$ (ft/s)	$\delta$ (inch)	H	$u_*$ (ft/s)	$\Lambda_{\theta calc}$
0.29	26.10	1.10	1.38	4.58	-0.21
0.36	24.80	1.25	1.39	4.21	-0.23
0.43	23.50	1.50	1.42	3.78	-0.27
0.50	22.80	1.70	1.45	3.51	-0.30
0.57	21.30	1.85	1.46	3.31	-0.32
0.71	20.20	2.25	1.50	2.99	-0.32
0.86	18.90	2.60	1.52	2.75	-0.31
1.00	18.10	2.95	1.53	2.60	-0.28

Flow 3500					
$x/x_{max}$	$U_e$ (ft/s)	$\delta$ (in)	H	$u_*$ (ft/s)	$\Lambda_{\theta calc}$
0.41	152.6	0.43	1.59	4.50	-0.137
0.56	134.9	0.77	1.63	3.75	-0.21164
0.71	119.4	1.22	1.74	2.88	-0.22847
0.81	111.6	1.69	1.84	2.38	-0.25325
0.92	103.9	2.30	1.95	1.92	-0.25648
0.97	100.8	2.57	2.16	1.42	-0.22941
1.00	99.6	2.99	2.45	0.95	-0.18787

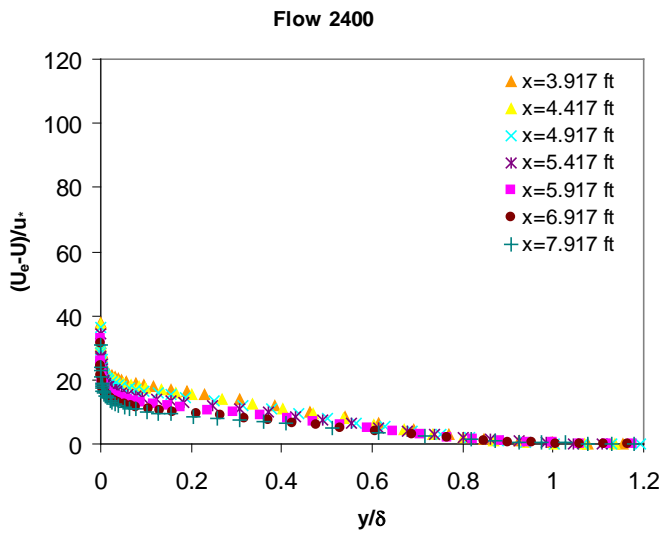
### Appendix VIII Velocity deficit scaled with friction velocity for 'other' flows.



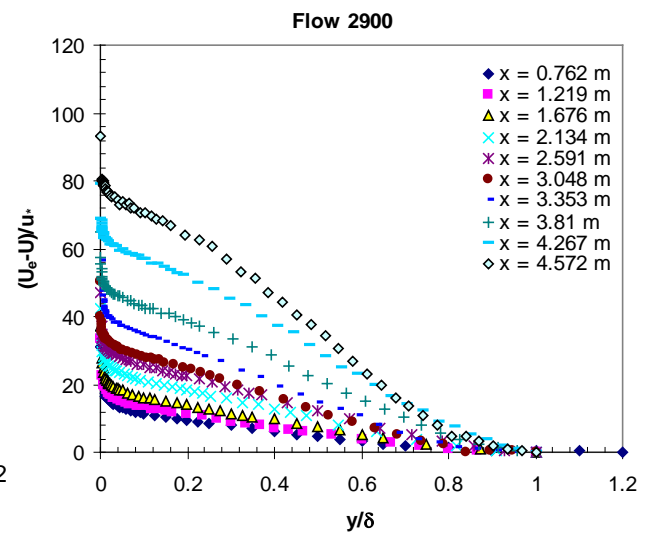
(a)



(b)



(c)



(d)

(figure continues next page)

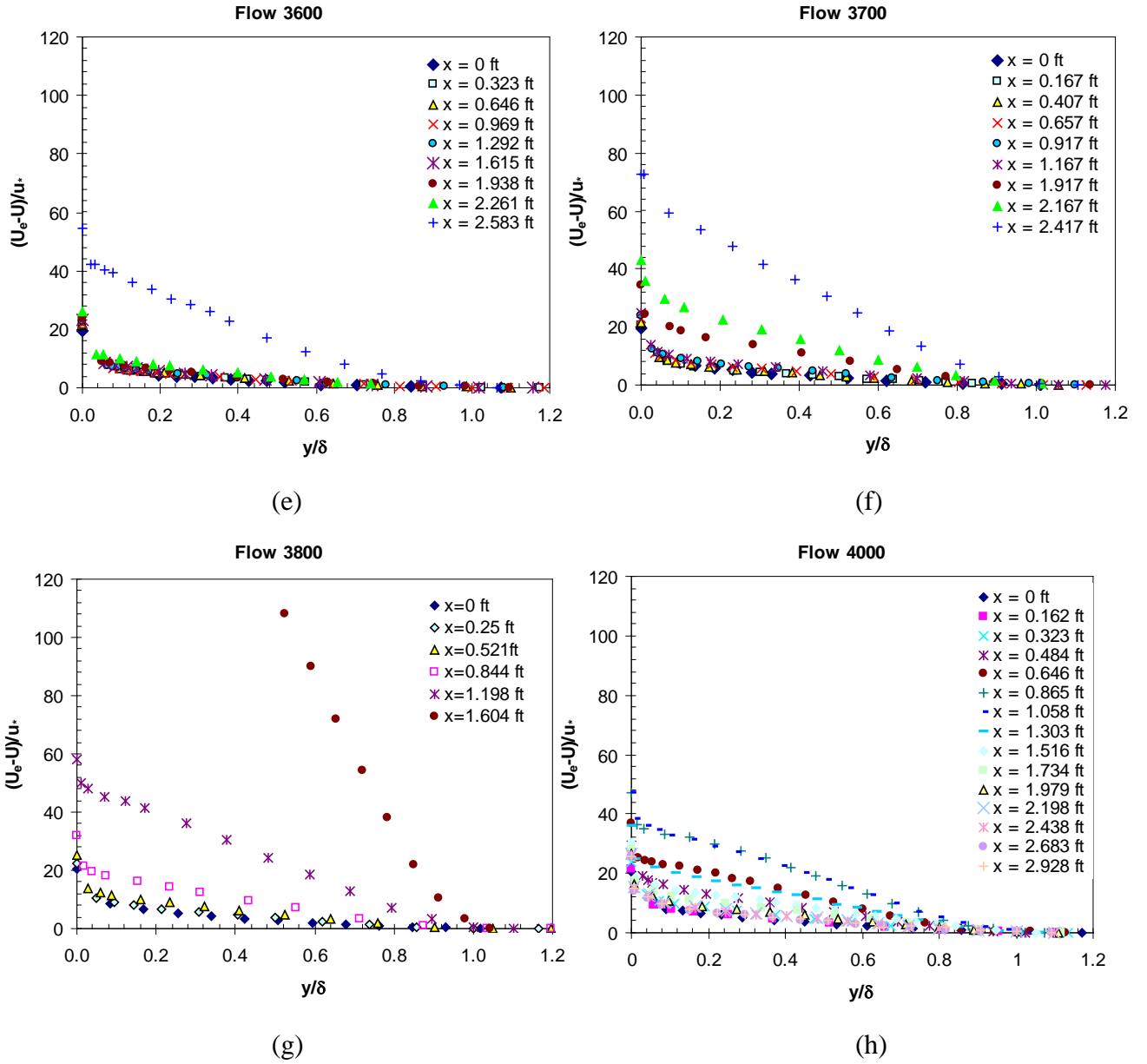


(figure continues next page)

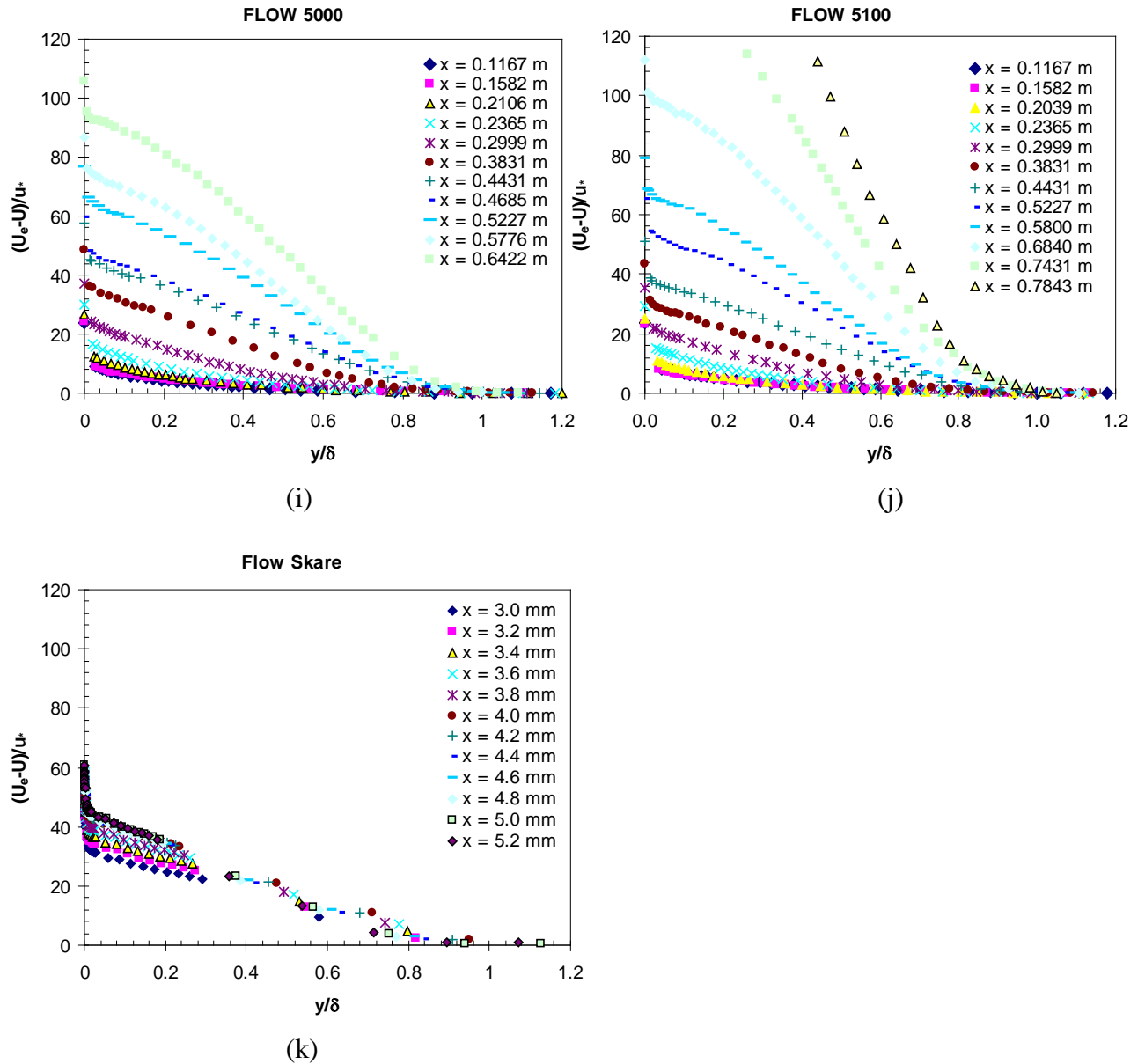
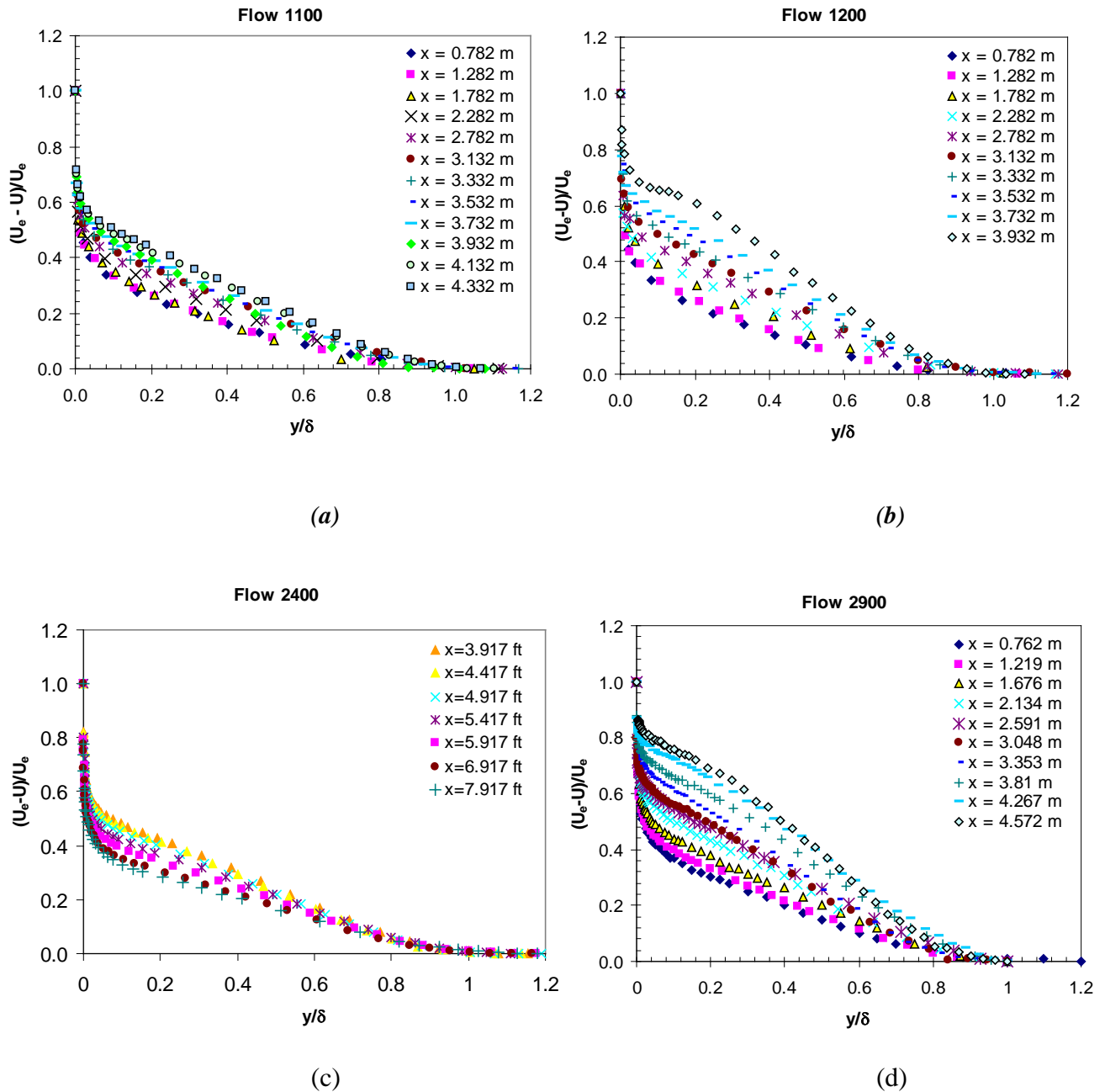
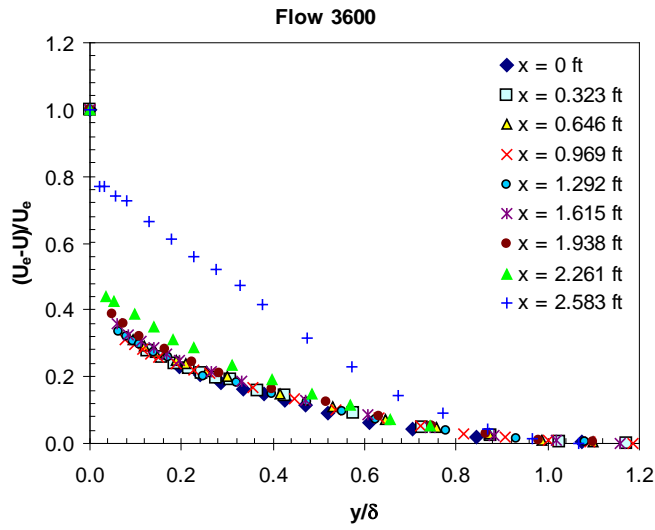


Figure 10.2 Velocity deficit scaled with friction velocity,  $u^*$  for a) Flow 1100, b) Flow 1200, c) Flow 2400, d) Flow 2900, e) Flow 3600, f) Flow 3700, g) Flow 3800, h) Flow 4000, i) Flow 5000, j) Flow 5100 and k) Flow Skare.

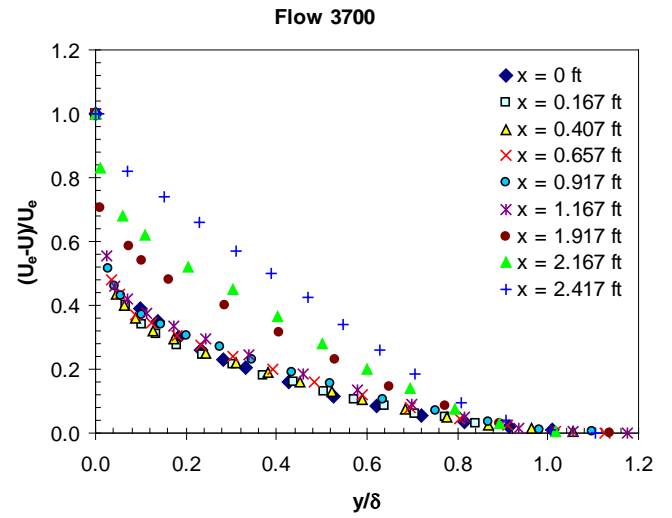
## Appendix IX Velocity deficit scaled with freestream velocity for 'other' flows.



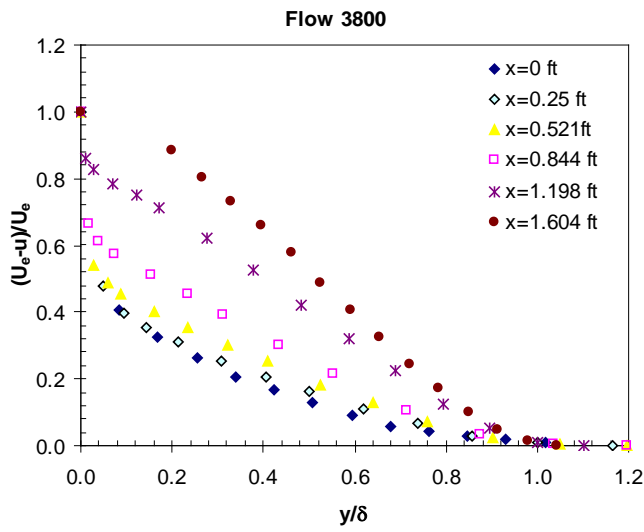
(figure continues next page)



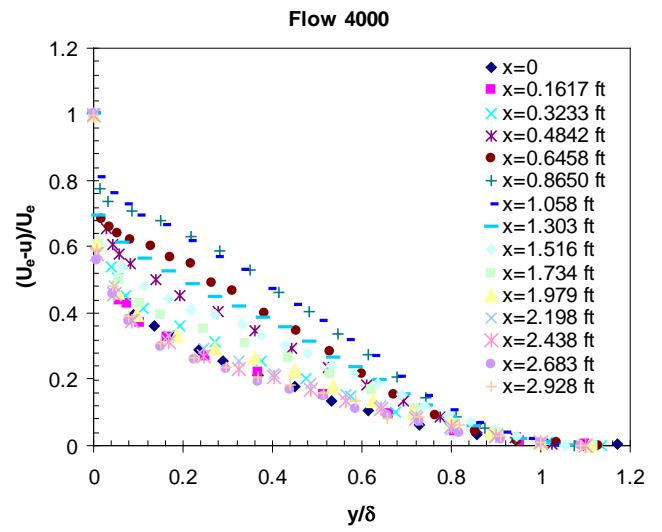
(e)



(f)



(g)



(h)

(figure continues next page)

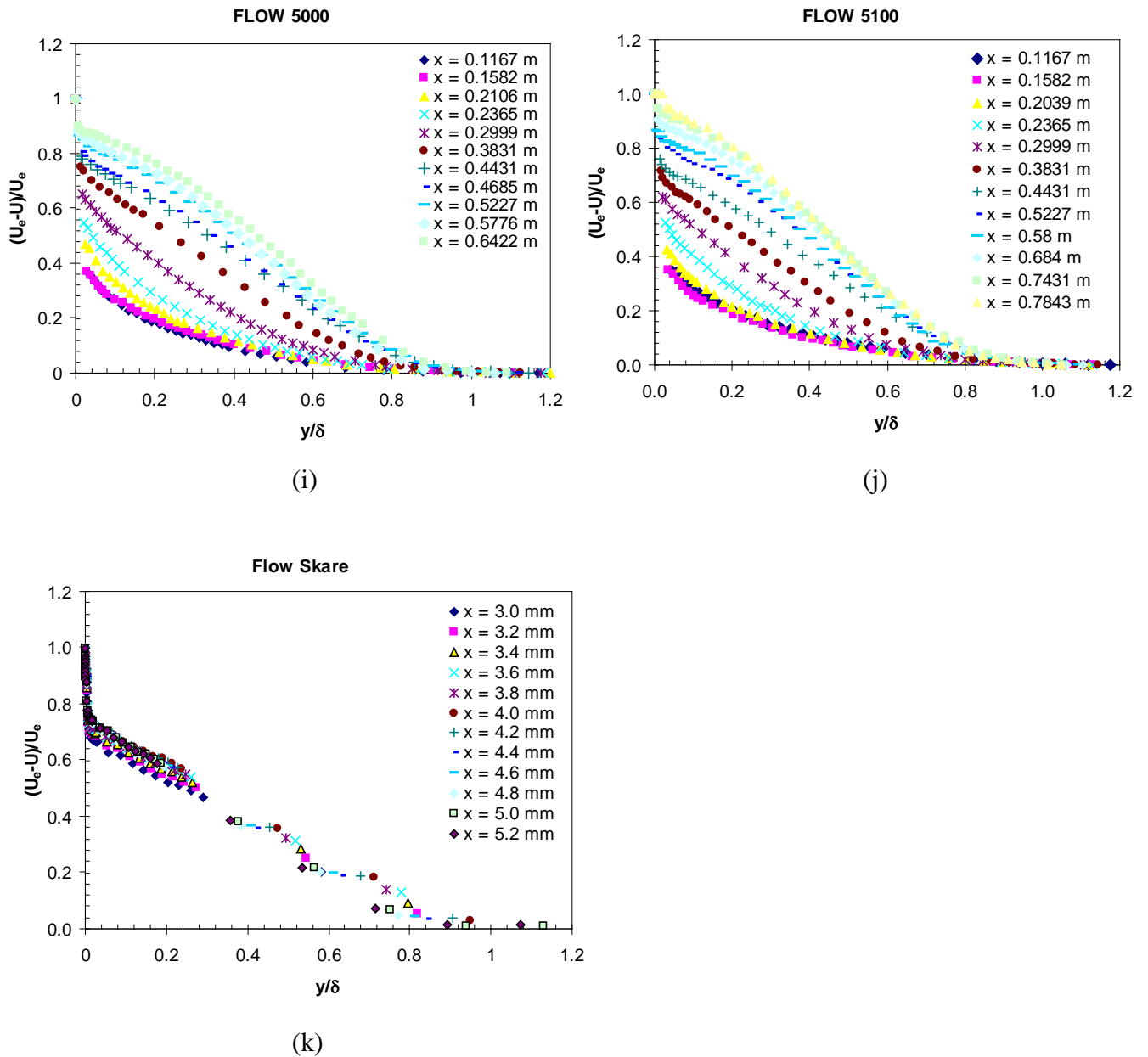


Figure 10.3 Velocity deficit scaled with free stream velocity,  $U_e$  for a) Flow 1100, b) Flow 1200, c) Flow 2400, d) Flow 2900, e) Flow 3600, f) Flow 3700, g) Flow 3800, h) Flow 4000, i) Flow 5000, j) Flow 5100 and k) Flow Skare.

## Appendix X Flow 141, plots.

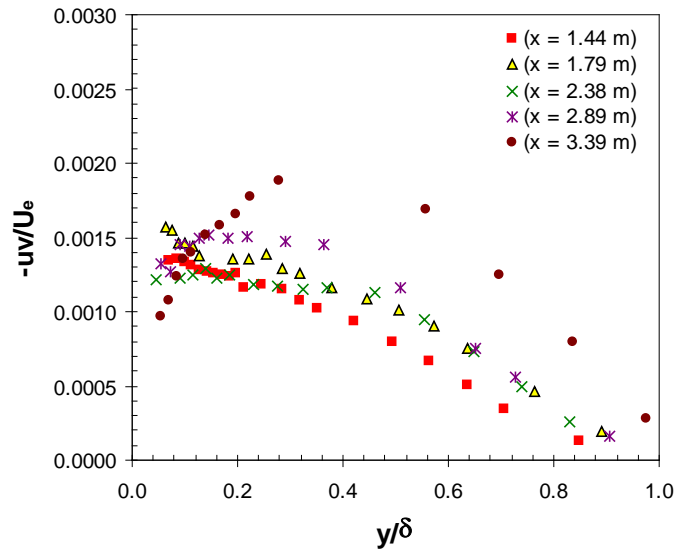


Figure 10.4 Flow 141,  $uv$  scaled with  $U_e$ . Demonstrating, in the flow direction,  $x$ , an increase in magnitude and a shift away from the wall of peak location.

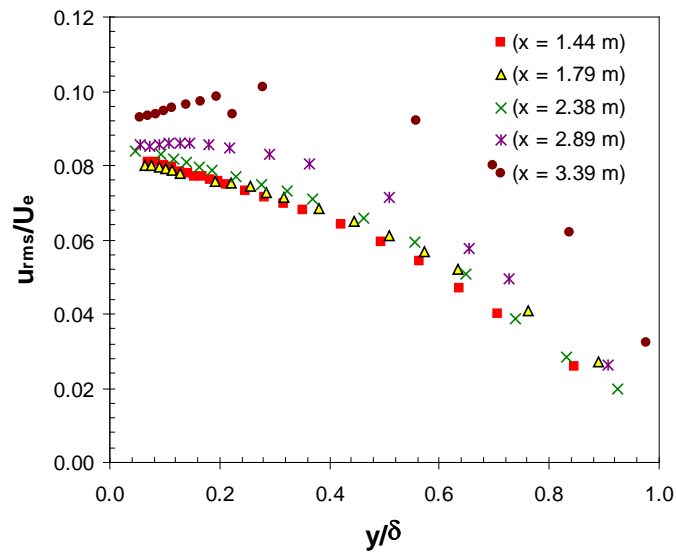


Figure 10.5 Flow 141.  $u_{rms}$  scaled with freestream velocity  $U_e$ .

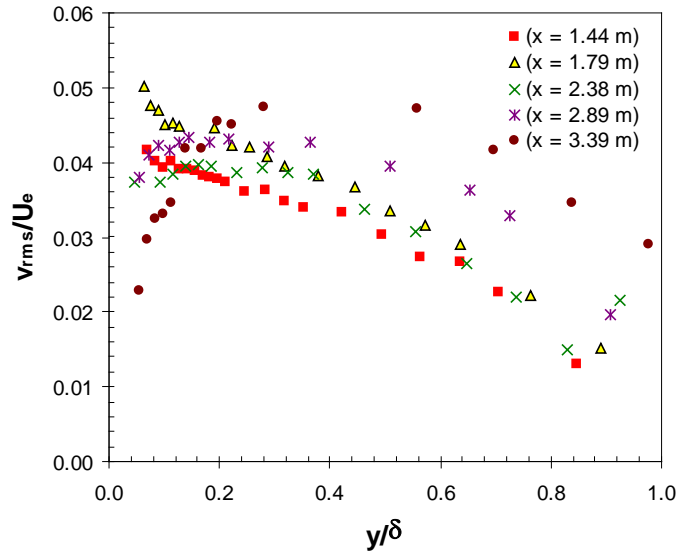


Figure 10.6 Flow 141.  $v_{rms}$  scaled with freestream velocity  $U_e$ .

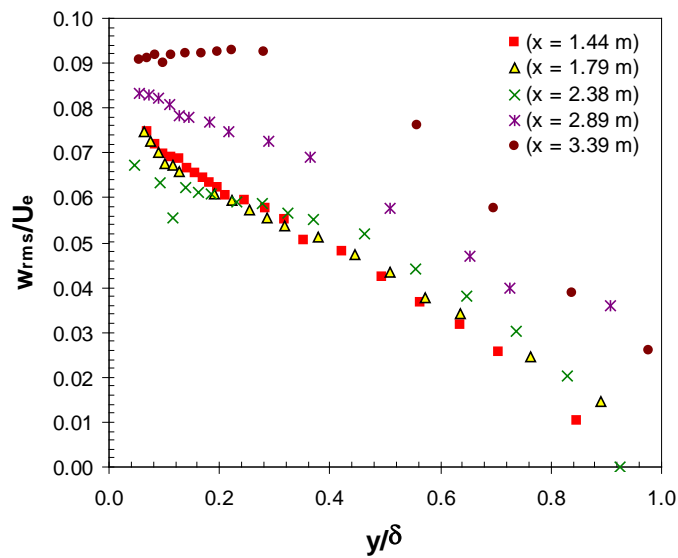


Figure 10.7 Flow 141.  $w_{rms}$  scaled with freestream velocity  $U_e$ .

## Appendix XI Comparison between Flow A and Flow B and Flow Skare

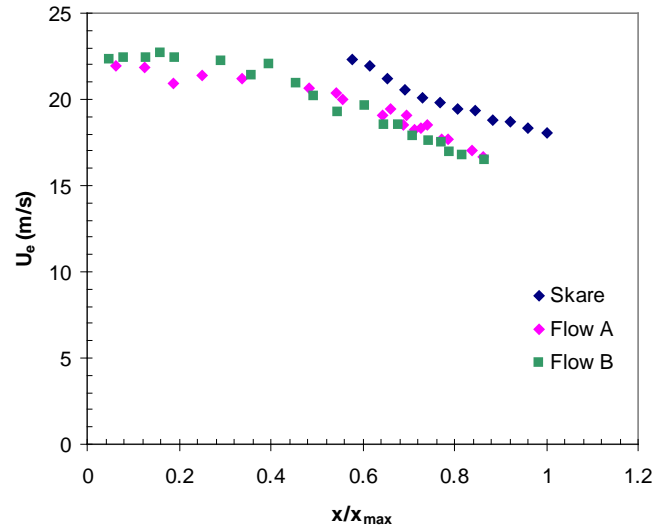


Figure 10.8 Comparison between Flow A, Flow B and Skare, demonstrating similarity of freestream velocity.

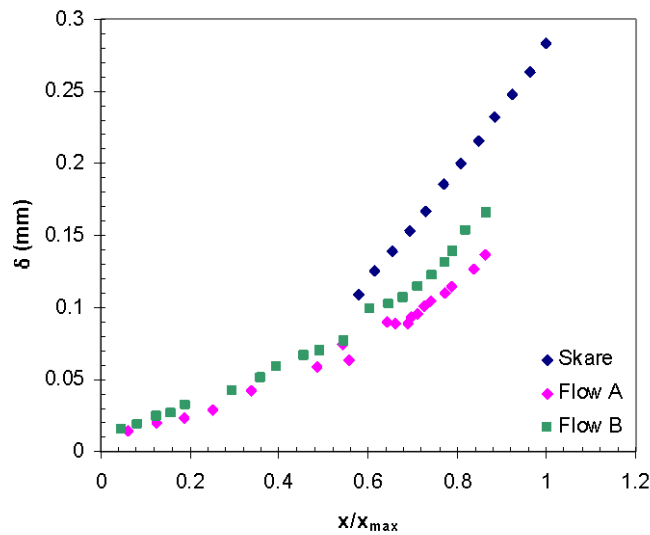


Figure 10.9 Comparison between Flow A, Flow B and Skare, demonstrating development of boundary layer thickness.

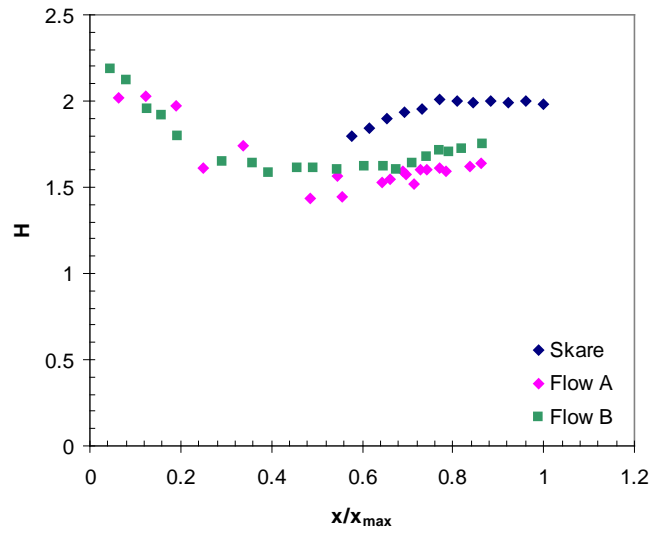


Figure 10.10 Comparison between Flow A, Flow B and Skare, demonstrating development of shape factor,  $H$ .

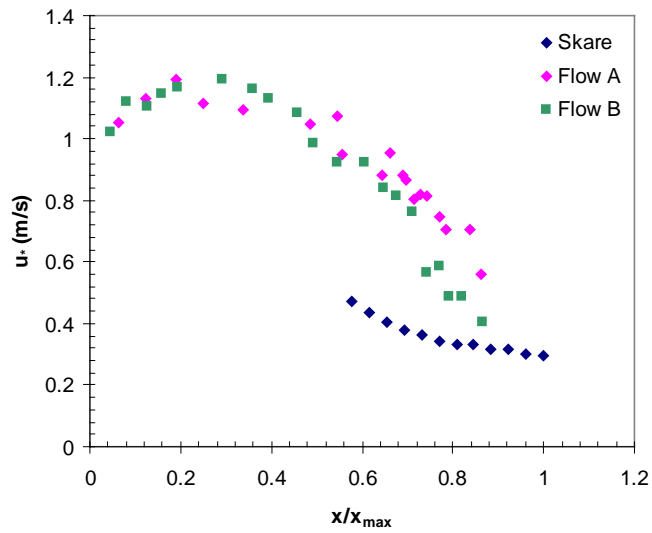


Figure 10.11 Comparison between Flow A, Flow B and Skare, demonstrating difference in behaviour of friction velocity.

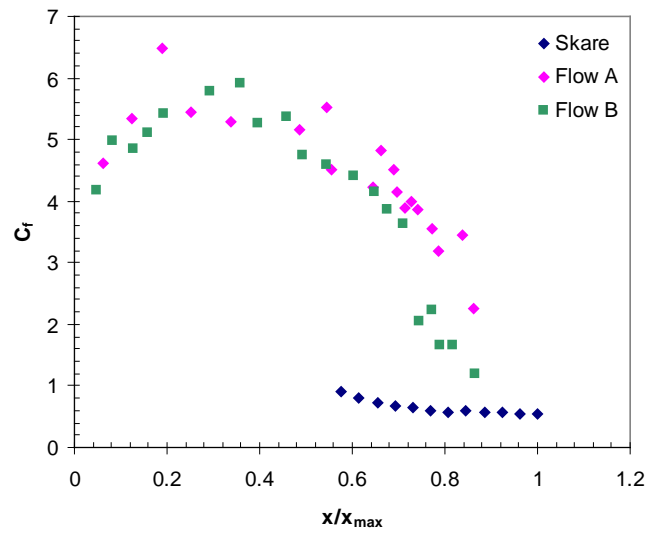


Figure 10.12 Comparison between Flow A, Flow B and Skare, demonstrating difference in skin friction coefficient,  $C_f$ .

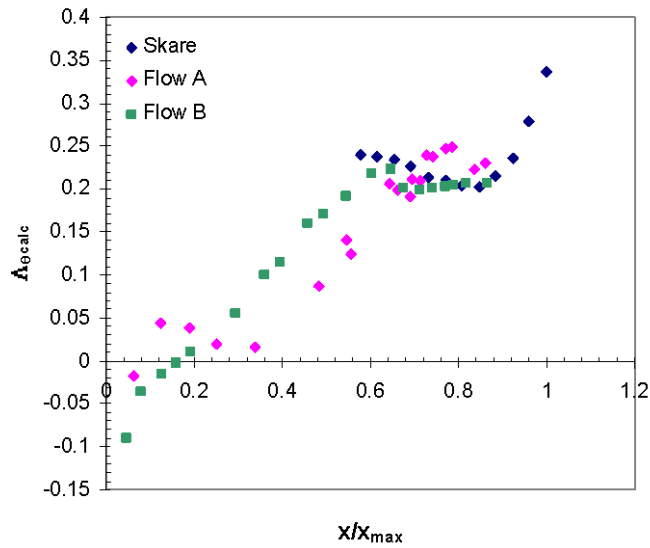
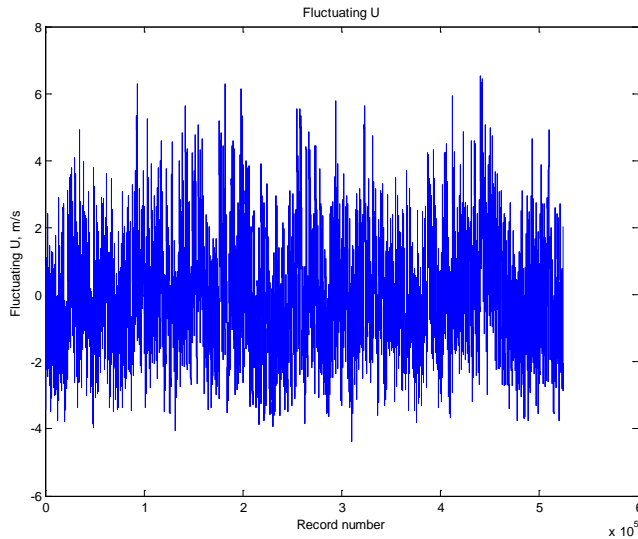


Figure 10.13 Comparison between Flow A, Flow B and Skare, demonstrating behaviour of  $A_{\theta_{calc}}$ . Note that all three flows exhibit a region of near constant  $A_{\theta_{calc}}$ .

## Appendix XII Matlab code for calculating isotropic dissipation.

### Step 1

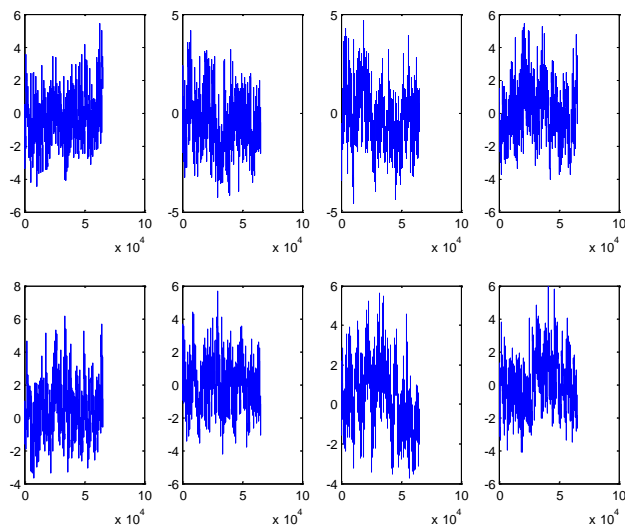
The original signal is converted to instantaneous velocity and then the fluctuating component is determined by subtracting the mean from each instantaneous velocity. Below is the signal as fluctuating U verses the record number.



### Step 2

The original signal is divided into 8 sub sections of equal length.

```
for i = 1:8
    segy(:,i) = y((i-1)*lengthofseg+1:lengthofseg*i,j);
end
```



### Step 3

Do an fft on each segment, scale and fold, Plot all 8 segments together.

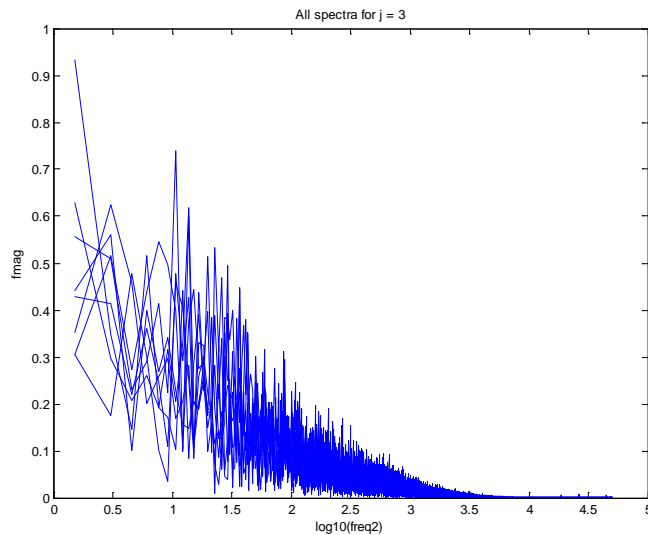
```

for k = 1: noofsegments
    spec(:,k) = fft(segY(:,k));
    spec(:,k) = spec(:,k)/npts;
    mag(:,k) = abs(spec(:,k));
    %figure(k)
    %plot(mag(:,k))

    % Fold spectra
    fmag(:,k) = mag(1:fpts,k);
    % Multitply by 2 except the first point
    fmag(2:fpts-1,k) = 2*fmag(2:fpts-1,k);
    % Create frequency scale
    freq2 = [linspace(0, sfreq/2, fpts)]';

    % Plot the freq spectrum of each section together.
    figure(j)
    plot(log10(freq2), fmag(:,k))
    words = ['All spectra for j = ', num2str(j)];
    title(words);
    xlabel('log10(freq2)')
    ylabel('fmag')
    hold on;
end

```

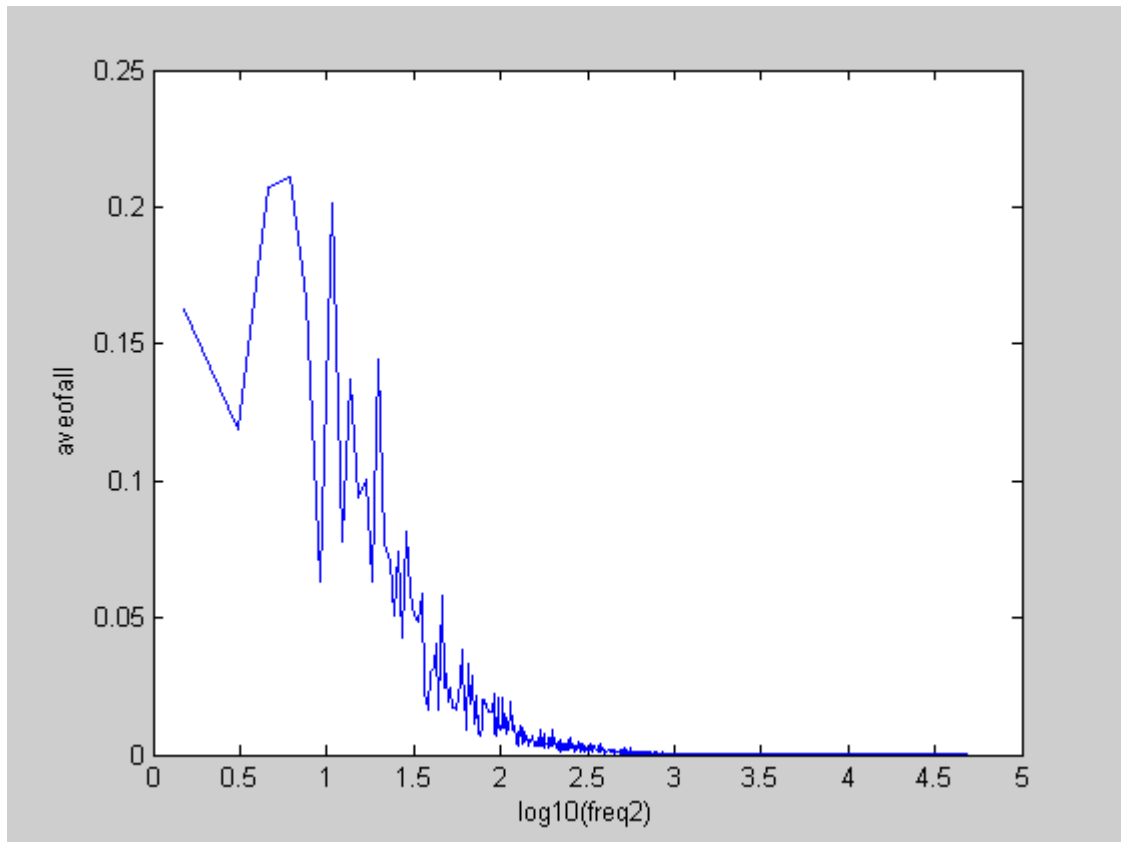


### Step 4

Average the spectra.

```
% Determine the average of these spectra
```

```
% The next line squares each element then average all columns to create a single
column
aveofall = mean(fmag.^2,2);
plot(log10(freq2), aveofall);
```



#### Step 5

Determine the sum of the element of the average spectra. This should be the same as the rms of the original signal.

```
uave(j) = sum(aveofall);
```

#### Step 6

Scale and plot

```
% Create the vertical and horizontal scales required, namely
```

```
% Vertical: aveU/2pi
```

```
% Horizontal: 2pi Freq /aveU
```

```
vertical = aveofall./freq2*(aveV(j)/(2*pi));
```

```
horz = 2*pi*freq2/aveV(j);
```

```
figure(j+200)
```

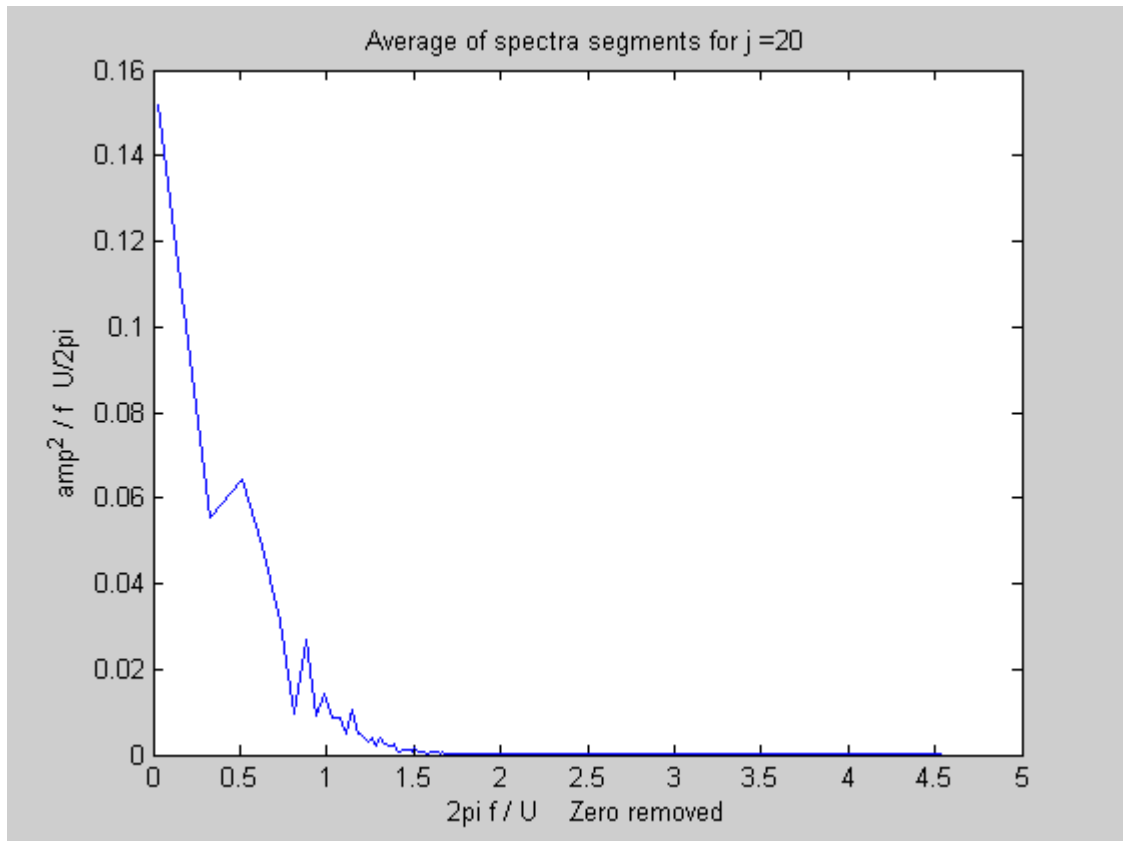
```
plot(log10(horz), vertical)
```

```
words = ['Average of spectra segments for j =', num2str(j)];
```

```
title(words);
```

```
xlabel('2pi f / U Zero removed')
```

```
ylabel('amp^2 / f U/2pi')
```



%The sum of the power spectrum array should be equal to the RMS^2 of the original signal.

```
uave(j) = sum(aveofall);
```

```
k1 = (2*pi*freq2)/aveV(j);
```

```
horizontal = k1; %height(j)/1000.*k1;
```

```
%vertical =( k1.^(5/3).*(aveofall.^2) .*aveV(j))./(2*pi);
```

```
E1k1 =aveofall./(df*2*pi/aveV(j));
```

```
vertical2 =( k1.^2) .* E1k1;
```

```
vertical3 =(E1k1 .* k1.^(5/3));
```

```
k1(1) = [];
```

```
horizontal(1) = [];
```

```
E1k1(1) = [];
```

```
vertical2(1) = [];
```

```
vertical3(1) = [];
```

```
line5 = -5/3*log10(horizontal);
```

```
area(j)=trapz(k1, E1k1);
```

```
area2(j)=trapz(k1, vertical2);
```

```
dissipation(j) = 15 * 1.5E-5 * area2(j);
```

```
end
```